Disentangling the chemodynamical history of the Milky Way disc with asteroseismology and spectroscopy

Friedrich Anders
Leibniz-Institut für Astrophysik Potsdam (AIP)

Publikationsbasierte Dissertation
zur Erlangung des akademischen Grades
doctor rerum naturalium (Dr. rer. nat.)
in der Wissenschaftsdisziplin Astrophysik

Eingereicht an der Mathematisch-Naturwissenschaftlichen Fakultät
der Universität Potsdam

Potsdam, den 15. Februar 2017

Eingereicht am 15.02.2017

1. Gutachter:	Dr. Cristina Chiappini Leibniz-Institut für Astrophysik Potsdam (AIP)
2. Gutachter:	Prof. Dr. Matthias Steinmetz Leibniz-Institut für Astrophysik Potsdam (AIP) /Universität Potsdam (UP)
3. Gutachter:	Prof. Dr. Kenneth Freeman The Australian National University (ANU)

Published online at the
Institutional Repository of the University of Potsdam:
URN urn:nbn:de:kobv:517-opus4-396681
http://nbn-resolving.de/urn:nbn:de:kobv:517-opus4-396681

Abstract

Galaxies are among the most complex systems that can currently be modelled with a computer. A realistic simulation must take into account cosmology and gravitation as well as effects of plasma, nuclear, and particle physics that occur on very different time, length, and energy scales. The Milky Way is the ideal test bench for such simulations, because we can observe millions of its individual stars whose kinematics and chemical composition are records of the evolution of our Galaxy. Thanks to the advent of multi-object spectroscopic surveys, we can systematically study stellar populations in a much larger volume of the Milky Way. While the wealth of new data will certainly revolutionise our picture of the formation and evolution of our Galaxy and galaxies in general, the big-data era of Galactic astronomy also confronts us with new observational, theoretical, and computational challenges.

This thesis aims at finding new observational constraints to test Milky-Way models, primarily based on infra-red spectroscopy from the Apache Point Observatory Galactic Evolution Experiment (APOGEE) and asteroseismic data from the CoRoT mission. We compare our findings with chemical-evolution models and more sophisticated chemodynamical simulations. In particular we use the new powerful technique of combining asteroseismic and spectroscopic observations that allows us to test the time dimension of such models for the first time. With CoRoT and APOGEE (CoRoGEE) we can infer much more precise ages for distant field red-giant stars, opening up a new window for Galactic archaeology. Another important aspect of this work is the forward-simulation approach that we pursued when interpreting these complex datasets and comparing them to chemodynamical models.

The first part of the thesis contains the first chemodynamical study conducted with the APOGEE survey. Our sample comprises more than 20,000 red-giant stars located within 6 kpc from the Sun, and thus greatly enlarges the Galactic volume covered with high-resolution spectroscopic observations. Because APOGEE is much less affected by interstellar dust extinction, the sample covers the disc regions very close to the Galactic plane that are typically avoided by optical surveys. This allows us to investigate the chemo-kinematic properties of the Milky Way's thin disc outside the solar vicinity. We measure, for the first time with high-resolution data, the radial metallicity gradient of the disc as a function of distance from the Galactic plane, demonstrating that the gradient flattens and even changes its sign for mid-plane distances greater than 1 kpc. Furthermore, we detect a gap between the high- and low-[α/Fe] sequences in the chemical-abundance diagram (associated with the thin and thick disc) that unlike in previous surveys can hardly be explained by selection effects. Using 6D kinematic information, we also present chemical-abundance diagrams cleaned from stars on kinematically hot orbits. The data allow us to confirm without doubt that the scale length of the (chemically-defined) thick disc is significantly shorter than that of the thin disc.

In the second part, we present our results of the first combination of asteroseismic and spectroscopic data in the context of Galactic Archaeology. We analyse APOGEE follow-up observations of 606 solar-like oscillating red giants in two CoRoT fields close to the Galactic plane. These stars cover a large radial range of the Galactic disc (4.5 kpc $\lesssim R_{\rm Gal} \lesssim$ 15 kpc) and a large age baseline (0.5 Gyr $\lesssim \tau \lesssim$ 13 Gyr), allowing us to study the age- and radius-dependence of the [α/Fe] vs. [Fe/H] distributions. We find that the age distribution of the high-[α/Fe] sequence appears to be broader than expected from a monolithically-formed old thick disc that stopped to form stars 10 Gyr ago. In particular, we discover a significant population of apparently young, [α/Fe]-rich stars in the CoRoGEE data whose existence cannot be explained by standard chemical-evolution models. These peculiar stars are much more abundant in the inner CoRoT field LRc01 than in the outer-disc field LRc01, suggesting that at least part of this population has a chemical-evolution rather than a stellar-evolution origin, possibly due to a peculiar chemical-enrichment history of the inner disc. We also find that strong radial migration is needed to explain the abundance of super-metal-rich stars in the outer disc.

Finally, we use the CoRoGEE sample to study the time evolution of the radial metallicity gradient in the thin disc, an observable that has been the subject of observational and theoretical debate for more than 20 years. By dividing the CoRoGEE dataset into six age bins, performing a careful statistical analysis of the radial [Fe/H], [O/H], and [Mg/Fe] distributions, and accounting for the biases introduced by the observation strategy, we obtain reliable gradient measurements. The slope of the radial [Fe/H] gradient of the young red-giant population (-0.058 ± 0.008 [stat.] ± 0.003 [syst.] dex/kpc) is consistent with recent Cepheid data. For the age range of $1 - 4$ Gyr, the gradient steepens slightly ($-0.066 \pm 0.007 \pm 0.002$ dex/kpc), before flattening again to reach a value of ~ -0.03 dex/kpc for stars with ages between 6 and 10 Gyr. This age dependence of the [Fe/H] gradient can be explained by a nearly constant negative [Fe/H] gradient of ~ -0.07 dex/kpc in the interstellar medium over the past 10 Gyr, together with stellar heating and migration. Radial migration also offers a new explanation for the puzzling observation that intermediate-age open clusters in the solar vicinity (unlike field stars) tend to have higher metallicities than their younger counterparts. We suggest that non-migrating clusters are more likely to be kinematically disrupted, which creates a bias towards high-metallicity migrators from the inner disc and may even steepen the intermediate-age cluster abundance gradient.

Zusammenfassung

Galaxien gehören zu den komplexesten physikalischen Systemen, die derzeit mit Computern modelliert werden können. Eine realistische Galaxiensimulation muss kosmologische Effekte genauso berücksichtigen wie die Gesetze der Plasma-, Kern-, und Teilchenphysik. Die Milchstraße ist ein ideales Labor für die Überprüfung solcher Simulationen, da moderne Teleskope die Kinematik und chemische Zusammensetzung von Millionen von Milchstraßensternen einzeln analysieren können und uns so einen Einblick in die Entstehungsgeschichte unserer Galaxie geben. Dank groß angelegter spektroskopischer Himmelsdurchmusterungen lassen sich seit Neuestem auch stellare Populationen in fernen Regionen der Milchstraße systematisch studieren. Dieser Datenreichtum hat das Potential, unseren Blick auf die Entstehung unserer kosmischen Heimat zu revolutionieren, konfrontiert die Forschung aber auch mit neuen beobachtungstechnischen, theoretischen und numerischen Herausforderungen.
Das Ziel dieser Arbeit ist es, moderne numerische Modelle der Milchstraße mittels neuer Beobachtungen zu testen. Hierbei benutzen wir vor Allem Infrarotspektroskopiedaten des Apache Point Observatory Galactic Evolution Experiment (APOGEE), sowie asteroseismische Daten der europäischen Exoplanetenmission CoRoT. Wir vergleichen unsere Resultate mit semianalytischen chemischen Entwicklungsmodellen und komplexeren chemodynamischen Simulationen, wobei uns die Kombination von asteroseismischen und spektroskopischen Daten erlaubt, zum ersten Mal die Zeitdimension solcher Modelle zu testen. Mit den CoRoT-APOGEE-Beobachtungen (kurz: CoRoGEE) lassen sich viel präzisere Altersbestimmungen für entfernte Riesensterne berechnen. Ein weiterer wichtiger Bestandteil dieser Arbeit ist die Verwendung sogenannter Mock-Beobachtungen, bei denen ein chemodynamisches Milchstraßenmodell so "beobachtet" wird wie die Milchstraße selbst, unter möglichst realistischer Berücksichtigung aller Beobachtungseffekte. Dies erlaubt uns akkuratere Vergleiche von Modellen und Daten, und ermöglicht eine einfachere Interpretation.
Der erste Teil dieser Arbeit enthält eine chemodynamische Untersuchung von mehr als 20,000 roten Riesensternen, die sich bis zu 6 kpc (20,000 Lichtjahre) entfernt befinden. Diese Studie, die mit den ersten APOGEE-Daten gemacht wurde, konnte so das galaktische Volumen, das mit hochauflösender Spektroskopie je beobachtet wurde, dramatisch vergrößern. Weil die Sensitivität von APOGEE als Infrarotexperiment weit weniger durch interstellare Extinktion behindert wird, dringt unsere Stichprobe außerdem in die Regionen nahe der galaktischen Ebene vor, die typischerweise von optischen Durchmusterungen vermieden werden. Das erlaubt es uns, die chemodynamischen Eigenschaften der dünnen Milchstraßenscheibe außerhalb der unmittelbaren Sonnenumgebung zu studieren. Wir können beispielsweise zum ersten Mal mit hochauflösender Spektroskopie den radialen Metallizitätsgradienten der Scheibe als Funktion des Abstands von der Scheibenebene messen und zeigen, dass dieser Gradient oberhalb von 1 kpc positiv ist. Außerdem detektieren wir eine Lücke zwischen den Populationen I und II im chemischen [α/Fe]-[Fe/H]-Häufigkeitsdiagramm, die im Gegensatz zur früheren Datenerhebungen schwerlich durch Selektionseffekte erklärt werden kann. Da für viele Sterne außerdem 6-dimensionale Phasenrauminformationen vorliegen, können wir außerdem chemische Häufigkeitsdiagramme analysieren, in denen stellare Passanten aus anderen galaktischen Regionen ausgeblendet werden. Unsere Daten bestätigen außerdem zweifelsfrei die kurze Skalenlänge der dicken Milchstraßenscheibe (Population II).
Im zweiten Teil der Arbeit nutzen wir zum ersten Mal kombinierte seismisch-spektroskopische Beobachtungen zum Zwecke der Galaktischen Archäologie. Wir analysieren dabei APOGEE-Beobachtungen von 606 roten Riesensternen in zwei CoRoT-Himmelsfeldern nahe der Galaktischen Ebene. Die Sterne sind über einen weiten Bereich der Galaktischen Scheibe verteilt (4.5 kpc $\lesssim R_{\rm Gal} \lesssim$ 15 kpc) und decken eine große Altersspanne ab (0.5 Gyr $\lesssim \tau \lesssim$ 13 Gyr), was es uns erlaubt, sowohl die Alters- als auch die radiale Abhängigkeit der [α/Fe]-[Fe/H]-Verteilungen zu untersuchen. Dabei konstatieren wir, dass die Altersverteilung der Population-II-Sterne breiter ist als man es für ein monolithisches Kollaps-Szenario der dicken Scheibe erwarten würde. Vor Allem liegt das an einer vorher nicht bekannten, aber signifikanten Population scheinbar junger [α/Fe]-reicher Sterne, deren Existenz mit Standardmodellen für die chemische Evolution der Galaktischen Scheibe nicht erklärbar ist. Diese eigentümlichen Objekte sind viel häufiger in der inneren Scheibe zu finden als in der äußeren, was darauf hindeutet, dass zumindest ein Teil dieser Population tatsächlich einen physikalischen Ursprung hat (etwa eine besondere chemische Entwicklung nahe des Galaktischen Balkens) und nicht etwa auf systematische Fehler in der Altersbestimmung zurückzuführen ist. Ein weiteres Resultat ergibt sich aus der Fülle von super-metallreichen Sternen in der äußeren Scheibe: der Effekt radialer Sternmigration scheint dort eine größere Rolle zu spielen als bisher angenommen.
Im letzten Teil nutzen wir die CoRoGEE-Stichprobe, um die Zeitentwicklung des radialen Metallizitätsgradienten der dünnen Scheibe zu studieren; eine Unbekannte, die sowohl unter Theoretikern als auch unter Beobachtern in den letzten zwanzig Jahren immer wieder für Diskussionen sorgte. Wir teilen dazu die CoRoGEE-Daten in sechs Altersgruppen ein und erhalten durch eine sorgfältige statistische Analyse der radialen [Fe/H] Verteilungen unter Berücksichtigung systematischer Unsicherheiten verlässliche Werte für den Metallizitätsgradienten. Dessen Anstieg für die junge Population der roten Riesen (-0.058 ± 0.008 [stat.] ± 0.003 [syst.] dex/kpc) ist konsistent mit den neuesten Messungen an Cepheiden. Im Altersbereich $1 - 4$ Gyr verzeichnen wir einen leicht steileren Gradienten ($-0.066 \pm 0.007 \pm 0.002$ dex/kpc), der für ältere Sterne (6–10 Gyr) wieder flacher ausfällt (~ -0.03 dex/kpc). Diese Altersabhängigkeit des Metallizitätsgradienten lässt sich unter anderem durch ein Modell erklären, in dem der Metallizitätsgradient des interstellaren Medium etwa konstant bei -0.07 dex/kpc liegt und in alten stellaren Populationen durch kinematische Effekte wie stellare Migration verwaschen wird. Stellare radiale Migration eröffnet uns außerdem eine elegante Erklärung für die verwundernde Tatsche, dass Sternhaufen mittleren Alters in der Sonnenumgebung oft höhere Metallizitäten aufweisen als junge Haufen. Um das zu erklären, schlagen wir ein Szenario vor, in dem nichtmigrierende Haufen eher durch gravitative Wechselwirkungen in der Scheibe zerstört werden als migrierende, was in der Sonnenumgebung eine Verzerrung zu Gunsten metallreicherer Haufen aus der inneren Scheibe nach sich zöge und, wie ebenfalls beobachtet, zur Folge hätte, dass der Metallizitätsgradient der mittelalten Haufenpopulation viel steiler wäre als der der jungen Haufen.

Contents

hoje eu não tô afim
de corre-corre e confusão
eu quero passar a tarde
estourando plastico bolha

Karina Buhr, Plastico Bolha, 2012

[...] Man rufe sich am Abend den vergangenen Tag zurück, also die »jüngste Vergangenheit« (die auch getrost noch als »älteste Gegenwart« definiert werden könnte): hat man das Gefühl eines »epischen Flusses« der Ereignisse? Eines Kontinuums überhaupt?
Es gibt diesen epischen Fluß, auch der Gegenwart, gar nicht; Jeder vergleiche sein eigenes beschädigtes Tagesmosaik!
Die Ereignisse unseres Lebens springen vielmehr. Auf dem Bindfaden der Bedeutungslosigkeit, der allgegenwärtigen langen Weile, ist die Perlenkette kleiner Erlebniseinheiten, innerer und äußerer, aufgereiht. Von Mitternacht zu Mitternacht ist gar nicht »1 Tag«, sondern »1440 Minuten« (und von diesen wiederum sind höchstens 50 belangvoll!). Aus dieser porösen Struktur auch unserer Gegenwartsempfindung ergibt sich ein löcheriges Dasein [...]

Arno Schmidt, Bargfelder Werkausgabe, III, 3, S. 167f., 1995

Sin humildad no hay aprendizaje posible.

Juan Carlos Monedero, Curso urgente de política para gente decente, 2013

Chapter 1

Introduction: The Galactic disc

Friedrich Anders

(Affiliations can be found after the references)

Abstract

The field of Galactic astronomy is currently one of the most active branches of astrophysics. While systematic studies of Milky-Way stellar populations were until recently confined to a very small region in the solar vicinity, the advent of multi-object spectroscopy has enlarged the observable volume of our Galaxy by several magnitudes. A multitude of spectroscopic stellar surveys, operating at different wavelengths and resolutions, has opened up the big-data era of Galactic astrophysics. This has undoubtedly enlarged our knowledge about the Milky Way and galaxy evolution, but it also presents new observational, theoretical, and computational challenges. Here I review the current state of research within the topic of this thesis, focussing on observational results related to the Galactic stellar disc. I give a short overview on the formation of galaxies in the cosmological context, the structure of the Milky Way, formation scenarios of the Galactic stellar disc, and recent developments in spectroscopic stellar surveys. I then focus on a new powerful technique: asteroseismology, especially when combined with spectroscopic observations, allows to infer much more precise ages for field red-giant stars, opening up a new window for Galactic archaeology. The application of this technique to study the Galactic disc is the central theme of this thesis. The thesis outline and summary of the results of each chapter conclude this introduction.

1.1. The Milky Way galaxy

Our galaxy, the Milky Way (MW), is but one of a myriad of its kind: a giant gravitationally bound system of nuclear reactors dispersed into the expanding Universe, producing and recycling the chemical elements necessary to build complex lifeforms. At a first glance, an external observer would probably classify it as a barred spiral galaxy of Hubble type SBbc (Bland-Hawthorn & Gerhard 2016). In an edge-on view of the MW, the Galactic disc (hosting most of the MW's stars, dust, and gas) is clearly the dominant characteristic, followed by the bulge and bar, and the Galactic halo.

Our Sun lies about 8 kpc from the Galactic centre, in the rotating stellar disc. The amount of stars and dust in the disc, in combination with the Sun's position, made it difficult for the first astronomers to infer the galactic nature of the MW. Although the MW has been suspected to consist of stars even by the ancient Greeks, it took until Galilei to resolve the silvery band that stretches across the night sky into stars. And it was only the observations of Slipher (1917) and Hubble (1926) that demonstrated that the Milky Way does not contain the entire visible Universe (the Great Debate of the 1920s), but is one of many galaxies.

The field of galaxy astrophysics is one of the cornerstones of modern astronomy, and has been evolving rapidly since the last century. Several fundamental questions about galaxy evolution can best be answered by detailed studies of Local Group galaxies, most notably, the Milky Way (Freeman & Bland-Hawthorn 2002; Turon et al. 2008). Through the analysis of the light of stars and gas we see in our Galaxy today, we can infer their motions, chemical compositions and ages, and thus form a comprehensive picture of how our galaxy assembled and evolved (Scheffler & Elsässer 1982; Binney & Merrifield 1998; Binney & Tremaine 2008; Pagel 2009). However, the problem of the formation history of the MW is entwined with problems of nuclear and particle physics, stellar evolution, and cosmology, that have to be tackled simultaneously.

Within the widely accepted Lambda Cold Dark Matter Theory (ΛCDM), our expanding Universe was produced in a Big Bang, cooled down rapidly, dark matter decoupled from baryonic matter and began to form gravitationally bound haloes from tiny inhomogeneities of the primordial matter distribution. Baryonic matter then also decoupled, forming the elementary particles of the Standard Model of Particle Physics, and started to fall into the dark-matter haloes to form the first stars, galaxies, clusters of galaxies, and bigger structures, that can still be observed today. The main parameters of ΛCDM and other cosmological models can be determined very accurately by jointly analysing the angular power spectrum of the cosmic microwave background radiation, galaxy clustering, weak gravitational lensing, and supernova distance-redshift relations.

In some aspects, however, galaxy formation theory appears to be posing significant challenges to Cosmology. At low redshift, smaller-scale baryonic processes appear to smear out or even destroy the initial distribution of baryonic matter. Among these processes are satellite accretion and galaxy mergers, tidal disruption of stellar systems and secular processes in spiral galaxies (e.g. gas flows, radial mixing, disc heating etc., see section 3.4.2 for details). Is our current understanding of cosmology and the physics of the early Universe compatible with galaxy counts at intermediate and low redshift, especially with the properties of our Galactic environment? Which processes are dominating galaxy evolution at different times? Can we reconstruct the accretion and star formation history of our Galaxy in detail? The newly emerged field of Galactic Archaeology or Near-field Cosmology (Freeman & Bland-Hawthorn 2002) provides tools that help answer these questions. On the observational side, the astrometric Gaia mission, accompanied by massive wide-field photometric and spectroscopic stellar surveys, is opening new views on the more remote regions of the Galaxy and the Local

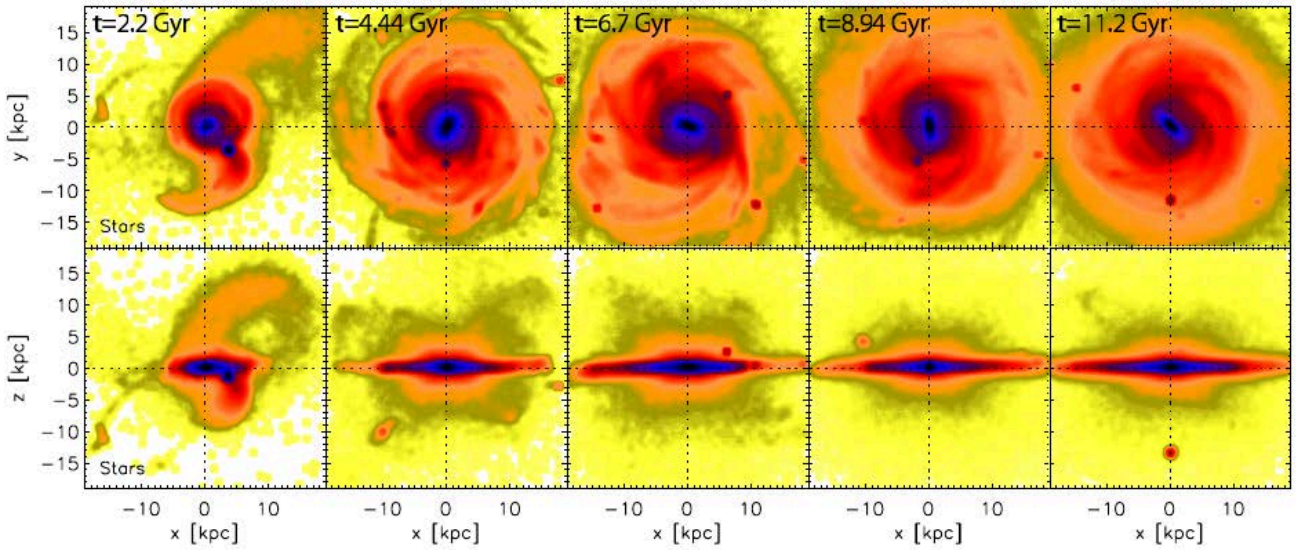

Figure 1.1. Example of a simulated MW-like galaxy in the cosmological context. The top row shows five face-on snapshots, the bottom row the corresponding edge-on views. The underlying tree-SPH N-body simulation of a barred spiral galaxy by Martig et al. (2012) has an early major-merger event at ∼ 2 Gyr and a more quiescent accretion history afterwards. Minchev, Chiappini, & Martig (2013) employed this simulation for their hybrid chemo-dynamical MCM model that was used extensively throughout this thesis. Figure from Minchev et al. (2013).

Group (see 3.2.2). On the theoretical side, N-body and hydrodynamic computer simulations of galaxy formation are starting to produce realistic MW-like galaxies that satisfy a multitude of observational constraints.

1.2. The structure of the Galactic stellar disc

Following Rix & Bovy (2013), I will distinguish characterising the present-day state of the Galaxy from inferring its formation and evolution. Although these tasks are naturally entwined, a satisfying answer to the latter is much more challenging and requires highly-sophisticated models that have begun to emerge over the past years. Even the seemingly simple problem of measuring the current overall characteristics of the Milky Way, such as its gravitational potential, its detailed stellar density profile, or the spatial distribution of chemical abundances over the entire disc, is far from solved to a satisfactory degree (Binney & Tremaine 2008; Binney & Sanders 2016). In this section, we briefly summarise the overall characteristics of the Galactic stellar disc. The most recent compilation of all relevant Galactic structural parameters can be found in Bland-Hawthorn & Gerhard (2016).

The MW's stellar disc (which I will refer to as "the disc" in the following) is a very thin and almost circular structure; when we look at the sky on a dark night, the Disc stars appear as a narrow luminous band stretching across the heavens. Like most spiral-galaxy discs, it has a flat rotation profile: stars move around the Galactic centre in nearly circular orbits at about 240 km/s, so that the Sun takes roughly 250 Myr to complete its orbit. The total luminosity of the disc is estimated to be about $2 \cdot 10^{10} L_{\odot}$, its stellar mass amounts to around $5 \cdot 10^{10} M_{\odot}$, the local stellar disc density is $\rho_{\odot} \simeq 0.043 M_{\odot}/\mathrm{pc}^3$ (McKee et al. 2015).

1.2.1. Thin and thick disc(s)

The disc is composed of multiple stellar populations that follow roughly exponential density profiles and stretch out to at least 15 kpc, probably further. In the inner Galaxy, the disc overlaps with the Galactic bulge, in the outer part it appears to be strongly warped and flaring (López-Corredoira et al. 2002; Reylé et al. 2009; Amores et al. 2017). It is often decomposed into two or more subpopulations, defined by either geometry, kinematics, chemistry, or age. The most popular division was introduced by Gilmore & Reid (1983) who used stellar number counts towards the Northern Galactic Pole to establish the existence of an older, metal-poor, and kinematically warm *thick disc* and a younger *thin disc*, a stellar population which is richer in metals and more confined to the Galactic plane. Although the thin disc accounts for 80 – 94% of the stars in the immediate solar vicinity (Fuhrmann 2008; Jurić et al. 2008; Just & Jahreiß 2010), and most of the MW's young massive stars as well as gas and dust, the thick disc could be as massive as the thin disc, because it is more centrally concentrated (Bensby et al. 2011; Cheng et al. 2012; Anders et al. 2014) and is likely to host a significant population of dim low-mass stars and dark stellar remnants (Fuhrmann et al. 2012, 2017, but see Bland-Hawthorn & Gerhard 2016 for a different view).

In addition to the kinematic and geometric separation of the thick and thin disc, high-resolution spectroscopic surveys have revealed two distinct populations in the [α/Fe] vs. [Fe/H] diagram.[1] α-elements (or rather: isotopes) can be built from $^4_2$He nuclei, e.g. ^{12}C, ^{16}O, ^{20}Ne, ^{24}Mg etc., and are mostly produced by massive short-lived stars exploding in type II supernovae (SNe). Type Ia SNe, on the other hand, produce mostly iron-peak elements and typically explode after ∼ 1 Gyr. Therefore, the features of the [α/Fe] vs. [Fe/H] diagram often serve as a chemical clock in the absence of a more fundamental age measurement (Pagel 2009; Matteucci 2012). In the solar vicinity, the two disc populations in this diagram correlate well with the kinematic thin and thick discs (Gratton et al. 1996, 2000; Fuhrmann 1998). Fig. 1.2 illustrates that the existence of two distinct chemical patterns of the two populations could be explained by a double peak

[1] Throughout this text, the abundance of a chemical element X heavier than helium (commonly dubbed "metals") is defined as $[\mathrm{X/H}] = \log_{10}(n_\mathrm{X}/n_\mathrm{H}) - \log_{10}(n_\mathrm{X}/n_\mathrm{H})_{\odot}$. Here, n_X and n_H are the number densities of nuclei of element X and hydrogen in the stellar photosphere, and $\odot$ denotes solar values.

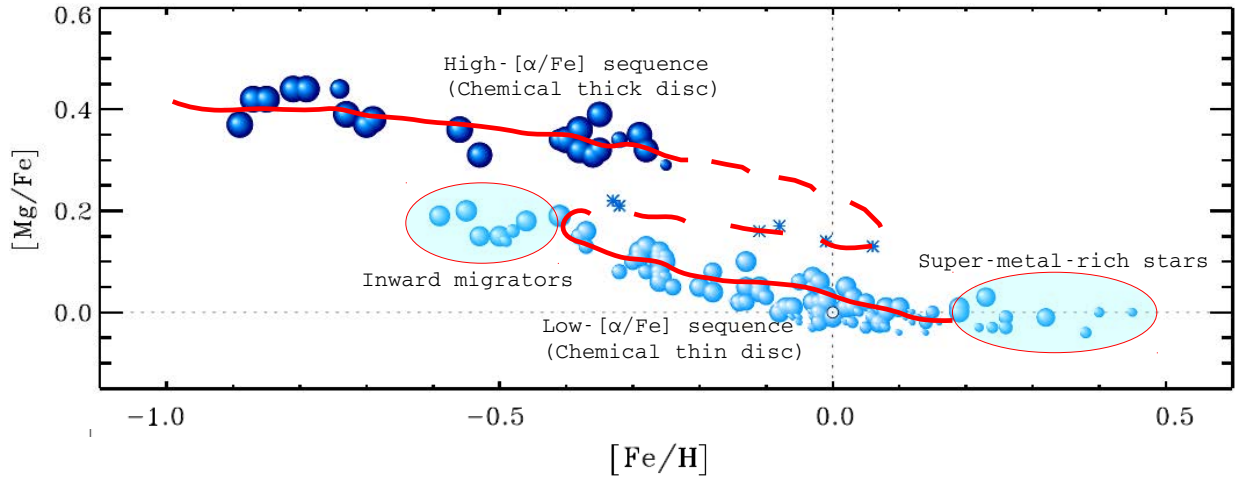

Figure 1.2. Illustration of the two-infall scenario for the formation of the Galactic thin and thick discs. In this [Mg/Fe] vs. [Fe/H] diagram of the volume-complete solar-neighbourhood sample of Fuhrmann et al. (2017) we are highlighting the thin- and thick-disc sequences, as well as populations that cannot be explained by simple chemical-evolution models even in the two-infall scenario (red line). Figure adapted from Fuhrmann et al. (2017).

in the Galactic star-formation rate, with an early star-formation burst forming the halo as well as part of the bulge and thick disc, and a second, more quiescent phase of star formation, triggered by newly infalling gas, forming the thin disc (e.g. Chiappini et al. 1997, 2001; Bournaud et al. 2009; Chiappini 2009; Fuhrmann et al. 2017).

Other possible thick-disc formation scenarios, motivated by cosmological simulations of galaxy formation and observations of external galaxies, include a thick disc created by minor mergers (Abadi et al. 2003), disc heating by satellite infall (Villalobos & Helmi 2008), and secular disc heating. Over the past years it has become clearer that probably all of the above effects are important ingredients for a realistic picture of the formation of our Galaxy (e.g. Chiappini 2015). The question that remains is which effects dominate during which phases of the evolution, and how can we quantify them?

1.2.2. The disc's relation to the Galactic bulge and halo

Apart from the Disc, two other important components contribute to the stellar mass of the MW: the Bulge (30% of the total stellar mass), and the Halo (∼ 1%). The Galaxy's central regions in the Southern sky form an elliptical Bulge that extends well beyond the disc's thickness. Whereas the motions of stars in the disc are dominated by rotation, the Bulge is dominated by random motion. While interstellar dust extinction heavily obscures our view of the Galactic plane, infrared (IR) and radio observations have established that the center of the Bulge harbours a supermassive black hole ($M_{\rm BH} \approx 4.2 \cdot 10^6 M_\odot$; Bland-Hawthorn & Gerhard 2016 and references therein). The total stellar mass in the bulge amounts to $\sim 2 \cdot 10^{10} M_\odot$ (Minniti & Zoccali 2008). The dynamics of the inner Disc and Bulge are strongly influenced by the Galactic Bar, whose presence has also been established by IR photometry and radio observations of gas kinematics (e.g., Blitz & Spergel 1991). Its gravitational potential creates several orbital resonances in the Disc, even in the Solar Neighbourhood where several co-moving groups of stars can be explained by resonances induced by the Galactic Bar (Martinet 1984; Dehnen 2000; Bovy 2010; Minchev et al. 2010), sometimes in combination with spiral arms (Antoja et al. 2009).

The MW stellar halo comprises a slightly oblate inner spheroid containing an old population of field stars and globular clusters that can be almost as old as the Galaxy itself (Carollo et al. 2007; Jurić et al. 2008), and an outer halo consisting of accreted material from disrupted satellite galaxies. The net rotation of the inner halo is consistent with zero, while the outer parts seem to be even counterrotating with respect to the Disc (Ivezić et al. 2008). Halo stars can be very metal-poor, reaching down to below 10^{-7} of the solar iron content (Keller et al. 2014). The metallicity distribution of halo stars is broad and exhibits a gradient with Galactocentric distance (Carollo et al. 2007, 2010; Fernández-Alvar et al. 2015). The baryonic halo, however, forms only a tiny fraction of the Galaxy's mass, no more than about $10^9 M_\odot$, compared to the total mass inferred from measurements of the orbital velocities of gas and stars in the outer Galaxy ($M_{\rm MW} \gtrsim 10^{12} M_\odot$; e.g., Reid et al. 2009; Gnedin et al. 2010; Piffl et al. 2014), providing strong evidence for the existence of a non-baryonic dark matter halo.

1.3. Industrial Galactic astronomy

1.3.1. Spectroscopic stellar surveys

The era of spectroscopic stellar surveys started in 2003: the RAdial Velocity Experiment (RAVE; Steinmetz et al. 2006; Zwitter et al. 2008; Siebert et al. 2011; Kordopatis et al. 2013; Kunder et al. 2017) used the vacant multi-object facility of the 6dF redshift survey (Jones et al. 2004) at the UK Schmidt Telescope at AAO in Siding Spring to conduct a massive survey of the Southern Sky. RAVE assembled medium-resolution CaII-triplet spectra ($R \sim 7500, \lambda = 8410 - 8795$ Å) for almost 500,000 stars at typical distances of 0.3 – 3 kpc from the Sun, thereby constraining local Galactic-disc properties (Siebert et al. 2008; Veltz et al. 2008; Ruchti et al. 2011; Boeche et al. 2013a,b, 2014; Williams et al. 2013) and the mass of the Milky Way (Piffl et al. 2014), enabling the search for chemo-dynamical substructures (Seabroke et al. 2008; Kunder et al. 2014), and providing a test bench for spectral classification and analysis algorithms (Boeche et al. 2011; Matijevič et al. 2012; Casey et al. 2016). Following the example of RAVE, two other medium-resolution surveys of smaller scope were soon conducted: the

BRAVA (Rich et al. 2007; Howard et al. 2008; Kunder et al. 2012) and ARGOS (Ness et al. 2012; Freeman et al. 2013; Ness et al. 2013a,b) surveys were able to gain unprecendented knowledge about the central parts of the MW (for a review, see Sec. 4.2 of Bland-Hawthorn & Gerhard 2016).

The Sloan Extension for Galactic Understanding and Exploration (SEGUE-I/II; Yanny et al. 2009b, Rockosi et al., in prep.) was the next big stellar survey impacting the field of Galactic Archaeology. Using the SDSS telescope at APO (Gunn et al. 2006), it obtained lower-resolution spectra ($R \sim 2000$) for about 360,000 fainter stars, covering a broad spectral range in the optical (385 − 920 nm). Focussing on distant stellar populations, SEGUE contributed to several important results both regarding the structure of the disc (Lee et al. 2011b; Bovy et al. 2012a,b; Cheng et al. 2012; Schlesinger et al. 2012; Minchev et al. 2013, 2014b, Brauer et al. 2017, in prep.) and the formation of the halo (e.g. Aoki et al. 2008; Yanny et al. 2009a; Kollmeier et al. 2010; Gómez et al. 2012; Janesh et al. 2016). As in the case of RAVE, the development of a fast and efficient software for deriving stellar atmospheric parameters and elemental abundances was essential for the success of the survey. The SEGUE Stellar Parameter Pipeline (Allende Prieto et al. 2008; Lee et al. 2008a,b; Smolinski et al. 2011; Lee et al. 2011a) is able to compute reliable effective temperatures, metallicities, [α/Fe] and [C/Fe] abundances even for low-resolution, low-signal-to-noise SEGUE spectra, to the point that the SSPP results can even be used to calibrate other lower-resolution surveys such as LAMOST (Lee et al. 2017) or the Pristine photometric survey (Youakim et al., in prep.).

Indeed, LAMOST (the Large sky Area Multi-Object Spectroscopic Telescope; Zhao et al. 2006, 2012; Deng et al. 2012; Newberg et al. 2012; Liu et al. 2014) represents a further step in the industrialisation of Galactic astronomy: it encompasses not only a custom multi-object low-resolution spectrograph with that can take spectra of 4000 objects simultaneously, but also the telescope itself. The LAMOST surveys have to date collected data for more than 3,000,000 stars, mostly probing the outer parts of the disc and halo. When carefully calibrated (e.g. Ho et al. 2016; Wang et al. 2016; Xiang et al. 2017), this wealth of information is likely to revolutionise our view on the evolution of the Galactic disc. First scientific results from LAMOST include a dissection of the MW disc's radial metallicity profile as a function of (approximate) age and height above the Galactic disc (Huang et al. 2015; Xiang et al. 2015), the discovery of a disrupted globular-cluster candidate (Vickers et al. 2016), and a detailed stellar-density mapping of the outer disc, to Galactocentric distances of ∼ 20 kpc (Liu et al. 2017).

After it became clear that also high-resolution multi-object spectroscopic surveys were becoming feasible, several complementary projects were launched to decipher the stellar chemical-abundance patterns that bear record of the star-formation history of the MW. The Gaia-ESO survey (Gilmore et al. 2012) uses the VLT/FLAMES instruments to carry out a variety of high-resolution ($R \sim 18,000 - 80,000$) optical subsurveys dedicated to specific MW stellar populations such as star-forming regions, open clusters, or bulge stars. The GALactic Archaeology with HERMES project (GALAH; Martell et al. 2017) has already observed over 300,000 stars at a resolution of $R \sim 28,000$ with the HERMES spectrograph at AAT (Traven et al. 2016). Like RAVE, GALAH profited from the existence of a fibre positioner (that of the 2dF galaxy survey; Lewis et al. 2002). Since it can measure chemical abundances of more than 20 elements, the GALAH survey provides an ideal database for chemical-tagging studies (Freeman & Bland-Hawthorn 2002; Bland-Hawthorn & Freeman 2004). The other major high-resolution survey still in operations is the Apache Point Observatory Galactic Evolution Experiment (APOGEE; Majewski et al. 2015). Since this thesis is based primarily on APOGEE observations, I discuss it in more detail below (Sec. 1.3.2, see also Fig. 1.3).

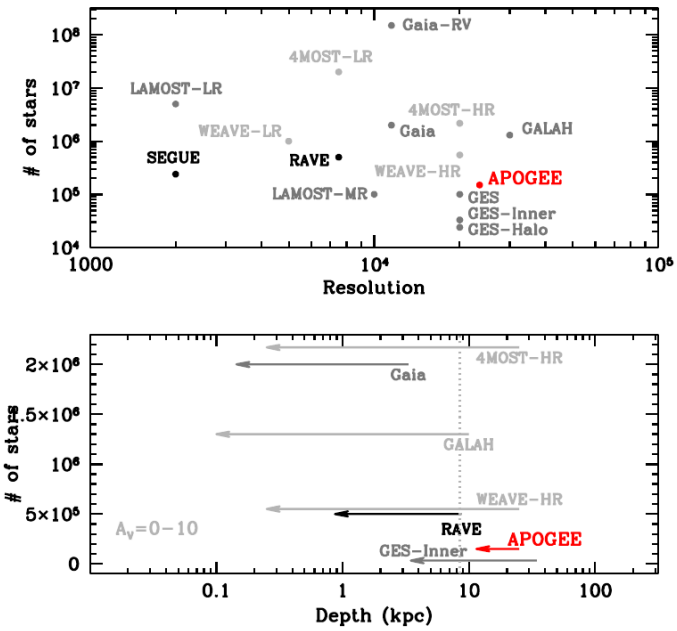

Figure 1.3. APOGEE in the context of past, present and future spectroscopic stellar surveys. The top panel shows the number of Milky Way stars to be observed as a function of spectral resolution. The bottom panel shows the expected survey depth for stars with $M_V = -1$ (e.g. K4 giants), including the effect of interstellar extinction (arrows). Completed surveys are shown in black, ongoing surveys in dark gray, and planned surveys in light grey. Figure from Majewski et al. (2015).

Upcoming endeavours like 4MOST (de Jong 2011), WEAVE (Dalton et al. 2012), MOONS (Cirasuolo et al. 2012), and possibly SDSS-V, will enlarge both the stellar statistics and the studied MW volume by another magnitude. With the major data releases of the Gaia satellite (see Chapter 7) yet to come, the epoch of industrialised Galactic astronomy has only just begun.

1.3.2. APOGEE

APOGEE was designed as part of the third epoch of the Sloan Digital Sky Survey (Allende Prieto et al. 2008; Eisenstein et al. 2011) and has been extended into the SDSS-IV phase (2014-2019; Blanton et al., in prep.), including a southern survey with a cloned instrument that will operate from the duPont telescope at Las Campanas (Majewski et al. 2016). To penetrate the thick dust layers that obscure the inner regions of the MW, a custom high-resolution ($R \sim 22,500$) infrared ($\lambda = 1.51 - 1.69\mu$m) multi-object spectrograph (Wilson et al. 2010, 2012) was built to operate at the SDSS telescope, mainly during bright time. Following a simple selection function (for details see Zasowski et al. 2013), APOGEE primarily targets red-giant stars, which are numerous in the disc, intrinsically bright in the H-band, and span a wide range of ages. By combining several 1h observations (typically between 3 and 12 per star), the APOGEE pipeline delivers wavelength-calibrated high-signal-to-noise spectra ($S/N \sim 100$ pixel^{-1}) with very precise (∼ 100 m/s) radial velocities (Nidever et al. 2015). The APOGEE Stellar Parameters and Chemical Abundances

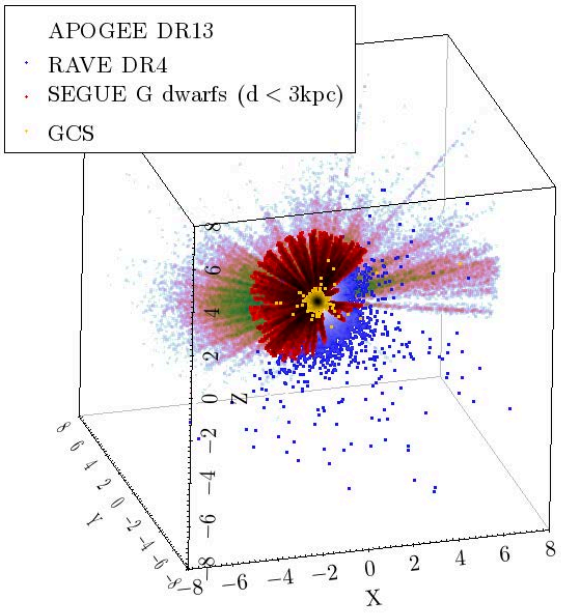

Figure 1.4. Location of representative samples from spectroscopic stellar surveys in heliocentric Cartesian coordinates (in kpc). The Galactic centre is located at $(X, Y, Z) = (8.3, 0, 0)$. The distances for the APOGEE, RAVE, and SEGUE samples were obtained with the spectrophotometric `StarHorse` code (see Appendix A; Santiago et al. 2016), the GCS stars have Hipparcos parallaxes from van Leeuwen (2007).

Pipeline (ASPCAP; García Pérez et al. 2016) delivers precise stellar parameters and chemical abundances of more than 15 elements. The highly efficient and parallelisable pipeline has been under steady development from the start of observations in 2011 (e.g. Mészáros et al. 2013; Alam et al. 2015; Holtzman et al. 2015; SDSS Collaboration et al. 2016). For a more detailed introduction to the pipeline and the APOGEE dataflow, see Sec. 2.2.

The good performance of the chemical-abundance pipeline, along with the SDSS policy to publish all software as well as raw and higher-level data products, has been key to the success of the APOGEE survey. Already the first APOGEE data release (SDSS DR10, Ahn et al. 2014) opened a window to much more distant disc stellar populations than ever. Imeediately, a series of papers on the chemo-dynamic structure of the MW disc could be produced, among them the work presented in Chapter 2 of this thesis (Anders et al. 2014), the work of Hayden et al. (2014) on the disc metallicity gradients of the chemically-separated discs, and the paper of Nidever et al. (2014) on the spatial constancy of the thick-disc [α/Fe]-abundance pattern over a large Galactic volume.

The following data releases (DR11/12, Alam et al. 2015; DR13 SDSS Collaboration et al. 2016) steadily increased the number of observed stars to over 160,000, and DR14 (planned for July 2017) will include more than 270,000 stars. With this increase in statistics, a number of new studies were possible. For example, using a sample of more than 60,000 red giants, Hayden et al. (2015) showed that the metallicity distribution function close to the Galactic plane changes its skewness when moving from the inner to the outer disc. In a joint analysis of the APOGEE red-clump catalogue (Bovy et al. 2014), RAVE, and the Geneva-Copenhagen survey (GCS; Nordström et al. 2004; Casagrande et al. 2011, see Fig. 1.4), Bovy et al. (2015) measured the power spectrum of the velocity fluctuations in the disc, concluding that most of the perturbations can be explained by a heavy and fast Galactic bar. Martell et al. (2016) and Schiavon et al. (2017) presented the first chemical-tagging results from APOGEE: they discovered a large population of nitrogen-rich stars mostly residing in the Galactic bulge (Schiavon et al. 2017), but also in the halo (Martell et al. 2016), that can be explained as second-generation stars originating in disrupted globular clusters.

1.3.3. The problem of selection biases

Recently, Bovy et al. (2016) analysed the spatial distribution of mono-abundance subpopulations (MAPs), defined as bins in the APOGEE [α/Fe] vs. [Fe/H] diagram, in a similar fashion as done in Bovy et al. (2012b) using SEGUE data, finding that the low-[α/Fe] MAPs follow a broken-exponential radial distribution peaking at smaller radii for higher [Fe/H]. While the study of MAPs has certainly proven an elegant way to describe the chemo-dynamical structure of the disc (see Rix & Bovy 2013, for a review), it has recently been shown by Minchev et al. (2017), using APOGEE data as well as the MW model of Minchev, Chiappini, & Martig (2013, 2014a), that MAPs should not a priori be considered mono-age populations, in particular in the presence of non-negligible abundance uncertainties and population biases. Indeed, Minchev et al. (2017) showed that the MAP broken-exponential density profiles measured by Bovy et al. (2016) can be explained by a combination of uncertainties, a strong bias towards young ages as present in the red-clump population (Girardi 2016), and smooth exponential density distributions for each mono-age population. This example demonstrates the advantage of realistic forward simulations and mock observations when interpreting the complex datasets delivered by spectroscopic stellar surveys. This is also one of the main focuses of this thesis (especially in Chapters 3, 4, and 6).

1.4. A new tool: asteroseismology of red giant stars

Since the ultimate goal of Galactic Archaeology is to unveil the star-formation, accretion, and dynamical history of the MW, accurate ages for a vast number of stellar tracers would provide the most straightforward constraint for a comparison to MW formation models (Chiappini et al. 2014). Unfortunately, ages for field stars are extremely hard to estimate (Soderblom 2010, 2013), in particular for red giants. However, the new field of red-giant asteroseismology offers promising tools to obtain red-giant ages with unprecedented precision (Davies & Miglio 2016).

Highly-sensitive photometric time series from the ground and from space have shown that a wide class of stars from the main sequence to the asymptotic giant branch exhibits solar-like oscillations (stochastically-excited soundwaves originating in the turbulent convection zone near the surface). These oscillations occur at a broad range of frequencies, some of which correspond to standing waves that are mostly driven by the geometry of the star, thus allowing us to measure its radius, mass, the depth of the convection zone, or the extent of the stellar core by analysing the oscillation power spectrum (see Chaplin & Miglio 2013 for a review).

The asteroseismology programs of the CoRoT (Baglin et al. 2006) and *Kepler* (Gilliland et al. 2010) missions led to a revolution of the field: the first CoRoT observational run had yielded detections of solar-like oscillations in thousands of faint red-giant stars (De Ridder et al. 2009; Hekker et al. 2009, see also Noels et al. 2016), which implied that the distribution of oscillation parameters could open up a new way to study

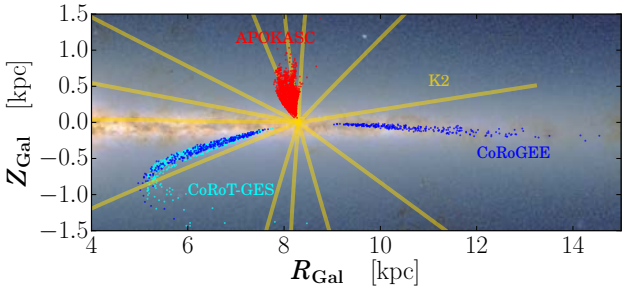

Figure 1.5. Location of the currently available red-giant samples observed with asteroseismology and spectroscopy in Galactocentric cylindrical coordinates. The APOGEE-*Kepler* sample (APOKASC; Pinsonneault et al. 2014) is shown in red, the CoRoT-GES sample (Valentini et al. 2016b) in cyan, and the CoRoT-APOGEE sample (Chapters 3-6; Anders et al. 2017b) in dark blue. The fields to be observed by the K2 mission are shown as yellow rays.

Galactic stellar populations. This was demonstrated by Miglio et al. (2009, 2013) who compared the observed seismic properties of the giant population in two CoRoT fields with predictions of a population-synthesis model. The use of large samples of stars for statistical studies of Galactic populations was subsequently dubbed "ensemble asteroseismology" (e.g. Bedding et al. 2011; Chaplin et al. 2011). Until now, the method has focussed on the two main characteristics of red-giant frequency spectra: the large frequency separation $\Delta\nu$ (Tassoul 1980; Ulrich 1986; Christensen-Dalsgaard 1993) and the frequency of maximum oscillation power $\nu_{\rm max}$ (Brown et al. 1991; Kjeldsen & Bedding 1995; Belkacem et al. 2011), which can be related to individual stellar masses and radii via the so-called seismic scaling relations (see also Sec. 3.1).

Apart from ensemble seismology, these scaling relations have also proven very useful in another respect: they provide the most precise measurements of the stellar surface gravity, a quantity that is needed to derive spectroscopic abundances and that is often subject to significant systematic errors in spectroscopic analyses (Noels & Bragaglia 2015). Within the recent years, most spectroscopic surveys have therefore co-observed CoRoT and *Kepler* stars to calibrate their surface gravity measurements (e.g. Mészáros et al. 2013; Holtzman et al. 2015; Valentini et al. 2016a; Wang et al. 2016). Substantial effort has also flown into the development of spectral-analysis pipelines that can integrate seismic measurements in a self-consistent fashion (Valentini et al. 2013, 2016b; Boeche & Grebel 2016).

Combining asteroseismology with spectroscopic observations has another advantage: since the seismic scaling relations provide precise mass and radius measurements, and spectroscopy yields precise effective temperatures and abundances, it is possible to obtain much tighter constraints on the ages of red giants when combining the two (Chiappini et al. 2016). The demonstration and application of this new technique using data from APOGEE and CoRoT (see Fig. 1.5) is the subject of Chapters 3-6 (Anders et al. 2017b, 2016; Chiappini et al. 2015; Anders et al. 2017a).

1.5. Thesis outline and authorship remarks

This work is structured as a cumulative thesis, meaning that Chapters 2-6 have already been published as stand-alone articles in peer-reviewed journals. Therefore, each chapter has its own introduction and can be understood without knowledge of the previous chapters. However, there is a central theme that connects all presented works: we use the APOGEE survey to study specific aspects of Galactic structure and evolution, with a particular focus on the disc(s).

Chapter 2 of this dissertation was published in *Astronomy & Astrophysics*, Vol. 564, id. A115 (Anders et al. 2014). The article focusses on the scientific exploration of the first APOGEE data release (SDSS DR10 Ahn et al. 2014) and is a continuation of a study presented in my diploma thesis (Anders 2013)[2]. At the time of its publication, the DR10 sample enlarged the Galactic volume covered by spectroscopic surveys by almost a factor of ten (and the sample size of high-resolution red-giant studies by several hundreds). Thanks to APOGEE's capability to peer through the interstellar dust, it also provided the first statistical stellar sample very close to the Galactic plane. We therefore re-investigated the chemo-kinematic properties of the MW disc outside the solar vicinity. The article includes several seminal results: we measured, for the first time with high-resolution data, the dependence of the disc radial metallicity gradient on the distance from the Galactic plane, we corroborated the existence of the famous gap between the high- and low-[α/Fe] sequences in the abundance diagram, and we unambiguously confirmed that the scale length of the (chemically-defined) thick disc is significantly shorter than that of the thin disc. Using 6D kinematic information, we presented chemical-abundance diagrams cleaned from stars passing the extended solar vicinity on eccentric orbits. Finally, our data hinted a small difference in the [α/Fe] ratios of bulge and thick-disc stars. For the publication, parts of the analysis were repeated in a more sophisticated fashion, the text was rewritten and restructured. Although part of a large collaboration effort, the paper reprensents a largely independent work, incorporating, of course, numerous comments and some contributions from my co-authors, most notably Cristina Chiappini (AIP) and Basílio Santiago (UFRGS Porto Alegre). C. Chiappini steered the overall direction of the work, and B. Santiago computed the stellar distances for our red-giant sample at that time. Later on, our AIP-UFRGS collaboration (F. Anders, B. Santiago, A. Queiroz, C. Chiappini, D. Brauer) implemented major upgrades of the distance code (see Fig. 1.4), resulting in another publication (Santiago et al. 2016, see Appendix A). These changes (translating the code from `Fortran` to `python`, implementing an option to simultaneously obtain posterior probability distributions for stellar parameters, distances, and extinction from spectro-photometric observations) were mostly carried out by me, and I also sign responsible for the code performance analyses, the stellar orbit calculations, and significant parts of the text presented in Santiago et al. (2016).

Chapters 3-6 present our results of the first combination of asteroseismic and spectroscopic data in the context of Galactic Archaeology. Chapters 3 and 5 were recently published in *Astronomy & Astrophysics* (Anders et al. 2017b, Vol. 597, id. A30; Chiappini et al. 2015, Vol. 576, id. L12), and Chapter 4 was published in *Astronomische Nachrichten* (Anders et al. 2016, Vol. 337, pp. 926-930). Chapter 6 has been accepted for publication on Dec 19, 2016 (Anders et al. 2017a), and is available on the *A&A* webpages[3]. All four papers analyse APOGEE follow-up observations of 606 solar-like oscillating red giants in the CoRoT exoplanet fields LRa01 and LRc01. These fields cover a large radial baseline of the Galactic disc and therefore allowed us to study the age- and radius-dependence of the [α/Fe] vs. [Fe/H] distributions. This work was only possible to carry out in an even bigger collaboration, since in addition to spec-

[2] `iktp.tu-dresden.de/IKTP/pub/15/Diplomarbeit_FA.pdf`
[3] `http://dx.doi.org/10.1051/0004-6361/201629363`

troscopy, it involved seismic lightcurve analysis and the use of a complex Bayesian inference tool (PARAM; da Silva et al. 2006; Rodrigues et al. 2014) to obtain stellar masses, ages, distances, and extinctions. The lightcurve analysis was carried out by Benoît Mosser (Obs Paris), Josefina Montalbán (U Padova), and Andrea Miglio (U Birmingham). The PARAM results were computed by Thaíse Rodrigues (OAPD Padova), A. Miglio, and Léo Girardi (OAPD). On the theoretical side, my work relied on the chemo-dynamical MW model of Minchev, Chiappini, & Martig (2013, 2014a), kindly provided by Ivan Minchev (AIP). C. Chiappini also provided her semi-analytic chemical-evolution models for the thin and thick disc (Chiappini 2009) for comparison. I am also indebted to Tilmann Piffl (Oxford) for providing his modified version of the Galaxia mock-observation tool (Piffl 2013; Sharma et al. 2011). Without the fortunate combination of the new data with state-of-the-art models and appropriate statistical and mock-observation tools, the interpretation of the CoRoT-APOGEE data would have been very limited, and the collaboration much less fruitful.

In Chapter 3 (Anders et al. 2017b), I set out to describe the provenance of the CoRoT-APOGEE data, as well as the analysis leading to the higher-level data products (seismic parameters, spectroscopic stellar parameters and abundances, stellar masses, distances, ages, extinctions, and kinematics). I also provide a series of sanity checks, and a detailed evaluation of the statistical and systematic uncertainties involved in the age determination. I also sign responsible for the scientific part of this chapter: a discussion of the age- and radius-dependence of the [α/Fe] vs. [Fe/H] distributions in the Galactic disc, and a comparison to mock observations of the MCM model. The main results of the paper are that 1. the age distribution of the high-[α/Fe] sequence (the chemical thick disc) appears to be broader than expected from a monolithically-formed old thick disc that stopped to form stars 10 Gyr ago, and 2. to explain the abundace of super-metal-rich stars in the outer disc, even stronger radial migration than present in the MCM model seems to be required.

The mock observations needed to justify the conclusions of Chapter 3 are described in some more detail in Chapter 4 (Anders et al. 2016). For this project I used the modified Galaxia code of T. Piffl (Piffl 2013; Sharma et al. 2011), adjusted the selection algorithm to account for the complex CoRoT-APOGEE target selection, and improved the interstellar extinction prescription using the new 3D interstellar dust map of Green et al. (2015). Because the sophisticated mock algorithm yielded unsatisfactory results, I also implemented a simpler but better-performing mock-observation procedure for the MCM model, which was used in the following papers (Anders et al. 2017b,a).

Chapter 5 reports the first important CoRoGEE science result, already published in 2015. In Chiappini et al. (2015), we discovered a significant population of apparently young, [α/Fe]-rich stars in the CoRoGEE data, i.e. stars that do not follow the age-abundance trends predicted by standard chemical-evolution models. Most importantly, we found these peculiar stars to be much more abundant in the inner CoRoT field LRc01 than in the outer-disc field LRc01, suggesting that this population cannot completely be explained by measurement uncertainties or systematic errors, but has a physical origin, possibly due to a peculiar chemical-enrichment history of the inner disc. I carried out the analysis for that paper and also wrote major parts of the text, in particular sections 2 & 3.

Chapter 6 (Anders et al. 2017a) uses the CoRoGEE sample to study the time evolution of the disc radial metallicity gradient, an observable that has been subject of debate both observationally and theoretically for more than 20 years. I divided the CoRoGEE dataset into six age bins and performed a careful statistical analysis of the [Fe/H] vs. $R_{\rm Gal}$ distributions to obtain reliable gradient measurements, accounting for the biases introduced by the observation strategy. By again comparing the results with the MCM model, I concluded that the age-dependence of the iron gradient can be explained by a non-varying negative iron gradient of -0.07 dex/kpc, together with stellar heating and migration. This result is also discussed in the context of the vast literature (using planetary nebulae, open clusters, and field stars) on the subject. In the paper, we also found that radial migration offers a new explanation for the puzzling observation that, unlike field stars, older open clusters in the solar vicinity tend to have higher metallicities than their younger counterparts. We suggested that non-migrating clusters are more likely to be disrupted, which, at intermediate ages, leaves us with the high-metallicity migrators from the inner disc.

Chapter 7 summarises the thesis, puts it in the context of the present literature, and gives a brief outlook onto future plans and developments.

Bibliography

Abadi, M. G., Navarro, J. F., Steinmetz, M., & Eke, V. R. 2003, ApJ, 597, 21
Ahn, C. P., Alexandroff, R., Allende Prieto, C., et al. 2014, ApJS, 211, 17
Alam, S., Albareti, F. D., Allende Prieto, C., Anders, F., & Anderson, S. F., e. 2015, ApJS, 219, 12
Allende Prieto, C., Majewski, S. R., Schiavon, R., et al. 2008, Astronomische Nachrichten, 329, 1018
Amores, E. B., Robin, A. C., & Reyle, C. 2017, ArXiv e-prints
Anders, F. 2013, Diploma Thesis: *Chemodynamical constraints on Milky Way models from spectroscopic stellar surveys*, Technische Universität Dresden
Anders, F., Chiappini, C., Minchev, I., et al. 2017a, A&A, in press, `http://dx.doi.org/10.1051/0004-6361/201629363`
Anders, F., Chiappini, C., Rodrigues, T. S., et al. 2017b, A&A, 597, A30
Anders, F., Chiappini, C., Rodrigues, T. S., et al. 2016, Astronomische Nachrichten, 337, 926
Anders, F., Chiappini, C., Santiago, B. X., et al. 2014, A&A, 564, A115
Antoja, T., Valenzuela, O., Pichardo, B., et al. 2009, ApJ, 700, L78
Aoki, W., Beers, T. C., Sivarani, T., et al. 2008, ApJ, 678, 1351
Baglin, A., Auvergne, M., Barge, P., et al. 2006, in ESA Special Publication, ed. M. Fridlund, A. Baglin, J. Lochard, & L. Conroy, Vol. 1306, 33
Bedding, T. R., Mosser, B., Huber, D., et al. 2011, Nature, 471, 608
Belkacem, K., Goupil, M. J., Dupret, M. A., et al. 2011, A&A, 530, A142
Bensby, T., Alves-Brito, A., Oey, M. S., Yong, D., & Meléndez, J. 2011, ApJ, 735, L46
Binney, J. & Merrifield, M. 1998, Galactic Astronomy
Binney, J. & Sanders, J. L. 2016, Astronomische Nachrichten, 337, 939
Binney, J. & Tremaine, S. 2008, Galactic Dynamics: Second Edition (Princeton University Press)
Bland-Hawthorn, J. & Freeman, K. C. 2004, PASA, 21, 110
Bland-Hawthorn, J. & Gerhard, O. 2016, ARA&A, 54, 529
Blitz, L. & Spergel, D. N. 1991, ApJ, 379, 631
Boeche, C., Chiappini, C., Minchev, I., et al. 2013a, A&A, 553, A19
Boeche, C. & Grebel, E. K. 2016, A&A, 587, A2
Boeche, C., Siebert, A., Piffl, T., et al. 2014, A&A, 568, A71
Boeche, C., Siebert, A., Piffl, T., et al. 2013b, A&A, 559, A59
Boeche, C., Siebert, A., Williams, M., et al. 2011, AJ, 142, 193
Bournaud, F., Elmegreen, B. G., & Martig, M. 2009, ApJ, 707, L1
Bovy, J. 2010, ApJ, 725, 1676
Bovy, J., Bird, J. C., García Pérez, A. E., et al. 2015, ApJ, 800, 83
Bovy, J., Nidever, D. L., Rix, H.-W., et al. 2014, ApJ, 790, 127
Bovy, J., Rix, H.-W., Hogg, D. W., et al. 2012a, ApJ, 755, 115
Bovy, J., Rix, H.-W., Liu, C., et al. 2012b, ApJ, 753, 148
Bovy, J., Rix, H.-W., Schlafly, E. F., et al. 2016, ApJ, 823, 30
Brown, T. M., Gilliland, R. L., Noyes, R. W., & Ramsey, L. W. 1991, ApJ, 368, 599
Carollo, D., Beers, T. C., Chiba, M., et al. 2010, ApJ, 712, 692
Carollo, D., Beers, T. C., Lee, Y. S., et al. 2007, Nature, 450, 1020
Casagrande, L., Schönrich, R., Asplund, M., et al. 2011, A&A, 530, A138
Casey, A. R., Hawkins, K., Hogg, D. W., et al. 2016, ArXiv e-prints
Chaplin, W. J., Kjeldsen, H., Christensen-Dalsgaard, J., et al. 2011, Science, 332, 213
Chaplin, W. J. & Miglio, A. 2013, ARA&A, 51, 353

Cheng, J. Y., Rockosi, C. M., Morrison, H. L., et al. 2012, ApJ, 752, 51
Chiappini, C. 2009, in IAU Symposium, Vol. 254, IAU Symposium, ed. J. Andersen, B. Nordström, & J. Bland-Hawthorn, 191–196
Chiappini, C. 2015, in EAS Publications Series, Vol. 73, EAS Publications Series, 309–341
Chiappini, C., Anders, F., & Minchev, I. 2014, in EAS Publications Series, Vol. 67, EAS Publications Series, 169–176
Chiappini, C., Anders, F., Rodrigues, T. S., et al. 2015, A&A, 576, L12
Chiappini, C., Matteucci, F., & Gratton, R. 1997, ApJ, 477, 765
Chiappini, C., Matteucci, F., & Romano, D. 2001, ApJ, 554, 1044
Chiappini, C., Montalbán, J., & Steffen, M. 2016, Astronomische Nachrichten, 337, 773
Christensen-Dalsgaard, J. 1993, in Astronomical Society of the Pacific Conference Series, Vol. 42, GONG 1992. Seismic Investigation of the Sun and Stars, ed. T. M. Brown, 347
Cirasuolo, M., Afonso, J., Bender, R., et al. 2012, in Proc. SPIE, Vol. 8446, Ground-based and Airborne Instrumentation for Astronomy IV, 84460S
da Silva, L., Girardi, L., Pasquini, L., et al. 2006, A&A, 458, 609
Dalton, G., Trager, S. C., Abrams, D. C., et al. 2012, in Proc. SPIE, Vol. 8446, Ground-based and Airborne Instrumentation for Astronomy IV, 84460P
Davies, G. R. & Miglio, A. 2016, Astronomische Nachrichten, 337, 774
de Jong, R. 2011, The Messenger, 145, 14
De Ridder, J., Barban, C., Baudin, F., et al. 2009, Nature, 459, 398
Dehnen, W. 2000, AJ, 119, 800
Deng, L.-C., Newberg, H. J., Liu, C., et al. 2012, Research in Astronomy and Astrophysics, 12, 735
Eisenstein, D. J., Weinberg, D. H., Agol, E., et al. 2011, AJ, 142, 72
Fernández-Alvar, E., Allende Prieto, C., Schlesinger, K. J., et al. 2015, A&A, 577, A81
Freeman, K. & Bland-Hawthorn, J. 2002, ARA&A, 40, 487
Freeman, K., Ness, M., Wylie-de-Boer, E., et al. 2013, MNRAS, 428, 3660
Fuhrmann, K. 1998, A&A, 338, 161
Fuhrmann, K. 2008, MNRAS, 384, 173
Fuhrmann, K., Chini, R., Hoffmeister, V. H., & Bernkopf, J. 2012, MNRAS, 420, 1423
Fuhrmann, K., Chini, R., Kaderhandt, L., & Chen, Z. 2017, MNRAS, 464, 2610
García Pérez, A. E., Allende Prieto, C., Holtzman, J. A., et al. 2016, AJ, 151, 144
Gilliland, R. L., Brown, T. M., Christensen-Dalsgaard, J., et al. 2010, PASP, 122, 131
Gilmore, G., Randich, S., Asplund, M., et al. 2012, The Messenger, 147, 25
Gilmore, G. & Reid, N. 1983, MNRAS, 202, 1025
Girardi, L. 2016, ARA&A, 54, 95
Gnedin, O. Y., Brown, W. R., Geller, M. J., & Kenyon, S. J. 2010, ApJ, 720, L108
Gómez, F. A., Minchev, I., O'Shea, B. W., et al. 2012, MNRAS, 423, 3727
Gratton, R., Carretta, E., Matteucci, F., & Sneden, C. 1996, in Astronomical Society of the Pacific Conference Series, Vol. 92, Formation of the Galactic Halo...Inside and Out, ed. H. L. Morrison & A. Sarajedini, 307
Gratton, R. G., Carretta, E., Matteucci, F., & Sneden, C. 2000, A&A, 358, 671
Green, G. M., Schlafly, E. F., Finkbeiner, D. P., et al. 2015, ApJ, 810, 25
Gunn, J. E., Siegmund, W. A., Mannery, E. J., et al. 2006, AJ, 131, 2332
Hayden, M. R., Bovy, J., Holtzman, J. A., et al. 2015, ApJ, 808, 132
Hayden, M. R., Holtzman, J. A., Bovy, J., et al. 2014, AJ, 147, 116
Hekker, S., Kallinger, T., Baudin, F., et al. 2009, A&A, 506, 465
Ho, A. Y. Q., Ness, M. K., Hogg, D. W., et al. 2016, ArXiv e-prints
Holtzman, J. A., Shetrone, M., Johnson, J. A., et al. 2015, AJ, 150, 148
Howard, C. D., Rich, R. M., Reitzel, D. B., et al. 2008, ApJ, 688, 1060
Huang, Y., Liu, X.-W., Zhang, H.-W., et al. 2015, Research in Astronomy and Astrophysics, 15, 1240
Hubble, E. P. 1926, ApJ, 64
Ivezić, Ž., Sesar, B., Jurić, M., et al. 2008, ApJ, 684, 287
Janesh, W., Morrison, H. L., Ma, Z., et al. 2016, ApJ, 816, 80
Jones, D. H., Saunders, W., Colless, M., et al. 2004, MNRAS, 355, 747
Jurić, M., Ivezić, Ž., Brooks, A., et al. 2008, ApJ, 673, 864
Just, A. & Jahreiß, H. 2010, MNRAS, 402, 461
Keller, S. C., Bessell, M. S., Frebel, A., et al. 2014, Nature, 506, 463
Kjeldsen, H. & Bedding, T. R. 1995, A&A, 293, 87
Kollmeier, J. A., Gould, A., Rockosi, C., et al. 2010, ApJ, 723, 812
Kordopatis, G., Gilmore, G., Steinmetz, M., et al. 2013, AJ, 146, 134
Kunder, A., Bono, G., Piffl, T., et al. 2014, A&A, 572, A30
Kunder, A., Koch, A., Rich, R. M., et al. 2012, AJ, 143, 57
Kunder, A., Kordopatis, G., Steinmetz, M., et al. 2017, AJ, 153, 75
Lee, Y. S., Beers, T. C., Allende Prieto, C., et al. 2011a, AJ, 141, 90
Lee, Y. S., Beers, T. C., An, D., et al. 2011b, ApJ, 738, 187
Lee, Y. S., Beers, T. C., Kim, Y. K., et al. 2017, ArXiv e-prints
Lee, Y. S., Beers, T. C., Sivarani, T., et al. 2008a, AJ, 136, 2022
Lee, Y. S., Beers, T. C., Sivarani, T., et al. 2008b, AJ, 136, 2050
Lewis, I. J., Cannon, R. D., Taylor, K., et al. 2002, MNRAS, 333, 279
Liu, C., Xu, Y., Wan, J.-C., et al. 2017, ArXiv e-prints
Liu, X.-W., Yuan, H.-B., Huo, Z.-Y., et al. 2014, in IAU Symposium, Vol. 298, Setting the scene for Gaia and LAMOST, ed. S. Feltzing, G. Zhao, N. A. Walton, & P. Whitelock, 310–321
López-Corredoira, M., Cabrera-Lavers, A., Garzón, F., & Hammersley, P. L. 2002, A&A, 394, 883
Majewski, S. R., APOGEE Team, & APOGEE-2 Team. 2016, Astronomische Nachrichten, 337, 863
Majewski, S. R., Schiavon, R. P., Frinchaboy, P. M., et al. 2015, ApJS, submitted, arXiv:1509.05420
Martell, S. L., Sharma, S., Buder, S., et al. 2017, MNRAS, 465, 3203
Martell, S. L., Shetrone, M. D., Lucatello, S., et al. 2016, ApJ, 825, 146
Martig, M., Bournaud, F., Croton, D. J., Dekel, A., & Teyssier, R. 2012, ApJ, 756, 26
Martinet, L. 1984, A&A, 132, 381
Matijevič, G., Zwitter, T., Bienaymé, O., et al. 2012, ApJS, 200, 14
Matteucci, F. 2012, Chemical Evolution of Galaxies
McKee, C. F., Parravano, A., & Hollenbach, D. J. 2015, ApJ, 814, 13
Mészáros, S., Holtzman, J., García Pérez, A. E., et al. 2013, AJ, 146, 133
Miglio, A., Chiappini, C., Morel, T., et al. 2013, in European Physical Journal Web of Conferences, Vol. 43, 3004
Miglio, A., Montalbán, J., Baudin, F., et al. 2009, A&A, 503, L21
Minchev, I., Boily, C., Siebert, A., & Bienayme, O. 2010, MNRAS, 407, 2122
Minchev, I., Chiappini, C., & Martig, M. 2013, A&A, 558, A9
Minchev, I., Chiappini, C., & Martig, M. 2014a, in IAU Symposium, Vol. 298, IAU Symposium, ed. S. Feltzing, G. Zhao, N. A. Walton, & P. Whitelock, 130–141
Minchev, I., Chiappini, C., Martig, M., et al. 2014b, ApJ, 781, L20
Minchev, I., Steinmetz, M., Chiappini, C., et al. 2017, ApJ, 834, 27
Minniti, D. & Zoccali, M. 2008, in IAU Symposium, Vol. 245, IAU Symposium, ed. M. Bureau, E. Athanassoula, & B. Barbuy, 323–332
Ness, M., Freeman, K., Athanassoula, E., et al. 2013a, MNRAS, 430, 836
Ness, M., Freeman, K., Athanassoula, E., et al. 2013b, MNRAS, 432, 2092
Ness, M., Freeman, K., Athanassoula, E., et al. 2012, ApJ, 756, 22
Newberg, H. J., Carlin, J. L., Chen, L., et al. 2012, in Astronomical Society of the Pacific Conference Series, Vol. 458, Galactic Archaeology: Near-Field Cosmology and the Formation of the Milky Way, ed. W. Aoki, M. Ishigaki, T. Suda, T. Tsujimoto, & N. Arimoto, 405
Nidever, D. L., Bovy, J., Bird, J. C., et al. 2014, ApJ, 796, 38
Nidever, D. L., Holtzman, J. A., Allende Prieto, C., et al. 2015, AJ, 150, 173
Noels, A. & Bragaglia, A. 2015, Astrophysics and Space Science Proceedings, 39, 167
Noels, A., Montalbán, J., & Chiappini, C. 2016, Astronomische Nachrichten, 337, 982
Nordström, B., Mayor, M., Andersen, J., et al. 2004, A&A, 418, 989
Pagel, B. E. J. 2009, Nucleosynthesis and Chemical Evolution of Galaxies
Piffl, T. 2013, PhD thesis, Universität Potsdam
Piffl, T., Scannapieco, C., Binney, J., et al. 2014, A&A, 562, A91
Pinsonneault, M. H., Elsworth, Y., Epstein, C., et al. 2014, ApJS, 215, 19
Reid, M. J., Menten, K. M., Zheng, X. W., et al. 2009, ApJ, 700, 137
Reylé, C., Marshall, D. J., Robin, A. C., & Schultheis, M. 2009, A&A, 495, 819
Rich, R. M., Reitzel, D. B., Howard, C. D., & Zhao, H. 2007, ApJ, 658, L29
Rix, H.-W. & Bovy, J. 2013, A&A Rev., 21, 61
Rodrigues, T. S., Girardi, L., Miglio, A., et al. 2014, MNRAS, 445, 2758
Ruchti, G. R., Fulbright, J. P., Wyse, R. F. G., et al. 2011, ApJ, 737, 9
Santiago, B. X., Brauer, D. E., Anders, F., et al. 2016, A&A, 585, A42
Scheffler, H. & Elsässer, H. 1982, Bau und Physik der Galaxis
Schiavon, R. P., Zamora, O., Carrera, R., et al. 2017, MNRAS, 465, 501
Schlesinger, K. J., Johnson, J. A., Rockosi, C. M., et al. 2012, ApJ, 761, 160
SDSS Collaboration, Albareti, F. D., Allende Prieto, C., et al. 2016, ArXiv e-prints
Seabroke, G. M., Gilmore, G., Siebert, A., et al. 2008, MNRAS, 384, 11
Sharma, S., Bland-Hawthorn, J., Johnston, K. V., & Binney, J. 2011, ApJ, 730, 3
Siebert, A., Bienaymé, O., Binney, J., et al. 2008, MNRAS, 391, 793
Siebert, A., Williams, M. E. K., Siviero, A., et al. 2011, AJ, 141, 187
Slipher, V. M. 1917, Proceedings of the American Philosophical Society, 56, 403
Smolinski, J. P., Lee, Y. S., Beers, T. C., et al. 2011, AJ, 141, 89
Soderblom, D. 2013, in Asteroseismology of Stellar Populations in the Milky Way
Soderblom, D. R. 2010, ARA&A, 48, 581
Steinmetz, M., Zwitter, T., Siebert, A., et al. 2006, AJ, 132, 1645
Tassoul, M. 1980, ApJS, 43, 469
Traven, G., Matijevič, G., Zwitter, T., et al. 2016, ArXiv e-prints
Turon, C., Primas, F., Binney, J., et al. 2008, ESA-ESO Working Group on Galactic Populations, Chemistry and Dynamics, Tech. rep.
Ulrich, R. K. 1986, ApJ, 306, L37

Valentini, M., Chiappini, C., Davies, G. R., et al. 2016a, A&A, accepted, arXiv:1609.03826
Valentini, M., Chiappini, C., Miglio, A., et al. 2016b, ArXiv e-prints
Valentini, M., Morel, T., Miglio, A., Fossati, L., & Munari, U. 2013, in European Physical Journal Web of Conferences, Vol. 43, European Physical Journal Web of Conferences, 3006
van Leeuwen, F., ed. 2007, Astrophysics and Space Science Library, Vol. 350, Hipparcos, the New Reduction of the Raw Data
Veltz, L., Bienaymé, O., Freeman, K. C., et al. 2008, A&A, 480, 753
Vickers, J. J., Smith, M. C., Hou, Y., Wang, Y., & Zhang, Y. 2016, ApJ, 816, L2
Villalobos, Á. & Helmi, A. 2008, MNRAS, 391, 1806
Wang, L., Wang, W., Wu, Y., et al. 2016, AJ, 152, 6
Williams, M. E. K., Steinmetz, M., Binney, J., et al. 2013, MNRAS, 436, 101
Wilson, J. C., Hearty, F., Skrutskie, M. F., et al. 2010, in Society of Photo-Optical Instrumentation Engineers (SPIE) Conference Series, Vol. 7735, Society of Photo-Optical Instrumentation Engineers (SPIE) Conference Series
Wilson, J. C., Hearty, F., Skrutskie, M. F., et al. 2012, in Society of Photo-Optical Instrumentation Engineers (SPIE) Conference Series, Vol. 8446, Society of Photo-Optical Instrumentation Engineers (SPIE) Conference Series
Xiang, M.-S., Liu, X.-W., Shi, J.-R., et al. 2017, MNRAS, 464, 3657
Xiang, M.-S., Liu, X.-W., Yuan, H.-B., et al. 2015, Research in Astronomy and Astrophysics, 15, 1209
Yanny, B., Newberg, H. J., Johnson, J. A., et al. 2009a, ApJ, 700, 1282
Yanny, B., Rockosi, C., Newberg, H. J., et al. 2009b, AJ, 137, 4377
Zasowski, G., Johnson, J. A., Frinchaboy, P. M., et al. 2013, AJ, 146, 81
Zhao, G., Chen, Y.-Q., Shi, J.-R., et al. 2006, Chinese J. Astron. Astrophys., 6, 265
Zhao, G., Zhao, Y.-H., Chu, Y.-Q., Jing, Y.-P., & Deng, L.-C. 2012, Research in Astronomy and Astrophysics, 12, 723
Zwitter, T., Siebert, A., Munari, U., et al. 2008, AJ, 136, 421

4

Chapter 2

Chemodynamics of the Milky Way. I. The first year of APOGEE data

F. Anders[1,2], C. Chiappini[1,3], B. X. Santiago[3,4], H. J. Rocha-Pinto[3,5], L. Girardi[3,6], L. N. da Costa[3,7], M. A. G. Maia[3,7], M. Steinmetz[1], I. Minchev[1], M. Schultheis[8], C. Boeche[9], A. Miglio[10], J. Montalbán[11], D. P. Schneider[12,13], T. C. Beers[14,15], K. Cunha[7,16], C. Allende Prieto[17], E. Balbinot[3,4], D. Bizyaev[18], D. E. Brauer[1], J. Brinkmann[18], P. M. Frinchaboy[19], A. E. García Pérez[20], M. R. Hayden[21], F. R. Hearty[20,12], J. Holtzman[21], J. Johnson[22], K. Kinemuchi[18], S. R. Majewski[20], E. Malanushenko[18], V. Malanushenko[18], D. L. Nidever[23], R. W. O'Connell[20], K. Pan[18], A. C. Robin[24], R. P. Schiavon[25], M. Shetrone[26], M. F. Skrutskie[20], V. V. Smith[14], K. Stassun[27], G. Zasowski[28]

(Affiliations can be found after the references)

Abstract

The Apache Point Observatory Galactic Evolution Experiment (APOGEE) features the first multi-object high-resolution fiber spectrograph in the Near-infrared (NIR) ever built, thus making the survey unique in its capabilities: APOGEE is able to peer through the dust that obscures stars in the Galactic disc and bulge in the optical wavelength range. Here we explore the APOGEE data included as part of the Sloan Digital Sky Survey's 10th data release (SDSS DR10). The goal of this paper is to a) investigate the chemo-kinematic properties of the Milky Way disc by exploring the first year of APOGEE data, and b) to compare our results to smaller optical high-resolution samples in the literature, as well as results from lower resolution surveys such as the Geneva-Copenhagen Survey (GCS) and the RAdial Velocity Experiment (RAVE). We select a high-quality (HQ) sample in terms of chemistry (amounting to around 20.000 stars) and, after computing distances and orbital parameters for this sample, we employ a number of useful subsets to formulate constraints on Galactic chemical and chemodynamical evolution processes in the Solar neighbourhood and beyond (e.g., metallicity distributions – MDFs, [α/Fe] vs. [Fe/H] diagrams, and abundance gradients). Our red giant sample spans distances as large as 10 kpc from the Sun. Given our chemical quality requirements, most of the stars are located between 1 and 6 kpc from the Sun, increasing by at least a factor of eight the studied volume with respect to the most recent chemodynamical studies based on the two largest samples obtained from RAVE and the Sloan Extension for Galactic Understanding and Exploration (SEGUE). We find remarkable agreement between the MDF of the recently published local (d < 100 pc) high-resolution high-S/N HARPS sample and our local HQ sample (d < 1 kpc). The *local* MDF peaks slightly below solar metallicity, and exhibits an extended tail towards [Fe/H] = −1, whereas a sharper cutoff is seen at larger metallicities (the APOGEE sample shows a slight overabundance of stars with metallicities larger than ≃ +0.3 w.r.t. the HARPS sample). Both samples also compare extremely well in an [α/Fe] vs. [Fe/H] diagram. The APOGEE data also confirm the existence of a gap in the abundance diagram. When expanding our sample to cover three different Galactocentric distance bins (inner disc, solar vicinity and outer disc), we find the *high-[α/Fe]* stars to be rare towards the outer zones (implying a shorter scale-length of the thick disc with respect to the thin disc) as previously suggested in the literature. Finally, we measure the gradients in [Fe/H] and [α/Fe], and their respective MDFs, over a range of 6 < R < 11 kpc in Galactocentric distance, and a 0 < z < 3 kpc range of distance from the Galactic plane. We find a good agreement with the gradients traced by the GCS and RAVE dwarf samples. For stars with 1.5 < z < 3 kpc (not present in the previous samples), we find a positive metallicity gradient and a negative gradient in [α/Fe].

2.1. Introduction

Our Galaxy and its companions are the only systems for which large numbers of individual stars can be resolved and analysed spectroscopically. These stars carry a fossil record of the processes involved in the formation and evolution of the Milky Way. By measuring the chemical abundances in the stellar atmospheres, we have access to the gas composition at the time and place of the star's birth. Combining these chemical fossil imprints with the current kinematical properties of a large number of stars (covering large portions of our Galaxy), one can then infer the main processes at play during the formation and evolution of the Milky Way. This method, sometimes referred to as *Galactic Archaeology* or *Near-Field Cosmology*, has proven to be extremely powerful in helping to answer questions related not only to the Milky Way formation but also to stellar evolution, the origin and evolution of chemical elements, and cosmology (Pagel 2009, Matteucci 2001, 2012, Freeman & Bland-Hawthorn 2002, Gilmore 2012, Rix & Bovy 2013).

From the Galactic Archaeology viewpoint, one of the most important issues is the determination and relative quantification of processes shaping the galaxy disc structure and constraining its assembly history. This explains the unprecedented efforts now in place to obtain detailed chemical and kinematical information for a large number of stars in our Galaxy. A suite of vast stellar astrometric, photometric and spectroscopic surveys has been designed to map the Milky Way and answer questions related to its formation. With the data provided by medium- and low-resolution surveys such as RAVE (Steinmetz et al. 2006), LAMOST/LEGUE (Zhao et al. 2006; Newberg et al.

† This Chapter is published in *Astronomy & Astrophysics*, Vol. 564, 2014, p. A115+.

2012) and SEGUE (Yanny et al. 2009), together with information coming from high-resolution surveys such as Gaia-ESO (GES, Gilmore et al. 2012); HERMES/GALAH (Zucker et al. 2012) and APOGEE (Allende Prieto et al. 2008), it will be possible to draw a new detailed picture of our Galaxy, providing an ideal testbench for galaxy formation models. Most importantly, the recently launched Gaia satellite (Perryman et al. 2001, `http://www.rssd.esa.int/Gaia`) and its spectroscopic follow-up missions will revolutionize not only our understanding of the Milky Way, but the whole field of Near-Field Cosmology[1]. The combination of these datasets with complementary information coming from asteroseismology (Miglio et al. 2013a) data will be an important asset.

The big challenge ahead of us is to build theoretical models able to make predictions to be compared with these huge datasets. The only way to understand the high-dimensional problem of the formation and evolution of a late-type barred spiral galaxy like the MW in a cosmological context is through sophisticated simulations combining chemical and dynamical evolution (see detailed discussion in Minchev et al. 2013). Constraining these models has become a primary task of current and future surveys.

In this first of a forthcoming series of papers, we focus on finding new and tighter chemodynamical constraints on models of our Galaxy using data from the Apache Point Observatory Galactic Evolution Experiment (APOGEE; Allende Prieto et al. 2008, Majewski et al. 2014, in prep.), one of four experiments operating in the third epoch of the Sloan Digital Sky Survey (SDSS-III; Eisenstein et al. 2011), using the 2.5m Sloan telescope (Gunn et al. 2006) at Apache Point Observatory (APO). We define a subsample of APOGEE data from the recent data release (DR10; Ahn et al. 2013) for which full kinematical information was obtained for red giant stars spanning distances as large as 10 kpc from the Sun (although most of the high quality data in our sample is confined to distances below 5 kpc). A complementary paper (Hayden et al. 2013) presents the spatial distribution of mean metallicities for the full DR10 sample, which extends to even larger distances, but without kinematical information. Future work will further develop the analyses of these samples, including comparisons with predictions from star count models like TRILEGAL (Girardi et al. 2005, 2012), chemical evolution models for the Galactic disc and (semi-)cosmological chemodynamical simulations of the MW, such as the recent model of Minchev et al. (2013).

In Section 2.2 we describe how our APOGEE high-quality sample (HQ) was selected, both in terms of chemistry and kinematics, carefully discussing what *minimal quality requirements* are necessary to define samples to be used for detailed chemodynamical studies. Section 2.3 focusses on the kinematical parameters: we present our computed distances, the adopted proper motions and the computed orbital parameters (along with their uncertainties). By pruning our sample to include stars with best-determined chemical *and* orbital parameters, we construct what we refer to as the *Gold sample*. In Section 5.3, we first discuss a *local* (Solar vicinity) sample (with d < 1 kpc), and compare it with the high-resolution, very-high S/N HARPS sample of Adibekyan et al. (2011). We then extend our discussion to further regions outside of the Solar neighborhood. Section 5.5 summarizes our main results and discusses some future prospects.

[1] Primary task of ESA's astrometric mission *Gaia* is to measure the parallaxes and proper motions of up to one billion (mostly disc) stars with unprecedented accuracy ($\sigma(\pi) \sim 20\mu$as and $\sigma(\mu) \sim 20\mu$as at magnitude $G \sim 15$ – providing a distance accuracy of 1–2% at 1 kpc; see Turon et al. 2005), but it also provides medium-resolution spectra in the CaII triplet region (the 848 . . . 874 nm wavelength range) for stars brighter than 17th magnitude, obtaining high precision radial velocities ($\sigma(v_{\rm los}) \sim 10$ km/s; (Katz et al. 2004)), in addition to low-resolution optical spectra providing well-determined stellar parameters. Thus, Gaia will be able to probe the kinematics of the disc out to several kpc in all directions (Bailer-Jones 2009).

2.2. Observations and Sample Selection

APOGEE delivers high-resolution ($R \sim 22,500$) high signal-to-noise ($S/N \sim 100$ pixel^{-1}) spectra of primarily red giant stars in the H band ($\lambda = 1.51 - 1.69\mu$m), enabling the determination of precise (~ 100 m/s) radial velocities as well as stellar parameters and chemical abundances of up to 15 elements. In addition, APOGEE has already proven to be useful in various other fields as well, such as the determination of the Galactic rotation curve (Bovy et al. 2012a), detection of (sub-)stellar companions (Nidever et al. 2014, in prep.), spectral variability of hot stars (Chojnowski et al. 2014, in prep.), dark matter distribution in the Sgr dSph galaxy (Majewski et al. 2013), characterisation of diffuse interstellar absorption bands (Zasowski et al. 2014, in prep.) or open star clusters (Frinchaboy et al. 2013; Covey et al. 2014, in prep.).

APOGEE's final goal is to measure accurate and precise radial velocities, stellar parameters and chemical abundances for around 100,000 red giants candidates. APOGEE's target selection is a key part of the survey, because it has to be assured that the sample is minimally biased and homogeneous to draw robust conclusions about the underlying stellar populations (see Zasowski et al. 2013 for details). Here we will explore chemodynamical constraints already produced from the first year of APOGEE data.

The database of APOGEE spectra released in SDSS DR10 forms the largest catalogue of high-resolution IR spectra ever obtained. For more than 57,000 stars observed by APOGEE before July 2012, stellar parameters and chemical abundances have been determined by the APOGEE Stellar Parameters and Chemical Abundances Pipeline (ASPCAP; Ahn et al. 2013, García Pérez et al. 2014, in prep.). We use these data to assemble a sample of red giant stars with high-quality chemical abundances that will be employed to probe the chemodynamical properties of the Galactic disc. In this Section we describe the selection criteria and the calibration relations applied to the DR10 catalogue, leading to our "HQ Sample". A summary of the applied cuts is given in Table 2.1.

2.2.1. Photometry

Although the APOGEE targeting strategy for the main survey was chosen to ensure high quality data, consistency in the input catalogue and a straightforward selection function, this is not always true for stars selected for ancillary science programs, among them giant stars in the *Kepler* (Gilliland et al. 2010) and CoRoT (Baglin et al. 2006) fields. Hence, the NIR magnitudes and errors for the final sample were taken directly from the 2MASS Point Source Catalogue (Cutri et al. 2003), requiring the original quality criteria for the main survey described in Zasowski et al. (2013, see their Table 3 for details) and, as some of the ancillary targets[2] were not strictly selected on the basis of 2MASS astrometry, also requiring positional consistency.

[2] The main group of ancillary targets in our final sample are the asteroseimic targets from *Kepler* and CoRoT. Known cluster members and

The mid-IR data used for the estimation of interstellar extinction was adopted from the WISE (Wright et al. 2010) and Spitzer-IRAC photometry (Benjamin et al. 2005) contained in the APOGEE targeting (requiring only that the uncertainties of the corresponding $[4.5\mu]$ magnitude be ≤ 0.1 mag), as well as the actual extinction values $A(K_s)$ calculated with the RJCE method (Majewski et al. 2011; Nidever et al. 2012a), as described in Zasowski et al. (2013).

2.2.2. APOGEE data reduction

APOGEE's reduction pipeline delivers 1D flux-calibrated spectra corrected for telluric absorption and sky emission, along with precise ($\delta(v_{\rm los}) \lesssim 0.2$ km/s) and accurate (zero-point accuracy $\approx 0.26 \pm 0.22$ km/s) heliocentric velocities (Nidever et al. 2012b), and data-quality flags that are also included in the higher level catalogues. In particular, we use the data-quality flags, the signal-to-noise ratio (S/N) and the visit-to-visit scatter of the heliocentric velocities $\sigma(v_{\rm los})$ to clean our sample (see Table 2.1 for a summary).

ASPCAP works in two steps: first, the main stellar parameters are estimated from synthetic template fit to the entire APOGEE spectrum provided by the APOGEE reduction pipeline (see Ahn et al. 2013 and Nidever et al. 2014 (in prep.) for details). Next, these values are used to fit various small spectral windows containing line features from individual elements to derive their abundances. Before DR10, the pipeline development was focussed on the first step, so that only the set of overall stellar parameters are reported in DR10. Because molecular features (CN, CO, and OH) can be very prominent in cool stellar atmospheres, a global fit needs to allow for variations in at least seven parameters: effective temperature $T_{\rm eff}$, surface gravity $\log g$, microturbulence ξ_t, overall metal abundance [M/H], and relative α-element (including oxygen) [α/M], carbon [C/M], and nitrogen [N/M] abundances[3]. As the microturbulence is currently approximated as a fixed function of $\log g$ to save computing time, six independent parameters are released from the DR10 ASPCAP run.

2.2.3. Spectra quality, signal-to-noise ratio and radial velocities

Various tests have shown that ASPCAP requires at least a S/N of 50/pixel, but optimally 100/pixel, to deliver robust chemical abundances (Allende Prieto et al. 2008; Eisenstein et al. 2011; Ahn et al. 2013). In the present work, we adopt a signal-to-noise ratio cut of 70. Our choice is a trade-off to yield a clean, yet statistically significant, sample.

The radial velocities are taken from the ASPCAP files, and their uncertainties calculated as the quadratic sum of the visit-to-visit scatter and the median visit error in $v_{\rm los}$ (usually the visit-to-visit scatter dominates). To eliminate likely binaries, it is required that $\sigma(v_{\rm los}) < 1$km/s.

probable candidates have not been used in the final analysis, due to the additional selection biases this might introduce.

[3] The Solar abundance values are adopted from Asplund et al. (2005). [M/H] is defined as the overall logarithmic metal abundance with respect to the Solar abundance ratio pattern. [X/M] denotes the deviation of an element X from the corresponding Solar abundance ratio, [X/M] = [X/H] − [M/H]. The α-elements considered by ASPCAP are O, Ne, Mg, Si, S, Ca, and Ti.

ASPCAP convergence

ASPCAP finds the best-fit stellar model atmosphere based on a χ^2 minimisation of the cross-correlation between the observed spectrum and a grid of synthetic model spectra (Mészáros et al. 2012; Ahn et al. 2013). However, for a number of stars the algorithm does not yet find a satisfactory match in the set of synthetic spectra, due to a variety of reasons. The most common case in DR10 is that a star has a much cooler atmosphere than even the coolest grid models currently available; this occurs for the extremely luminous M (super-)giants. In some cases the ASPCAP algorithms also fail to find the absolute minimum in the χ^2 landscape of the model grids, and thus the best-fitting synthetic atmosphere. As such cases must be avoided, it is necessary to:

- Eliminate stars whose ASPCAP parameters lie too near the edges of the current grids of synthetic spectra.
- Set an upper limit on the (reduced) χ^2 of the ASPCAP fit to avoid poorly converged results.

Both these considerations have entered into our sample selection; in this work we require $\chi^2 < 25$.

While there is a clear trend of the ASPCAP fit χ^2 with temperature, this fact alone does not mean that cooler stars have more uncertain parameters. In fact, this trend is expected because the spectra of cool stars become considerably more crowded due to the numerous molecular features, and are harder to fit by automated software. But loosening the overall χ^2 criterion for cool stars by allowing, e.g., $\chi^2 < 40$ for $T_{\rm eff} < 4200$ K, shows that high χ^2 is indeed correlated with issues in the [C/M] and [α/M] parameters in the cool regime (see left panel of Fig. 2.1). We have thus maintained the same χ^2 limit for all temperatures. We are aware that this choice induces a small bias against the most metal-rich part of the upper giant branch. This point should be kept in mind when interpreting our results in Section 5.3.

ASPCAP parameters

Most importantly, the giant stars for the HQ sample are selected from the ASPCAP *Kiel* diagram ($T_{\rm eff}$ vs. $\log g$, right panel of Figure 2.1) based on a generous cut of the giant branch, resulting in a $T_{\rm eff}$ upper limit of 5200 K and an (uncalibrated) $\log g$ upper limit of 3.8 dex (see below). ASPCAP DR10 metallicities are generally well-behaved and reliable in the metallicity regime of the Galactic disc ($-1.5 \lesssim$ [M/H] $\lesssim +0.4$, Mészáros et al. 2013) with small systematic shifts at the metal-rich end as well as larger shifts in the very low-metallicity regime. In this study we applied a more conservative cut in the metal-poor regime ([M/H]= -1.0), which was based on tests with previous ASPCAP versions. To cover the entire metallicity regime of the thin disc and still avoid the ASPCAP grid edge at [M/H] = +0.5, we cut the metal-rich end at [M/H] = +0.45. As has also been shown by Mészáros et al. (2013), α-element abundances derived by ASPCAP match the results from cluster literature fairly well for $-0.5 <$ [M/H] $< +0.1$; outside this metallicity range some systematic dependencies on the other fit parameters are seen. The applied calibrations and adopted uncertainties for these parameters are discussed in the next Sections.

Table 2.1. Summary Table for the selection of the APOGEE HQ Giant Sample

Parameter	Requirement	Notes
S/N	> 70/pixel	
$\sigma(v_{\rm los})$	≤ 1 km/s	no RV-identified binaries
APOGEE_STARFLAG bits	$\notin \{0, 1, 3\}$	no commissioning data or obviously bad spectra
APOGEE_TARGET1 bits	$\notin \{10, 15, 16, 18, 19, 23, 24\}$	avoid, e.g., extended objects, M31 clusters, M dwarfs
APOGEE_TARGET2 bits	$\notin \{4, 9, 10, 13, 15, 16, 17\}$	avoid, e.g., sky fibres, telluric standards, known cluster members
ASPCAP χ^2	< 25	
$T_{\rm eff}$	$\in \{3800\,{\rm K}, 5200\,{\rm K}\}$	avoid too low temperatures
$\log g$	$\in \{0.5\,{\rm dex}, 3.8\,{\rm dex}\}$	select red giant stars
[M/H]	$\in \{-1.0, 0.45\}$	avoid low metallicities

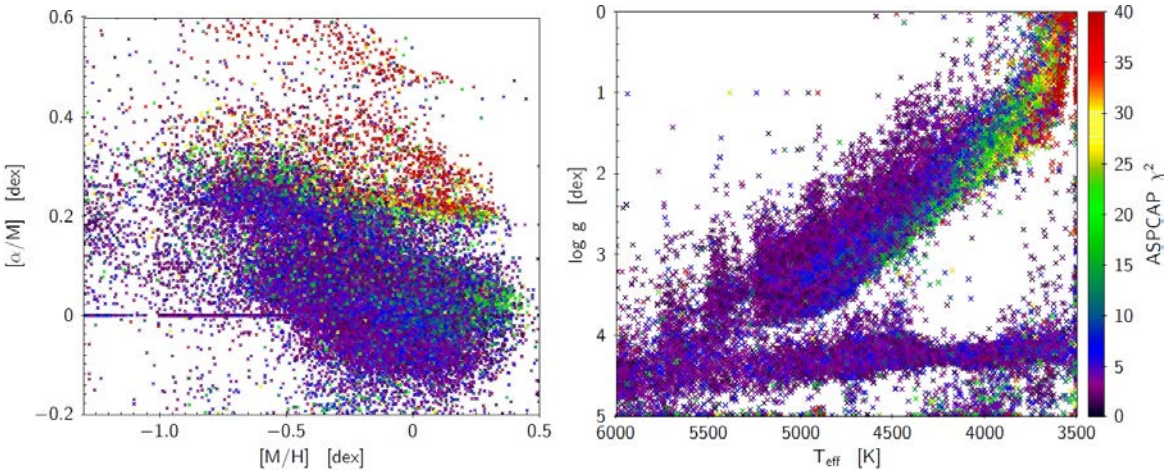

Figure 2.1. Two 2D slices through the 6-dimensional hypercube of ASPCAP parameter space, colour-coded by χ^2. Left panel: [α/M] vs. [M/H], the so-called chemical plane. Some artificial features introduced by ASPCAP are also visible (the region of unphysical, poorly converged best-fit models appearing in red; the line at [α/M]= 0.0 corresponding to the A and F dwarfs forced to Solar α-abundances; see Section 2.2.2 for details). Right panel: The ASPCAP *Kiel* diagram ($T_{\rm eff}$ vs. $\log g$). Giant stars lie on the diagonal branch, while main sequence stars are aligned in the horizontal sequence in the lower part of the diagram. The latter behaviour is somewhat unphysical – cooler main sequence stars should have higher surface gravities – and shows that the pipeline is not optimised for dwarf stars yet.

2.2.4. Calibrations

Effective temperature

DR10 effective temperatures derived by ASPCAP are fairly reliable over a wide parameter range, showing a good agreement with independently-derived temperatures from high-resolution spectroscopy (deviating on average by 8 ± 161 K), and a good agreement with effective temperatures derived with the IR flux method using the relations of González Hernández & Bonifacio (2009), modulo a zero-point shift of 113 K (see Mészáros et al. 2013 for details).

Whereas Mészáros et al. (2013) decided to correct for this shift, we currently use the uncorrected DR10 temperatures because of the good agreement with high-resolution optical spectroscopy. It is known that systematic differences between the photometric and spectroscopic temperature scales exist: spectroscopic excitation temperatures often yield lower values than colour–temperature calibrations by a few hundred Kelvins (e.g., Johnson 2002).

Surface gravity

Whereas ASPCAP effective temperatures are currently considered to be remarkably accurate when compared to surveys of similar size, the pipeline still has considerable difficulties in providing reliable estimates for surface gravities; log g offsets of order 0.3 – 0.5 dex are documented (Mészáros et al. 2013).

In the present work, we correct for these systematics by calibrating log g using asteroseismic data from 279 Kepler stars contained in the APOKASC[4] catalogue (Epstein et al. 2014, in prep.), as well as 115 stars observed by the CoRoT satellite that have been followed up by APOGEE (CoRoT field LRa01, data published in Miglio et al. 2013a,b). As shown in Figure 2.2, the following linear correction as a function of temperature was applied for $T_{\rm eff} > 4000$ K:[5]

[4] The collaboration between *Kepler* and APOGEE (where KASC stands for the Kepler Asteroseismic Science Consortium).

[5] As shown in Mészáros et al. (2013), a pure asteroseismic analysis suggests that the uncorrected DR10 gravities are overestimated in the full metallicity range, whereas a comparison with the cluster isochrones suggest that the DR10 surface gravities are nearly correct, hence implying a dependency of the gravity correction on metallicity only in the metal-poor regime. We instead provide a pure asteroseismic calibration based on an extended sample, also including the CoRoT targets, which

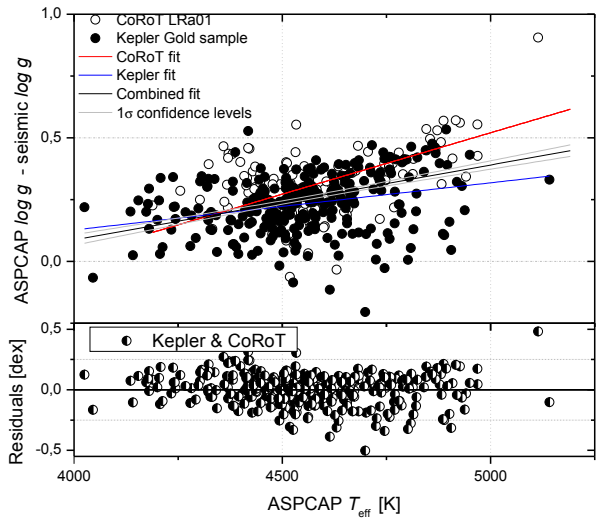

Figure 2.2. Illustration of the applied $\log g$ calibration using asteroseismology data. ASPCAP DR10 $\log g$ is higher with respect to the seismic values by on average ~ 0.25 dex, with the discrepancy increasing with increasing effective temperature. A linear fit using only CoRoT data (115 stars, open circles) is given by the red line, a fit using only Kepler data (279 stars, black circles) is indicated by the blue line. The fit obtained by combining the two datasets is illustrated by the thick black line. The lower panel shows the residuals, revealing some remaining possible systematics.

$$\log g_{\rm calib} = \log g_{\rm ASPCAP} + 1.13 - 3.03 \cdot 10^{-4} \cdot T_{\rm eff}.$$

For temperatures between 3800 K $< T_{\rm eff} <$ 4000 K, no correction was applied.

Metallicity

For our analysis, we use the calibration described in Mészáros et al. (2013), derived using a sample of well-studied open and globular clusters covering a wide range of metallicities ([Fe/H] $\in \{-2.3, +0.4\}$).

α-element abundance

Several tests suggest that APOGEE DR10 α-element abundances are still to be treated with caution, but can in principle be used in scientific analyses (Ahn et al. 2013). While α in principle tracks the elemental abundances of O, Ne, Mg, Si, S, Ca and Ti, the spectral features corresponding to these elements are very sensitive to changes in the effective temperature (in cooler atmospheres, [α/M] mainly tracks O and Ti, whereas in warmer atmospheres Ca, Mg and Si features are more important), so that any trends seen with α-element abundance should be checked in narrower temperature bins. For cooler metal-poor stars, the lack of Fe lines seems to be the primary source of ambiguity for the overall metal and oxygen abundance. The sytematic trends seen at the metal-rich end still remain poorly understood.

is appropriate for the metallicity range considered in the present work (with [M/H] > -1).

2.2.5. Uncertainties

Adopted errors

The initial ASPCAP parameter error estimates are based on the the random contributions to the errors as derived by inverting the FERRE χ^2 curvature matrix, following the favoured prescription of Press et al. (1992). However, these values are too small to represent reliable random uncertainties by roughly a factor of 15 when compared to the scatter observed in the calibration clusters (García Pérez et al. 2014, in prep.). For DR10, it has therefore been decided to follow the conservative (though somewhat artificial) uncertainty treatment of Allende Prieto et al. (2006). The final error on each parameter is calculated as the larger of a) the individual FERRE errors times 15, and b) the general scatter of the clusters as given by Mészáros et al. (2013):

$$\begin{aligned} \Delta T_{\rm eff} &= (83.8 - 39.8 \cdot [{\rm M/H}])\ {\rm K} \\ \Delta \log g &= 0.2\ {\rm dex} \\ \Delta[{\rm M/H}] &= (0.055 - 0.036 \cdot [{\rm M/H}])\ {\rm dex} \\ \Delta[\alpha/{\rm M}] &= 0.08\ {\rm dex} \end{aligned} \quad (2.1)$$

We have adopted this prescription for this work, which delivers at least reliable upper limits to the uncertainties.

Binarity

It has long been established that a high percentage of the local F- and G-dwarf population lives in multiple stellar systems (e.g., Duquennoy & Mayor 1991 and Duquennoy et al. 1991 estimate a multiplicity fraction of 65%, while recent estimates by Fuhrmann (2011) suggest a value of 50% for Solar-type stars). This underlines the importance of understanding how unresolved companions affect stellar parameter estimates. Schlesinger et al. (2010) used the SEGUE Stellar Parameter Pipeline to estimate the effects of potential contamination by the light from a binary companion on their high-S/N sample of $\sim 20,000$ G-K dwarf stars observed by SEGUE, and find that 11±2% of the latter is expected to be significantly affected in its temperature or metallicity determination by an undetected companion, resulting most importantly in a systematic shift to cooler temperatures.

Although we cannot provide quantitative estimates of binarity effects on ASPCAP's stellar parameter estimates yet, the affected sample percentage should be even smaller than in SEGUE, for two reasons. First, giant stars are quite luminous, so that the light of the primary is likely to dominate the resulting spectrum. Secondly, APOGEE's split multi-epoch observations permit accurate detections of temporal radial-velocity variations, so that by requiring the radial-velocity scatter $\sigma(v_{\rm los})$ to be small we already eliminate a significant fraction of the multiple systems (which on the other hand means introducing another bias into our sample).

2.2.6. Adopted subsamples

We have defined, for the first time, a high-quality chemical sample extending at least 4 to 6 kpc beyond the solar circle. This dataset is crucial for constraining chemodynamical models outside the solar region, something urgently needed in the field and so far addressed with SEGUE & RAVE – low- and medium-resolution samples heavily biased to high Galactic latitudes. We will use the chemical high-quality (HQ) sample to study the inner and outer parts of the disc.

We further define four high-quality (sub-)samples with different characteristics (see Table 2.2 for details):

- An (extended) Solar-vicinity sample of APOGEE red giants confined to a sphere of radius 1 kpc around the Sun, for comparison with previous high-resolution studies, in particular the recent HARPS FGK dwarf sample of Adibekyan et al. (2011).
- The HQ^k sample – a subsample of the HQ sample with fully-determined 6-D phase space coordinates, i.e., valid distance determinations and proper motions (see Sect. 2.3). The superscript k stands for 'kinematics'.
- A chemodynamical disc sample with as precise kinematical information as possible – not as local as existing high-resolution samples in the literature, but extending to 1–2 kpc in distance. We will define an APOGEE "Gold Sample" which meets these criteria, by imposing quality limits on distance and proper motion error.

While the first two samples are free from any further biases that might be introduced by the proper motion catalogue, the other two samples might possess some biases. In addition, in the case of the extended sample, biases are expected towards the inner Galactic regions mainly due to a sparse coverage of the stellar disc (additional biases affecting the APOGEE DR10 sample as a whole are discussed in Hayden et al. 2013). In a forthcoming paper we intend to simulate our sample with a population synthesis model to be able to quantify better the impact of those biases on our results. The present paper mainly focuses on observables that are less affected by potential observational biases.

2.3. Kinematics

To perform a thorough chemodynamical analysis of a stellar survey, it is necessary to measure and interpret the motion of the stars inside the Galaxy and to calculate their orbital parameters.[6] Here, we particularly aim at finding correlations between chemical-abundance patterns and orbital properties. To obtain the full 6-dimensional phase space coordinates of the stars in the HQ sample, the 2MASS astrometry and APOGEE line-of-sight velocities must be complemented by information on stellar distances and proper motions.

2.3.1. Distances

The development of sophisticated spectrophotometric parallax methods has been undertaken by many different groups in the past several years (e.g., Rocha-Pinto et al. 2003; Allende Prieto et al. 2006; Breddels et al. 2010; Zwitter et al. 2010; Burnett & Binney 2010; Burnett et al. 2011). For APOGEE stars, preliminary distance estimates from various groups exist (Hayden et al. 2014, in prep.; Santiago et al. 2014; Schultheis et al. 2014, subm.). We have computed our distances based on the Bayesian approach of Allende Prieto et al. (2006), which was further developed by us (see Santiago et al. 2014) to compute SDSS distances both for APOGEE (giants) and SEGUE (dwarfs). In this section, the general features of the method are briefly described; for a detailed description, the reader is referred to Santiago et al. (2014).

The goal of isochrone-based distance codes is to find stellar models that fit as many spectrophotometric observables as possible (magnitudes, colours, stellar parameters, abundances), and are most likely to be close to the true one. In the Bayesian method adopted in Santiago et al. (2014), an efficient use is being made of all the available uncertainties and several simple priors (stellar density distribution, initial mass function, uniform star formation history with different cut-offs for the different stellar components, metallicity distributions). A general framework for spectrophotometric distances using Bayesian methods is provided by, e.g., Burnett & Binney (2010).

In brief, one can write the probability of finding the "true" parameter set for a star $\mathbf{x} = (l, b, s, M, \tau, [\mathrm{M/H}])$ when observing the quantities $\mathbf{y} = (T_{\rm eff}, \log g, [\mathrm{M/H}]_{\rm obs}$, magnitudes, colours, $l_{\rm obs}, b_{\rm obs}, \dots)$ via Bayes' theorem as

$$p(\mathbf{x}|\overline{\mathbf{y}}, \boldsymbol{\sigma}_{\mathbf{y}}, S) \propto P(S|\overline{\mathbf{y}}, \mathbf{x}, \boldsymbol{\sigma}_{\mathbf{y}}) \cdot p(\overline{\mathbf{y}}|\mathbf{x}, \boldsymbol{\sigma}_{\mathbf{y}}) \cdot p(\boldsymbol{\sigma}_{\mathbf{y}}|\mathbf{x}) \cdot p(\mathbf{x}) \quad (2.2)$$

Here, (l, b) are the position angles in the Heliocentric Galactic coordinate frame, s the distance from the Sun, M the initial stellar mass, τ its age and [M/H] the overall metallicity. Quantities with subscript 'obs' stand for the corresponding observed values.

The actual measured values of the observed parameters $\mathbf{y}$ and their uncertainties are denoted as $\overline{\mathbf{y}}$ and $\boldsymbol{\sigma}_{\mathbf{y}}$, respectively, whereas the property S stands for the fact that the star belongs to our sample. The four factors in eq. 2.2 are

1. The selection function (SF) of the sample, $P(S|\overline{\mathbf{y}}, \mathbf{x}, \boldsymbol{\sigma}_{\mathbf{y}})$.
2. The likelihood $p(\overline{\mathbf{y}}|\mathbf{x}, \boldsymbol{\sigma}_{\mathbf{y}})$ that, given the true values $\mathbf{x}$ and the measurement uncertainties $\boldsymbol{\sigma}_{\mathbf{y}}$, the set $\overline{\mathbf{y}}$ is measured.
3. The probability $p(\boldsymbol{\sigma}_{\mathbf{y}}|\mathbf{x})$ to observe the quoted errors given the variable set $\mathbf{x}$.
4. A number of multiplicative priors subsumed under the expression $p(\mathbf{x})$.

Each of these terms has to be modeled separately, which in the case of large stellar surveys usually proves a challenging task. However, some of the (sub-)terms peak more sharply than others, thus dominating the full probability distribution function (pdf) in eq. 2.2. The statistically relevant set of 'true' parameters $\mathbf{x}$ and its uncertainties can then be calculated by computing the moments of this pdf. In particular, a distance estimate s^* is computed by marginalizing the pdf over the other parameters and then computing the mean, mode or median of the one-dimensional probability distribution.

For our APOGEE sample, we adopt the following assumptions for the four terms in eq. 2.2:

1. The dependency of the pdf on the selection function is assumed to be slowly-varying, which may be the main caveat of our current method. However, the sharp magnitude and colour limits in the selection function are already being accounted for by the likelihood term, and we include a term to deal with the Malmquist bias in the priors (see below). In the future, the full selection function or at least a field dependent magnitude distribution will be included in this term: $P(S|\overline{\mathbf{y}}, \mathbf{x}, \boldsymbol{\sigma}_{\mathbf{y}}) \propto p(l, b, H)$, representing the distortion of the underlying distribution introduced by APOGEE's targeting scheme.
2. The likelihood $p(\overline{\mathbf{y}}|\mathbf{x}, \boldsymbol{\sigma}_{\mathbf{y}})$ is modelled by a multivariate Gaussian, meaning that all parameters are assumed to have independent Gaussian errors. We use the photometric uncertainties from 2MASS and the spectroscopic uncertainties as quoted in Section 2.2.

[6] In turn, stellar motions and their statistics can in principle also be used to determine the form of the Milky Way potential. The usefulness of APOGEE in this context was recently demonstrated by Bovy et al. (2012a).

Table 2.2. Definitions and sizes of useful subsamples of the HQ sample.

Name	Requirements	Number of stars
HQ sample	see Table 1	21,288
HQ sample with reliable α-element abundances	4000 K $< T_{\rm eff} <$ 5000 K	18,855
HQ sample with valid distance determination	distance code (Santiago et al. 2014) converges	21,105
HQ sample with (valid) UCAC-4 proper motions	PM criteria (see Sect. 2.3.2) are fulfilled	17,882
HQ^k sample	valid proper motions & distances	17,758
Local HQ sample	$d < 1$ kpc	1,975
Local HQ^k sample	$d < 1$ kpc $\wedge$ HQ^k	1,654
Gold sample	$\sigma(\mu) < 4.0$ mas/yr $\wedge$ $\sigma(d)/d < 20\%$	3,984

3. The term $p(\boldsymbol{\sigma}_{\mathbf{y}}|\mathbf{x})$ is set to unity for simplicity, as the dependence of the full pdf on variations of $\boldsymbol{\sigma}_{\mathbf{y}}$ with $\mathbf{x}$ will be sufficiently weak.
4. As priors on $\mathbf{x}$ we assume a Chabrier-type initial mass function $p(M)$ (Chabrier 2001), and assume different density and metallicity distributions as well as star-formation histories (SFH) for the Galactic components Bulge, Thin Disc, Thick Disc and Halo, following Burnett et al. (2011). In addition, we correct for the Malmquist selection bias resulting from the fact that more luminous stars are preferentially detected by magnitude-limited surveys (Malmquist 1936). We account for this effect by including a term $p(M_{\rm abs}) \propto 10^{0.6 M_{\rm abs}}$.

Whereas the first three assumptions are fairly straightforward and well-accepted, the discussion of how restrictive the priors of the underlying $\mathbf{x}$ distribution should be is still ongoing. Burnett & Binney (2010) argue that the approach of starting from simple uniform priors to not overload the modeling with prejudices is difficult to defend, because the justification to prefer, e.g., a uniform age distribution over a uniform distribution in log(age) is not clear. A rigorous calibration of these priors using a combination of asteroseismology and high-resolution spectroscopy is urgently needed in the field and an ongoing project of the SDSS-III/Brazilian Participation Group.

Differences to other approaches, encountered difficulties and recent upgrades

Despite the fact that our method is similar to many other approaches used in the field, we wish to stress some refinements, namely:

– In principle, a number of measures (e.g., the mean, the median and the mode) could be used for finding the best distance to a star from the full probability distribution (eq. 2.2). As the mode is an unstable quantity when the pdf is rather flat or multi-peaked, and the median is sometimes expensive to compute, we here use the mean, and the second moments of the pdf to obtain an estimate of the uncertainties. Alternatively, we define a different and more extensive prescription for the uncertainties, which is a major advantage of our code, and is described in Section 2.3.1.

– The main difficulties in estimating distances for our dataset are the heavy interstellar extinction in the Galactic plane and the not-yet fully-understood systematic uncertainties in the log g parameter, which impacts any spectrophotometric distance estimate[7]. Unlike for most of the stars in GCS, RAVE and SEGUE, interstellar reddening is a dominant factor for our APOGEE sample, influencing primarily the NIR photometry. We have accounted for this effect by using RJCE-dereddened magnitudes and colours (see Section 2.2.1).

– Differing from other groups, the surface gravity parameter was calibrated using only asteroseismology data, as described in Section 2.2.4.

We have used the newly computed PARSEC isochrones (Bressan et al. 2012), which have a much more detailed grid of theoretical isochrones for the 2MASS JHK_s photometric system than the ones previously available. As the adopted isochrones do not take [α/Fe] enhancement into account, we adopted an ad-hoc approach to include the α-abundance in the overall metallicity Z of the scaled-solar Padova models using the approximation[8] [Z/H] $\approx$ [Fe/H] + [α/Fe].

Ideally, one would want to use self-consistent stellar models with variable α-element content, thus adding an [α/Fe] dimension to the isochrone set. New BaSTI (Cassisi et al. 2006) and PARSEC models are now being computed with consistent alpha-enhanced compositions, which will solve this problem in the near future. At present, the available sets are still too limited and heterogeneous to be used for producing isochrones over a wide range of ages and metallicities.

Uncertainties

Reliable estimates for the uncertainties of the computed distances are quite complicated to evaluate. Changing a model prior, changing a term in the selection function, or dropping one of the observed parameters can, in some cases, change the weighted mean absolute magnitude and thus the distance by a significant amount. In Santiago et al. (2014), we estimate uncertainties in two different ways. First, we calculate an "internal" uncertainty by taking the second moment of the pdf in equation 2.2. To assess how sensitive the derived distances are to changes in the choice of the matching parameters, we also define an alternative "external" uncertainty, based on distance estimates from different subsets of the observables $\mathbf{y} = \{\log g, T_{\rm eff}, [{\rm Z/H}], J-H, H-K_s\}$

Various tests have been performed on possible measures of distance uncertainty. An *internal* measure of the variation of the pdf (Eq. 2.2) could be its confidence intervals, standard deviation or the difference between the mode and the mean of the pdf. It has been shown that both the maximum difference of the

[7] In fact, the latter issue is true for every currently operating spectroscopic survey.

[8] For our APOGEE sample, the relation translates to [Z/H] $\approx$ [M/H]$_{\rm calib}$ + [α/M]. This approximation is still justified because ASPCAP's [M/H] which – when uncalibrated – tracks the overall metal abundance (as explained in footnote 3), was calibrated on literature *iron* values, so that we can use [M/H]$_{\rm calib}$ as a proxy for [Fe/H].

distances using different sub-datasets and the pdf's standard deviation yield similar and robust error estimates (Santiago et al. 2014).

In the following, we will generally use the internal distance uncertainties. The distance uncertainty distribution for the APOGEE HQ sample is shown in the right panel of Fig. 2.3.

Resulting distances

We have computed distances for ~ 21.000 stars in the HQ sample. In the left panel of Fig. 2.3, we show the distance distribution for the APOGEE HQ sample, and the Gold sample defined in Section 2.2. The Gold sample, as indicated in the right panel of Fig. 2.3, satisfies $\sigma(d)/d < 0.2$, along with a criterion on proper motion error (see Section 2.3.2). The Gold sample consequently samples a smaller volume of the Galaxy, and the selection function for this subsample is not straightforward to calculate.

In Fig. 2.4 we compare the volume covered by our Year-1 HQ sample (using our spectrophotometric distances) with the expectations for the 3-year survey data. Through multiple observations in many lines of sight, APOGEE will eventually cover a considerably larger part of the Galaxy than presented in this work.

Distance validation

To validate our code, we have compared our results with a number of completely independent distance measurements determined via asteroseismology, astrometric parallaxes and cluster isochrones. A detailed and quantitative comparison is presented in Santiago et al. (2014). The comparison shows that the method also works reasonably well in an absolute sense. Despite a significant scatter, there is a clear one-to-one correlation with parallax and, modulo small systematic dependencies on the cluster age, with isochrone distances to open and globular clusters. The rms difference is $\lesssim 20\%$, as also expected from our error estimates.

Additionally, our spectrophotometric distances compare favourably with the distances obtained from CoRoT data for 120 stars in the anticenter field LRa01 that have been observed by APOGEE. Despite the substantial (~ 20%) scatter for stars with distances > 3 kpc and a small ($\lesssim$ 15%) systematic shift in the absolute scale, a remarkable concordance of both methods is found.

2.3.2. Proper Motions

Proper motions were added to the APOGEE data from an existing astrometric catalogue via crossmatching. There are two recent catalogues with sufficient sky coverage – PPMXL (Roeser et al. 2010) and UCAC-4 (Zacharias et al. 2012, 2013). The PPMXL catalogue, however, is partly based on images obtained with Schmidt photographic plates, and thus suffers from distortions in some regions of the plate and other systematic errors that are difficult to correct (e.g., Roeser et al. 2010). As UCAC-4 (based only on imaging with CCD cameras) also supersedes PPMXL in the achieved precision, and the number of stars in common with APOGEE for both catalogues is roughly the same (around 80%), it was decided to use only UCAC-4 proper motions in the subsequent analyses to maintain a homogeneous catalogue.

For our APOGEE stars, the following steps were taken:

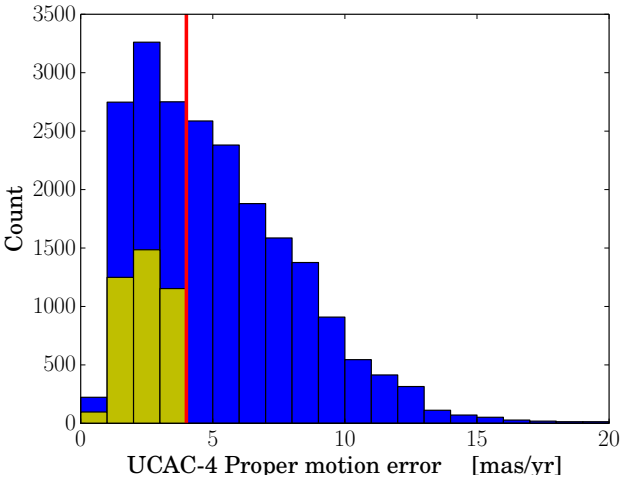

Figure 2.5. Histogram of uncertainties in the absolute error in the UCAC-4 proper motions for the HQ sample with reliable proper motions. The quality cut for the Gold sample is indicated by the vertical red line.

1. We performed a multicone crossmatch with a fixed radius $r = 5''$ of APOGEE's apStar302 survey data targeting file (47.622 stars) with the UCAC-4 catalogue using the VizieR crossmatch service (Ochsenbein 1998; Landais & Ochsenbein 2012) and TOPCAT[9] to identify the nearest object. Because APOGEE targets are required to have distances to their nearest 2MASS neighbours $< 6''$, this criterion is expected to result in a small number of mismatches. A match was found for 42.514 objects (89%).
2. We used 2MASS J, H, K_s magnitudes to cross-check identity: $\Delta(J), \Delta(H)$ or $\Delta(K_s) > 0.01$ mag could mean confusion with a nearby 2MASS object, or careless targeting. A total of 170 such targets were found in the catalogue, and eliminated.
3. The coordinate separations between the two catalogues have also been checked: stars with separations $d > 2''$ are suspicious of having problematical proper motions and have to be inspected visually using the original images. No such stars were found, however.
4. Based on the UCAC-4 input catalogue flags (from the AC2000, AGK2 Bonn, AGK2 Hamburg, Zone astrographic, Black Birch, Lick Astrographic, NPM Lick, SPM Lick catalogues: A, b, h, Z, B, L, N, S flags < 2; 37.004 objects), and the UCAC-4 Hipparcos flag identifying known double stars from the Hipparcos (Perryman et al. 1997; van Leeuwen 2007) and Tycho-2 (Høg et al. 2000) catalogues ($H \neq 2, 4, 5$; 42.362 objects), a combined UCAC-4 reliability flag was assigned (PMflag = 1, if the star suffices all the criteria, PMflag = 0, if not). This flag determines 6.913 of the 42.514 matched objects as problematical – meaning that for 75 % of the survey data we have reliable proper motions. The percentage for the HQ sample is even higher (79%), because the applied S/N cut effectively removes fainter targets, which are less likely to have (reliable) UCAC-4 proper motion measurements.

Figure 2.5 shows the typical uncertainties of UCAC-4 data for our samples. Our Gold sample, as indicated in this Figure and Fig. 2.3, includes only stars with absolute proper motion errors below 4 mas/yr and distance errors below 20%.

[9] The **T**ool for **OP**erating **C**atalogues **A**nd **T**ables (Taylor 2005).

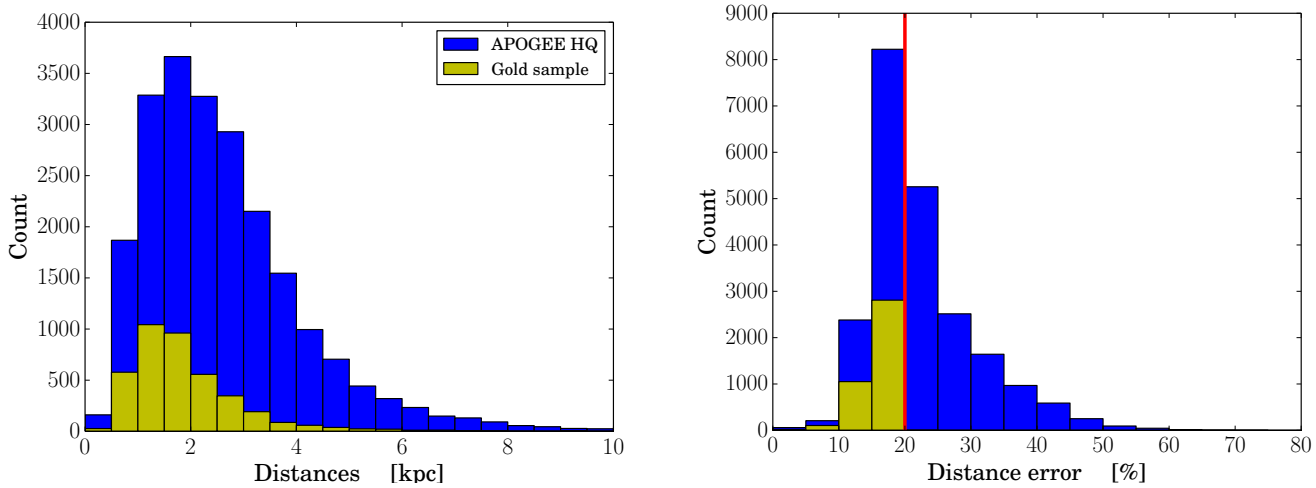

Figure 2.3. Histogram of the distribution of spectrophotometric distances and their errors for the HQ (blue) and the Gold sample. Note that, in addition to the cut in relative distance error, indicated by the red line in the right panel, the Gold sample also satisfies a quality criterion for proper motions (see Section 2.3.2).

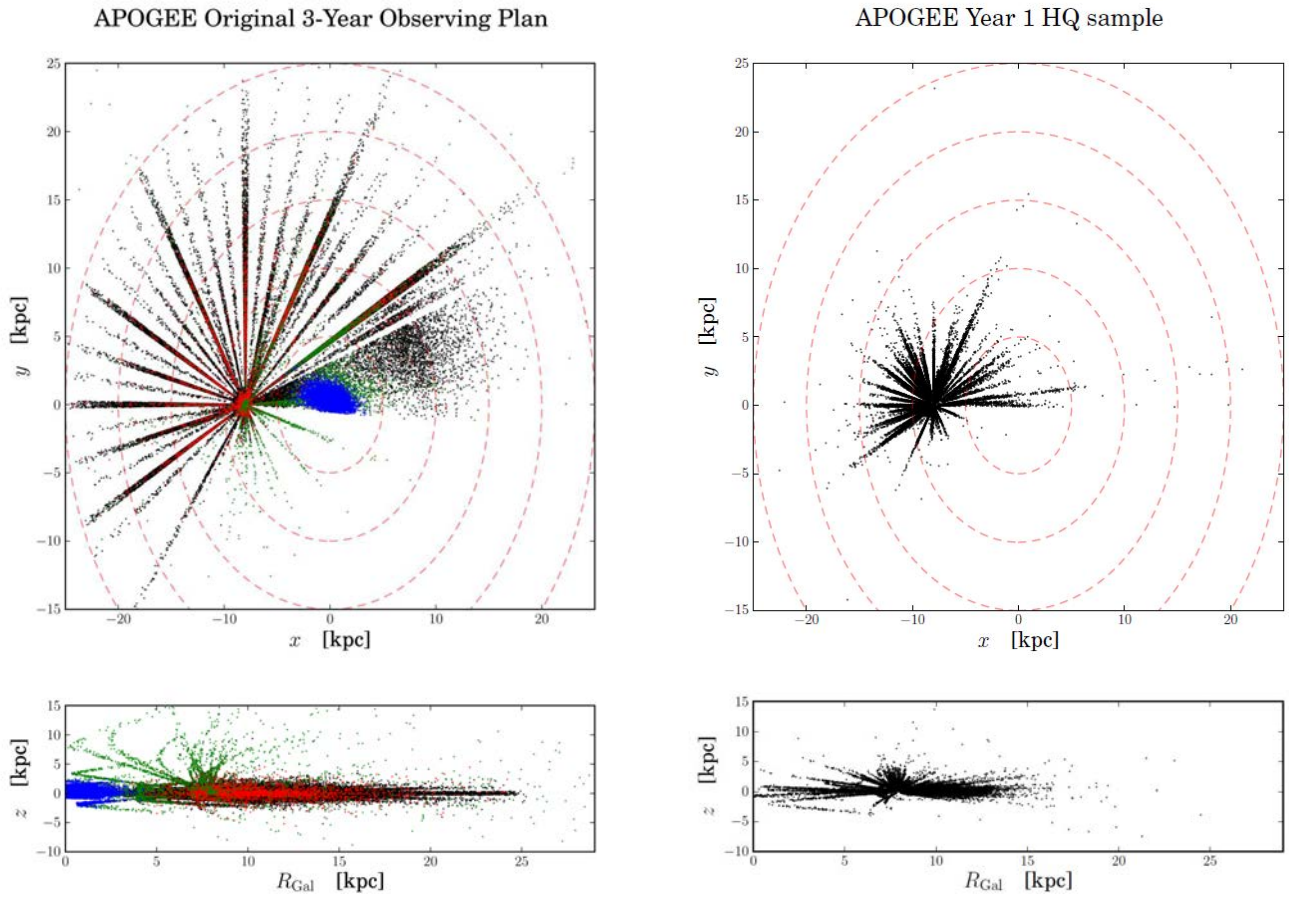

Figure 2.4. Left: TRILEGAL "Strawman" simulation of the APOGEE 3-year survey sample in Galactocentric coordinates. Different colours correspond to different Galactic populations: blue – bulge, green – halo, black – thin disc, red – thick disc. Right: Distribution of the Year-1 APOGEE HQ sample in the same coordinates.

2.3.3. Orbital parameters

It has been known for decades (e.g., Eggen et al. 1962; Scheffler & Elsässer 1982) that different stellar populations may be characterised by their orbital properties. From the full phase-space information $(\alpha, \delta, d, \mu_\alpha, \mu_\delta, v_{\rm los})$, the stellar orbits for our samples were calculated using the Python module *galpy*[10], developed and maintained by J. Bovy (IAS Princeton).

We have assumed a standard Milky Way type potential, consisting of an NFW-type dark matter halo (Navarro, Frenk,

[10] http://github.com/jobovy/galpy

& White 1997), a Miyamoto-Nagai disc (Miyamoto & Nagai 1975) and a Hernquist stellar bulge (Hernquist 1990), in such a way that a flat rotation curve is achieved for the model Galaxy, and that the correct value for the circular velocity at the solar position(R_0 = 8.0 kpc) is recovered ($v_{\rm circ}^{\odot}$ = 220 km/s, see e.g. Bovy et al. 2012a). The Solar motion with respect to the local standard of rest have been adopted from Hogg et al. (2005): $(U, V, W)_{\odot}$ = (10.1, 4.0, 6.7) km/s. The stellar motions are integrated with the *scipy*[11] routine `odeint` over at least 2.5 Gyr and 6 revolutions around the Galaxy.

Various tests have shown that the small deviations in the form of the potential do not lead to significant changes in the properties of the computed orbits, and the time step size for the integration has been chosen sufficiently small that stable and smooth orbits are recovered, but not too small to pose an issue for the required computing time resources.

From the integrated Galactic orbits, characterizing quantities such as orbital eccentricity e, median and mean Galactocentric radii $R_{\rm med}, R_{\rm mean}$, apo- and pericenter $R_{\rm apo}, R_{\rm peri}$, maximum vertical amplitude $z_{\rm max}$, rotational velocity v_{ϕ} as well as the energy E, angular momentum L_z and actions. We currently limit our analysis to the widely used parameter set ($e, R_{\rm med}, z_{\rm max}$).

Uncertainties

The most likely orbital parameters and their uncertainties are estimated using a simple Monte Carlo procedure (similar to, e.g., Gratton et al. 2003; Boeche et al. 2013a) in the following manner. For each star, 100 orbits are computed under variation of the initial conditions (distance modulus, proper motions and radial velocity) according to their estimated errors, where the errors were assumed to follow a Gaussian distribution[12]. From the 100 realisations, the median value of each orbital parameter and its 1σ quantiles are used to estimate the most likely value and its uncertainties.

The left column of Fig. 2.6 shows the calculated uncertainties for the main parameters Galactocentric radius $R_{\rm med}$, eccentricity e and maximum height above the plane $z_{\rm max}$. These plots provide the justification for the introduction of the Gold sample. Whereas the error distributions for the whole HQ^k sample are unsatisfactory (often the orbital parameter uncertainties are far too large to allow for any meaningful interpretation, even in a statistical sense), the additional distance and proper motion quality cuts applied for the Gold sample result in considerably more reliable orbital data for this subset.

Based on tests like these, the final decisions on the definition of the Gold sample were made, essentially as a trade-off between sample size and high-precision parameters. The decision to cut in the observational parameters $\sigma(\mu)$ and $\sigma(d)$, rather than the actual orbital parameter errors, is motivated by the idea to keep the selection function as simple as possible. In the near future, we are planning to simulate the selection of this sample, which also requires a careful modeling of these observational uncertainties.

2.4. Results

We now have the full 6-dimensional phase-space coordinates of the stars in our HQ sample for which proper motions were available (the HQ^k sample), and particularly reliable orbital parameters and distances for a sub-sample of it (the Gold sample). With this information we can perform a first chemodynamical analysis of APOGEE's first-year data.

Our sample is unique with respect to previous samples used in the literature. Indeed, before APOGEE (and GES), high-resolution spectroscopic surveys of the Galactic disc have been limited to very small Galactic volumes – 25 pc in the case of Fuhrmann's Solar neighbourhood survey (Fuhrmann 1998, 2002, 2004, 2008, 2011), ~ 100 pc in the case of Bensby et al. (2003) and Adibekyan et al. (2011), a small number of pencil beams in the case of Kordopatis et al. (2011) and Bensby et al. (2011). Although low- and medium-resolution data from SEGUE, RAVE and ARGOS (Ness et al. 2012) have significantly extended the volume covered by spectroscopic stellar surveys, key observables of chemical evolution such as radial metallicity gradients in the disc are still confined to Heliocentric distances of ~ 2−3 kpc,[13] and often affected by non-trivial selection biases (e.g., Bovy et al. 2012b; Schlesinger et al. 2012). Instead, the sample studied here extends over larger volumes, and can be used to complement previous works. Biases are certainly still present, and we will carefully discuss results that might suffer from these biases, although in the case of APOGEE we expect them to be small (a detailed study of the possible biases will be the topic of our next paper).

Here we focus on the results obtained with a local subsample of our main HQ sample (to discuss the Solar vicinity) and then extend our results to a larger portion of the disc (as explained in Section 2.2).

2.4.1. The Solar Vicinity

What is a local sample?

To separate kinematically hot "visitor stars" from inner and outer Galactic regions that are passing through the (extended) Solar neighbourhood on highly eccentric orbits, we can make use of the computed orbital parameters. Fig. 2.7 shows a histogram of the median Galactocentric radii of APOGEE HQ^k giants currently located within a 1 kpc sphere around the Sun (d < 1 kpc). The Figure illustrates that both stars with guiding radii in the inner as well as the outer disc contribute to the *local* field population as they are passing by on eccentric orbits.

Radial migration is radically different from this effect, because it cannot be recognised from the present kinematics of a star if it has migrated from its birthplace. A migrated star on a cool disc orbit can only be distinguished from a locally born star by using chemistry (e.g., Freeman & Bland-Hawthorn 2002), but only if the chemical imprints of their birth places differ by measurable amounts (which are, however, expected to be small). In particular, extreme migrators will then appear in the wings of the *cleaned local* metallicity distribution, defined as stars with median orbital radii $R_{\rm med}$ (or similarly, mean Galactocentric radii or angular momenta) close to the Solar value. We will therefore often use $R_{\rm med}$ instead of the current Galactocentric radius R.

[11] http://www.scipy.org/

[12] The error distribution for distance (in contrast to the distance modulus) is *not* Gaussian!

[13] Perhaps with the exception of Cheng et al. (2012b), who cover a large range of the outer Galactic disc with SEGUE main-sequence turn-off stars. Samples of HII regions, open clusters, cepheids and young stellar objects still cover a larger volume (e.g., Cescutti et al. 2007), but in contrast to red giants and long-lived dwarfs, these tracers do not cover the Galaxy uniformly in age. Another possibility is to use planetary nebulae as tracers of chemical evolution (Maciel & Chiappini 1994; Maciel & Köppen 1994), although their ages and even their abundances are still subject to considerable uncertainties (Stasińska 2010).

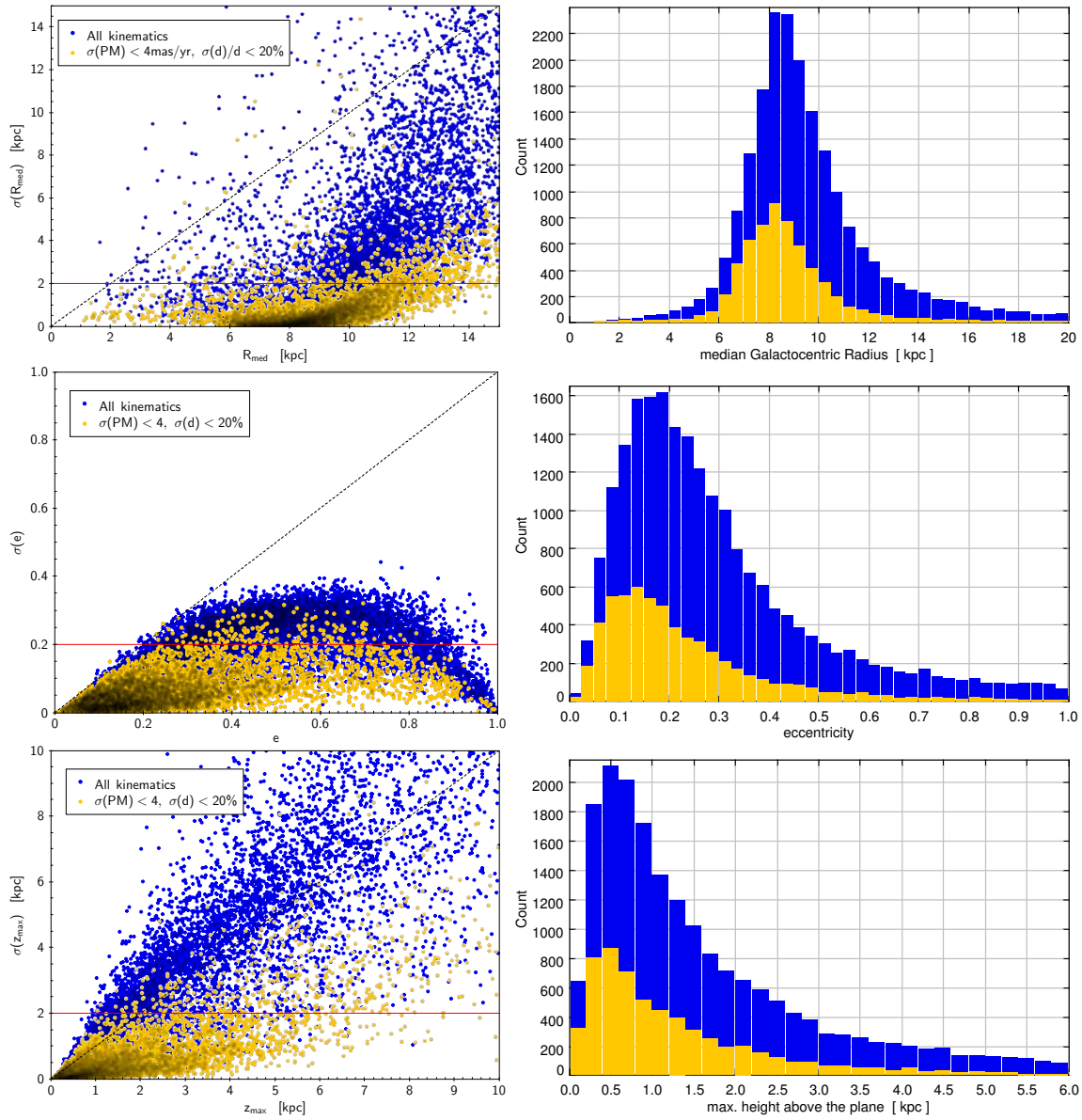

Figure 2.6. Left column: Calculated Monte Carlo uncertainties for the three commonly used orbital parameters median Galactocentric radius $R_{\rm med}$, eccentricity e and maximum height above the plane $z_{\rm max}$ (from top to bottom), for both the HQ^k and the Gold samples, as a function of the corresponding median value. Right column: Histograms of the corresponding median orbital parameters, showing the estimated dynamical properties of our samples.

The Metallicity Distribution Function

The metallicity distribution function (MDF) of the extended Solar neighbourhood is one of the most important and widely used observables to constrain chemical evolution models.

In Fig. 2.8, we compare the local MDF of the high-resolution HARPS FGK dwarf sample of Adibekyan et al. (2011) with the "local" APOGEE HQ and Gold samples. The overall concordance is quite remarkable: both the HQ and the HARPS sample exhibit a peak at metallicity slightly below the Solar value, and their low-metallicity tails agree well within statistical uncertainties. However, a slight discrepancy is found in the percentage of super-Solar metallicity stars. The MDF for the Gold and the HQ sample differ somewhat in this regime, owing to the fact that the additional selection criteria for the Gold sample introduce some subtle biases. Careful modelling of the selection criteria is expected to resolve these discrepancies.

Here, the reader should be reminded that APOGEE's *local* HQ sample still extends to 1000 pc (and has almost no stars with d < 250 pc, see Fig. 2.3), whereas the HARPS sample is confined to ∼ 60 pc, so that the similarity of the MDFs may not be straightforward to explain.

The chemical plane

Stellar chemical-abundance ratio diagrams can be rich in information about the chemical evolution of a galaxy, as they encode the star-formation and chemical-enrichment history of the ISM at the time of a star's birth. Particularly widely used is the [α/Fe] vs. [Fe/H] diagram, because iron and the α-elements are produced and returned to the ISM on different timescales.[14]

[14] For example, the α-element oxygen is mainly produced by type II SNe, i.e., in short-lived massive stars, whereas type Ia SNe produce predominantly more iron (Matteucci & Brocato 1990).

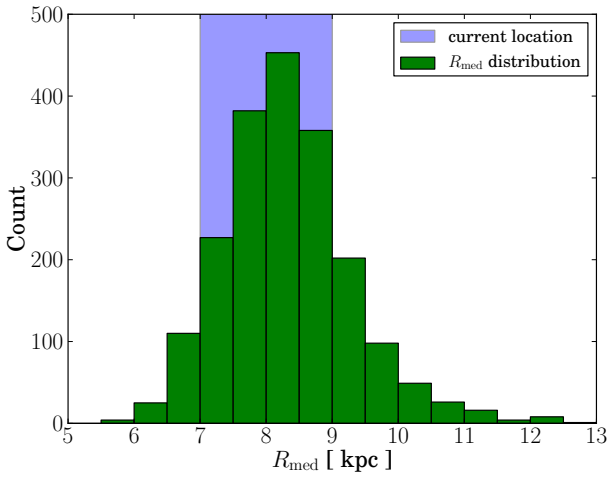

Figure 2.7. Illustration of the "blurring" effect: A sizeable fraction of stars observed to be located less than 1 kpc from the Sun's current position (with $7 < R_{gal} < 9$ kpc; blue-shaded region) move on eccentric inner or outer disc orbits, and are only passing through the Solar neighbourhood.

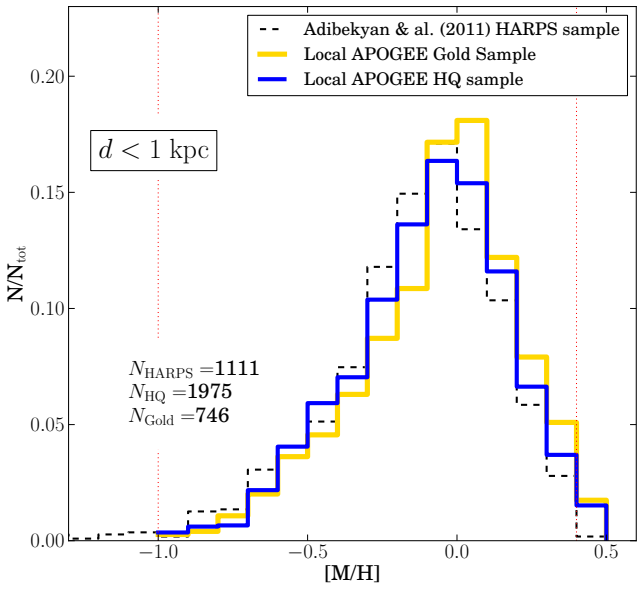

Figure 2.8. The "local" metallicity distribution for the HARPS FGK dwarf sample of Adibekyan et al. (2011) and the APOGEE HQ and Gold red giant samples (blue and gold histograms). The red dotted vertical line at [Fe/H]= −1.0 indicates our adopted metallicity limit for the HQ sample, while the line at +0.4 indicates a possible upper reliabilty limit for ASPCAP metallicities.

Comparing these two abundance ratios for a statistically significant sample constrains the formation history of different Galactic components, the shape of the IMF, stellar yields, the efficiency of dynamical mixing and other parameters (see, e.g., Pagel 2009; Matteucci et al. 2012).

The usefulness of abundance-ratio diagrams for Galactic Archaeology purposes has been recently challenged by the fact that stellar radial migration can mix stars born at different Galactocentric radii (Sellwood & Binney 2002; Roškar et al. 2008; Schönrich & Binney 2009). The quantification of the effects of radial stellar migration and its causes is thus of crucial importance (see Minchev et al. 2013 for a discussion). It is also known that pure chemical evolution models fail to explain the existence of local *super-metal-rich (SMR) stars*[15] (see, e.g., Chiappini 2009 and references therein), and that dynamical mixing mechanisms may affect stellar orbits by heating and/or radial migration.[16] Whereas (radial) heating mainly changes the eccentricity of a star and does not significantly alter its guiding radius, radial migration shifts the angular momentum and thus the guiding radius of a stellar orbit, while it may remain on a circular orbit. In fact, radial migration has been shown to preferentially affect stars on kinematically cool orbits (Minchev et al. 2012). Heating can be caused by, e.g., scattering off of giant molecular clouds (Spitzer & Schwarzschild 1951; Mihalas & Binney 1981), by interaction with the bar and spiral arms (Minchev et al. 2010; Minchev & Quillen 2006), or by merging satellites (Quinn et al. 1993; Villalobos & Helmi 2008). Similarly, several scenarios have been proposed to trigger radial migration, although their relative importance is still under discussion.

The consensus view is that even in the presence of radial migration the chemical diagrams are still extremely useful, and sometimes abundance ratios can be less prone to migration effects than absolute abundances, as shown in Minchev et al. (2013). In the following we discuss the abundance plots obtained with our samples, as this is the first time we can study the chemical plane close to the disc, in a region extending far beyond the Solar vicinity, and with large statistics.

Comparison with other local high-resolution samples

Local high-resolution studies have found a significant gap in the [α/Fe] vs. [Fe/H] chemical-abundance plane, whose origin is still under discussion. The high-resolution volume-complete FOCES sample obtained by K. Fuhrmann (e.g., Fuhrmann 2011) seems to imply that this gap corresponds to a star formation hiatus as advocated by the Two-Infall model (Chiappini et al. 1997). Similar analyses carried out recently by Haywood et al. (2013) and Adibekyan et al. (2013), using the HARPS sample of Adibekyan et al. (2011), lead to the same conclusion, identifying the two regimes in [α/Fe] as chemical signatures of the different formation epochs of thin and thick disc. The recent study by Bensby et al. (2013a), analyzing high-resolution spectra of more than 700 solar-neighbourhood dwarf stars, also points into this direction. The authors find that the different abundance trends for thin and thick disc, and hence the gap, are subject to less scatter when discarding more uncertain chemical abundance data. APOGEE appears to confirm the reality of the gap, displaying a similar gap in the [α/M] vs. [M/H] diagram (see Fig. 2.9).

Figure 2.9 displays the APOGEE chemical abundance plane ([α/M] vs. [M/H]) for stars with $d < 1$ kpc, and compares this picture with the high-resolution ($R \sim 40,000$) high-S/N HARPS sample of Adibekyan et al. (2011), using their individual abundances for Mg, Si and Fe.[17] The similarity of the plots may serve as an initial validation of the ASPCAP pipeline for [M/H] and [α/M]. In both the APOGEE and the HARPS sample there is no a-priori reason to expect the observed gap to be caused by selection biases, because unlike in SEGUE, RAVE or the high-

[15] Stars whose atmospheric metal abundance is significantly higher than the local interstellar medium, first found by Grenon (1972).

[16] Or, in the terminology of Schönrich & Binney (2009): "blurring" and "churning".

[17] Although APOGEE in principle tracks all α-elements, it is expected to be most sensitive to atomic lines like Mg I and Si I in the temperature regime corresponding to the lower giant branch, and thus to smaller distances.

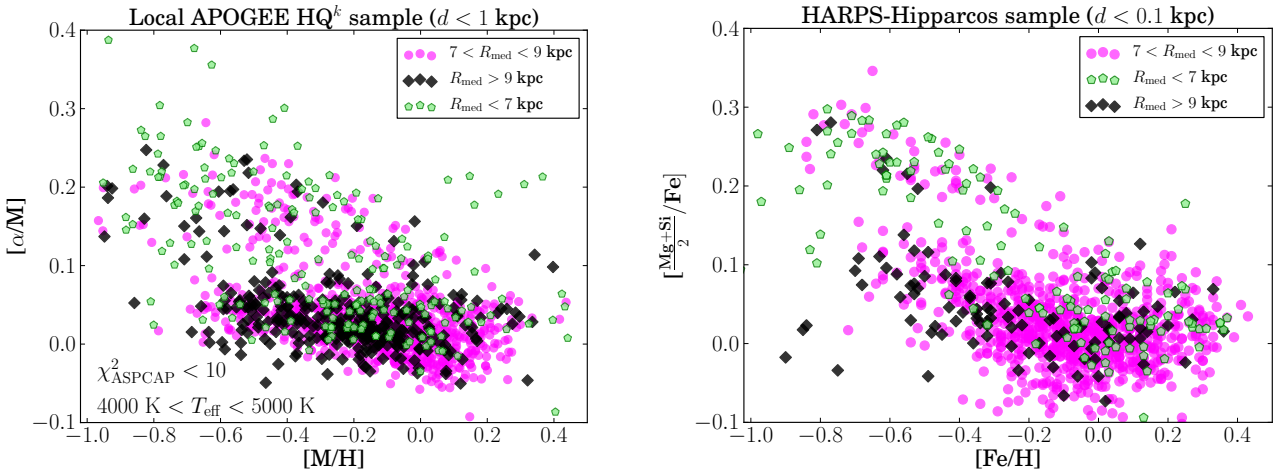

Figure 2.9. The chemical plane using "local" APOGEE HQ^k stars ($d < 1$ kpc, left) compared to the *very* local high-resolution HARPS FGK dwarf sample of Adibekyan et al. (2011). Orbits for the HARPS sample were computed in the same manner as for the APOGEE stars. Although the sampled volumes are quite different in size, the general resemblance of both plots is reassuring. Both plots exhibit the intriguing gap between high- and low-α population, and in both samples it is not straightfroward to explain by selection effects.

resolution studies of Bensby et al. (2003) and Ramírez et al. (2013), the thick disc was not targeted preferentially by these surveys. However, we cannot ultimately confirm nor dismiss this statement until the selection function for APOGEE is properly accounted for (as will be shown in a forthcoming paper).

In Fig. 2.9 (left panel) the APOGEE stars are labelled according to three groups of $R_{\rm med}$ (again showing that the *local* sample contains stars on eccentric orbits whose most probable birth radii, apart from radial migration, are outside/inside the Solar circle $7 < R_{\rm med} < 9$ kpc). The high [α/M] cloud is more populated by stars coming from the inner regions (see discussion on this particular point in Section 2.4.2). On the other hand, the low [α/M] cloud extends down to [M/H]~ -0.8, independently of the studied $R_{\rm med}$ bin, in an almost flat manner. This behaviour is different from what is seen in the *thin-disc-like* stars from HARPS where the low [α/Fe] cloud shows an increase of [α/Fe] towards low metallicities. This difference, most probably, arises from the different biases present in the HARPS and APOGEE sample used here (as both samples have used different colour and temperature cuts). Another contributing factor is that the HARPS data were analysed using an equivalent-width pipeline (ARES; Sousa et al. 2007), whereas ASPCAP uses a cross-correlation technique.

The kinematical properties of a chemically-divided disc

It is tempting to interpret the two clouds in the [α/M] vs. [M/H] diagram as two distinct stellar populations (i.e., *chemical* thin and thick discs[18]). Here, we will briefly explore this approach, and divide the chemical plane in a similar way to Lee et al. (2011) and Adibekyan et al. (2011), as illustrated in Fig. 2.10. For the moment, we focus only on stars whose median Galactocentric radius (as determined by the orbit integration routine) is near the Solar circle ($7 < R_{\rm med} < 9$ kpc). It is now also interesting to see where the two populations defined above are located in orbital-parameter space: In Fig. 2.11, we show how our chemically-divided local sample distributes kinematically (see caption for details).

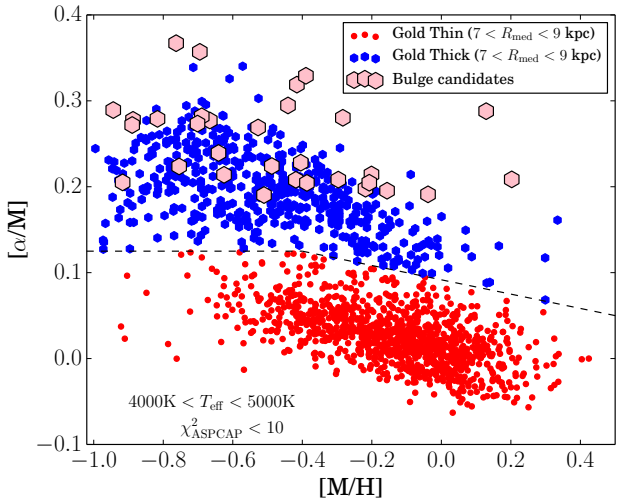

Figure 2.10. The APOGEE chemical plane at the Solar circle ($7 < R_{\rm med} < 9$ kpc) for the Gold sample. To avoid spurious [α/M] data, we only show stars satisfying $\chi^2 < 10$ and $4000 < T_{\rm eff} < 5000$ K. A possible (purely chemical) definition of thin and thick disc, consistent with, e.g., Lee et al. (2011), is indicated by the division into the red and blue points, and the dashed line. For comparison, we also plot kinematically selected candidate bulge stars (pink hexagons).

A few characteristics can be noticed immediately from Figures 8–10:

- The local sample spans a wide range in metallicities, from below [M/H]= −1 to above +0.3.[19]
- When dividing the sample according to the [α/Fe] cut shown in Fig. 2.10, we find that the peak of the metallicity distribution of the chemical thin disc is at [M/H]~ -0.1, and that of the thick disc is at [M/H] ~ -0.5, in concordance with the Geneva-Copenhagen survey and high-resolution spectro-

[18] Another possibility is to separate populations on the basis of kinematics (e.g., Bensby et al. 2003)

[19] Although our sample is currently restricted to [M/H]> −1.0.

scopy literature(e.g., Nordström et al. 2004; Holmberg et al. 2007; Rocha-Pinto & Maciel 1996; Kotoneva et al. 2002).
- The thin disc's spread in [α/M] for a given metallicity is comparable to the quoted observational scatter ($\sim$ 0.08 dex). This result implies that, provided the gap is real, random uncertainties can in principle account for the [α/M] scatter in the thin disc. While this result at first sight leaves little room for radial migration, Minchev et al. (2013) have shown that the presence of strong radial migration does not necessarily imply a large scatter in the abundance ratios.
- The [α/M] ratio in the thick disc increases as the metallicity decreases, reaching a plateau of [α/M]$\sim$ +0.2 at [M/H]$\sim$ $-$0.6. Also, the scatter in [α/M] increases with decreasing [M/H].

In a forthcoming paper, we will study orbital families (groups of stars with similar orbital properties, see, e.g., right panel of Figure 2.11) to be able compare with the RAVE red giant sample of Boeche et al. (2013a). Similar to their results, we find orbital parameter distributions like the Toomre diagram (Feltzing et al. 2003) of chemically-defined thin and thick disc to change considerably with slight variations of the cut in the [α/M] vs. [M/H] plane (see caption of Fig. 2.11). We therefore plan to study mono-abundance populations (Bovy et al. 2012b) in the near future, to investigate if, instead of a rigid dichotomy in the kinematics, a smooth transition from thick to thin disc exists, and to compare these findings with results from RAVE and SEGUE.

2.4.2. Outside the Solar vicinity

The locus of bulge stars selected only by kinematics/position

Although APOGEE's first-year data contain a rather small number of HQ^k stars in the Galactic bulge, we also show where purely kinematically-selected HQ^k bulge star candidates (i.e., stars with $R_{\rm med} < 4$ kpc, $z_{\rm max} < 3$ kpc) fall in Figure 2.10. The bulge candidates (which could also be members of the inner disc) seem to display yet a different chemical-abundance pattern from the thick disc. From our small sample, we tentatively suggest that they are generally more α-enhanced than the local thick disc at a fixed metallicity, and that the so-called knee in the chemical-abundance plane, corresponding to the metallicity value of the ISM at the time of the bulk contribution of SNe type Ia, might be located at a higher metallicity. These preliminary results, while in agreement with earlier studies by, e.g., Zoccali et al. (2006), Fulbright et al. (2007) and Lecureur et al. (2007), are somewhat different from the more recent homogeneous abundance analyses of Meléndez et al. (2008), Alves-Brito et al. (2010)[20] and Gonzalez et al. (2011) who find a similar abundance pattern for bulge and thick disc giants for [Fe/H]< -0.2, and need to be confirmed or dismissed with future APOGEE data for more stars. Similar to our findings, the recent study of microlensed bulge dwarfs by Bensby et al. (2013b) suggests that the bulge stars are slightly more α-enhanced than the local thick disc. If true, these observations would imply either a) a different IMF for the bulge and the thick disc (e.g., Ballero et al. 2007), and/or b) a different origin for the bulge and the local thick disc, where the bulge formed in a shorter timescale than the thick disc.

[20] Indeed, Alves-Brito et al. (2010) re-analysed the same equivalent widths of Fulbright et al. (2007) and found Solar α-element abundances instead of elevated [α/Fe].

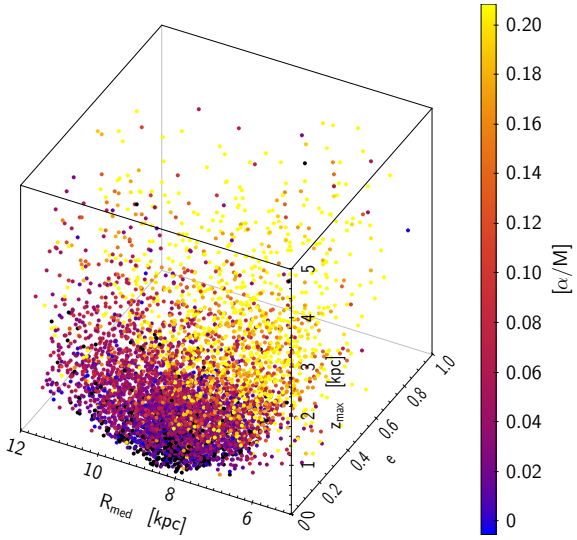

Figure 2.12. Distribution of the Gold sample in orbital-parameter space ($e, R_{\rm med}, z_{\rm max}$), colour-coded by α-element abundance. As expected, α-enhanced stars are on vertically hotter and more eccentric orbits. Also, as previously suggested by Bensby et al. (2011), the density of α-enhanced stars (the chemical thick disc) rapidly decreases with Galactocentric orbital radius. This latter result does not appear to depend critically on selection biases.

The chemical plane at three different radial bins

It was first shown by the high-resolution observations of Edvardsson et al. (1993) that disc stars at different Galactocentric guiding radii differ also in their chemical abundance patterns. With APOGEE, we are now able to systematically scan the Galaxy to large distances, eventually creating a chemo-dynamical map. In this section we present a few useful examples.

Figs. 2.12 and 2.13 show the distribution of our samples in orbital-parameter space ($e, R_{\rm med}, z_{\rm max}$). In particular, Fig. 2.12 nicely displays how stellar kinematics correlate with chemical properties. In the following, we will use projections of this cube to extract and highlight some of these relationships, focussing mainly on the $R_{\rm med} - z_{\rm max}$ and the $e - z_{\rm max}$ planes.

One major drawback of the current Gold sample constructed from Year-1 APOGEE data is its lack of stars in the inner parts of the Galaxy (Fig. 2.13).[21] We will therefore often use the HQ sample to accomplish a statistically robust sample, separating stars into wide $R_{\rm med}$ bins. At this point, the reader is reminded that the uncertainties in the orbital parameters can be quite sizeable (see Fig. 2.6), and that orbital parameters of the HQ sample should generally be used in wide bins, and only for statistical purposes.

To highlight APOGEE's potential in chemical mapping, we compare the APOGEE [α/Fe] vs. [Fe/H] abundance plane in different bins of $R_{\rm med}$ with the recent high-resolution study of disc field red giants by Bensby et al. (2011) reproduced here in the upper row of Fig. 2.14. Several characteristics can be noted immediately:

- By comparing the compilation of Bensby et al. (2011, first row in Fif. 2.14) with what is obtained with our first-year APOGEE data (second and third rows), we see a general

[21] This is expected to improve slightly when Year-2 data are added, and especially with the additional APOGEE dark-time observations of the inner Galaxy in spring 2014.

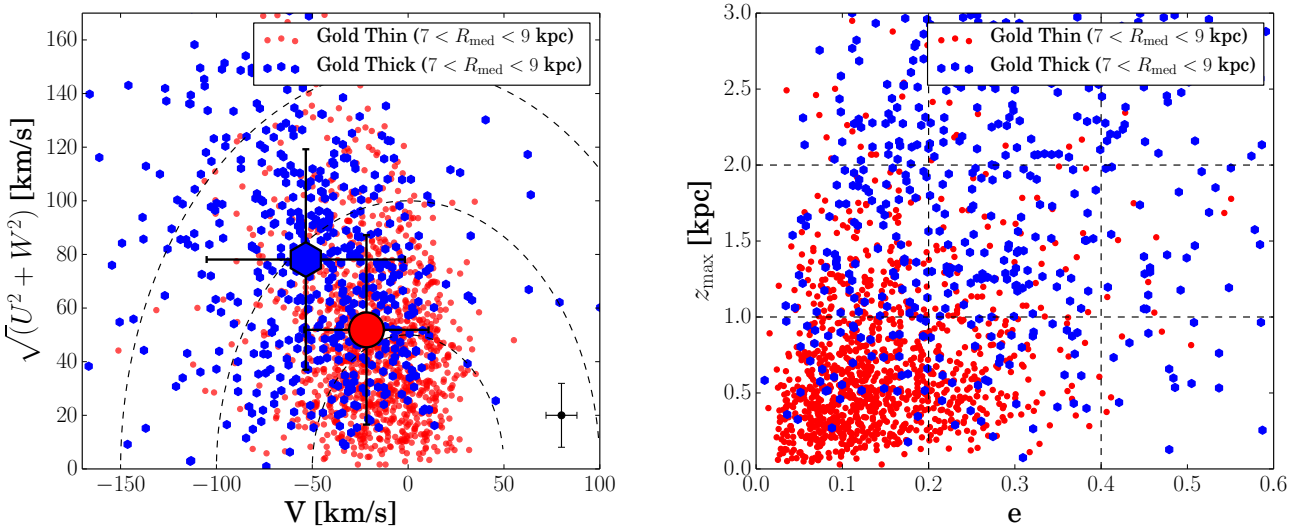

Figure 2.11. Kinematical properties of the local chemically defined thick and thin discs (cf. Fig. 2.10). Middle: The Toomre diagram ($\sqrt{U^2 + W^2}$ vs. V, see Feltzing et al. 2003) of Galactocentric velocities (with respect to the Local Standard of Rest). The dashed curves indicate constant space motion. We can confirm the rotational lag of the thick disc found by numerous other studies, but find the value of this lag to be very much dependent on the exact separation between thick and thin disc in the chemical plane ($\Delta V \approx 20 - 70$ km/s). Right: The $e - z_{max}$ plane used by Boeche et al. (2013a) to separate stellar populations into orbital families, indicated by the dashed lines. We will use this kinematical division in future analyses to compare with their findings.

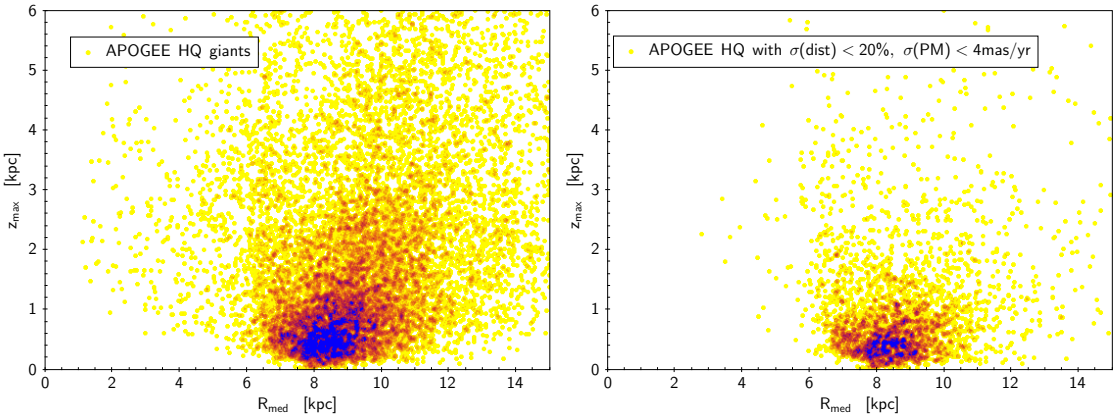

Figure 2.13. Density distribution of the HQ (left) and the Gold sample (right) in the $R_{med} - z_{max}$ plane (light colours denote low density). There is a striking deficiency of Gold-sample stars with inner-Galaxy kinematics ($R_{med} < 6$ kpc).

agreement of the abundance trends. However, the Bensby et al. data extend to larger [α/Fe] ratios than our APOGEE sample (by no more than ~ 0.1 dex in the inner and solar neighborhood subsamples). The main differences between the Bensby et al. sample and ours are caused by different abundance analysis techniques and the narrower $J - K_s$ colour range considered by Bensby et al. in order to estimate reliable photometric distances.

– In the plots shown in the second row, our sample was divided into wide bins in R_{med}, in order to minimize the contamination by stars moving on very eccentric orbits, whose most probable guiding radii lie outside the defined bins ("blurring"). This allows us to conclude that the local thin disc extends from quite low ([M/H] ~ -0.7) to super-solar metallicities ([M/H] $\sim +0.4$) which may be currently, but not definitively explained by radial migration. Also in the outer disc, we find a sizeable number of super-metal-rich (SMR) stars ([Fe/H] > 0.2) which probably originate from an inner Galactic region. Notice that these stars are not observed in the corresponding Bensby et al. sample shown in the first row, most probably because of low statistics. For comparison, the corresponding diagrams where the "blurring" contamination has not been taken into account are shown in the third row.

– The proportion of thin disc to thick disc increases with Galactocentric orbital radius. In the left panels (corresponding to the inner disc), the large fraction of high-α stars as well as the significant difference between the abundance distributions when using orbital parameters (R_{med}, z_{max}) instead of real-space coordinates (R, z) may in part be explained by a selection bias in the inner-disc sample, as we preferentially detect stars passing through the Solar neighbourhood on eccentric orbits – and these tend to be older, α-enriched stars from the inner disc. This bias should be small in the other two panels, suggesting that the scale length of the thick disc is shorter than that of the thin disc (Bensby et al. 2011; Bovy et al. 2012c; Cheng et al. 2012a).

– The metallicity distributions in the different radial bins are shown in the last row of Fig. 2.14. Again, a clear difference is seen between the distributions when defining the bins with respect to orbital median radius or real space coordinates. For instance, a clear contamination from stars with different guiding radii is seen on the left panel where the large contribution from high-metallicity stars disappears once $R_{\rm med}$ is used instead of R.
– As predicted by pure chemical-evolution models for the thin disc (e.g., Chiappini et al. 2001), the metallicity distribution is broader in the inner disc than towards the outer parts. This happens because of the shorter infall timescales assumed for the inner regions which produces a larger number of metal-poor stars (also known as the G-dwarf problem). In the outer parts, where the star formation is less strong (and the infall timescales are longer), the resulting metallicity distribution is narrower. The predicted change in the metallicity distributions peak are small in the galactocentric distance range considered here. The data shown in the last row of the figure, when using $R_{\rm med}$, does not show a strong peak variation and shows that the MDF is broader in the inner regions when compared to the outer ones. This is also in good agreement with the recent predictions of the chemodynamical model of Minchev et al. (2013, 2014) (but see below).
– Another crucial constraint on chemodynamical models is the percentage of SMR stars at the different radial bins. Unfortunately, the biases involved in our sample could be playing an important role when determining this observable (as they will certainly influence the final shape of the MDFs shown in this row). Although we must currently refrain from quantitative interpretations of the MDF before taking into account all the selection effects involved in our samples, we find that the fraction of SMR stars increases with decreasing Galactocentric distance. Indeed, it is not clear how ASPCAP contributes with further biases in the high-metallicity regime (e.g., some of the SMR stars could have been cut out by our colour, temperature and χ^2 selections; further ASPCAP difficulties at metallicities beyond $\sim +0.4$ are currently not fully understood). One could then imagine the number of SMR stars seen in the present figure to represent lower limits on the fraction of SMR stars in the respective Galactic regions.

Disc abundance gradients and variations of the MDF with height above the plane

Chemical gradients are among the main observables constraining chemical-evolution models, determining the relative enrichment history of different Galactocentric annuli, the amount of gas infall (Chiappini et al. 2001), radial mixing (Schönrich & Binney 2009), etc. To date, however, the main tracers used to determine the chemical gradients of the Galaxy are young objects, and often suffer from low number statistics (see, e.g., Stasińska et al. 2012). Red giant stars span a wide range of ages and are therefore a better tool to reconstruct star-formation histories (Miglio et al. 2013a).

The metallicity gradient and the MDF at different distances from the Galactic plane

In Fig. 2.15, we show results for the radial metallicity gradient and the MDF as a function of maximum height above the plane, for both the HQ and the Gold samples (for a complementary work, extending to more inner Galactocentric distances – but without kinematics – see Hayden et al. 2013).

In the recent paper by Boeche et al. (2013b), the authors compare the gradients obtained from a RAVE dwarf sample with those of the Geneva-Copenhagen survey (similar to our approach, the authors provide their results with respect to the orbital parameter space ($R_{\rm g}$, $z_{\rm max}$)[22], but only for three bins of $z_{\rm max}$). For comparison, their results are summarised in Table 2.3, along with our measured values. The agreement between the APOGEE and RAVE samples used here is remarkable. Despite the use of different tracer populations, different surveys with vastly different selections, different distance estimates and a different orbit integration codes assuming different MW potentials, the tendencies for the gradients found for dwarfs and giants agree.

As reported in previous works, our results show that the kinematically coolest stellar population ($z_{\rm max} < 0.4$ kpc) exhibits the steepest (negative) radial gradient ($\frac{d[{\rm Fe/H}]}{dR_{\rm g}} = -0.066 \pm 0.006$ dex/kpc); as we move to higher $z_{\rm max}$, the gradient flattens (Carrell et al. 2012; Cheng et al. 2012b; Boeche et al. 2013b). Furthermore, thanks to the fact that our sample extends well above the plane (compared with previous works), we can confirm that the gradient changes its sign ($\frac{d[{\rm Fe/H}]}{dR_{\rm g}} \simeq +0.05$ dex/kpc) for $1.5 < z_{\rm max} < 3$ kpc. The latter result as well as the overall trend of the metallicity gradient with height above the plane, is seen in both the Gold and the HQ^k sample, suggesting that the measured gradients do not critically depend on potential selection biases.[23] The measured gradients for the Gold and the HQ^k sample differ significantly only in one $z_{\rm max}$-bin. We suggest this to be caused the additional kinematical selection of the Gold sample, along with contamination of the high-$z_{\rm max}$ panels of Fig. 2.15 by thin-disc stars with poorly-determined orbital parameters (see discussion below).

While the general consistency of the radial abundance trends of RAVE and APOGEE may suggest that the measured value of the abundance gradients at low Galactic latitudes is a rather robust observable, the agreement of both surveys with GCS results is only of qualitative nature. The metallicity gradient values at different distances from the Galactic plane measured by Boeche et al. (2013b) for the GCS sample typically differ from the corresponding APOGEE and RAVE values by +0.03 dex/kpc (see Boeche et al. 2013b for a discussion).

From these considerations, we suggest that the inversion of the [M/H] gradient above $z \sim z_{\rm max} \approx 1.5$ kpc could be:

– A consequence of the smaller scale length of the thick disc with respect to the thin disc. In this case, the more metal poor stars of the thick disc would be concentrated towards smaller Galactocentric distances, creating the impression of a positive gradient (Boeche et al. 2013b), or
– Due to yet another selection effect related to the inhomogeneous coverage of the Galactic disc(s) by finite-sightline observations (Bovy et al. 2012c), which is present in all the currently available large-scale Galactic survey data (APOGEE, RAVE and SEGUE).[24] Initial simulations for a SEGUE sample with the stellar population synthesis model TRILEGAL have shown that selection effects may well produce a significant gradient that is not present in the underlying simulation (Brauer et al. 2014, in prep.).

[22] $R_{\rm g} \approx R_{\rm med}$ is the orbital guiding radius, a quantity directly related to the angular momentum of a star (Boeche et al. 2013a).

[23] Indeed, Boeche et al. (2013b) show that different cuts in R_g result in only small differences of their abundance gradients.

[24] Although RAVE as a hemisphere survey should be less affected by this type of bias.

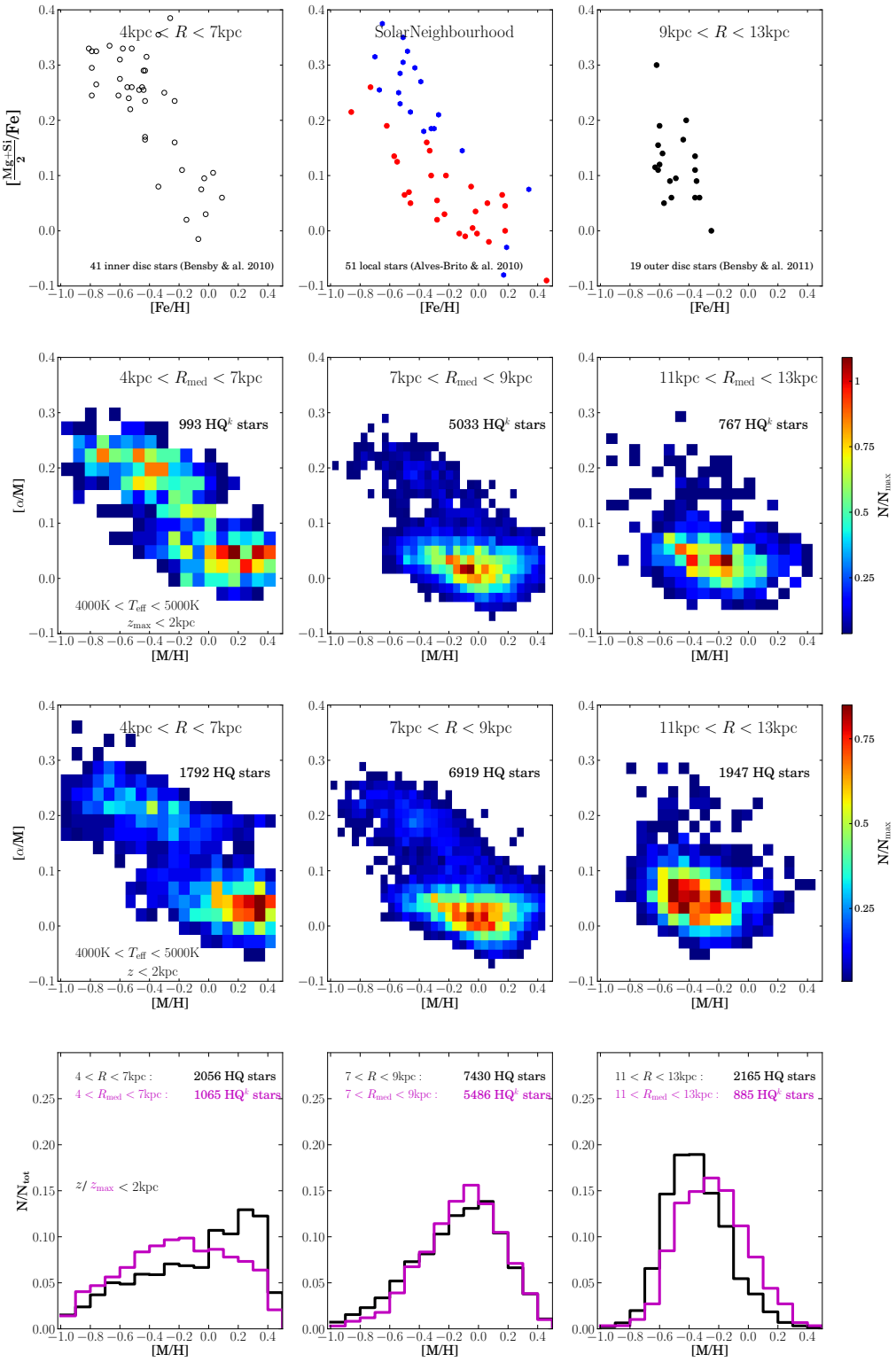

Figure 2.14. Chemical abundances of red giant stars in the Galactic disc in three bins of Galactocentric radius. Top row: [α/Fe] vs. [Fe/H] diagrams for the high-resolution samples of Bensby et al. (2010); Alves-Brito et al. (2010) and Bensby et al. (2011). The authors collected high-resolution spectra and performed a manual spectroscopic analysis for their sample. Second and third row: Density plot of the chemical abundance plane in the same radiall bins for the APOGEE HQ^k and HQ samples, with respect to the orbital parameters ($R_{\rm med}, z_{\rm max} < 2$ kpc) and the real-space coordinates ($R, z < 2$ kpc), respectively. As before, in this plot we restrict these samples to a smaller temperature range (4000 K $< T_{\rm eff} <$ 5000 K), for which ASPCAP currently gives the most reliable values for the [α/Fe] abundance ratio. We confirm the result of (Bensby et al. 2011) that the radial scale length of the thick disc is much shorter than that of the thin disc: In the $11 < R_{\rm med} < 13$ kpc bin, almost no stars with thick disc abundance pattern are present. Bottom row: MDFs for the three radial bins, again with respect to orbital (magenta) and real-space (black) coordinates (here we are using the full temperature range of the HQ sample defined in Table 2.1).

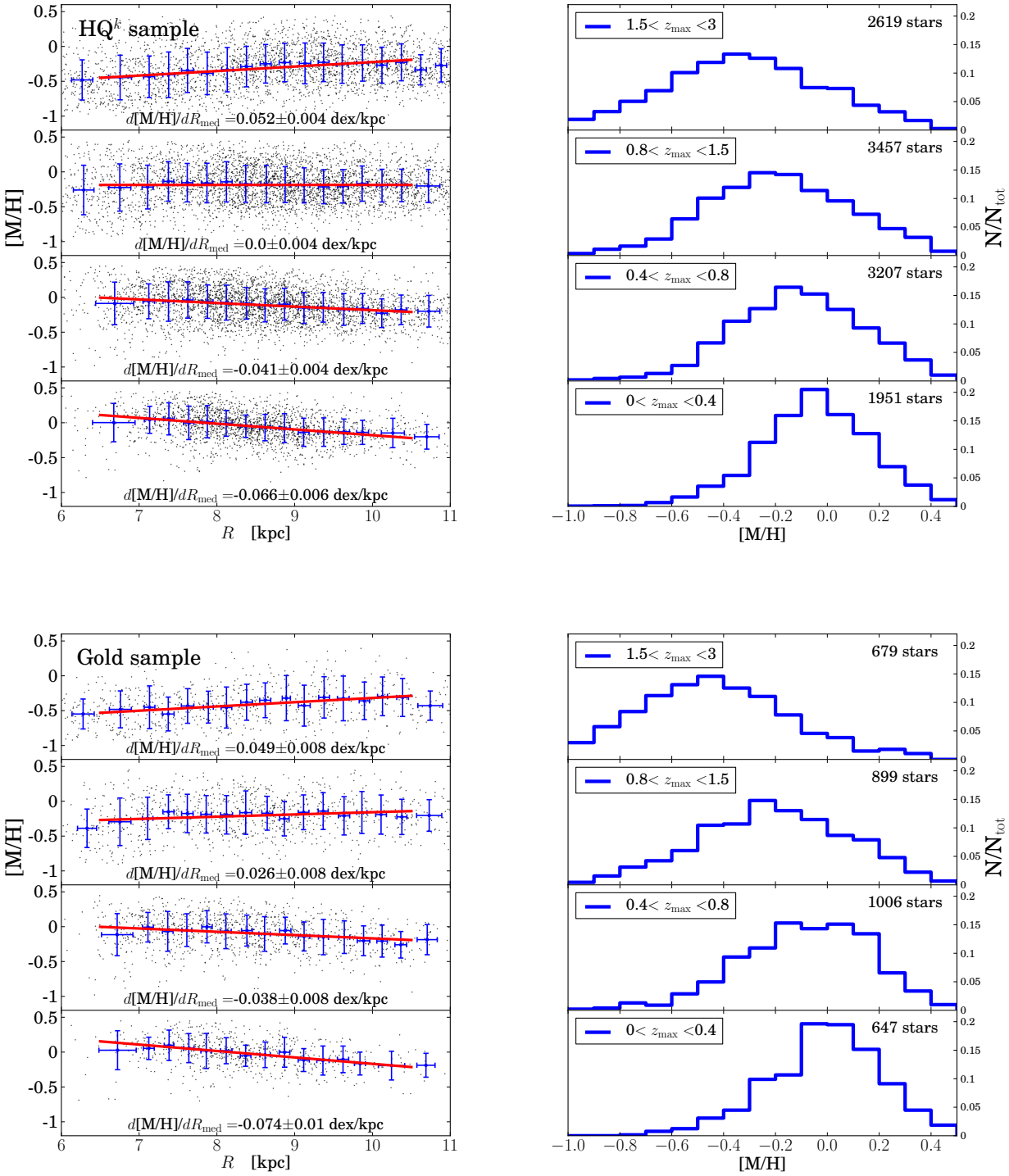

Figure 2.15. Top: Radial metallicity gradients (using the median orbital radii $R_{\rm med}$) and metallicity distribution functions as a function of $z_{\rm max}$ for the HQ sample. The gradients were computed using a simple least-squares optimisation, errors were estimated via bootstrapping. Note that we still do not account for any selection biases. Bottom: The same for the Gold sample.

The observed flattening of the gradient with height above the plane does not depend on the choice of $z_{\rm max}$ instead of the stars' current height z above the Galactic plane (for the corresponding figure, using the current R and z positions, see Fig. 2.17). On the other hand, the exact values of the gradients do very much depend on the set of (orbital-) space coordinates used. See Appendix A for a discussion.

Although we do not exclude the possibility that the gradient inversion may be a "real" characteristic of the Galactic disc at intermediate Galactocentric distances ($6 \lesssim R \lesssim 11$ kpc), which could in this case be related to the flaring of young stellar populations in the outer disc (as previously seen in dynamical

simulations, e.g., Minchev et al. 2012), we caution the reader about the physical reality of of this feature.

The [α/Fe] gradient and distribution function at different distances from the plane

Fig. 2.16 presents the gradients and distributions in the [α/M] abundance ratio for the APOGEE HQ^k and the Gold sample, in the same fashion as Fig. 2.15. The radial trend for small Galactic heights is slightly negative but almost flat, and that the negative trend increases with $z_{\rm max}$. Again, our measured gradients are fully consistent with the results of Boeche et al. (2013b) for the RAVE dwarf sample; the values agree within 1σ-uncertainties. The general trend of the steepening gradient is also found in the GCS data[25]. As before, the corresponding figure using the current z and R values is given by Fig. 2.17.

For the two highest bins in z or $z_{\rm max}$, there are quite sizeable differences in the MDFs as well as in the [α/M] distributions for the HQ$^{(k)}$ samples. While for the ($z_{\rm max}, R_{\rm med}$) plots shown in Fig. 2.16, the low-α population dominates up to large distances from the plane, this is not the case for the corresponding diagram in the (R, z) plane (see Fig. 2.17, bottom). Again, this is true both for the HQ^k and Gold samples. Given the considerable errors in the orbital parameter $z_{\rm max}$ for a sizeable fraction of our sample (especially for the HQ^k sample at high distances from the Galactic plane), we suggest that this result may be due to the contamination of the upper panels by thin disc stars with poorly-determined orbits. This effect also has an impact on the exact value of the gradient at these Galactic heights. By enlarging our sample, we expect to explore this issue in more detail.

In particular, the [α/M] distribution at high z (see upper panels in the lower right plot of Fig. 2.17) set rather tight limits on the effect of flaring of the thin disc, at least in our Galactocentric radial range. At high distances from the plane, we see essentially no low-[α/M] stars. Because this figure is not subject to large uncertainties in the orbital parameters, we are close to seeing the real proportion of high-to-low [α/Fe] stars here.

2.5. Conclusions

In this first paper of a series of APOGEE papers, we have begun to explore the chemo-kinematical properties of the Milky Way disc using data from the first year of SDSS-III/APOGEE. We have compared our findings with results from local optical high-resolution samples in the literature as well as lower resolution surveys such as GCS and RAVE. In this section, we briefly summarize the main results of our work.

First, APOGEE appears to deliver reliable chemical abundances for [M/H] and [α/M], and confirms many results previously obtained with smaller high-resolution spectroscopic samples. Together with the Gaia-ESO survey, APOGEE extends the Galactic volume covered by high-resolution spectroscopy from the inner disc and bulge to the outskirts of the disc.

We obtained the metallicity distribution function (MDF) of stars within 1 kpc from the Sun (d < 1 kpc). This MDF turned out to be remarkably similar to the one obtained with the high-resolution HARPS FGK dwarf sample of Adibekyan et al. (2011), despite the different volumes covered by the two samples. In both cases the MDF peaks at a metallicity slightly below the Solar value, and show comparable tails towards lower metallicities.

We can confirm the gap in the [α/Fe] vs. [Fe/H] diagram reported by previous works and argue that, similar to the volume-complete sample of Fuhrmann (2011), it is unlikely to be caused by a selection effect. Using our large sample of red giants stars, we corroborate the results obtained by Bensby et al. (2011); Bovy et al. (2012c) and Cheng et al. (2012b) who found evidence for a shorter scale-length of the thick disc.

Although we have only of a small number of bulge candidates in our sample, APOGEE data appear to indicate different chemical signatures for the bulge and the thick disc,

Motivated by similar results of Boeche et al. (2013b) using dwarf stars from RAVE and the Geneva-Copenhagen survey, we measure an inversion of the radial [M/H] gradient for stars at greater Galactic heights. We interpret this partly as a signature of inside-out formation of the Galactic disc, and partly as an effect of selection biases. An overall quantitative agreement with results from RAVE is still hampered by the radically different selection functions for RAVE and APOGEE.

Performing initial tests with the population synthesis code TRILEGAL, we confirm the need for a careful modelling of the survey selection function for future analyses.

The coming papers of this series will focus on a more detailed comparison with the chemo-dynamical Galaxy simulation of Minchev et al. (2013), and include simulations of the APOGEE HQ and Gold samples with TRILEGAL and the Besançon model (Robin et al. 2003). We also plan to employ a newly developed selection interface (Piffl et al. 2014, in prep.) to create mock surveys from a full chemo-dynamical MW model.

[25] However, the photometric [α/Fe] estimates for the Geneva-Copenhagen survey used by Boeche et al. (2013b) are from Casagrande et al. (2011), and should only be treated as proxies for [α/Fe].

Bibliography

Adibekyan, V. Z., Figueira, P., Santos, N. C., et al. 2013, A&A, 554, A44
Adibekyan, V. Z., Santos, N. C., Sousa, S. G., & Israelian, G. 2011, A&A, 535, L11
Ahn, C. P., Alexandroff, R., Allende Prieto, C., et al. 2013, subm. to ApJS, arXiv:1307.7735
Allende Prieto, C., Beers, T. C., Wilhelm, R., et al. 2006, ApJ, 636, 804
Allende Prieto, C., Majewski, S. R., Schiavon, R., et al. 2008, Astronomische Nachrichten, 329, 1018
Alves-Brito, A., Meléndez, J., Asplund, M., Ramírez, I., & Yong, D. 2010, A&A, 513, A35
Asplund, M., Grevesse, N., & Sauval, A. J. 2005, in Astronomical Society of the Pacific Conference Series, Vol. 336, Cosmic Abundances as Records of Stellar Evolution and Nucleosynthesis, ed. T. G. Barnes, III & F. N. Bash, 25
Baglin, A., Auvergne, M., Barge, P., et al. 2006, in ESA Special Publication, Vol. 1306, ESA Special Publication, ed. M. Fridlund, A. Baglin, J. Lochard, & L. Conroy, 33
Bailer-Jones, C. A. L. 2009, in IAU Symposium, Vol. 254, IAU Symposium, ed. J. Andersen, Nordströara, B. m, & J. Bland-Hawthorn, 475–482
Ballero, S. K., Kroupa, P., & Matteucci, F. 2007, A&A, 467, 117
Benjamin, R. A., Churchwell, E., Babler, B. L., et al. 2005, ApJ, 630, L149
Bensby, T., Alves-Brito, A., Oey, M. S., Yong, D., & Meléndez, J. 2010, A&A, 516, L13
Bensby, T., Alves-Brito, A., Oey, M. S., Yong, D., & Meléndez, J. 2011, ApJ, 735, L46
Bensby, T., Feltzing, S., & Lundström, I. 2003, A&A, 410, 527
Bensby, T., Feltzing, S., & Oey, M. S. 2013a, arXiv:1309.2631
Bensby, T., Yee, J. C., Feltzing, S., et al. 2013b, A&A, 549, A147
Boeche, C., Chiappini, C., Minchev, I., et al. 2013a, A&A, 553, A19
Boeche, C., Siebert, A., Piffl, T., et al. 2013b, A&A, accepted; arXiv:1309.4279
Bovy, J., Allende Prieto, C., Beers, T. C., et al. 2012a, ApJ, 759, 131
Bovy, J., Rix, H.-W., & Hogg, D. W. 2012b, ApJ, 751, 131
Bovy, J., Rix, H.-W., Liu, C., et al. 2012c, ApJ, 753, 148
Breddels, M. A., Smith, M. C., Helmi, A., et al. 2010, A&A, 511, A90
Bressan, A., Marigo, P., Girardi, L., et al. 2012, MNRAS, 427, 127
Burnett, B. & Binney, J. 2010, MNRAS, 407, 339

Table 2.3. Radial [Fe/H][a] gradients with respect to the orbital guiding radius[b] in the range $6 < R_g < 11$ kpc, for four ranges of $z_{\rm max}$.

$\frac{d[{\rm Fe/H}]}{dR_{\rm g}}$ [dex/kpc]	APOGEE HQ[k]	APOGEE Gold	GCS dwarfs [c]	RAVE dwarfs[a]
$0.0 \leq z_{\rm max}$ [kpc] <0.4	-0.066 ± 0.006	-0.074 ± 0.010	-0.043 ± 0.004	-0.065 ± 0.003
$0.4 \leq z_{\rm max}$ [kpc] <0.8	-0.041 ± 0.004	-0.038 ± 0.008	-0.008 ± 0.011	-0.059 ± 0.005
$0.8 \leq z_{\rm max}$ [kpc] <1.5	$+0.000 \pm 0.004$	$+0.026 \pm 0.008$	$+0.056 \pm 0.019$	$+0.006 \pm 0.015$
$1.5 \leq z_{\rm max}$ [kpc] <3.0	$+0.052 \pm 0.004$	$+0.049 \pm 0.008$	–	–

Notes. [(a)] For the APOGEE data: $[{\rm M/H}]_{\rm calib}$; [(b)] For the APOGEE w.r.t. the median orbital Galactocentric radius $R_{\rm med}$. The 1σ–uncertainties are computed using a bootstrap method. ; [(c)] Values from Boeche et al. (2013b).

Table 2.4. Radial [α/Fe][a] gradients with respect to the orbital guiding radius[b] in the range $6 < R_g < 11$ kpc, for four ranges of $z_{\rm max}$

$\frac{d[\alpha/{\rm Fe}]}{dR_{\rm g}}$ [dex/kpc]	APOGEE HQ[k]	APOGEE Gold	GCS dwarfs[c]	RAVE dwarfs[a]
$0.0 \leq z_{\rm max}$ [kpc] <0.4	-0.005 ± 0.001	-0.005 ± 0.002	$+0.010 \pm 0.002$	-0.004 ± 0.001
$0.4 \leq z_{\rm max}$ [kpc] <0.8	-0.009 ± 0.001	-0.007 ± 0.002	-0.006 ± 0.005	-0.005 ± 0.002
$0.8 \leq z_{\rm max}$ [kpc] <1.5	-0.019 ± 0.001	-0.022 ± 0.002	-0.023 ± 0.007	-0.020 ± 0.005
$1.5 \leq z_{\rm max}$ [kpc] <3.0	-0.031 ± 0.001	-0.023 ± 0.002	–	–

Notes. [(a)] For the APOGEE data: [α/M]; [(b)] For the APOGEE data: the median orbital Galactocentric radius $R_{\rm med}$. The 1σ–uncertainties are computed using a bootstrap method; [(c)] Values from Boeche et al. (2013b).

Burnett, B., Binney, J., Sharma, S., et al. 2011, A&A, 532, A113
Carrell, K., Chen, Y., & Zhao, G. 2012, AJ, 144, 185
Casagrande, L., Schönrich, R., Asplund, M., et al. 2011, A&A, 530, A138
Cassisi, S., Pietrinferni, A., Salaris, M., et al. 2006, Mem. Soc. Astron. Italiana, 77, 71
Cescutti, G., Matteucci, F., François, P., & Chiappini, C. 2007, A&A, 462, 943
Chabrier, G. 2001, ApJ, 554, 1274
Cheng, J. Y., Rockosi, C. M., Morrison, H. L., et al. 2012a, ApJ, 752, 51
Cheng, J. Y., Rockosi, C. M., Morrison, H. L., et al. 2012b, ApJ, 746, 149
Chiappini, C. 2009, in IAU Symposium, Vol. 254, IAU Symposium, ed. J. Andersen, Nordströara, B. m, & J. Bland-Hawthorn, 191–196
Chiappini, C., Matteucci, F., & Gratton, R. 1997, ApJ, 477, 765
Chiappini, C., Matteucci, F., & Romano, D. 2001, ApJ, 554, 1044
Cutri, R. M., Skrutskie, M. F., van Dyk, S., et al. 2003, 2MASS All Sky Catalog of point sources.
Duquennoy, A. & Mayor, M. 1991, A&A, 248, 485
Duquennoy, A., Mayor, M., & Halbwachs, J.-L. 1991, A&AS, 88, 281
Edvardsson, B., Andersen, J., Gustafsson, B., et al. 1993, A&A, 275, 101
Eggen, O. J., Lynden-Bell, D., & Sandage, A. R. 1962, ApJ, 136, 748
Eisenstein, D. J., Weinberg, D. H., Agol, E., et al. 2011, AJ, 142, 72
Feltzing, S., Bensby, T., & Lundström, I. 2003, A&A, 397, L1
Freeman, K. & Bland-Hawthorn, J. 2002, ARA&A, 40, 487
Frinchaboy, P. M., Thompson, B., Jackson, K. M., et al. 2013, ApJ, 777, L1
Fuhrmann, K. 1998, A&A, 338, 161
Fuhrmann, K. 2002, New A, 7, 161
Fuhrmann, K. 2004, Astronomische Nachrichten, 325, 3
Fuhrmann, K. 2008, MNRAS, 384, 173
Fuhrmann, K. 2011, MNRAS, 414, 2893
Fulbright, J. P., McWilliam, A., & Rich, R. M. 2007, ApJ, 661, 1152
Gilliland, R. L., Brown, T. M., Christensen-Dalsgaard, J., et al. 2010, PASP, 122, 131
Gilmore, G. 2012, in Astronomical Society of the Pacific Conference Series, Vol. 458, Galactic Archaeology: Near-Field Cosmology and the Formation of the Milky Way, ed. W. Aoki, M. Ishigaki, T. Suda, T. Tsujimoto, & N. Arimoto, 147
Gilmore, G., Randich, S., Asplund, M., et al. 2012, The Messenger, 147, 25
Girardi, L., Barbieri, M., Groenewegen, M. A. T., et al. 2012, TRILEGAL, a TRIdimensional modeL of thE GALaxy: Status and Future, ed. A. Miglio, J. Montalbán, & A. Noels, 165
Girardi, L., Groenewegen, M. A. T., Hatziminaoglou, E., & da Costa, L. 2005, A&A, 436, 895
Gonzalez, O. A., Rejkuba, M., Zoccali, M., et al. 2011, A&A, 530, A54
González Hernández, J. I. & Bonifacio, P. 2009, A&A, 497, 497
Gratton, R. G., Carretta, E., Desidera, S., et al. 2003, A&A, 406, 131
Grenon, M. 1972, in IAU Colloq. 17: Age des Etoiles, ed. G. Cayrel de Strobel & A. M. Delplace, 55
Gunn, J. E., Siegmund, W. A., Mannery, E. J., et al. 2006, AJ, 131, 2332
Hayden, M. R., Holtzman, J., Bovy, J., et al. 2013, subm. to ApJ
Haywood, M., Di Matteo, P., Lehnert, M., Katz, D., & Gomez, A. 2013, A&A, accepted; arXiv:1305.4663
Hernquist, L. 1990, ApJ, 356, 359
Høg, E., Fabricius, C., Makarov, V. V., et al. 2000, A&A, 355, L27
Hogg, D. W., Blanton, M. R., Roweis, S. T., & Johnston, K. V. 2005, ApJ, 629, 268
Holmberg, J., Nordström, B., & Andersen, J. 2007, A&A, 475, 519
Johnson, J. A. 2002, ApJS, 139, 219
Katz, D., Munari, U., Cropper, M., et al. 2004, MNRAS, 354, 1223
Kordopatis, G., Recio-Blanco, A., de Laverny, P., et al. 2011, A&A, 535, A107
Kotoneva, E., Flynn, C., Chiappini, C., & Matteucci, F. 2002, MNRAS, 336, 879
Landais, G. & Ochsenbein, F. 2012, in Astronomical Society of the Pacific Conference Series, Vol. 461, Astronomical Data Analysis Software and Systems XXI, ed. P. Ballester, D. Egret, & N. P. F. Lorente, 383
Lecureur, A., Hill, V., Zoccali, M., et al. 2007, A&A, 465, 799
Lee, Y. S., Beers, T. C., An, D., et al. 2011, ApJ, 738, 187
Maciel, W. J. & Chiappini, C. 1994, Ap&SS, 219, 231
Maciel, W. J. & Köppen, J. 1994, A&A, 282, 436
Majewski, S. R., Hasselquist, S., Łokas, E. L., et al. 2013, ApJ, 777, L13
Majewski, S. R., Zasowski, G., & Nidever, D. L. 2011, ApJ, 739, 25
Malmquist, K. G. 1936, Stockholms Observatoriums Annaler, 12, 7
Matteucci, F., ed. 2001, Astrophysics and Space Science Library, Vol. 253, The chemical evolution of the Galaxy
Matteucci, F. 2012, Chemical Evolution of Galaxies
Matteucci, F. & Brocato, E. 1990, ApJ, 365, 539
Matteucci, F., Grieco, V., & Vincoletto, L. 2012, Memorie della Societa Astronomica Italiana Supplementi, 21, 86
Meléndez, J., Asplund, M., Alves-Brito, A., et al. 2008, A&A, 484, L21
Mészáros, S., Allende Prieto, C., Edvardsson, B., et al. 2012, AJ, 144, 120
Mészáros, S., Holtzman, J., García Pérez, A. E., et al. 2013, AJ, 146, 133
Miglio, A., Chiappini, C., Morel, T., et al. 2013b, in European Physical Journal Web of Conferences, Vol. 43, European Physical Journal Web of Conferences, 3004
Miglio, A., Chiappini, C., Morel, T., et al. 2013a, MNRAS, 429, 423
Mihalas, D. & Binney, J. 1981, Galactic astronomy: Structure and kinematics /2nd edition/
Minchev, I., Boily, C., Siebert, A., & Bienayme, O. 2010, MNRAS, 407, 2122
Minchev, I., Chiappini, C., & Martig, M. 2013, A&A, 558, A9
Minchev, I., Chiappini, C., & Martig, M. 2014, arXiv:1401.5796
Minchev, I., Famaey, B., Quillen, A. C., et al. 2012, A&A, 548, A127
Minchev, I. & Quillen, A. C. 2006, MNRAS, 368, 623
Miyamoto, M. & Nagai, R. 1975, PASJ, 27, 533
Navarro, J. F., Frenk, C. S., & White, S. D. M. 1997, ApJ, 490, 493
Ness, M., Freeman, K., Athanassoula, E., et al. 2012, ApJ, 756, 22

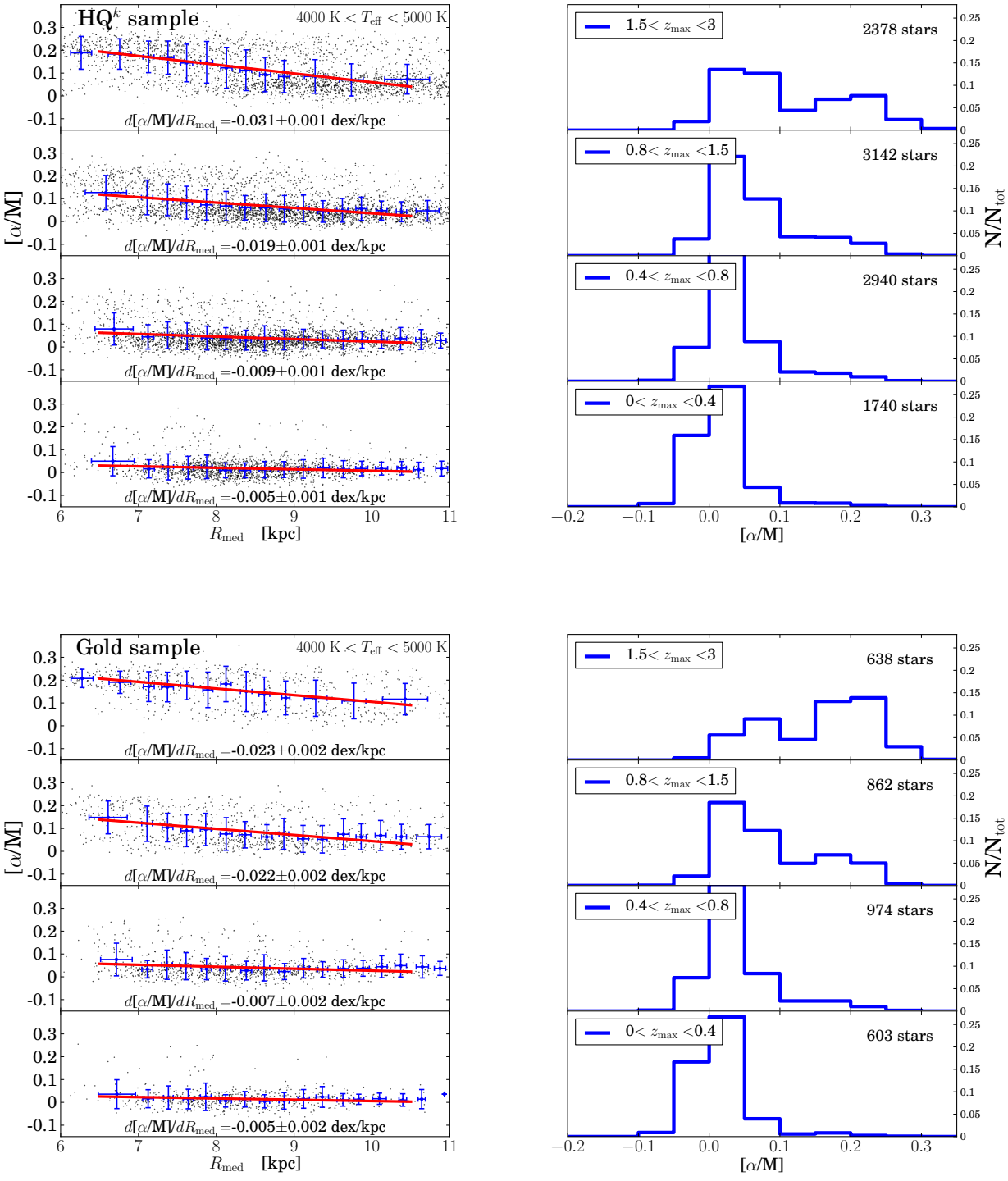

Figure 2.16. Same as Figure 2.15, but for [α/M].

Newberg, H. J., Carlin, J. L., Chen, L., et al. 2012, in Astronomical Society of the Pacific Conference Series, Vol. 458, Galactic Archaeology: Near-Field Cosmology and the Formation of the Milky Way, ed. W. Aoki, M. Ishigaki, T. Suda, T. Tsujimoto, & N. Arimoto, 405

Nidever, D. L., Zasowski, G., & Majewski, S. R. 2012a, ApJS, 201, 35

Nidever, D. L., Zasowski, G., Majewski, S. R., et al. 2012b, ApJ, 755, L25

Nordström, B., Mayor, M., Andersen, J., et al. 2004, A&A, 418, 989

Ochsenbein, F. 1998, in Astronomical Society of the Pacific Conference Series, Vol. 145, Astronomical Data Analysis Software and Systems VII, ed. R. Albrecht, R. N. Hook, & H. A. Bushouse, 387

Pagel, B. E. J. 2009, Nucleosynthesis and Chemical Evolution of Galaxies

Perryman, M. A. C., de Boer, K. S., Gilmore, G., et al. 2001, A&A, 369, 339

Perryman, M. A. C., Lindegren, L., Kovalevsky, J., et al. 1997, A&A, 323, L49

Press, W. H., Teukolsky, S. A., Vetterling, W. T., & Flannery, B. P. 1992, Numerical recipes in FORTRAN. The art of scientific computing

Quinn, P. J., Hernquist, L., & Fullagar, D. P. 1993, ApJ, 403, 74

Ramírez, I., Allende Prieto, C., & Lambert, D. L. 2013, ApJ, 764, 78

Rix, H.-W. & Bovy, J. 2013, A&A Rev., 21, 61

Robin, A. C., Reylé, C., Derrière, S., & Picaud, S. 2003, A&A, 409, 523

Rocha-Pinto, H. J. & Maciel, W. J. 1996, MNRAS, 279, 447

Rocha-Pinto, H. J., Majewski, S. R., Skrutskie, M. F., & Crane, J. D. 2003, ApJ, 594, L115

Roeser, S., Demleitner, M., & Schilbach, E. 2010, AJ, 139, 2440
Roškar, R., Debattista, V. P., Quinn, T. R., Stinson, G. S., & Wadsley, J. 2008, ApJ, 684, L79
Santiago, B. X., Brauer, D. E., Anders, F., et al. 2014, subm. to ApJ
Scheffler, H. & Elsässer, H. 1982, Bau und Physik der Galaxis
Schlesinger, K. J., Johnson, J. A., Lee, Y. S., et al. 2010, ApJ, 719, 996
Schlesinger, K. J., Johnson, J. A., Rockosi, C. M., et al. 2012, ApJ, 761, 160
Schönrich, R. & Binney, J. 2009, MNRAS, 396, 203
Sellwood, J. A. & Binney, J. J. 2002, MNRAS, 336, 785
Sousa, S. G., Santos, N. C., Israelian, G., Mayor, M., & Monteiro, M. J. P. F. G. 2007, A&A, 469, 783
Spitzer, Jr., L. & Schwarzschild, M. 1951, ApJ, 114, 385
Stasińska, G. 2010, in IAU Symposium, Vol. 262, IAU Symposium, ed. G. R. Bruzual & S. Charlot, 93–96
Stasińska, G., Prantzos, N., Meynet, G., et al., eds. 2012, EAS Publications Series, Vol. 54, Oxygen in the Universe
Steinmetz, M., Zwitter, T., Siebert, A., et al. 2006, AJ, 132, 1645
Taylor, M. B. 2005, in Astronomical Society of the Pacific Conference Series, Vol. 347, Astronomical Data Analysis Software and Systems XIV, ed. P. Shopbell, M. Britton, & R. Ebert, 29
Turon, C., O'Flaherty, K. S., & Perryman, M. A. C., eds. 2005, ESA Special Publication, Vol. 576, The Three-Dimensional Universe with Gaia
van Leeuwen, F., ed. 2007, Astrophysics and Space Science Library, Vol. 350, Hipparcos, the New Reduction of the Raw Data
Villalobos, Á. & Helmi, A. 2008, MNRAS, 391, 1806
Wright, E. L., Eisenhardt, P. R. M., Mainzer, A. K., et al. 2010, AJ, 140, 1868
Yanny, B., Rockosi, C., Newberg, H. J., et al. 2009, AJ, 137, 4377
Zacharias, N., Finch, C. T., Girard, T. M., et al. 2012, VizieR Online Data Catalog, 1322, 0
Zacharias, N., Finch, C. T., Girard, T. M., et al. 2013, AJ, 145, 44
Zasowski, G., Johnson, J. A., Frinchaboy, P. M., et al. 2013, AJ, 146, 81
Zhao, G., Chen, Y.-Q., Shi, J.-R., et al. 2006, Chinese J. Astron. Astrophys., 6, 265
Zoccali, M., Lecureur, A., Barbuy, B., et al. 2006, A&A, 457, L1
Zucker, D. B., de Silva, G., Freeman, K., Bland-Hawthorn, J., & Hermes Team. 2012, in Astronomical Society of the Pacific Conference Series, Vol. 458, Galactic Archaeology: Near-Field Cosmology and the Formation of the Milky Way, ed. W. Aoki, M. Ishigaki, T. Suda, T. Tsujimoto, & N. Arimoto, 421
Zwitter, T., Matijevič, G., Breddels, M. A., et al. 2010, A&A, 522, A54

[1] Leibniz-Institut für Astrophysik Potsdam (AIP), An der Sternwarte 16, 14482 Potsdam, Germany
e-mail: fanders@aip.de, cristina.chiappini@aip.de
[2] Technische Universität Dresden, Institut für Kern- und Teilchenphysik, Zellescher Weg 16, 01069 Dresden, Germany
[3] Laboratório Interinstitucional de e-Astronomia, - LIneA, Rua Gal. José Cristino 77, Rio de Janeiro, RJ - 20921-400, Brazil
[4] Instituto de Física, Universidade Federal do Rio Grande do Sul, Caixa Postal 15051, Porto Alegre, RS - 91501-970, Brazil
[5] Universidade Federal do Rio de Janeiro, Observatório do Valongo, Ladeira do Pedro Antônio 43, 20080-090 Rio de Janeiro, Brazil
[6] Osservatorio Astronomico di Padova – INAF, Vicolo dell'Osservatorio 5, I-35122 Padova, Italy
[7] Observatório Nacional, Rua Gal. José Cristino 77, Rio de Janeiro, RJ - 209 21-400, Brazil
[8] Observatoire de la Cote d'Azur, Laboratoire Lagrange, CNRS UMR 7923, B.P. 4229, 06304 Nice Cedex, France
[9] Astronomisches Rechen-Institut, Zentrum für Astronomie der Universität Heidelberg, Mönchhofstr. 12-14, 69120 Heidelberg, Germany
[10] School of Physics and Astronomy, University of Birmingham, Edgbaston, Birmingham, B15 2TT, United Kingdom
[11] Institut d'Astrophysique et de Géophysique, Allée du 6 août, 17 - Bât. B5c, B-4000 Liège 1 (Sart-Tilman), Belgium
[12] Department of Astronomy and Astrophysics, The Pennsylvania State University, University Park, PA 16802, USA
[13] Institute for Gravitation and the Cosmos, The Pennsylvania State University,
[14] National Optical Astronomy Observatory, 915 N. Cherry Ave., Tucson, AZ 85719, USA
[15] JINA: Joint Institute for Nuclear Astrophysics
[16] Steward Observatory, University of Arizona, Tucson, AZ, 85721, USA
[17] Instituto de Astrofisica de Canarias, C/ Vía Láctea, s/n, 38205, La Laguna, Tenerife, Spain
[18] Apache Point Observatory and New Mexico State University, P.O. Box 59, Sunspot, NM, 88349-0059, USA
[19] Department of Physics & Astronomy, Texas Christian University (TCU), P.O. Box 298840, Fort Worth, TX 76129, USA
[20] Department of Astronomy, University of Virginia, P.O. Box 400325, Charlottesville, VA 22904-4325, USA
[21] New Mexico State University, Box 30001 / Department 4500, 1320 Frenger St., Las Cruces, NM 88003, USA
[22] The Ohio State University, Department of Astronomy, 4055 McPherson Laboratory, 140 West 18th Ave., Columbus, OH 43210-1173, USA
[23] Department of Astronomy, University of Michigan, 1022 Dennison, 500 Church St., Ann Arbor, MI 48109, USA
[24] Institut Utinam, CNRS UMR6213, Université de Franche-Comté, OSU THETA de Franche-Comté-Bourgognen, Besançon, France
[25] Astrophysics Research Institute, IC2, Liverpool Science Park, Liverpool John Moores University, 146 Brownlow Hill, Liverpool, L3 5RF, United Kingdom University Park, PA 16802
[26] McDonald Observatory, The University of Texas at Austin, Austin, TX 78712, USA
[27] Vanderbilt University, Dept. of Physics & Astronomy, VU Station B 1807, Nashville, TN 37235, USA
[28] Johns Hopkins University, Department of Physics and Astronomy, 3701 San Martin Drive, Baltimore, MD 21210, USA

Acknowledgements. It is a pleasure to thank R.-D. Scholz for helpful discussions on astrometry, and J. Bovy & K. Schlesinger for their valuable input on the discussion. Furthermore, we thank J. Bovy for making his code publically available.

TCB acknowledges partial support from grant PHY 08-22648; Physics Frontier Center/ JINA, awarded by the U.S. National Science Foundation. KC acknowledges support from the National Science Foundation (AST-0907873). PMF is supported by an NSF grant AST-1311835.

Funding for the Brazilian Participation Group has been provided by the Ministério de Ciência e Tecnologia (MCT), Fundação Carlos Chagas Filho de Amparo à Pesquisa do Estado do Rio de Janeiro (FAPERJ), Conselho Nacional de Desenvolvimento Científico e Tecnológico (CNPq), and Financiadora de Estudos e Projetos (FINEP).

Funding for SDSS-III has been provided by the Alfred P. Sloan Foundation, the Participating Institutions, the National Science Foundation, and the U.S. Department of Energy Office of Science. The SDSS-III web site is http://www.sdss3.org/.

SDSS-III is managed by the Astrophysical Research Consortium for the Participating Institutions of the SDSS-III Collaboration including the University of Arizona, the Brazilian Participation Group, Brookhaven National Laboratory, Carnegie Mellon University, University of Florida, the French Participation Group, the German Participation Group, Harvard University, the Instituto de Astrofisica de Canarias, the Michigan State/Notre Dame/JINA Participation Group, Johns Hopkins University, Lawrence Berkeley National Laboratory, Max Planck Institute for Astrophysics, Max Planck Institute for Extraterrestrial Physics, New Mexico State University, New York University, Ohio State University, Pennsylvania State University, University of Portsmouth, Princeton University, the Spanish Participation Group, University of Tokyo, University of Utah, Vanderbilt University, University of Virginia, University of Washington, and Yale University.

2.A. Gradients with respect to (R, z)

In order to estimate the effect of blurring and the influence of orbital parameter uncertainties on our measured abundance gradients, we also computed the [M/H] and [α/M] abundance gradients with respect to the current Galactocentric distance R, for different bins in current distance from the Galactic plane z. The results are shown in Fig. 2.17.

Since $\frac{d[\mathrm{Fe/H}]}{dR}$ provides a more direct observable than $\frac{d[\mathrm{M/H}]}{dR_g}$, which depends also weakly on the adopted Galactic potential

and are influenced by subtle volume-based kinematic biases (see Boeche et al. 2013b for a discussion), it is useful to compare the two different gradient measurements.

It is also worth noting that our results on the abundance gradients compare very well with the findings of Hayden et al. (2013), who use a different set of spectrophotometric distances (Hayden et al., in prep.) for their APOGEE sample. The gradient measured by Hayden et al., using our adopted vertical and radial ranges, is compatible with the values we obtain in figure 2.17. For stars with $6 < R < 11$ and $0 < z < 0.4$ kpc, the authors also obtain a gradient of $\frac{d[\mathrm{M/H}]}{dR} \simeq -0.08$ dex/kpc. As the authors limit their analysis to smaller distances from the plane, they do not find a positive radial [M/H] gradient at large heights.

As discussed in Sect. 5.4, future work using more APOGEE data will certainly help to understand and resolve the discrepancies seen between Figs. 2.15, 2.16 and 2.17.

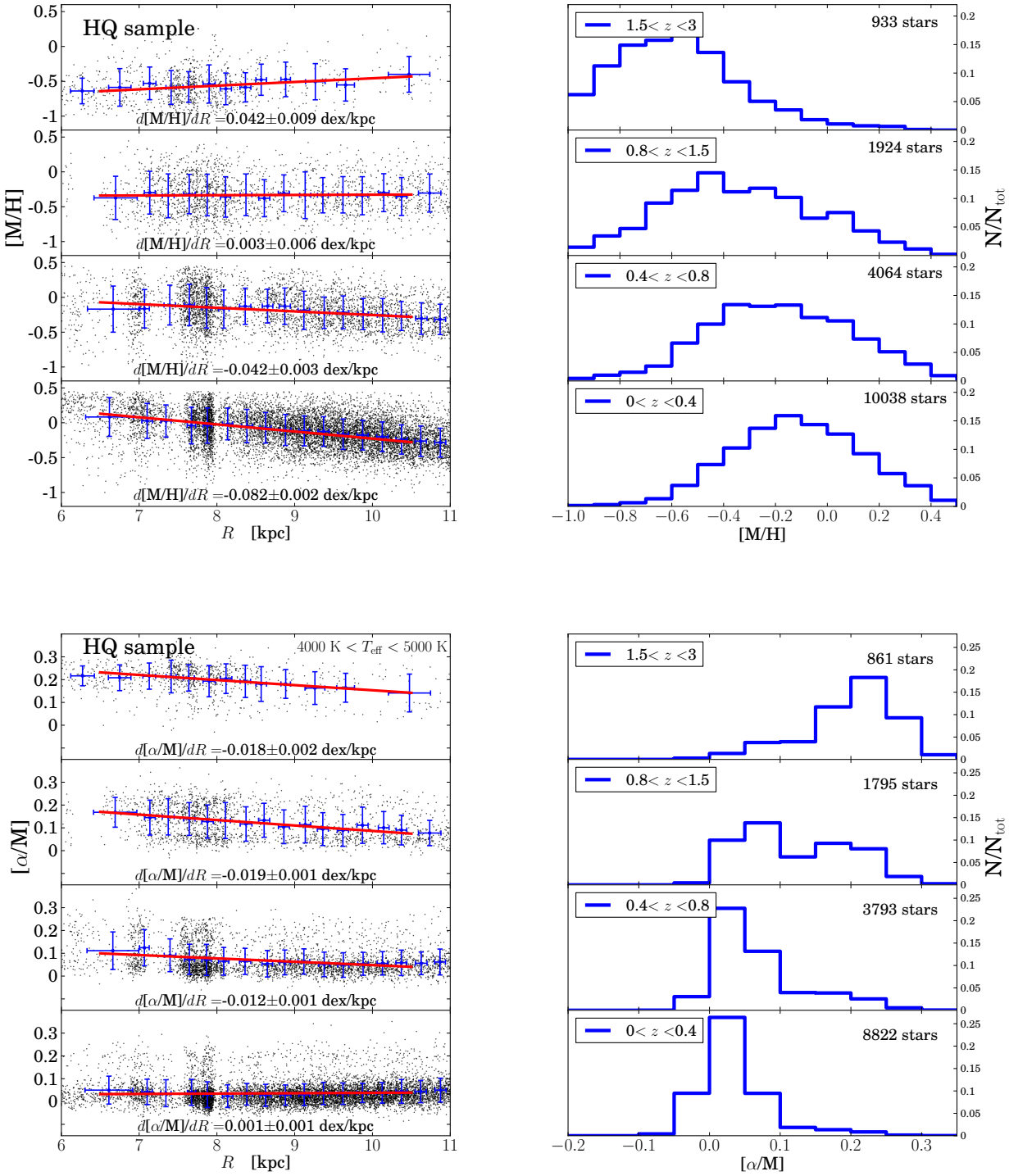

Figure 2.17. Top: Radial metallicity gradients (using now the *current* Galactocentric distance R) and metallicity distribution functions as a function of *current* Galactic height z for the Gold sample. Bottom: The same for the HQ sample. Bottom: Same as above, for the [α/M] distribution functions.

26

Chapter 3

Galactic archaeology with asteroseismology and spectroscopy: Red giants observed by CoRoT and APOGEE

F. Anders[1,2], C. Chiappini[1,2], T. S. Rodrigues[2,3,4], A. Miglio[5], J. Montalbán[4], B. Mosser[6], L. Girardi[2,3], M. Valentini[1], A. Noels[7], T. Morel[7], J. A. Johnson[8], M. Schultheis[9], F. Baudin[10], R. de Assis Peralta[6], S. Hekker[11,12], N. Themeßl[11,12], T. Kallinger[13], R. A. García[14], S. Mathur[15], A. Baglin[6], B. X. Santiago[2,16], M. Martig[17], I. Minchev[1], M. Steinmetz[1], L. N. da Costa[2,18], M. A. G. Maia[2,18], C. Allende Prieto[19,20], K. Cunha[18], T. C. Beers[21], C. Epstein[8], A. E. García Pérez[19,20], D. A. García-Hernández[19,20], P. Harding[22], J. Holtzman[23], S. R. Majewski[24], Sz. Mészáros[25,26], D. Nidever[27], K. Pan[23,28], M. Pinsonneault[8], R. P. Schiavon[29], D. P. Schneider[30,31], M. D. Shetrone[32], K. Stassun[33], O. Zamora[19,20], G. Zasowski[34]

(Affiliations can be found after the references)

Abstract

With the advent of the space missions CoRoT and *Kepler*, it has recently become feasible to determine precise asteroseismic masses and relative ages for large samples of red giant stars.

We present the CoRoGEE dataset, obtained from CoRoT light curves for 606 red giants in two fields of the Galactic disc that have been co-observed by the Apache Point Observatory Galactic Evolution Experiment (APOGEE). We used the Bayesian parameter estimation code PARAM to calculate distances, extinctions, masses, and ages for these stars in a homogeneous analysis, resulting in relative statistical uncertainties of $\lesssim 2\%$ in distance, $\sim 4\%$ in radius, $\sim 9\%$ in mass and $\sim 25\%$ in age. We also assessed systematic age uncertainties stemming from different input physics and mass loss.

We discuss the correlation between ages and chemical abundance patterns of field stars over a broad radial range of the Milky Way disc (5 kpc $< R_{\rm Gal} <$ 14 kpc), focussing on the [α/Fe]-[Fe/H]-age plane in five radial bins of the Galactic disc. We find an overall agreement with the expectations of pure chemical-evolution models computed before the present data were available, especially for the outer regions. However, our data also indicate that a significant fraction of stars now observed near and beyond the solar neighbourhood migrated from inner regions.

Mock CoRoGEE observations of a chemodynamical Milky Way disc model indicate that the number of high-metallicity stars in the outer disc is too high to be accounted for even by the strong radial mixing present in the model. The mock observations also show that the age distribution of the [α/Fe]-enhanced sequence in the CoRoGEE inner-disc field is much broader than expected from a combination of radial mixing and observational errors. We suggest that a thick-disc/bulge component that formed stars for more than 3 Gyr may account for these discrepancies.

Our results are subject to future improvements due to a) the still low statistics, because our sample had to be sliced into bins of Galactocentric distances and ages, b) large uncertainties in proper motions (and therefore guiding radii), and c) corrections to the asteroseismic mass-scaling relation. The situation will improve not only upon the upcoming *Gaia* data releases, but also with the foreseen increase in the number of stars with both seismic and spectroscopic information.

3.1. Introduction

To reconstruct the formation history of the Milky Way, one would ideally like to obtain precise and unbiased ages for thousands or millions of stars in all parts of our Galaxy. To date, this goal is still far beyond reach, at least until astrometric parallaxes from the *Gaia* satellite (Perryman et al. 2001) and asteroseismic data from K2 (Howell et al. 2014) and PLATO 2.0 (Rauer et al. 2014) will become available.

A common work-around for this problem is to use relative "chemical clocks" provided by element abundance ratios (Pagel 1997; Matteucci 2001): each star carries in its atmosphere the enrichment history of the gas from which it was formed, only minimally polluted by its own stellar evolution, and accessible through spectroscopy. By combining this wealth of information with kinematic properties of stellar populations in different Galactic environments, we can systematically unravel the importance of the various physical processes that led to the formation of the Milky Way as we see it today ("Galactic archaeology"; Freeman & Bland-Hawthorn 2002; Turon et al. 2008).

Still, age determinations provide crucial constraints on several astrophysical processes: For example, the ages of old halo stars can be used as a lower limit for the age of the Universe (Hill et al. 2002). The Galactic age-metallicity relation (e.g. Twarog 1980; Edvardsson et al. 1993; Ng & Bertelli 1998), the star-formation history (Gilmore 1999) or the evolution of abundance gradients (e.g. Carraro et al. 1998; Chen et al. 2003) are essential tools for understanding the evolution of our Milky Way.

During the past ten years, ever more sophisticated chemodynamical models of Milky-Way-mass galaxies have been developed in a cosmological context (e.g. Abadi et al. 2003;

This Chapter is published in *Astronomy & Astrophysics*, Vol. 597, 2017, p. A30+. The data described in Table 1.B are available in electronic form at the CDS via anonymous ftp to cdsarc.u-strasbg.fr (130.79.128.5) or via `http://cdsweb.u-strasbg.fr/cgi-bin/qcat?J/A+A/`.

Stinson et al. 2010; Guedes et al. 2011; Brook et al. 2012; Scannapieco et al. 2015; Roca-Fàbrega et al. 2016). However, detailed models that match many of the Milky Way's chemo-dynamical correlations (Minchev et al. 2013, 2014b) are still rare (see discussions in Scannapieco et al. 2012 and Minchev et al. 2013). These can be compared to observations, but it is often difficult to find observables that are powerful enough to discard certain scenarios of the Galaxy's evolution. With the availability of age estimates for large stellar samples – even if they are only valid in a relative sense – this situation changes drastically.

It is therefore important to revisit the full age–chemistry–kinematics space with samples that cover larger portions of the Galactic disc. In this high-dimensional space, we can then look for robust statistical relations that realistic models have to fulfil. With the joint venture of asteroseismology and spectroscopic surveys, we are now in a position to constrain key parameters of stellar and Galactic evolution.

Unlike stellar radii and masses, the ages of stars cannot be directly measured, only inferred through modelling. Among the various available stellar age indicators (e.g. Li abundance, U/Th ratio, stellar activity, rotation, X-ray luminosity, and position in the Hertzsprung-Russell diagram), one of the most promising methods that can deliver reliable age estimates for a wide range of ages is the comparison of measured atmospheric and asteroseismic parameters of evolved stars with models of stellar evolution (e.g. Miglio 2012).

It is well-known (e.g. Ulrich 1986; Christensen-Dalsgaard 1988) that detailed asteroseismic analyses involving individual oscillation frequencies may deliver precise age determinations. Depending on the spectral type of the star, a number of seismic characteristics can be used to investigate the stellar interior and infer an age estimate. However, this so-called "boutique" or "à la carte modelling" (Soderblom 2013; Lebreton et al. 2014) requires extremely accurate measurements of several pulsation modes. To date, this is only possible for the Sun (e.g. Gough 2001) and a relatively small number of bright dwarf stars observed by CoRoT and *Kepler* (e.g. Metcalfe et al. 2010; Batalha et al. 2011; Mathur et al. 2012; Silva Aguirre et al. 2013; Chaplin & Miglio 2013; Lebreton et al. 2014; Metcalfe et al. 2014).

For large samples of red giant stars (first-ascent red giants as well as red-clump stars), statistical studies follow a different approach called "ensemble asteroseismology" (e.g. Chaplin et al. 2011). This method typically focusses on two main seismic characteristics of the frequency spectrum of solar-like oscillating giants: the large frequency separation $\Delta\nu$, related to the stellar mean density (Tassoul 1980; Ulrich 1986; Christensen-Dalsgaard 1993), and the frequency of maximum oscillation power $\nu_{\rm max}$, related to the acoustic cut-off frequency (Brown et al. 1991; Kjeldsen & Bedding 1995; Belkacem et al. 2011). The mass and radius of a star have been shown to scale with these quantities via:

$$\begin{aligned} \frac{M}{M_\odot} &\simeq \Big(\frac{\nu_{\rm max}}{\nu_{\rm max,\odot}}\Big)^3 \Big(\frac{\Delta\nu}{\Delta\nu_\odot}\Big)^{-4} \Big(\frac{T_{\rm eff}}{T_{\rm eff,\odot}}\Big)^{3/2}, \\ \frac{R}{R_\odot} &\simeq \Big(\frac{\nu_{\rm max}}{\nu_{\rm max,\odot}}\Big) \Big(\frac{\Delta\nu}{\Delta\nu_\odot}\Big)^{-2} \Big(\frac{T_{\rm eff}}{T_{\rm eff,\odot}}\Big)^{1/2}, \end{aligned} \tag{3.1}$$

where $T_{\rm eff}$ is the star's effective temperature, and the solar values $\Delta\nu_\odot = 135.03\,\mu$Hz, $\nu_{\rm max,\odot} = 3140.0\,\mu$Hz, and $T_{\rm eff,\odot} = 5780$ K (Pinsonneault et al. 2014) are used in the following.

The scaling relations (3.1) have been tested with independent methods in the past years (eclipsing binaries, open clusters, interferometry, *Hipparcos* parallaxes), and shown to be valid for a broad parameter regime (see Chaplin & Miglio 2013 for a review). Possible systematic biases concerning the mass determination are introduced by departures from a simple scaling of $\Delta\nu$ with the square root of the stellar mean density (see e.g. White et al. 2011; Miglio 2012; Miglio et al. 2013b; Belkacem et al. 2013). Suggested corrections to the $\Delta\nu$ scaling probably depend (to a level of a few percent) on the stellar structure itself. Moreover, the average $\Delta\nu$ is known to be affected (to a level of around 1% in the Sun) by inaccurate modelling of near-surface layers.

The seismic mass of a red giant provides a powerful constraint on its age, because its red-giant branch (RGB) lifetime is relatively short compared to its main-sequence lifetime. Combined with independent measurements of metallicity and effective temperature, the main seismic characteristics provide good statistical measures for the primary derived parameters of a star, such as mass, radius, distance, and age (e.g. Miglio 2012; Rodrigues et al. 2014; Casagrande et al. 2016).

Unfortunately, the overall quality (in terms of precision and accuracy) of age determinations for giant stars is still fairly limited (e.g. Jørgensen & Lindegren 2005; Soderblom 2010; Casagrande et al. 2016). Systematic age uncertainties depend on the quality of the observables and on theoretical uncertainties of stellar models (e.g. Noels & Bragaglia 2015; see also Sect. A.2.5.).

With the recently established synergy of asteroseismology and high-resolution spectroscopy surveys, it has become possible to determine more precise ages for red giants.

The detection of solar-like oscillations in thousands of field stars by CoRoT and *Kepler* has opened the door to detailed studies of the Milky Way's stellar populations. Data from the first CoRoT observing run revealed solar-like oscillations in thousands of red giants (Hekker et al. 2009). Miglio et al. (2009) presented a first comparison between observed and predicted seismic properties of giants in the first CoRoT field, which highlighted the expected signatures of red-clump stars in the $\Delta\nu$ and $\nu_{\rm max}$ distributions. Miglio et al. (2013b) presented a first comparison between populations of red giants observed by CoRoT in two different parts of the Milky Way (the CoRoT fields LRa01 and LRc01 also investigated here; see Fig. 3.1), which showed significant differences in the mass distributions of these two samples, and were interpreted as mainly due to the vertical gradient in the distribution of stellar masses (hence ages) in the disc (see also Casagrande et al. 2016 for a first measurement of the vertical disc age gradient). However, the precision of the age determinations used in this pilot study was still limited to 30−40%, due to the absence of constraints on photospheric chemical composition (Miglio et al. 2013a).

Recently, large-scale follow-up observations of seismic targets have begun. The SAGA project (Casagrande et al. 2014, 2016) is covering the *Kepler* field with Strömgren photometry, thereby obtaining more precise stellar parameters. Similarly, spectroscopic stellar surveys such as RAVE (Steinmetz et al. 2006), APOGEE (Majewski et al. 2015), the Gaia-ESO survey (Gilmore 2012), LAMOST (Zhao et al. 2012), and GALAH (Zucker et al. 2012) are observing CoRoT and *Kepler* targets to anchor their spectroscopic surface gravity and distance measurements (e.g. Bovy et al. 2014; Holtzman et al. 2015) – and to ultimately use the combined datasets to constrain the chemo-dynamical evolution of the Milky Way. The CoRoT-APOGEE (CoRoGEE) dataset paves the way for future advances in this direction.

Our paper is structured as follows: the CoRoGEE sample and the provenance of the different data (asteroseismology, spectro-

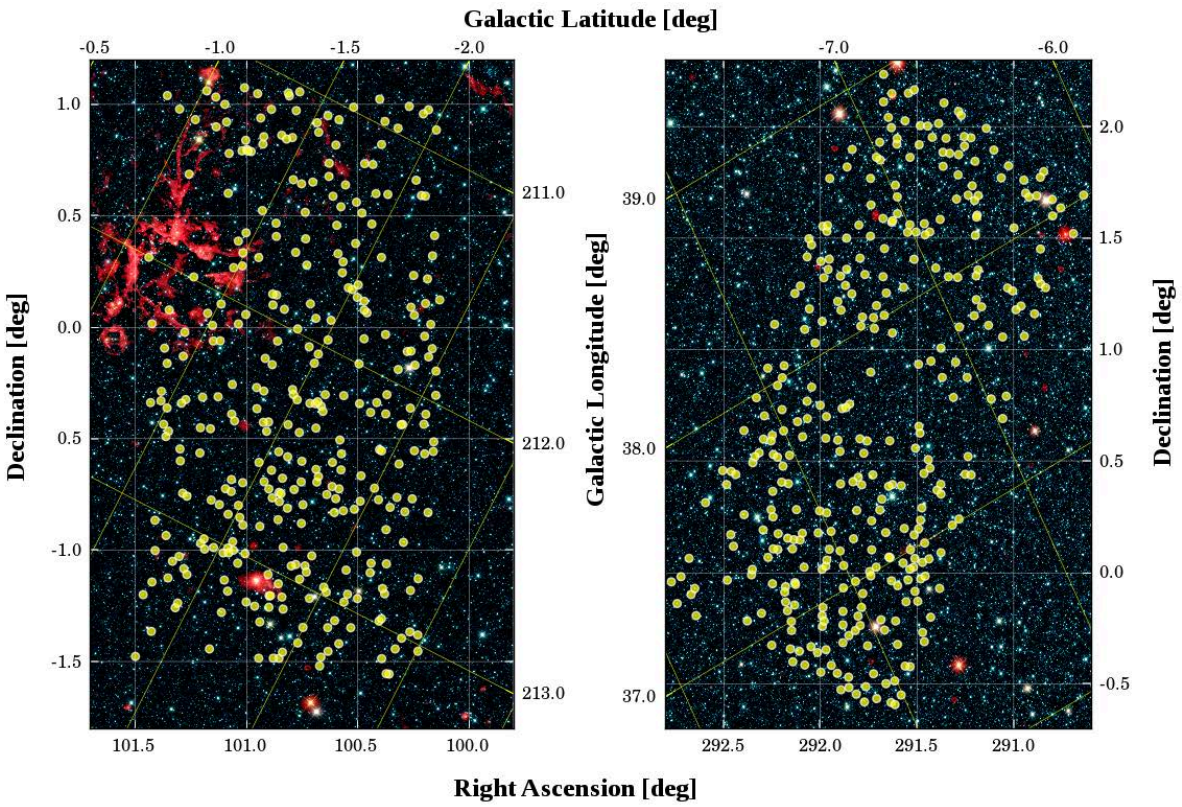

Figure 3.1. Location of the stars observed with APOGEE in the two CoRoT exoplanet fields LRa01 (left) and LRc01 (right). Indicated in yellow are the stars for which asteroseismic parameters were available. The background colour image is composed of near-infrared WISE *W1, W2* and *W3* images from the AllWISE data release (Cutri et al. 2013). Bottom and outside vertical labels display equatorial coordinates, while the top and central vertical labels refer to Galactic coordinates. Corresponding coordinate grids are also shown.

scopy, photometry and astrometry) are presented in Sect. 6.2. Section 3.3 summarises our analysis and leads to our estimates of the main stellar "desirables", such as mass, radius, age, distance, extinction, and kinematical parameters. We emphasise that our age estimates should be considered relative age indicators that are to be used in a statistical sense only.

In Sect. 3.4, we use our sample to study for the first time the variation of the [α/Fe]-vs.-[Fe/H][1] relation with Galactocentric distance in three broad age bins, and compare our data with predictions from a chemodynamical Galaxy model. We conclude and discuss future paths to improve our analysis in Sect. 3.5.

The CoRoGEE dataset covers a wide radial range of the Galactic disc and provides precise stellar parameters, distances, and chemical abundances. Therefore, the presented data provide material for a number of subsequent analyses. In two companion papers, we focus on specific results: 1. the discovery of an apparently young stellar population with enhanced [α/Fe] ratio (Chiappini et al. 2015), and 2. the variation of the disc radial metallicity profile with stellar age (Anders et al. 2016a). The data are publicly available at the CDS (see online Appendix B).

3.2. Observations

Our observations combine the global asteroseismic parameters derived from precision light curves obtained by the CoRoT satel-

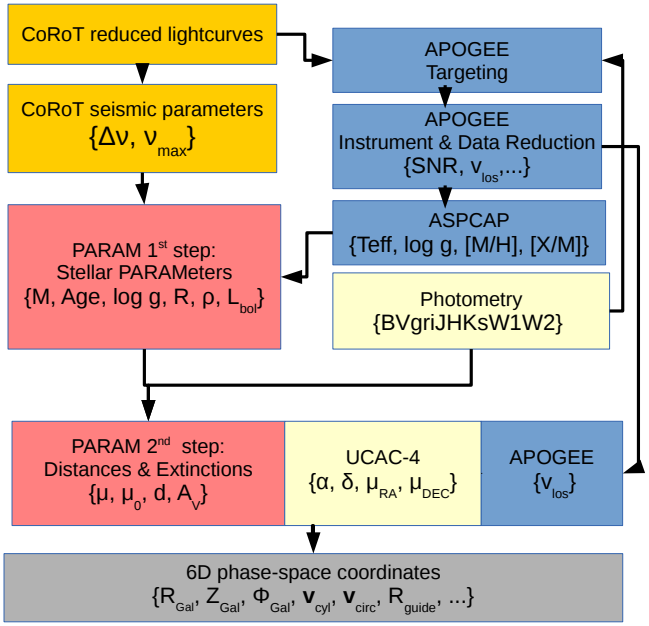

Figure 3.2. Overview of the data provenance and analysis steps performed for the CoRoT-APOGEE (CoRoGEE) data. Blue boxes correspond to APOGEE data products, orange boxes to CoRoT data, and light yellow boxes to existing catalogue data. Red boxes summarise the two parts of the PARAM pipeline, while the grey box summarises the kinematical data used for this work.

[1] The abundance ratio of two chemical elements X and Y is defined as $[X/Y] = \lg \frac{n_X}{n_Y} - \lg(\frac{n_X}{n_Y})_\odot$, where n_X and n_Y are respectively the numbers of nuclei of elements X and Y, per unit volume in the stellar photosphere.

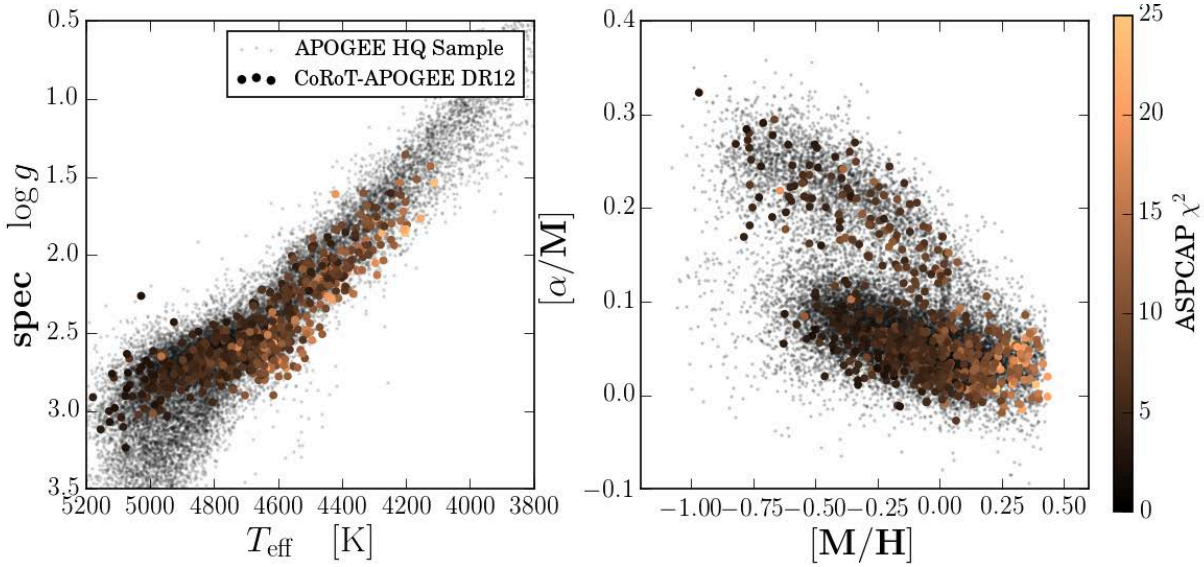

Figure 3.3. Location of the CoRoT-APOGEE stars in the ASPCAP log g-vs.-$T_{\rm eff}$ *Kiel* diagram (left) and the [α/Fe]-vs.-[Fe/H] chemical abundance plane. The colour encodes the reduced χ^2 of the ASPCAP fit. In the background, we plot the APOGEE DR10 high-quality giant sample (Anders et al. 2014), updated to DR12 atmospheric parameters, for comparison.

lite (Baglin et al. 2006; Michel et al. 2008) with stellar parameters and chemical abundances inferred from near-infrared (NIR) high-resolution spectra taken by the Apache Point Observatory Galactic Evolution Experiment (APOGEE). The field maps of the two CoRoT fields observed with APOGEE are shown in Fig. 3.1. An overview on the data assembly and analysis is given in Fig. 3.2.

3.2.1. Adopted seismic parameters

The CoRoT data used in this work are a subset of the data analysed by Mosser et al. (2010) and Miglio et al. (2013b): The CoRoT long runs in the LRa01 and LRc01 exoplanet fields comprise photometric time series for several thousand stars of about 140 days, resulting in a frequency resolution of $\sim 0.08\,\mu$Hz. For stars with detectable solar-like oscillations, Mosser et al. (2010) determined the large frequency separation, $\Delta\nu$, and the frequency of maximum oscillation power, $\nu_{\rm max}$, from the frequency spectra with the envelope autocorrelation-function method (Mosser & Appourchaux 2009), but without reporting individual uncertainties for these quantities.

In the following, we use the seismic parameters obtained from CoRoT N2 light curves[2] in the same way as in Mosser et al. (2010), updated to deliver individual uncertainties on $\Delta\nu$ and $\nu_{\rm max}$. When the envelope autocorrelation signal is high enough, a more precise estimate of the large separation is provided by the use of the so-called universal pattern method (Mosser et al. 2011). A comprehensive data release of newly reduced CoRoT light curves and higher-level science products, using analyses of several different seismic pipelines, will be presented in a separate paper.

As shown in Mosser et al. (2010) and Miglio et al. (2013b), the target selection for the CoRoT asteroseismology program is homogeneous in both fields: solar-like oscillations were searched for in giant stars obeying the following cuts in the colour-magnitude diagram: $K_s < 12, 0.6 < J - K_s < 1.0$. Mosser et al. (2010) also demonstrated that, for a wide parameter range, the selection bias introduced by the additional requirement of detected oscillations does not measurably affect the $\Delta\nu$ or $\nu_{\rm max}$ distributions in the two fields.

3.2.2. Spectroscopic data

APOGEE (Majewski et al. 2015) is a Galactic archaeology experiment operating during the third and fourth epochs of the Sloan Digital Sky Survey (SDSS-III, Eisenstein et al. 2011; SDSS-IV). It uses the 2.5 m telescope at APO (Gunn et al. 2006) to feed a multi-object NIR fiber spectrograph (Wilson et al. 2010, 2012) that delivers high-resolution ($R \sim 22,500$) H-band spectra ($\lambda = 1.51 - 1.69\,\mu$m) of mostly red giants. Dedicated processing and analysis pipelines (Nidever et al. 2015; Holtzman et al. 2015) allow for the determination of precise ($\sim$ 100 m/s) and accurate ($\sim$ 350 m/s) radial velocities. In addition, the APOGEE Stellar Parameter and Chemical Abundances Pipeline (ASPCAP; García Pérez et al. 2015) provides stellar parameters and elemental abundances of 15 chemical elements from the best fit over extensive grids of pre-calculated synthetic stellar spectra (Zamora et al. 2015) to the observed spectra.

As an SDSS-III/APOGEE ancillary program, 690 stars with detected seismic oscillations in the two CoRoT exoplanet fields LRa01 (APOGEE fields COROTA and COROTA3; $(l, b)_{\rm cen} = (212, -2)$) and LRc01 (COROTC; $(l, b)_{\rm cen} = (37, -7)$) were observed with the APOGEE instrument, at high signal-to-noise ratios (median S/N of 230 per resolution element). The field maps of the observed targets are shown in Fig. 3.1. The APOGEE targeting scheme allows for the combination of spectra taken at different times, so-called visits. Most of the stars ($\sim$ 80%) have been observed at least three times to reach the signal-to-noise ratio goal of 100, which is necessary to infer precise chemical abundance information (Zasowski et al. 2013).

Unfortunately, the actual target selection for APOGEE observations of CoRoT solar-like oscillating red giants has not been carried out on the basis of a simple selection function. The targets on the plates observed by APOGEE are a mixture of:

1. solar-like oscillating stars identified by Mosser et al. (2011) – preferentially selected to be RGB stars,

[2] `http://idoc-corot.ias.u-psud.fr/jsp/doc/DescriptionN2v1.3.pdf`

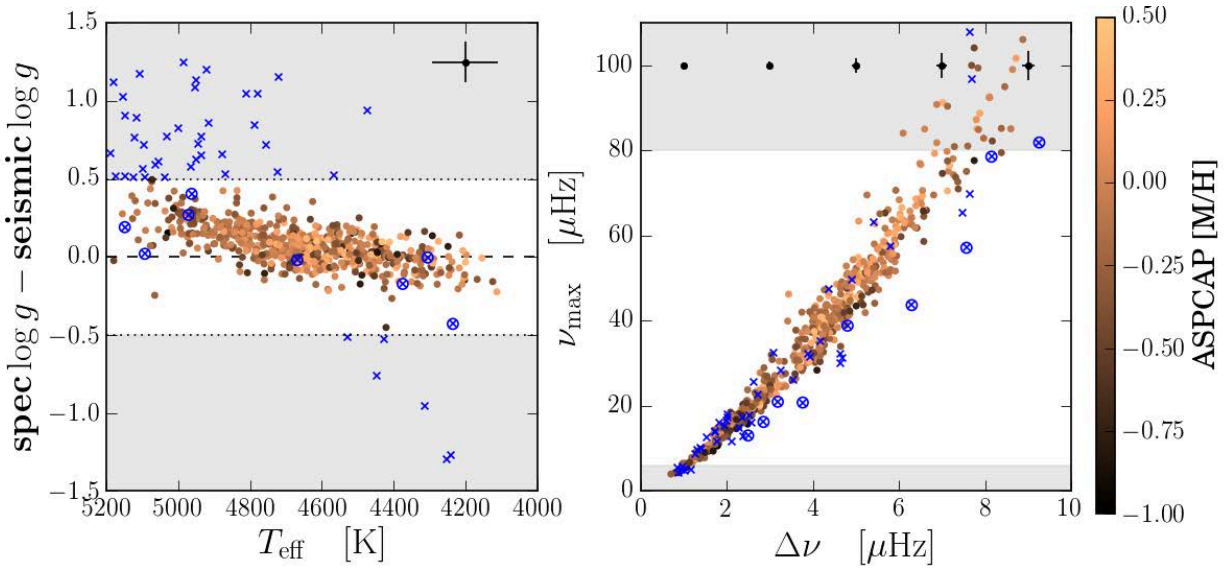

Figure 3.4. Left: Difference between ASPCAP (calibrated) $\log g$ and gravity determined from seismic scaling relations, as a function of effective temperature. Stars located in the grey-shaded area ($|\log g_{\rm ASPCAP} - \log g_{\rm seismo}| > 0.5$ dex; blue crosses) were excluded from the analysis. Right: $\nu_{\rm max} - \Delta\nu$ diagram for our program stars. In addition to the $\log g$ consistency requirement, nine stars (mostly located far from the $\nu_{\rm max} - \Delta\nu$ sequence; blue crossed circles) were also rejected by the PARAM pipeline. Error bars in the upper part of the diagrams represent average uncertainties.

2. CoRoT stars observed by the Gaia-ESO survey (Gilmore 2012) for the purpose of cross-calibration, and
3. APOGEE main-survey targets that were found to show solar-like oscillations in CoRoT, but were not selected on that basis.

Therefore, the best way to correct for the CoRoGEE selection function is to compare what was observed with what could have been observed (i.e., compare the resulting spectro-seismic sample with the underlying photometric sample). In addition, it is necessary to assess whether the photometric parent sample (red giants in the fields LRa01 and LRc01) is representative of the overall stellar content in these fields (as done in Miglio et al. 2013b,a). Both steps can be accomplished with stellar population synthesis modelling (see Anders et al. 2016b). One intermediate selection effect that we cannot address with the current CoRoGEE sample is whether the red giants with detected solar-like oscillations are fully representative of the underlying population. For the *Kepler* field, Casagrande et al. (2016) found that this is only true for a narrower region in the colour-magnitude diagram than we are considering here; our giant sample may therefore be slightly biased against redder colours (more evolved stars).

For this work, we make use of the ASPCAP-derived stellar parameters effective temperature, $T_{\rm eff}$, scaled-solar metallicity, [M/H], and relative α-element abundance, [α/M], from the SDSS data release 12 (DR12 Alam et al. 2015; Holtzman et al. 2015)[3]. For the comparison to stellar isochrones, we approximated the overall metal abundance by the sum [Z/H] $\simeq$ [M/H]$_{\rm uncalib}$ +[α/M]$_{\rm uncalib}$ (e.g. Salaris et al. 1993; Anders et al. 2014). Fig. 3.3 summarises the distribution of the CoRoGEE stars in ASPCAP parameter space. We used calibrated values for the ASPCAP $T_{\rm eff}$ and surface gravity $\log g$.

To ensure that the ASPCAP stellar parameters and chemical abundances do not suffer from unknown problems, we discarded 12 stars that did not satisfy the high-quality criteria laid out in Anders et al. (2014). We also flagged and removed 14 stars for which a visual inspection of the CoRoT light curves revealed spurious detection of solar-like oscillations. In addition, we required that the difference between the spectroscopically derived surface gravity be not too far from the value predicted by the seismic scaling relations: $|\log g^{\rm calib}_{\rm ASPCAP} - \log g_{\rm seismo}| < 0.5$ dex. This criterion removed 47 stars for which the ASPCAP solution is incompatible with the seismic measurements (crosses in Fig. 3.4, left panel). In addition, 11 stars were rejected by our stellar parameter pipeline because their measured input values $\{\Delta\nu, \nu_{\rm max}, T_{\rm eff}, [{\rm M/H}]\}$ were incompatible with any stellar model within their uncertainties (crossed circles in Fig. 3.4, right panel).

3.2.3. Photometry and astrometry

To determine distances to the stars in our sample with the best possible precision, the spectroscopic and asteroseismic information was complemented by photometric data obtained over a wide wavelength range.

Standard Harris B and V as well as Sloan-Gunn r' and i' magnitudes are available for our CoRoT targets from the OBSCAT catalogue which was released as a supplement to the EXODAT archive (Meunier et al. 2007; Damiani et al. 2016). The observations were performed with the Wide Field Camera (WFC) at the 2.5 m Isaac Newton Telescope (INT) at Roque de los Muchachos Observatory (La Palma) in 2002[4].

Because the photometry of the USNO-B catalogue (which is also provided by EXODAT) is based on digitised photographic Schmidt plates and its calibration suffers from inaccuracies and inhomogeneities of about 0.2 mag (Monet et al. 2003), we refrained from using this database.

We also added Johnson BV and Sloan $g'r'i'$ photometry from the APASS survey's 6$^{\rm th}$ data release (Henden & Munari 2014), with photometric accuracies of about 0.02 mag.

[3] We estimate the uncertainties in these abundances as σ[M/H] = σ[Fe/H] and σ[α/M] = $\sqrt{\sigma[{\rm Mg/H}]^2 + \sigma[{\rm Fe/H}]^2}$.

[4] http://cesam.oamp.fr/exodat/index/exodat-documentation\#Photometryavailableforsubsamples

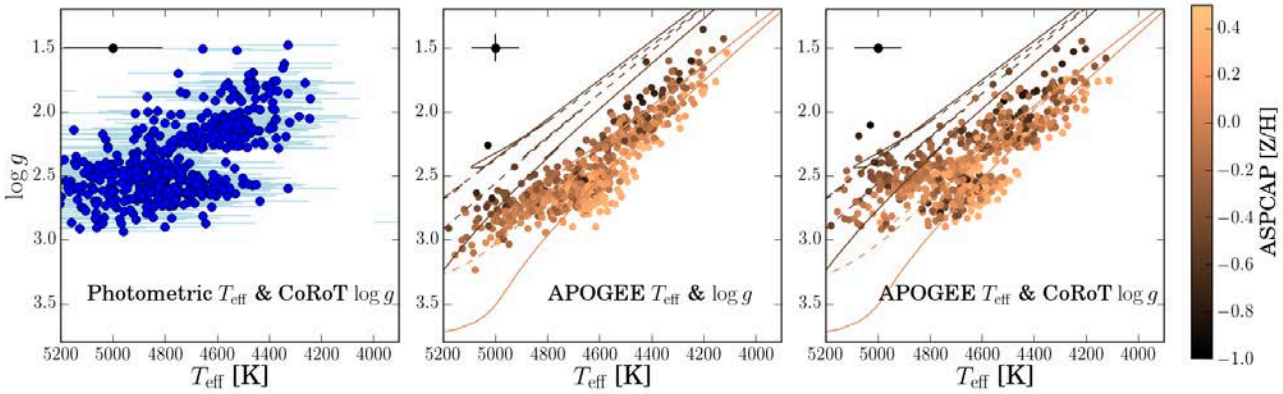

Figure 3.5. $\log g - T_{\rm eff}$ *Kiel* diagrams. Left: Photometric temperatures and $\log g$ from CoRoT seismic parameters + scaling relations. Middle: Purely spectroscopic diagram using APOGEE stellar parameters, colour-coded by metallicity. Right: Joint CoRoT-APOGEE *Kiel* diagram. Overplotted are PARSEC isochrones (Bressan et al. 2012) for metallicities −0.6 and 0.0 at ages 1.4 (dashed lines) and 4.5 Gyr (solid lines) for comparison. As noted by Martig et al. (2015), there is a slight temperature discrepancy between models and data for sub-solar metallicities. Error bars in the upper left of each panel indicate median uncertainties.

Sample criterion	Stars
CoRoT-APOGEE stars	690
with good ASPCAP results	678
and good seismic results	664
and $\lvert \log g_{\rm ASPCAP}^{\rm calib} - \log g_{\rm seismo} \rvert < 0.5$ dex	617
Converged stellar PARAMeters and distances	606
LRa01	281
LRc01	325
and reliable UCAC-4 proper motions (OK flag)	504
and good orbits ($\sigma(v_T) < 50$ km/s)	234

Table 3.1. Summary of the number of CoRoT-APOGEE stars satisfying different quality criteria.

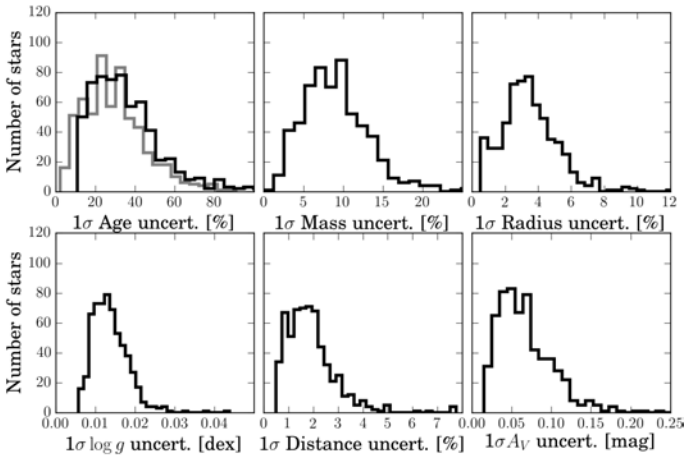

Figure 3.6. Distributions of the 1σ-uncertainties in stellar age, mass, radius, $\log g$, distance, and extinction for our sample. For the ages (top left panel), we show the distributions of statistical (grey histogram) and total uncertainties.

In the infrared, accurate JHK_s photometry is available from the 2MASS Point Source Catalog (Cutri et al. 2003), which served as the major input catalogue for APOGEE. We also added WISE $W1W2$ filters from the AllWISE Catalog (Cutri et al. 2013) for which the photometric precision is sufficient to constrain the mid-infrared region of the stellar spectral energy distribution[5].

For kinematical studies, proper motions were compiled from the recent UCAC-4 catalogue (Zacharias et al. 2013), using only astrometric data that meet several high-quality criteria encoded in the UCAC-4 flags (∼ 80% of the stars), in the same manner as in Anders et al. (2014).

3.3. Analysis

3.3.1. Masses, radii, and ages

To derive primary stellar parameters such as mass, luminosity, radius, and age, we used the Bayesian parameter estimation code PARAM[6] (da Silva et al. 2006) with the recent improvements presented in Rodrigues et al. (2014). The code uses standard grid-based modelling (see Chaplin & Miglio 2013 and references therein for an overview) to estimate stellar properties by comparison with theoretical stellar models, in our case the PARSEC isochrone models (Bressan et al. 2012).

When computing the desired stellar parameters, PARAM naturally accounts for the statistical uncertainties in the input parameters $\{\Delta\nu, \nu_{\rm max}, T_{\rm eff}, [{\rm Z/H}]\}$, and transforms them into the posterior probability distribution in stellar model space. We therefore denote uncertainties that are reflected in the shape of stellar parameter probability distribution functions (PDFs) *statistical*, because they arise from a (non-linear) propagation of uncertainties in the measured quantities.[7]

Stellar evolution models predict a rather tight relation between mass, metallicity, and age for red giants, with the age spread increasing with decreasing mass. Therefore, an uncertainty in stellar mass of about 10% typically results in a (statistical) age uncertainty of about 30% (see e.g. Miglio et al. 2013b). In addition, depending on its location in the Hertzsprung-Russell diagram, a star may have broad or multi-peaked stellar parameter PDFs; the age PDFs show a wide variety of shapes. But even in the case of very broad PDFs, their shape does add valuable information: in the sense that we can quantify the knowledge we lack.

[5] As in Rodrigues et al. (2014), we discard the filters $W3$ and $W4$ because of possible contamination by warm interstellar dust (e.g. Davenport et al. 2014) and larger measurement uncertainties.

[6] `http://stev.oapd.inaf.it/cgi-bin/param`

[7] Because we chose a particular set of isochrones, our statistical uncertainties are of course not model-independent.

We therefore report the mode and 68% or 95% credible intervals of the marginalised PDF in mass, radius, age, distance, and extinction[8] in our catalogue. We achieve typical statistical uncertainties of 0.015 dex in $\log g$, 4% in radius, 9% in mass[9], 25% in age, and 2% in distance (median values; see Fig. 3.6).

As discussed in the Introduction, stellar ages are by far more uncertain than any other classical stellar parameter and should be used only in a statistical, relative sense. This is due to a combination of the simple propagation of the stellar mass uncertainties with systematic uncertainties (mostly related to mass loss and the mass scaling relation). The magnitude of these uncertainties and their influence on stellar age estimates are discussed in Sect. A.2.5.. For a more detailed discussion of the systematic uncertainties involved in stellar modelling see Noels & Bragaglia (2015), for instance.

3.3.2. Age uncertainties: a closer look

Statistical uncertainties

The age PDFs (which were not shown by Rodrigues et al. 2014) merit closer examination. Fig. 3.7 shows the collection of all 606 age CoRoGEE PDFs, grouped in bins of mode age. Among them we find "well-behaved" (single-peaked) as well as more complex (double-, multi-peaked, very broad or grid-edge-affected) stellar parameter PDFs.

It has been known for some time that isochrone-grid derived stellar age PDFs may show a great diversity (e.g. Takeda et al. 2007). As there is no straightforward way to classify or even quantify the behaviour of such diverse PDF shapes, the following numbers should be used with caution:

- Of the 606 stars passing all quality criteria, 246 display well-behaved single-peaked age PDFs, 205 age PDFs are double-peaked, 143 have three or more peaks, and 12 do not have local extrema because the PDF increases monotonically towards the upper age limit.
- Many of the multi-peaked PDFs have negligible PDF contributions from the secondary, tertiary etc. maxima, but a sizeable fraction exhibits genuinely complex function profiles.
- Figure 3.8 shows the distribution of stars classified according to the overall form of their age PDF in the Hertzsprung-Russell diagram. Multi-peaked age PDFs occur predominantly for stars with $\log g \simeq 2.4$, that is, parameter regions that are occupied by first-ascent RGB stars as well as red-clump stars and asymptotic giant-branch (AGB) stars. The metallicity measurement does not add sufficient information to disentangle the different evolutionary stages. As noted by Rodrigues et al. (2014), the limiting factor is the accuracy of the effective temperatures, both in terms of models and measurements.
- An independent possibility of distinguishing between evolutionary phases (and thereby reducing the number of multi-peaked solutions) is offered by asteroseismology: Mosser et al. (2011) have measured mixed-mode period spacings (see also Bedding et al. 2011) for a fraction of the CoRoGEE targets (139 stars in LRc01, 28 stars in LRa01). This information was used to better constrain the age PDFs, as done in Rodrigues et al. 2014 for the APOGEE-*Kepler* (APOKASC) sample (Pinsonneault et al. 2014), and in Casagrande et al. (2014, 2016) for the SAGA survey.

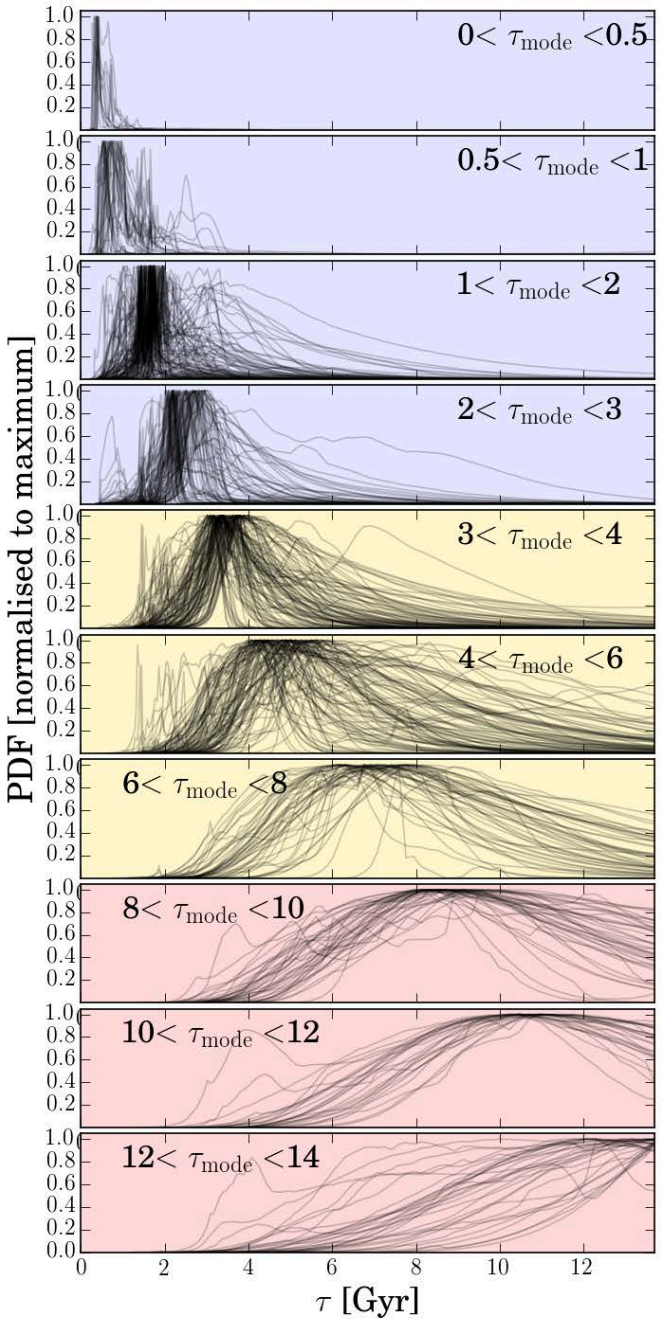

Figure 3.7. Diversity of the computed age PDFs: All age PDFs of the CoRoGEE sample, grouped in bins of mode age. Background colours correspond to the three age bins used in Fig. 3.14.

Systematic uncertainties

For population studies of red giants, there are three main sources of systematic age uncertainties:

1. *The accuracy of seismic masses*: An important source of age bias comes from possible systematic errors in mass, which

[8] Differently from Rodrigues et al. (2014), we computed these statistics from the interpolated PDF in linear units, and our formal 1σ (2σ) parameter uncertainties are defined as the smallest parameter interval around the mode that contain 68% (95%) of the PDF.

[9] Even in the very local volume the comparison of absolute magnitude (based on *Hipparcos* parallax), $B - V$ colour, and [Fe/H] with stellar evolution models yields typical uncertainties in radius and mass of 6% and 8%, respectively (Allende Prieto & Lambert 1999).

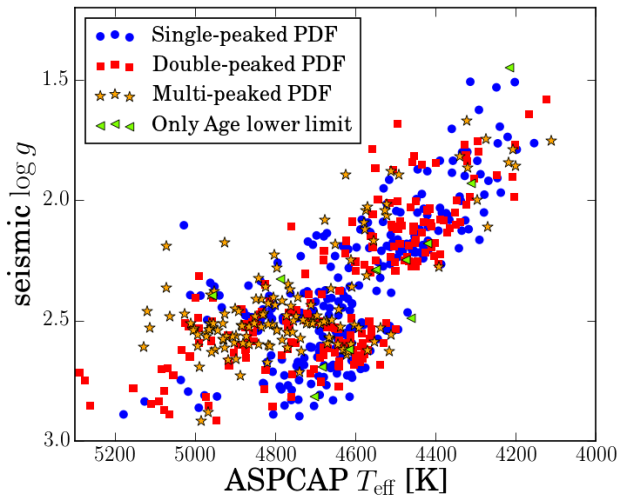

Figure 3.8. Seismo-spectroscopic Hertzsprung-Russell diagram of the CoRoGEE stars, with the symbols indicating the qualitative behaviour of the age PDFs, as described in the legend.

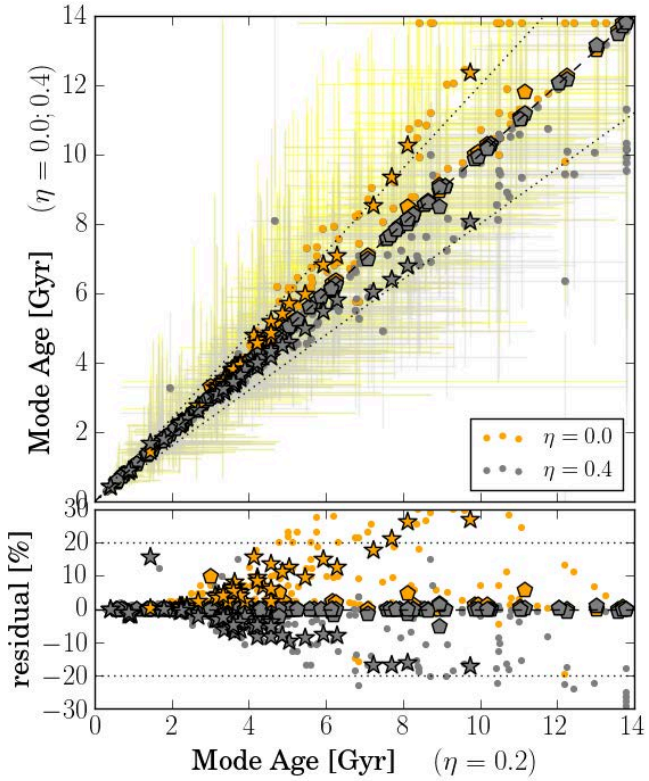

Figure 3.9. Effect of non-canonical mass-loss assumptions on our derived ages. The upper panel shows the ages derived using a non-canonical mass-loss parameter $\eta_{\rm Reimers} = 0.0$ (0.4) in orange (grey), while the lower panel zooms into the differences. Again, known RC stars are plotted as stars, RGB stars as pentagons.

are likely to be small (< 10%), but are very hard to quantify given that only a few objects or stars in clusters have masses known to within 10% or better. Because hard constraints on the accuracy of the seismic masses have started to appear only very recently (e.g. Miglio et al. 2016), we refrain from a quantitative analysis in this paper. Future analyses will use a revised version of the $\Delta\nu$ scaling relation.

2. *Mass loss*: The accuracy of age-mass relations for red giants relies on our incomplete knowledge of stellar physics. While a relatively simple mass-age relation is expected for RGB stars, the situation for RC or early AGB stars is different: If these stars undergo a significant mass loss near the tip of the RGB, then the mass-age relation is not unique (for a given composition and input physics), since the mass observed at the RC or early-AGB stage may differ from the initial one (for a review see e.g. Catelan 2009; Miglio 2012).[10] In the PARSEC isochrones, mass loss is included following the prescription of Reimers (1975). Figure 3.9 demonstrates the effect of varying our canonical value of the mass-loss efficiency $\eta = 0.2$ to extreme values (0 or 0.4, respectively). Our overall results are similar to the findings of Casagrande et al. (2016) for the SAGA sample: The impact of mass-loss on the age uncertainty increases with evolutionary stage, in the sense that RGB stars (especially seismically confirmed RGB stars) are almost unaffected by changes in η, while for RC stars we can change the age by up to ±30% in some cases. However, for the vast majority of our stars the age uncertainty due to mass loss is $\lesssim 20\%$.
3. *Other input physics:* It is well-known that the stellar physics input of theoretical isochrones (e.g. reaction rates, opacities, rotation, diffusion, He abundance, mass loss, or core overshooting) significantly affect the age and luminosities of the predicted stellar models at a given mass (e.g. Miglio et al. 2015; Noels & Bragaglia 2015). At this time, the quantitative effects of each of the adopted input physics parameters on the isochrones are known in some detail through asteroseismology (e.g. Montalbán et al. 2013; Broomhall et al. 2014; Lebreton & Goupil 2014). However, a real calibration of stellar models through seismology has only started recently[11]. A detailed comparison of the available stellar models has not yet been performed, but a recent study (Miglio et al., in prep.) suggests that the age spread models computed with different stellar evolution codes for an early AGB star at solar metallicity is around 7% for a $1M_\odot$ star, 11% for a $1.5M_\odot$ star, and 25% for a $2M_\odot$ star. For this paper, we extrapolated these values to the full mass range, and neglected any possible dependency on metallicity.

We can now define our total age uncertainty as the quadratic sum of the (asymmetric) formal 1σ uncertainty coming from PARAM, the uncertainty derived from the mass-loss test (Fig. 3.9), and the mass-dependent uncertainty coming from the comparison of different evolutionary codes.

Figure 3.10 displays the distribution of these total 1σ age uncertainties as a function of age, colour-coded by field. The plot shows some important features:

– For stars between 4 and 10 Gyr, we observe an overall linear relation between age uncertainty and age. Because the finite age of the Universe (taken here as $\tau_{\rm max} = 13.8$ Gyr) is included in the age prior (which is flat in $\log\tau$), the method-intrinsic age uncertainties reach a maximum at $\tau = 9$ Gyr and decrease again towards greater ages.

[10] In this context, the characterisation of populations of giants benefits greatly from estimates of the period spacings of the observed gravity modes, which allows a clear distinction to be made between RGB and RC stars (Bedding et al. 2011), and early-AGB stars (Montalbán & Noels 2013).

[11] For example, it has become possible to determine the amount of convective-core overshooting during the main-sequence phase (Silva Aguirre et al. 2013; Deheuvels 2015)

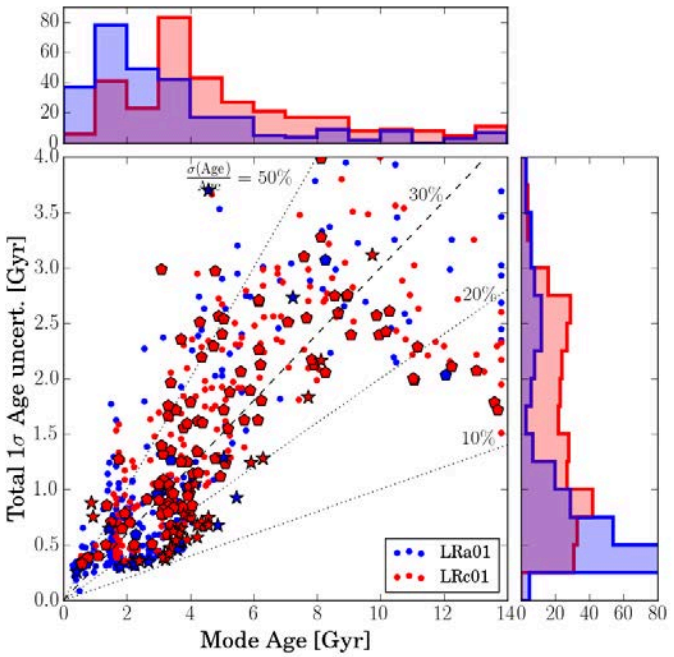

Figure 3.10. Total age uncertainties as a function of age (or more precisely, the mode of the age PDF), for stars in LRc01 (red) and LRa01 (blue). Known RC stars are plotted as stars, RGB stars as pentagons. The black lines indicate lines of constant fractional age uncertainties (from left to right: 50%, 30%, 20%, 10%). The histograms in the top and right panels show the distribution of ages and age uncertainties, respectively.

- A sizeable number of stars have a PDF maximum at the age limit: Most of these objects can be safely assumed to be old thick-disc stars.
- In the younger regime, we see a complicated behaviour in the age uncertainty–age diagram: Some stars appear to cluster around certain age values. These do not correspond to the grid points of our PARSEC models (which is much finer: $\Delta \log(\tau[\mathrm{yr}]) = 0.01$). The observed dip in the LRc01 age distribution is not statistically significant.
- Although the age uncertainties are certainly non-negligible, the top panel of Fig. 3.10 suggests the indirect result of Miglio et al. (2013b), who used stellar population synthesis models to conclude that the stars in LRa01 are typically younger than the LRc01 population. To make this statement more quantitative, the histograms have to be corrected for selection effects, as we discuss in Sect. 3.4.2 below.

Estimating age errors from simulated stars

As an additional check of our age estimates, we opted to simulate the CoRoGEE sample based on the chemodynamical model of Minchev et al. (2013, 2014a, MCM)[12]. The final snapshot of the MCM galaxy consists of 953,206 N-body particles with age, chemical, and kinematic information. To translate these mass particles into simulated stars, Piffl (2013) first used the MCM model as an input for the Galaxia code (Sharma et al. 2011) in the context of a simulated RAVE survey. Here, we used the same code to simulate a CoRoGEE-like sample from the MCM galaxy. A detailed description of the chemodynamical mock is given in Anders et al. (2016b). In the following, we briefly summarise the procedure.

We first simulated the stellar populations in the CoroT fields and calculated observed magnitudes for these mock stars using the new PanSTARRS-1 3D extinction map of Green et al. (2015) as our Galactic extinction model. In the next step, we applied the effective CoRoGEE selection function (assuming that it only depends on H and $J - K_s$) by selecting stars randomly from small boxes in the colour-magnitude diagram (see Fig. 4 of Anders et al. 2016b). While this is certainly a simplification of the true CoRoGEE selection (see Sect. 6.2), it was the only way in which our forward model could be realised. We also simulated Gaussian observational errors in the stellar parameters $T_{\mathrm{eff}}, \Delta\nu, \nu_{\mathrm{max}}$, [Z/H] and magnitudes, and then ran the Bayesian parameter estimation code PARAM, exactly as was done with the real data.

Using this simulation, we can now address the question of how well our recovered PARAM age estimates correspond to the true stellar ages given by the model: The upper panel of Fig. 4.5 shows estimated vs. true ages, the lower panel presents the relative age error $\frac{\tau_{\mathrm{PARAM}} - \tau_{\mathrm{true}}}{\tau_{\mathrm{true}}}$ as a function of the true age. The black symbols correspond to the median age error in each age bin indicated on the x-axis, demonstrating that our method tends to systematically overestimate the true ages by around $10-15\%$, with the scatter increasing towards greater ages. A small systematic shift is expected, as the Galaxia input isochrones (Padova; Marigo et al. 2008) are slightly different from those used by PARAM (PARSEC; Bressan et al. 2012). The histograms to the sides of the top plot show how the true age distributions (in the model) of the two CoRoT fields are distorted by the measurement procedures.

As is clear from Fig. 4.5 and as shown in the previous section, our derived age estimates should be treated with caution, and considered relative age indicators rather than unbiased absolute age estimates. Therefore, in this paper we only use the age information to separate our stars into three wide age bins: Stars with derived PARAM ages younger than 3 Gyr ("young"), stars with PARAM ages between 3 and 8 Gyr ("intermediate"), and stars measured to be older than 8 Gyr ("old"). The typical forms of age PDFs for stars in these three bins are shown in Fig. 3.7 (coloured panels). The same coloured regions in the top panel of Fig. 4.5 can be used to assess the contamination in each of the three age bins. In summary, the simulation suggests that the contamination by old stars in the young bin and the contamination by young stars in the old bin are negligible.

3.3.3. Distances and extinctions

As in Rodrigues et al. (2014), distances and extinctions were calculated by comparing the previously derived absolute magnitude with the observed magnitudes in several passbands (see Sect. 3.2.3), assuming a single extinction curve (Cardelli et al. 1989; O'Donnell 1994), using the bolometric corrections of Marigo et al. (2008) and the corresponding extinction coefficients (Girardi et al. 2008). Because PARAM uses photometric measurements from many filters over a wide wavelength range (see Sect. 3.2.3), our distance uncertainties are much smaller than the uncertainties expected from the distance-radius relation (as adopted in e.g. Miglio et al. 2013b). For more details, we refer to Sect. 3 of Rodrigues et al. (2014), and to Appendix 3.A.

We carried out comparisons with extinction estimates from the literature in Appendix 3.A.3, finding that our precise extinc-

[12] The results are largely independent of the model used. However, we note that the MCM model is a thin-disc model only, and therefore does not include stars older than 11.7 Gyr.

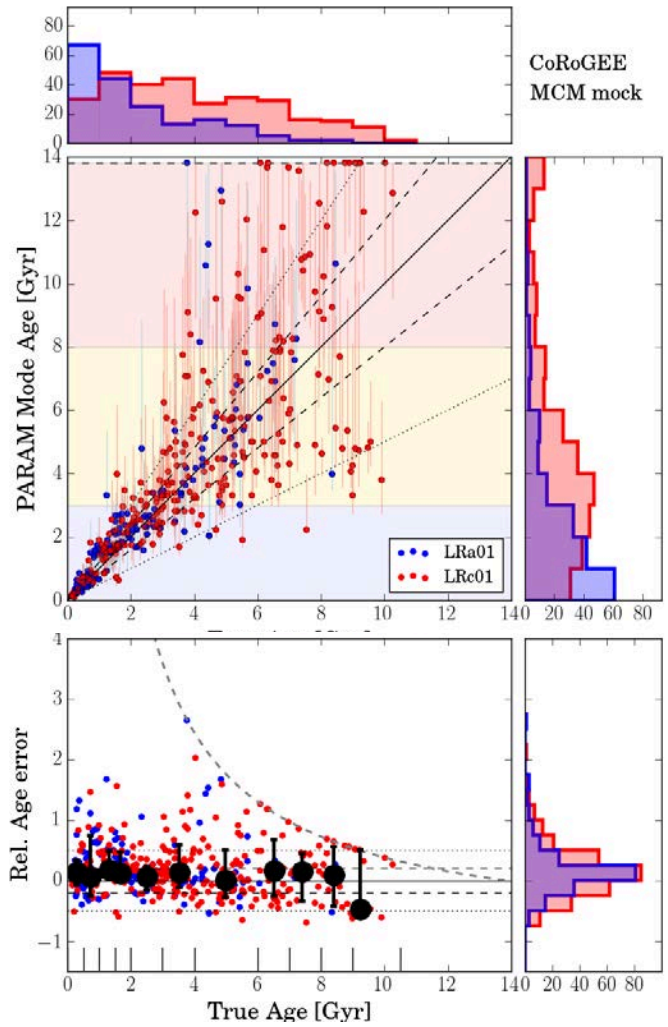

Figure 3.11. Estimating systematics of our age estimates using simulated stars. The scatter plot in the upper panel shows estimated PARAM ages of the CoRoGEE mock stars (and their statistical 1σ uncertainties as error bars) vs. the true ages of the parent N-body particle. The histograms to the sides of this plot show the corresponding age distributions of the two CoRoT fields. The background colours correspond to the three age bins used in Sect. 3.4. The lower plot shows the relative age error $\frac{\tau_{\rm PARAM}-\tau_{\rm true}}{\tau_{\rm true}}$ as a function of the true age. The black symbols correspond to the median age error in each age bin indicated on the x-axis. The various lines correspond to a one-to-one relation, 20% and 50% deviation, and the age boundary at 13.8 Gyr.

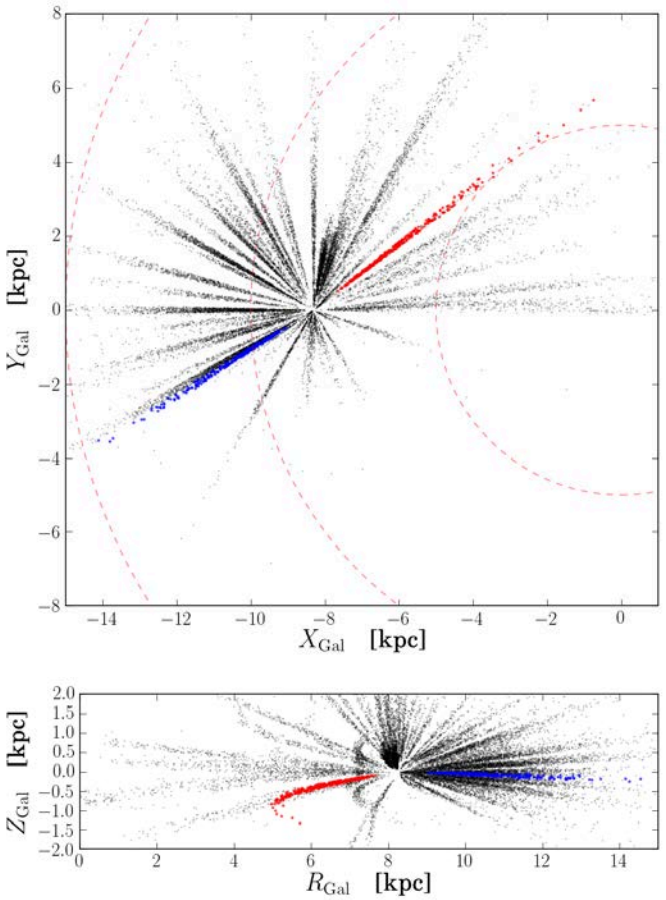

Figure 3.12. Location of the CoRoT-APOGEE stars in Galactocentric Cartesian coordinates ($X_{\rm Gal}, Y_{\rm Gal}$ – top panel) and Cylindrical coordinates ($R_{\rm Gal}, Z_{\rm Gal}$ – bottom). Blue dots correspond to LRa01 targets, red dots to LRc01 targets. The APOGEE DR10 high-quality giant sample (Anders et al. 2014) is shown in the background (black dots).

tion values are best matched by the spectro-photometric method developed in Schultheis et al. (2014).

3.3.4. Kinematics

The 6D phase-space coordinates, along with their uncertainties are available for a subset of 504 stars. For this subset, orbital parameters were computed in the same manner as in Anders et al. (2014). Most of the more distant stars, however, still have too large proper motion uncertainties (> 50 km/s in the tangential component of the space velocity, v_T) to be useful even for statistical kinematic studies, as our sample is too small to allow for good statistics in the presence of noisy kinematical data (see Table 3.1). When examining the kinematical properties of our sample, we therefore concentrated on the most reliable parameters whenever possible.

One relatively robust parameter is the guiding-centre radius of a stellar orbit, which we computed using the approximation $R_{\rm guide} = \frac{L_z}{v_c} = \frac{v_\phi \cdot R_{\rm Gal}}{v_c}$ (e.g. Casagrande et al. 2011). Here, L_z denotes the angular momentum, v_ϕ the ϕ-component of the space velocity, and $v_c \approx 220$ km/s the circular velocity at the star's position – which for for our purposes can be assumed to be approximately constant over the Galactocentric distance range considered.

3.4. The [α/Fe]-[Fe/H]-age diagram at different Galactocentric distances

In addition to the presentation of the CoRoT-APOGEE data in the past two sections, the goal of this and following work is to study the age-abundance-kinematics relationships of the Milky Way disc outside the solar cylinder. To illustrate the value of our sample for Galactic archaeology, in this section we study the [α/Fe]-vs.-[Fe/H] abundance relationship with Galactocentric distance and age.

The CoRoGEE sample has the novel advantage of covering a wide radial range of the Galactic disc (4 kpc < $R_{\rm Gal}$ < 14 kpc) with red giants for which both asteroseismic and high-resolution spectroscopic data are available. Our final sample comprises 606 stars with converged stellar parameters and distances in the two CoRoT fields LRa01 and LRc01. However, given the extended

radial and age baselines, this sample size forces us to constrain our analysis to broad bins of Galactocentric distances and ages instead of using full distribution functions. Moreover, we recall that systematic uncertainties probably affect the estimated ages presented here. Hence, we focus our analysis on larger age bins.

Following the path of Chiappini et al. (2015), we now examine the [Fe/H]-[α/Fe]-age space also outside the solar neighbourhood, analysing the CoRoGEE stars for which we now also have age information. We compare our findings to the predictions of chemical-evolution models, as well as to recent chemodynamics results.

3.4.1. Understanding [α/Fe] vs. [Fe/H] diagrams with a chemical-evolution model

[X/Fe] vs. [Fe/H] diagrams, and in particular the [α/Fe] vs. [Fe/H] diagram, are widely used diagnostic tools to constrain the enrichment history of stellar populations. High-resolution spectroscopic data reveal two clearly-separated disc components (thin and thick) in the [α/Fe] vs. [Fe/H] diagram, which follow their own age-metallicity relations (e.g. Gratton et al. 1996; Fuhrmann 1998; Ramírez et al. 2007; Anders et al. 2014). The valley between the two sequences in this diagram can hardly be attributed to simple sample selection effects (Anders et al. 2014; Nidever et al. 2014) and is probably a real characteristic of the Galactic disc[13], as we discuss below.

As a starting point, in Fig. 3.13 we compare the bulk of APOGEE DR10 data analysed in Anders et al. (2014) with the predictions of the set of Galactic chemical-evolution models of Chiappini (2009). The figure shows the location of Anders et al. (2014) high-quality disc sample in the [α/Fe] vs. [Fe/H] diagram, together with the histograms of these parameters. Overplotted are the chemical-evolution tracks of Chiappini (2009) for various bins in Galactocentric distance, colour-coded by age.

The thin-disc models shown in Fig. 3.13 were obtained by varying the accretion timescale onto the disc, assuming it to be shorter in the inner regions and longer in the outer parts (typical for MW chemical-evolution models with inside-out formation; e.g. Chiappini et al. 1997, 2001; Hou et al. 2000). For this reason, the thin disc at the solar vicinity formed on a longer timescale than the thick disc, and towards the inner disc regions the infall timescales of both components approach each other (but there is still a difference in the star-formation efficiency). This explains why the thin-disc model curve at 4 kpc is close to the thick disc curve (see Fig. 3.14 in the next section), but reaches a lower [Fe/H] value. The details of the thin-disc model can be found in Minchev, Chiappini, & Martig (2013, Sect. 3).

From a pure chemical-evolution point of view, the thick disc can be modelled as a separate Galactic component with high star-formation efficiency and a short infall timescale. Such a model naturally predicts a population of mostly old [α/Fe]-enhanced stars with a metallicity distribution peaking around -0.5 dex (e.g. Soubiran 1999) and explains some of the abundance patterns observed in high-resolution solar-vicinity samples that are classified as thick-disc-like (Chiappini 2009). When building a chemical-evolution thick-disc model of this type, one has considerable freedom in the choice of parameters because tight observational constraints are still lacking. As an example, for the thick disc models one can assume that its formation is completed within 2-3 Gyr (in order to obtain a population that is mostly older than 10 Gyr), but there is no tight constraint on the tail of the age distribution. While thin-disc models have to reproduce the chemical-abundance patterns at the present time in the local interstellar medium, the final metallicity and abundance pattern for the thick disc is still under debate (solar or super-solar depending on how this component is defined in the different datasets). Therefore, the thick-disc curve illustrated by the dashed line in Fig. 3.13 could be easily extended to higher metallicities, whereas the same is not true for the thin-disc curves (especially for the one at the solar-vicinity position).

Figure 3.13 shows that these chemical models broadly agree with the two main features of the Galactic disc [α/Fe] vs. [Fe/H] diagram: the location of the bulk of thin-disc stars at [α/Fe] < 0.1 and [Fe/H] > -0.8 (rectangular box labelled "chemical" thin disc in the figure), and the position of the stars following a thick-disc track (marked by the rose-coloured region and the thick red dashed line). Within the framework of these models, the thin-disc sequence can be explained as a mixture of relatively young (age $\lesssim 5$ Gyr) stars, originating from different birth regions within the Galactic disc that have had different enrichment histories. In contrast, for the thick disc the metallicity distribution peaks at ~ -0.5 (e.g. Rocha-Pinto & Maciel 1996; Kotoneva et al. 2002; Nordström et al. 2004; Holmberg et al. 2007), and a large number of stars is expected at high [α/Fe] ratios and metallcities below ~ -0.2. Because of the co-existence of thick and thin disc in this diagram, a gap or dip in the [α/Fe] vs. [Fe/H] diagram should thus be naturally produced.

Of course, the exact absolute position of the tracks with respect to the data depends not only on the calibration zeropoint of the APOGEE abundances[14], but also on the choice of stellar yields, IMF, and star-formation efficiency. As shown in Chiappini (2009), these models provide a good description of the observed shifts of several abundance ratios as a function of metallicity for the solar radial bin, once the thick and thin discs are defined via kinematics (as in Bensby et al. 2003).

The reason we present a comparison with a model computed before the data in Fig. 3.13 were available is to illustrate how the predictions of a pure chemical-evolution model that was in agreement with chemical abundances (among other observables) in the local volume performs when compared to the new samples of stars now covering larger portions of the disc. Clearly, one of our near-term goals is to further explore the parameter space (especially new constraints on the stellar yields and their metallicity dependency) of these models and identify those that best fit the new observational constraints. However, the main challenges to the interpretation of discrete thin and thick discs (as modelled in Chiappini et al. 1997; Chiappini 2009) are on the one hand the existence of so-called super-metal-rich (SMR) stars (Grenon 1972; Trevisan et al. 2011) in the solar neighbourhood [15], and on the other hand the fact that not all thin-disc stars with metallicities below -0.2 can be explained as high-eccentricity intruders from outer regions (Anders et al. 2014).

[13] However, see Bovy et al. (2012) for a different explanation.

[14] As an example, from SDSS DR10 to DR12, there has been a shift of ~ 0.1 dex in the calibrated metallicities (Holtzman et al. 2015; Martig et al. 2015), and further improvements might affect the metallicity scale at the same level. A +0.05 dex shift in [α/Fe] is also observed when moving from DR10 to DR12. As the same shift is observed between a Gaia-ESO Survey sample and the DR12 values, we opted to retain the DR10 values for the comparison in Fig. 3.13.

[15] SMR stars are defined as stars whose metal abundance exceeds the metallicity of the local present-day interstellar medium. This value is dependent on Galactocentric distance and is constrained by the present-day abundance gradient in the interstellar medium. For the solar vicinity, SMR stars are found in the region illustrated by the blue rectangular box in Fig. 3.13.

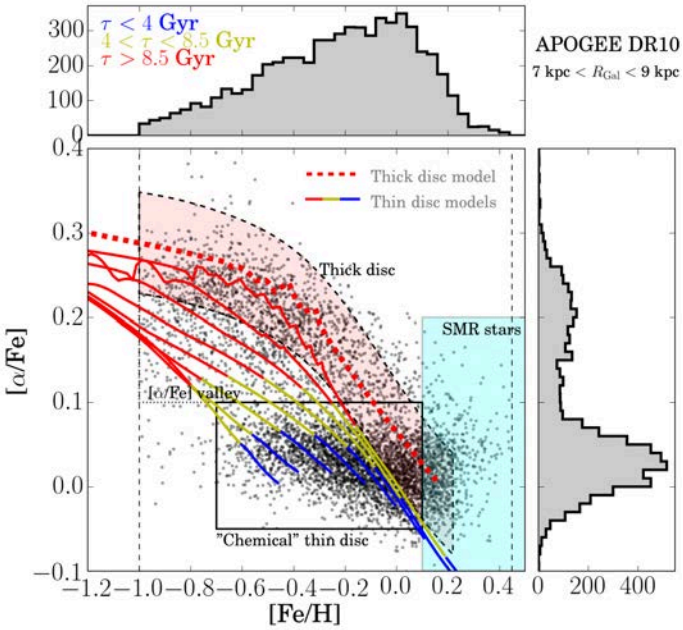

Figure 3.13. The [α/Fe] vs. [Fe/H] diagram of the APOGEE DR10 high-quality giant sample (Anders et al. 2014; grey dots) in the range 7 kpc < $R_{\rm Gal}$ < 9 kpc. Overplotted with colours are the thin- and thick-disc chemical-evolution models of Chiappini (2009): The solid lines correspond to the chemical tracks of the thin disc at different Galactocentric annuli (from left to right: 18 kpc, 16 kpc, 14 kpc, 12 kpc, 10 kpc, 8 kpc, 6 kpc, 4kpc). The colours indicate the age (or look-back time), as indicated in the top panel. The dashed line represents a thick-disc model (for $R_{\rm Gal}$ = 6 kpc - the Galactocentric dependency for the thick-disc models computed in Chiappini (2009) are minor - see text for more details).

The existence of SMR stars is commonly attributed to a significant radial mixing of stellar populations within the Galactic disc (e.g. Grenon 1989, 1999; Chiappini 2009; Kordopatis et al. 2015). In agreement with previous studies, Kordopatis et al. (2015) conclude that SMR stars in the solar neighbourhood must have migrated from far inside the solar annulus. Recently, Schönrich & Binney (2009); Brunetti et al. (2011); Minchev et al. (2013, 2014b) and Kubryk et al. (2015a,b) have argued that chemical-evolution models for the Milky Way cannot be viewed independently of its dynamical evolution, and found different prescriptions for the merging of these two aspects of Galactic evolution. In the next subsection we separate the [α/Fe]-[Fe/H] diagram into bins of age and Galactocentric distance and compare our data to a chemical-evolution model. This is useful because the latter form the backbone of many recent chemo-dynamical approaches.

Binning the data in Galactocentric distance and age

While the division of the massive APOGEE dataset into various Galactic zones has been the subject of previous investigations (Anders et al. 2014; Hayden et al. 2014; Nidever et al. 2014; Hayden et al. 2015), we now can make use of the unique seismic information from CoRoT to show, for the first time, [α/Fe]-[Fe/H]-age diagrams, outside the *Hipparcos* volume, in several Galactocentric bins.

Figure 3.14 presents one of the main results of this paper: the [α/Fe] vs. [Fe/H] diagram for the CoRoGEE sample, split into five bins of Galactocentric distance, as indicated in each panel.

As in Fig. 3.13, we include in Fig. 3.14 the [α/Fe] vs. [Fe/H] model tracks of Chiappini (2009). Figure 3.15 has the same format as Fig.3.14, only that the data are now binned in guiding-center radius $R_{\rm guide}$ instead of Galactocentric distance, to mitigate the effect of stellar mixing by "blurring" (Schönrich & Binney 2009). In this plot, the size and transparency of the symbols encode the uncertainty in both stellar age and guiding-center radius, because both quantities may have considerable uncertainties. The interpretation of these figures is difficult because of the low statistics and the noise arising from proper motion uncertainties and radial migration. We analyse the two figures simultaneously below.

The main results we derive from these figures are:

- The shift of the peak of the thin-disc metallicity distribution function from higher to lower metallicities as one moves towards larger Galactocentric distances (Anders et al. 2014; Hayden et al. 2015) is accompanied by a dominance of younger ages towards the outermost radial bins. However, the exact relative number of young and old stars in each radius bin can be slightly biased as a consequence of the detectability of oscillations: younger stars are on average more luminous, and therefore exhibit larger oscillation amplitudes that are easier to detect at large distances.
- While the inner Galaxy is dominated by stars with thick-disc-like chemistry (elevated [α/Fe] ratios) with a large number of old stars (but see below), almost no high-[α/Fe]-old stars are found in the outermost radial bin. This result is believed to be a manifestation of the shorter scale length of the thick disc with respect to the thin disc (Bensby et al. 2011; Bovy et al. 2012; Cheng et al. 2012).
- A greater number of young-[alpha/Fe]-rich stars is seen in the two innermost bins (Chiappini et al. 2015). The existence of these stars strongly disagrees with the predictions of chemical-evolution models and is also impossible to explain by radial migration. For a discussion of the origin of these stars see Chiappini et al. (2015); Jofre et al. (2016); Yong et al. (2016).
- Surprisingly, the thin-disc chemical-evolution model adopted here provides a fairly good description of the main abundance ratio trends shown in the figures (especially in the outer parts of the Galaxy), both in terms of the abundance trends and in terms of expected dominant age. In particular, when guiding radii are used instead of the current Galactocentric distances, the agreement with the models is improved (see the 5-6 kpc and 6-7 kpc $R_{\rm guide}$ bins). However, there is a clear disagreement above solar metallicity in all panels. Although part of the discrepancy might be attributed to uncertainties related to stellar yields[16], it is tempting to

[16] Currently there are several uncertainties affecting the stellar yields of the different α-elements. For core-collapse supernovae, few models were computed for metallicities above solar; moreover, most supernovae models tend to underestimate the ^{24}Mg yields. Other elements, such as Ca, Si, and S, can have some contribution of SNIa as well. Even more importantly, the Galactic SNIa rate is still very uncertain (e.g. Matteucci & Romano 1999; Mannucci et al. 2006). Although the thin disc model presented here reproduces the present SNIa rate at the solar vicinity well, overestimated SNIa rates at earlier times and/or at other Galactocentric distances cannot be excluded. In the inside-out thin-disc formation model, one of the assumptions is that the star-formation efficiency increases towards the inner regions. This feature was mainly constrained by the abundance gradients at present time. However, if the SNIa rate is overestimated, one would require lower star-formation efficiencies to reach the same final metallicity. The abundance ratios at the different Galactocentric distances can further constrain these mod-

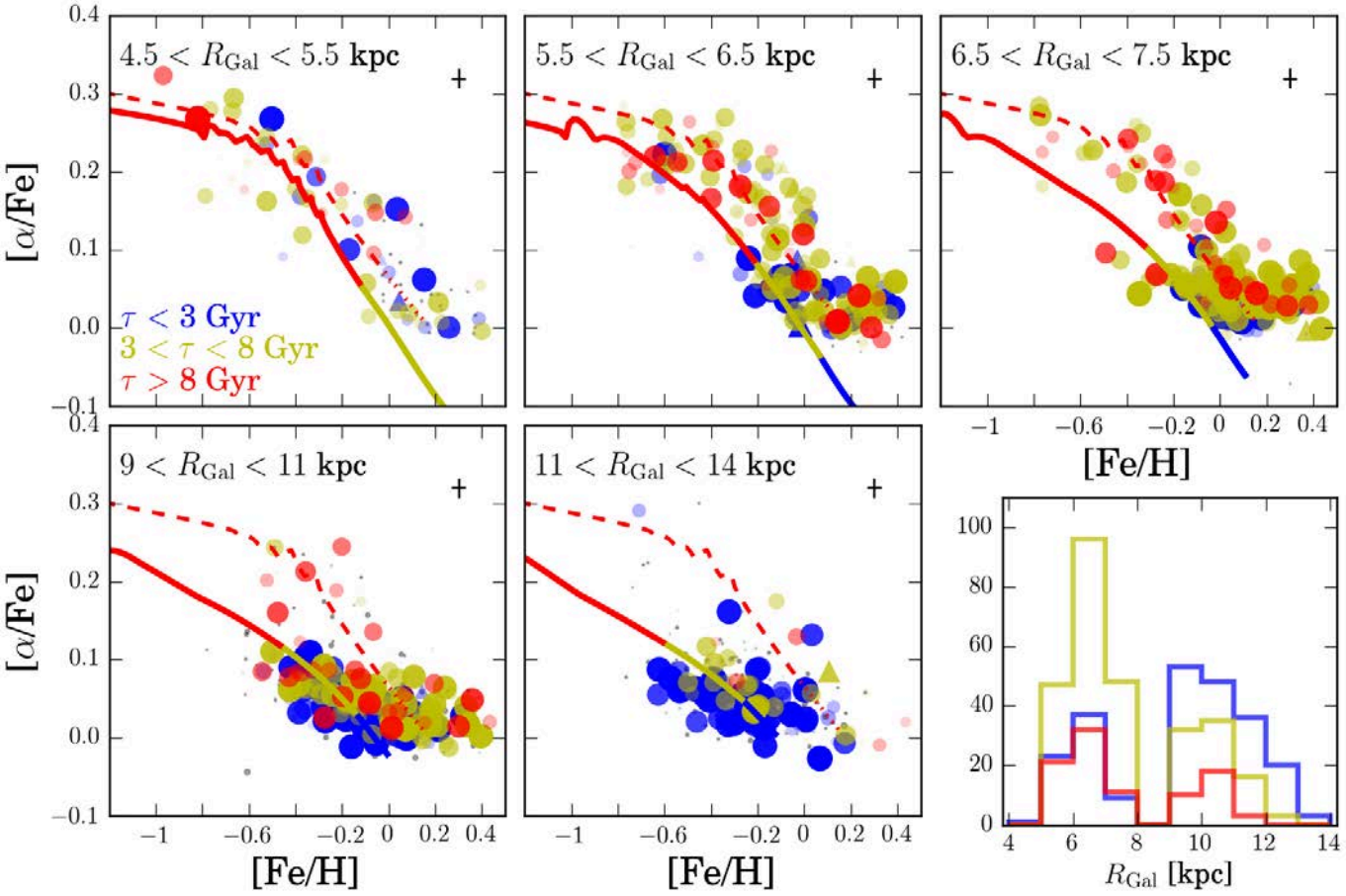

Figure 3.14. The [α/Fe]-vs.-[Fe/H] chemical plane for five different bins in Galactocentric distance R_{Gal}. The colour represents our stellar age estimates, as indicated in the first panel: blue indicates stars younger than 3 Gyr, red stars older than 8 Gyr, and yellow intermediate ages. The point size and transparency of each data point encode the age uncertainty, i.e., a smaller and more transparent symbol corresponds to a lower probability to belong to the particular age bin. The few triangles correspond to stars whose measured radial velocity scatter is greater than 800 m/s and which could be binaries. In the background of each panel, stars from the APOGEE DR12 main sample observed in similar Galactic regions are plotted as grey dots for comparison. The error bar in the upper right corner of each panel represents the typical (internal) uncertainty of the chemical abundances. The solid lines correspond to the thin-disc chemical-evolution model of Chiappini (2009) for different Galactocentric distances, and the dashed lines correspond to a thick-disc model at R_{Gal} = 6 kpc. The lower right panel displays the overall R_{Gal} distributions of our sample split into the three age bins.

interpret this result as a sign of radial migration, at least for the old and intermediate-age stars (see MCM13, Fig. 8).

– Interestingly, in each bin, stars with high [α/Fe] abundances, regardless of their age, show a tendency to lie close to the thick-disc curve. As the same thick-disc curve is shown in all panels, this result agrees with the relative constancy of the "high-[α/Fe] sequence" discussed in Nidever et al. (2014). It is clear from this comparison that these stars can either be explained as being part of the thick disc, or as migrators coming from the inner radii (the thick disc curve is similar to the that for R_{Gal} = 4 kpc, except for its higher star-formation efficiency, which leads to the appearance of [α/Fe]-enhanced stars at higher metallicities). These oldest metal-rich, [α/Fe]-enhanced stars also resemble Galactic bulge stars in chemistry, so that radial migration from the bulge cannot be excluded as one possible interpretation.

– SMR stars are present even in the two outermost R_{Gal}/R_{guide} bins studied here (Anders et al. 2014); they comprise stars of all ages, in agreement with what was found by Trevisan et al. (2011) for solar-vicinity SMR stars. As explained previously, the end of the thin-disc curves is constrained by the present abundance gradient, which amounts to around −0.07dex/kpc for Fe (e.g. Anders et al. (2014)) and references therein). While the excess of SMR stars is not a problem in the inner bins (where the thin-disc curve extends to higher metallicities), it demonstrates a clear discrepancy for the two outermost bins analysed here. From the comparison with the models it is clear that the chemistry of these SMR stars is compatible either with the thick-disc curve or with the thin disc at R_{Gal} = 4 kpc. We note, however, that the R_{Gal} = 4 kpc curve predicts intermediate ages for stars above metallicities ∼ −0.02, while there are clearly older SMR stars in all panels. This is an indication that these stars indeed migrated from R_{Gal} < 4 kpc. Unfortunately, the form of the present-day abundance gradients in the innermost regions of the Galactic disc is still unknown (see Stasińska et al. 2012 for a discussion): a constraint that would shed more light on the origin of these stars.

els, because a larger star-formation efficiency would also predict larger [α/Fe] ratios at larger metallicities. It is thus possible that, by exploring the parameter space of stellar yields and SNIa rates, one can obtain a better fit to the data shown in the Figure, but this is beyond the scope of the present work.

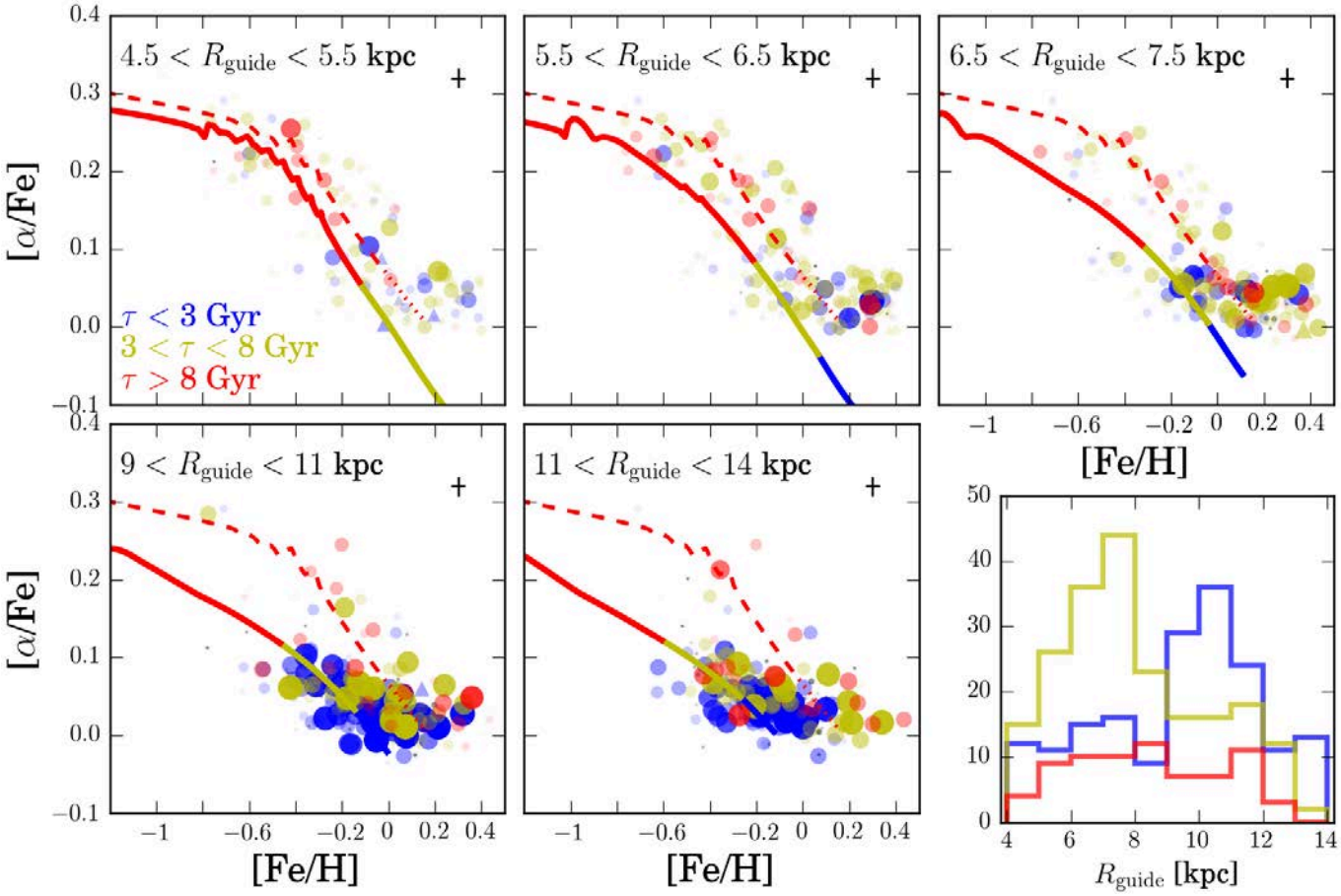

Figure 3.15. Same format as Fig.3.14, only that the data are now binned in guiding-center radius, R_{guide}, rather than Galactocentric distance, to mitigate the effect of stellar mixing by "blurring". Again, the colour-code represents the age, while the size and transparency now encode the uncertainty in stellar age and guiding-center radius. (If a star has a highly uncertain guiding radius – i.e. an R_{guide} PDF which extends over multiple R bins – it will appear as a faint dot in multiple panels of this Figure.)

3.4.2. Comparison with a chemo-dynamical model

As first shown in Minchev, Chiappini, & Martig (2013), when radial migration is taken into account in a chemodynamical model of the thin disc, the oldest stars in the simulation have properties similar to what we commonly identify as the thick disc (this result was later confirmed by Kubryk et al. 2015a[17]). Interestingly, although it is able to reproduce several properties of "the thick disc", our chemodynamical model does not predict a discontinuity in the [α/Fe] vs. [Fe/H] diagram[18]. The reason for this discrepancy might be the existence of a discrete thick-disc component (Chiappini et al. 1997; Chiappini 2009), with its specific chemical pattern, which was not included in the MCM model. To solve this problem, a proper comparison between the MCM model predictions and observations is required. Because astronomical surveys are often affected by non-trivial selection effects, the comparison of survey catalogues with a Galactic model is much easier when a mock observation of the model is created (e.g. Binney & Sanders 2015).

In this section we describe our selection of a CoRoGEE-like sample from an N-body simulation, using the example of the chemodynamical N-body model analysed in Minchev, Chiappini, & Martig (2013, 2014a, MCM). We have chosen two different paths to simulate the observations: 1. A "simple" mock in which we choose N-body particles such that we match the observed spatial distribution of our program stars (and simulating the red-giant age bias with a simple prior), and 2. A more sophisticated mock that used a modified version of the Galaxia synthetic stellar population code (Sharma et al. 2011; Piffl 2013), the new PanSTARRS-1 3D extinction map of Green et al. (2015), and a representation of the CoRoGEE selection function. The procedures leading to the two versions of mock observations are sketched in Fig. 4.2 and are explained in Anders et al. (2016b). As we show below, these two versions of an MCM-CoRoGEE mock sample each have their advantages and drawbacks. In summary, while the simple mock by construction matches the space distribution of the observed sample perfectly, the sophisticated mock recovers the observed age distribution very well (see Anders et al. 2016b).

Figure 3.17 shows the main result of our mock samples: each row contains the (observed or modelled) [α/Fe] vs. [Fe/H] diagrams in the same R_{Gal} and age bins as in Figs. 3.14 and 3.15, to

[17] In this case, differently from Minchev et al. (2013), the authors followed a suggestion made in Brunetti et al. (2011):the radial migration process was approximated by a diffusion process with diffusion coefficients that varied in time and position. These were extracted from an N-body+SPH simulation of a galaxy very different from the Milky Way and implemented in a standard chemical-evolution model. The coefficients were then re-scaled to fit the local G-dwarf metallicity distribution.

[18] However, when selecting particles using the same kinematical criteria as in Bensby et al. (2003), it was possible to recover the two sequences in the [α/Fe] vs. [Fe/H] diagram.

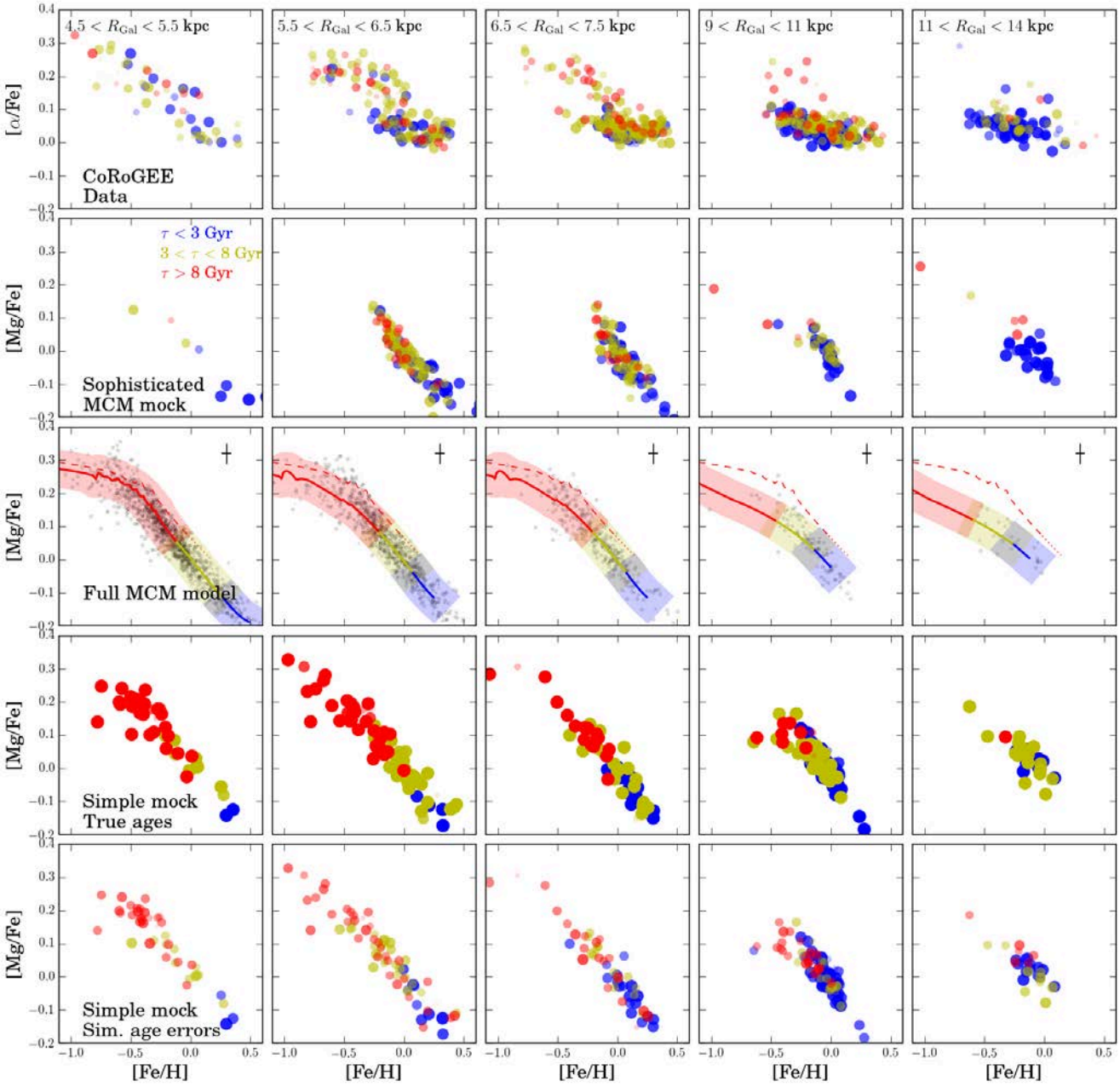

Figure 3.17. [α/Fe]-vs.-[Fe/H] diagram for five different bins in Galactocentric distance R_{Gal}. Top row: The CoRoGEE sample. The colours represent our stellar age estimates: blue indicates stars younger than 3 Gyr, red stands for stars older than 8 Gyr, and yellow for intermediate ages. The point size and transparency of each data point encode the age uncertainty, i.e., a smaller and more transparent symbol corresponds to a smaller probability of belonging to the particular age bin. Second row: The sophisticated MCM mock sample. Middle row: All mock particles from the MCM N-body simulation, shown as grey dots. The solid lines represent the predictions of the underlying thin disc chemical-evolution model by Chiappini (2009) for stars born in the corresponding Galactocentric distance bin. The colour-code represents the age; the shaded regions along the lines correspond to a 2σ-confidence band, given the typical uncertainties in [Fe/H] and [α/Fe]. The dashed lines show the chemical tracks of Chiappini (2009) for the thick disc. The error bar in the upper right of each panel represents the typical (internal) uncertainty of the chemical abundances. Fourth row: The simple MCM mock sample, without simulated age uncertainties. Last row: The simple MCM mock sample, with age uncertainties.

facilitate a qualitative comparison with the data. We discuss the main results from Fig. 3.17 below.

1. *Sophisticated mock:* Anders et al. (2016b) have shown that the observed age distributions in the two CoRoGEE fields are very well recovered by the sophisticated mock. This is also seen in the second row of Fig. 3.17: the age mix of CoRoGEE stars is better reproduced in the sophisticated mock than in the simple mock. However, the sophisticated mock obviously misses the distant and metal-poor ([Fe/H]< −0.5) stars that are present in the data. This indicates that our

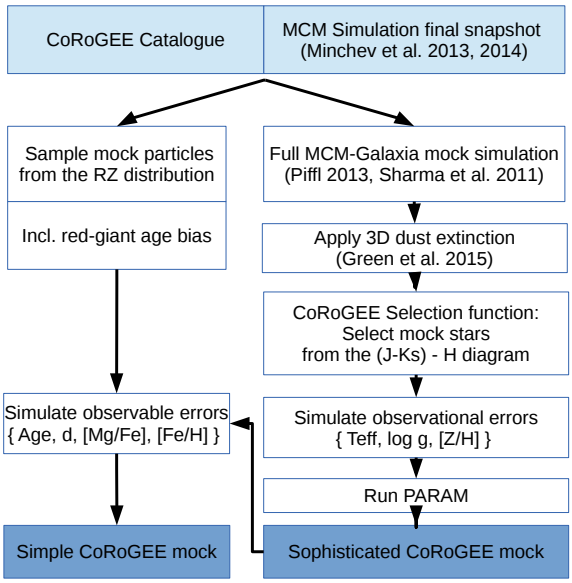

Figure 3.16. Scheme illustrating how the CoRoGEE mock observations were obtained from the MCM model. The steps are explained in more detail in Anders et al. (2016b).

forward modelling of the sample selection is imperfect for various reasons: 1. a mismatch between the MCM-Galaxia model's starcounts with 2MASS in the CoRoT fields (Anders et al. 2016b), 2. a stronger extinction in the PanSTARRS extinction maps (Schlafly et al. 2014; Green et al. 2015) compared to the CoRoGEE data (see App. 3.A.3), 3. a more complex selection function than $S \propto S(\text{field}, H, J-K_s)$ (see Sect. 3.2.2), and 4. stochasticity due to the small sample size. We therefore refrain from interpreting the number counts in the sophisticated CoRoGEE mock, as we did not recover the overall distributions in the abundance diagrams.

2. *Simple mock with true ages:* By construction (selection of mock particles from the $R_{\rm Gal} - Z_{\rm Gal}$ plane), the simple mock matches the space distribution of the CoRoGEE sample perfectly. The simple mock also matches the observed metallicity distributions much better than the sophisticated mock. The plot also demonstrates that despite the quite strong radial mixing in the MCM model, there is little age mixing in each of the [α/Fe] vs. [Fe/H] diagrams. The age−[α/Fe] relation of the input models is largely preserved, while the data show a significantly more complex situation. In concordance with the data, the density of the old [α/Fe]-enhanced thin disc (i.e. the "thick disc" in MCM) decreases towards outer regions. However, the data suggest that the [α/Fe]-enhanced component has a much broader age distribution than in the model. This result depends little on the functional form of the simulated age bias.
3. *Effect of adding age errors:* When we add realistic age errors using the PARAM results of the sophisticated mock (see Fig. 4.5 and Anders et al. 2016b), part of the age mixing in the [α/Fe] vs. [Fe/H] diagram can be explained by our measurement procedure. This is insufficient to explain the observed younger ages of many [α/Fe]-enhanced stars, however. In particular, our method-intrinsic age errors cannot explain the presence of young [α/Fe]-rich stars, while possible close-binary stellar evolution cannot explain the different abundance of these stars in the two CoRoT fields (see also Chiappini et al. 2015; Martig et al. 2015; Yong et al. 2016; Jofre et al. 2016).
4. *SMR stars in the outer disc:* As discussed in the previous section, the metal-rich stars in the two outer bins cannot be explained with the present chemical models. Since the MCM mocks also do not produce this metal-rich intermediate-age population in the outer parts of the disc, either a much stronger radial migration than present in MCM is at work, or the thick disc star-formation history extends to greater ages (i.e., for longer than 2 Gyr). Another explanation might also be bulge stars ending up in the outer disc (Barbuy & Grenon 1990); these were not included in the MCM simulation.

Our simple mock outperforms the sophisticated mock in almost all respects (except for the match with the overall age distributions). It highlights two important features in the data that are not reproduced by the MCM model: the broad observed age distribution of the [α/Fe]-enhanced sequence in the inner Galactic disc, and that more intermediate-age SMR stars are located in the outer disc than predicted.

3.5. Conclusions

In this first CoRoGEE paper, we have demonstrated the usefulness of combining asteroseismic and spectroscopic data in the framework of Galactic archaeology. Using global asteroseismic parameters $\Delta\nu$ and $\nu_{\rm max}$ determined from CoRoT light curves, together with atmospheric stellar parameters measured by SDSS-III/APOGEE and broad-band photometry, we have calculated masses, radii, ages, distances and extinctions for more than 600 red giants distributed over a large Galactocentric distance interval. In this section, we briefly summarise the main results of our work.

The relative statistical uncertainties in our primary derived quantities from the Bayesian model fitting performed by the PARAM code amount to $\lesssim$ 2% in distance, 0.08 mag in A_V, $\sim$ 4% in radius, $\sim$ 9% in mass and $\sim$ 25% in age. In agreement with previous studies, we find that the individual age probability distributions can be complex in shape, suggesting that the age information needs to be used with some care, for example, by using wide age bins. Equally importantly, systematic uncertainties in the fundamental seismic parameters as well as in the comparison with stellar models may affect the absolute scale of our derived ages to some degree.

We provide a number of checks (surface gravity comparison, grid-based vs. scaling relation results, extinction maps) that demonstrate the overall reliability of our analysis for the use with statistical samples in Appendix 3.A. The CoRoGEE sample enabled us to study for the first time the [α/Fe]-[Fe/H]-age relation beyond the solar vicinity. We separated the sample into large bins of age, guiding-centre radius, and Galactocentric distance, to study stellar populations in the [α/Fe] vs. [Fe/H] diagram. Even with this small sample and the sizeable systematic and statistical uncertainties attached to our age estimates, we can place reliable constraints on the chemical evolution of the Milky Way stellar disc:

1. In accordance with previous work, we find strong signatures of inside-out formation of the Galactic disc.
2. When we compared our results to a multi-zone chemical-evolution model that treats the thin and thick disc separately, we found that the thin-disc models generally provide a good description of the main abundance-age trends, with the exception of the flat [α/Fe] trend at high metallicity. The results

improved when the stellar guiding-centre radius was used instead of the current Galactocentric distance.
3. In agreement with previous studies, we find that these pure chemical-evolution models fail to reproduce several important features seen in the data, such as the existence of SMR stars ([Fe/H]> 0.2) in the solar neighbourhood and beyond, the exact shape of the [α/Fe]-[Fe/H] distribution (in particular in the inner regions of the disc), and the existence of [α/Fe]-rich young stars.
4. When we compared our results with the predictions of the chemo-dynamical model of Minchev, Chiappini, & Martig (2013, 2014b), we found that the radial mixing in the model is not efficient enough to account for the number of SMR stars in the outer disc. Either a stronger radial mixing or the inclusion of a thick disc/bulge that formed stars for more than 3 Gyr and produced SMR stars may resolve this discrepancy. In addition, the age distribution of the [α/Fe]-enhanced sequence in the CoRoGEE inner-disc field is much broader than expected from a combination of radial mixing and observational errors. Evolved blue stragglers may account for part of this population (Jofre et al. 2016; Yong et al. 2016), but do not offer an explanation for the different number counts in the inner and outer disc (Chiappini et al. 2015). Again, a thick-disc/bulge component with a more complex star-formation history than predicted by standard models might explain this observation.

In summary, we have demonstrated that the CoRoGEE sample is well-suited for the purpose of reconstructing the chemical enrichment history of the Milky Way disc. This first study will be followed by an investigation that focusses on exploring the detailed multi-element abundance patterns provided by APOGEE. It will be based on an analysis of newly reduced CoRoT light curves, resulting in more accurate seismic parameters, and will also include data from the CoRoT long run in the LRa02 field.

From the mid-term perspective, the CoRoGEE dataset can be viewed as a pathfinder and complementary dataset to the massive surveys that the *Kepler*-2 mission (K2; Howell et al. 2014) is currently conducting. The K2 Galactic Archaeology Program (Stello et al. 2015) will deliver seismic parameters for thousands of red giants in ten fields along the ecliptic plane, and, combined with the legacy of CoRoT as well as the original *Kepler* mission, will enable further improvements in the coverage of the Galactic disc with solar-like oscillating red giants.

Bibliography

Abadi, M. G., Navarro, J. F., Steinmetz, M., & Eke, V. R. 2003, ApJ, 597, 21
Alam, S., Albareti, F. D., Allende Prieto, C., Anders, F., & Anderson, S. F., e. 2015, ApJS, 219, 12
Allende Prieto, C. & Lambert, D. L. 1999, A&A, 352, 555
Anders, F., Chiappini, C., Minchev, I., et al. 2016a, A&A, submitted, arXiv:1608.04951
Anders, F., Chiappini, C., Rodrigues, T. S., et al. 2016b, Astronomische Nachrichten, in press, arXiv:1604.07771
Anders, F., Chiappini, C., Santiago, B. X., et al. 2014, A&A, 564, A115
Baglin, A., Auvergne, M., Barge, P., et al. 2006, in ESA Special Publication, ed. M. Fridlund, A. Baglin, J. Lochard, & L. Conroy, Vol. 1306, 33
Barbuy, B. & Grenon, M. 1990, in European Southern Observatory Conference and Workshop Proceedings, Vol. 35, European Southern Observatory Conference and Workshop Proceedings, ed. B. J. Jarvis & D. M. Terndrup, 83–86
Batalha, N. M., Borucki, W. J., Bryson, S. T., et al. 2011, ApJ, 729, 27
Bedding, T. R., Mosser, B., Huber, D., et al. 2011, Nature, 471, 608
Belkacem, K., Goupil, M. J., Dupret, M. A., et al. 2011, A&A, 530, A142
Belkacem, K., Samadi, R., Mosser, B., Goupil, M.-J., & Ludwig, H.-G. 2013, in Astronomical Society of the Pacific Conference Series, Vol. 479, Progress in Physics of the Sun and Stars: A New Era in Helio- and Asteroseismology, ed. H. Shibahashi & A. E. Lynas-Gray, 61
Bensby, T., Alves-Brito, A., Oey, M. S., Yong, D., & Meléndez, J. 2011, ApJ, 735, L46
Bensby, T., Feltzing, S., & Lundström, I. 2003, A&A, 410, 527
Binney, J. & Sanders, J. L. 2015, Astronomische Nachrichten, in press, arXiv:1511.08480
Bovy, J., Nidever, D. L., Rix, H.-W., et al. 2014, ApJ, 790, 127
Bovy, J., Rix, H.-W., Liu, C., et al. 2012, ApJ, 753, 148
Bressan, A., Marigo, P., Girardi, L., et al. 2012, MNRAS, 427, 127
Brook, C. B., Stinson, G. S., Gibson, B. K., et al. 2012, MNRAS, 426, 690
Broomhall, A.-M., Miglio, A., Montalbán, J., et al. 2014, MNRAS, 440, 1828
Brown, T. M., Gilliland, R. L., Noyes, R. W., & Ramsey, L. W. 1991, ApJ, 368, 599
Brunetti, M., Chiappini, C., & Pfenniger, D. 2011, A&A, 534, A75
Cardelli, J. A., Clayton, G. C., & Mathis, J. S. 1989, ApJ, 345, 245
Carraro, G., Ng, Y. K., & Portinari, L. 1998, MNRAS, 296, 1045
Casagrande, L., Schönrich, R., Asplund, M., et al. 2011, A&A, 530, A138
Casagrande, L., Silva Aguirre, V., Schlesinger, K. J., et al. 2016, MNRAS, 455, 987
Casagrande, L., Silva Aguirre, V., Stello, D., et al. 2014, ApJ, 787, 110
Catelan, M. 2009, in IAU Symposium, Vol. 258, IAU Symposium, ed. E. E. Mamajek, D. R. Soderblom, & R. F. G. Wyse, 209–220
Chaplin, W. J., Kjeldsen, H., Christensen-Dalsgaard, J., et al. 2011, Science, 332, 213
Chaplin, W. J. & Miglio, A. 2013, ARA&A, 51, 353
Chen, L., Hou, J. L., & Wang, J. J. 2003, AJ, 125, 1397
Cheng, J. Y., Rockosi, C. M., Morrison, H. L., et al. 2012, ApJ, 752, 51
Chiappini, C. 2009, in IAU Symposium, Vol. 254, IAU Symposium, ed. J. Andersen, B. Nordström, & J. Bland-Hawthorn, 191–196
Chiappini, C., Anders, F., Rodrigues, T. S., et al. 2015, A&A, 576, L12
Chiappini, C., Matteucci, F., & Gratton, R. 1997, ApJ, 477, 765
Chiappini, C., Matteucci, F., & Romano, D. 2001, ApJ, 554, 1044
Christensen-Dalsgaard, J. 1988, in IAU Symposium, Vol. 123, Advances in Helio- and Asteroseismology, ed. J. Christensen-Dalsgaard & S. Frandsen, 295
Christensen-Dalsgaard, J. 1993, in Astronomical Society of the Pacific Conference Series, Vol. 42, GONG 1992. Seismic Investigation of the Sun and Stars, ed. T. M. Brown, 347
Cutri, R. M., Skrutskie, M. F., van Dyk, S., et al. 2003, 2MASS All Sky Catalog of point sources.
Cutri, R. M., Wright, E. L., Conrow, T., et al. 2013, Explanatory Supplement to the AllWISE Data Release Products, Tech. rep.
da Silva, L., Girardi, L., Pasquini, L., et al. 2006, A&A, 458, 609
Damiani, C., Meunier, J.-C., Moutou, C., et al. 2016, A&A, accepted, arXiv:1608.07107
Davenport, J. R. A., Ivezić, Ž., Becker, A. C., et al. 2014, MNRAS, 440, 3430
Deheuvels, S. 2015, in Cambridge Workshop on Cool Stars, Stellar Systems, and the Sun, Vol. 18, 18th Cambridge Workshop on Cool Stars, Stellar Systems, and the Sun, ed. G. T. van Belle & H. C. Harris, 489–494
Edvardsson, B., Andersen, J., Gustafsson, B., et al. 1993, A&A, 275, 101
Eisenstein, D. J., Weinberg, D. H., Agol, E., et al. 2011, AJ, 142, 72
Freeman, K. & Bland-Hawthorn, J. 2002, ARA&A, 40, 487
Fuhrmann, K. 1998, A&A, 338, 161
Gilmore, G. 1999, Baltic Astronomy, 8, 203
Gilmore, G. 2012, in Astronomical Society of the Pacific Conference Series, Vol. 458, Galactic Archaeology: Near-Field Cosmology and the Formation of the Milky Way, ed. W. Aoki, M. Ishigaki, T. Suda, T. Tsujimoto, & N. Arimoto, 147
Girardi, L., Dalcanton, J., Williams, B., et al. 2008, PASP, 120, 583
Gough, D. O. 2001, in Astronomical Society of the Pacific Conference Series, Vol. 245, Astrophysical Ages and Times Scales, ed. T. von Hippel, C. Simpson, & N. Manset, 31
Gratton, R., Carretta, E., Matteucci, F., & Sneden, C. 1996, in Astronomical Society of the Pacific Conference Series, Vol. 92, Formation of the Galactic Halo...Inside and Out, ed. H. L. Morrison & A. Sarajedini, 307
Green, G. M., Schlafly, E. F., Finkbeiner, D. P., et al. 2015, ApJ, 810, 25
Grenon, M. 1972, in IAU Colloq. 17: Age des Etoiles, ed. G. Cayrel de Strobel & A. M. Delplace, 55
Grenon, M. 1989, Ap&SS, 156, 29
Grenon, M. 1999, Ap&SS, 265, 331
Guedes, J., Callegari, S., Madau, P., & Mayer, L. 2011, ApJ, 742, 76
Gunn, J. E., Siegmund, W. A., Mannery, E. J., et al. 2006, AJ, 131, 2332
Hayden, M. R., Bovy, J., Holtzman, J. A., et al. 2015, ApJ, 808, 132
Hayden, M. R., Holtzman, J. A., Bovy, J., et al. 2014, AJ, 147, 116
Hekker, S., Kallinger, T., Baudin, F., et al. 2009, A&A, 506, 465
Henden, A. & Munari, U. 2014, Contributions of the Astronomical Observatory Skalnate Pleso, 43, 518

Hill, V., Plez, B., Cayrel, R., et al. 2002, A&A, 387, 560
Holmberg, J., Nordström, B., & Andersen, J. 2007, A&A, 475, 519
Holtzman, J. A., Shetrone, M., Johnson, J. A., et al. 2015, AJ, 150, 148
Hou, J. L., Prantzos, N., & Boissier, S. 2000, A&A, 362, 921
Howell, S. B., Sobeck, C., Haas, M., et al. 2014, PASP, 126, 398
Ivezić, Ż., Connolly, A., VanderPlas, J., & Gray, A. 2013, Statistics, Data Mining, and Machine Learning in Astronomy
Jofre, P., Masseron, T., Izzard, R. G., et al. 2016, MNRAS, submitted, arXiv:1603.08992
Jørgensen, B. R. & Lindegren, L. 2005, A&A, 436, 127
Kaiser, N., Burgett, W., Chambers, K., et al. 2010, in Society of Photo-Optical Instrumentation Engineers (SPIE) Conference Series, Vol. 7733, Society of Photo-Optical Instrumentation Engineers (SPIE) Conference Series, 0
Kjeldsen, H. & Bedding, T. R. 1995, A&A, 293, 87
Kordopatis, G., Binney, J., Gilmore, G., et al. 2015, MNRAS, 447, 3526
Kotoneva, E., Flynn, C., Chiappini, C., & Matteucci, F. 2002, MNRAS, 336, 879
Kubryk, M., Prantzos, N., & Athanassoula, E. 2015a, A&A, 580, A126
Kubryk, M., Prantzos, N., & Athanassoula, E. 2015b, A&A, 580, A127
Lebreton, Y. & Goupil, M. J. 2014, A&A, 569, A21
Lebreton, Y., Goupil, M. J., & Montalbán, J. 2014, in EAS Publications Series, Vol. 65, EAS Publications Series, 99–176
Majewski, S. R., Schiavon, R. P., Frinchaboy, P. M., et al. 2015, ApJS, submitted, arXiv:1509.05420
Majewski, S. R., Zasowski, G., & Nidever, D. L. 2011, ApJ, 739, 25
Mannucci, F., Della Valle, M., & Panagia, N. 2006, MNRAS, 370, 773
Marigo, P., Girardi, L., Bressan, A., et al. 2008, A&A, 482, 883
Martig, M., Rix, H.-W., Aguirre, V. S., et al. 2015, MNRAS, 451, 2230
Mathur, S., Metcalfe, T. S., Woitaszek, M., et al. 2012, ApJ, 749, 152
Matteucci, F., ed. 2001, Astrophysics and Space Science Library, Vol. 253, The chemical evolution of the Galaxy
Matteucci, F. & Romano, D. 1999, Ap&SS, 265, 311
Metcalfe, T. S., Creevey, O. L., Doğan, G., et al. 2014, ApJS, 214, 27
Metcalfe, T. S., Monteiro, M. J. P. F. G., Thompson, M. J., et al. 2010, ApJ, 723, 1583
Meunier, J.-C., Deleuil, M., Moutou, C., et al. 2007, in Astronomical Society of the Pacific Conference Series, Vol. 376, Astronomical Data Analysis Software and Systems XVI, ed. R. A. Shaw, F. Hill, & D. J. Bell, 339
Michel, E., Baglin, A., Weiss, W. W., et al. 2008, Communications in Asteroseismology, 156, 73
Miglio, A. 2012, Asteroseismology of Red Giants as a Tool for Studying Stellar Populations: First Steps, ed. A. Miglio, J. Montalbán, & A. Noels, 11
Miglio, A., Chaplin, W. J., Brogaard, K., et al. 2016, MNRAS, 461, 760
Miglio, A., Chiappini, C., Morel, T., et al. 2013a, in European Physical Journal Web of Conferences, Vol. 43, 3004
Miglio, A., Chiappini, C., Morel, T., et al. 2013b, MNRAS, 429, 423
Miglio, A., Eggenberger, P., Girardi, L., & Montalbán, J. 2015, Astrophysics and Space Science Proceedings, 39
Miglio, A., Montalbán, J., Baudin, F., et al. 2009, A&A, 503, L21
Minchev, I., Chiappini, C., & Martig, M. 2013, A&A, 558, A9
Minchev, I., Chiappini, C., & Martig, M. 2014a, A&A, 572, A92
Minchev, I., Chiappini, C., & Martig, M. 2014b, in IAU Symposium, Vol. 298, IAU Symposium, ed. S. Feltzing, G. Zhao, N. A. Walton, & P. Whitelock, 130–141
Monet, D. G., Levine, S. E., Canzian, B., et al. 2003, AJ, 125, 984
Montalbán, J., Miglio, A., Noels, A., et al. 2013, ApJ, 766, 118
Montalbán, J. & Noels, A. 2013, in European Physical Journal Web of Conferences, Vol. 43, European Physical Journal Web of Conferences, 3002
Mosser, B. & Appourchaux, T. 2009, A&A, 508, 877
Mosser, B., Barban, C., Montalbán, J., et al. 2011, A&A, 532, A86
Mosser, B., Belkacem, K., Goupil, M.-J., et al. 2010, A&A, 517, A22
Ng, Y. K. & Bertelli, G. 1998, A&A, 329, 943
Nidever, D. L., Bovy, J., Bird, J. C., et al. 2014, ApJ, 796, 38
Nidever, D. L., Holtzman, J. A., Allende Prieto, C., et al. 2015, AJ, 150, 173
Nishiyama, S., Tamura, M., Hatano, H., et al. 2009, ApJ, 696, 1407
Noels, A. & Bragaglia, A. 2015, Astrophysics and Space Science Proceedings, 39, 167
Nordström, B., Mayor, M., Andersen, J., et al. 2004, A&A, 418, 989
O'Donnell, J. E. 1994, ApJ, 422, 158
Pagel, B. E. J. 1997, Nucleosynthesis and Chemical Evolution of Galaxies
Peek, J. E. G. & Graves, G. J. 2010, ApJ, 719, 415
Perryman, M. A. C., de Boer, K. S., Gilmore, G., et al. 2001, A&A, 369, 339
Piffl, T. 2013, PhD thesis, Universität Potsdam
Pinsonneault, M. H., Elsworth, Y., Epstein, C., et al. 2014, ApJS, 215, 19
Ramírez, I., Allende Prieto, C., & Lambert, D. L. 2007, A&A, 465, 271
Rauer, H., Catala, C., Aerts, C., et al. 2014, Experimental Astronomy, 38, 249
Reimers, D. 1975, Memoires of the Societe Royale des Sciences de Liege, 8, 369
Roca-Fàbrega, S., Valenzuela, O., Colín, P., et al. 2016, ApJ, 824, 94
Rocha-Pinto, H. J. & Maciel, W. J. 1996, MNRAS, 279, 447
Rodrigues, T. S., Girardi, L., Miglio, A., et al. 2014, MNRAS, 445, 2758
Salaris, M., Chieffi, A., & Straniero, O. 1993, ApJ, 414, 580
Santiago, B. X., Brauer, D. E., Anders, F., et al. 2016, A&A, 585, A42
Scannapieco, C., Creasey, P., Nuza, S. E., et al. 2015, A&A, 577, A3
Scannapieco, C., Wadepuhl, M., Parry, O. H., et al. 2012, MNRAS, 423, 1726
Schlafly, E. F. & Finkbeiner, D. P. 2011, ApJ, 737, 103
Schlafly, E. F., Green, G., Finkbeiner, D. P., et al. 2014, ApJ, 789, 15
Schlegel, D. J., Finkbeiner, D. P., & Davis, M. 1998, ApJ, 500, 525
Schönrich, R. & Binney, J. 2009, MNRAS, 396, 203
Schultheis, M., Zasowski, G., Allende Prieto, C., et al. 2014, AJ, 148, 24
Sharma, S., Bland-Hawthorn, J., Johnston, K. V., & Binney, J. 2011, ApJ, 730, 3
Silva Aguirre, V., Basu, S., Brandão, I. M., et al. 2013, ApJ, 769, 141
Soderblom, D. 2013, in Asteroseismology of Stellar Populations in the Milky Way
Soderblom, D. R. 2010, ARA&A, 48, 581
Soubiran, C. 1999, Ap&SS, 265, 353
Stasińska, G., Prantzos, N., Meynet, G., et al., eds. 2012, EAS Publications Series, Vol. 54, Oxygen in the Universe
Steinmetz, M., Zwitter, T., Siebert, A., et al. 2006, AJ, 132, 1645
Stello, D., Huber, D., Sharma, S., et al. 2015, ApJ, 809, L3
Stinson, G. S., Bailin, J., Couchman, H., et al. 2010, MNRAS, 408, 812
Takeda, G., Ford, E. B., Sills, A., et al. 2007, ApJS, 168, 297
Tassoul, M. 1980, ApJS, 43, 469
Trevisan, M., Barbuy, B., Eriksson, K., et al. 2011, A&A, 535, A42
Turon, C., Primas, F., Binney, J., et al. 2008, ESA-ESO Working Group on Galactic Populations, Chemistry and Dynamics, Tech. rep.
Twarog, B. A. 1980, ApJ, 242, 242
Ulrich, R. K. 1986, ApJ, 306, L37
White, T. R., Bedding, T. R., Stello, D., et al. 2011, ApJ, 743, 161
Wilson, J. C., Hearty, F., Skrutskie, M. F., et al. 2010, in Society of Photo-Optical Instrumentation Engineers (SPIE) Conference Series, Vol. 7735, Society of Photo-Optical Instrumentation Engineers (SPIE) Conference Series
Wilson, J. C., Hearty, F., Skrutskie, M. F., et al. 2012, in Society of Photo-Optical Instrumentation Engineers (SPIE) Conference Series, Vol. 8446, Society of Photo-Optical Instrumentation Engineers (SPIE) Conference Series
Yong, D., Casagrande, L., Venn, K. A., et al. 2016, MNRAS
Zacharias, N., Finch, C. T., Girard, T. M., et al. 2013, AJ, 145, 44
Zamora, O., García-Hernández, D. A., Allende Prieto, C., et al. 2015, AJ, 149, 181
Zasowski, G., Johnson, J. A., Frinchaboy, P. M., et al. 2013, AJ, 146, 81
Zhao, G., Zhao, Y.-H., Chu, Y.-Q., Jing, Y.-P., & Deng, L.-C. 2012, Research in Astronomy and Astrophysics, 12, 723
Zucker, D. B., de Silva, G., Freeman, K., Bland-Hawthorn, J., & Hermes Team. 2012, in Astronomical Society of the Pacific Conference Series, Vol. 458, Galactic Archaeology: Near-Field Cosmology and the Formation of the Milky Way, ed. W. Aoki, M. Ishigaki, T. Suda, T. Tsujimoto, & N. Arimoto, 421

[1] Leibniz-Institut für Astrophysik Potsdam (AIP), An der Sternwarte 16, 14482 Potsdam, Germany
e-mail: fanders@aip.de, cristina.chiappini@aip.de, thaise.rodrigues@oapd.inaf.it
[2] Laboratório Interinstitucional de e-Astronomia, - LIneA, Rua Gal. José Cristino 77, Rio de Janeiro, RJ - 20921-400, Brazil
[3] Osservatorio Astronomico di Padova – INAF, Vicolo dell'Osservatorio 5, I-35122 Padova, Italy
[4] Dipartimento di Fisica e Astronomia, Università di Padova, Vicolo dell'Osservatorio 2, I-35122 Padova, Italy
[5] School of Physics and Astronomy, University of Birmingham, Edgbaston, Birmingham, B15 2TT, United Kingdom
[6] LESIA, Observatoire de Paris, PSL Research University, CNRS, Université Pierre et Marie Curie, Université Denis Diderot, 92195 Meudon, France
[7] Institut d'Astrophysique et de Géophysique, Allée du 6 aout, 17 - Bat. B5c, B-4000 Liège 1 (Sart-Tilman), Belgium
[8] The Ohio State University, Department of Astronomy, 4055 McPherson Laboratory, 140 West 18th Ave., Columbus, OH 43210-1173, USA
[9] Observatoire de la Cote d'Azur, Laboratoire Lagrange, CNRS UMR 7923, B.P. 4229, 06304 Nice Cedex, France
[10] Institut d'Astrophysique Spatiale, CNRS, Université Paris XI, 91405 Orsay Cedex, France
[11] Max-Planck-Institut für Sonnensystemforschung, Justus-von-Liebig-Weg 3, 37077 Göttingen, Germany

[12] Stellar Astrophysics Centre, Department of Physics and Astronomy, Aarhus University, Ny Munkegade 120, 8000 Aarhus C, Denmark
[13] Institut für Astronomie, Universität Wien, Türkenschanzstr. 17, Wien, Austria
[14] Laboratoire AIM, CEA/DRF – CNRS - Univ. Paris Diderot – IRFU/SAp, Centre de Saclay, 91191 Gif-sur-Yvette Cedex, France
[15] Space Science Institute, 4750 Walnut Street Suite 205, Boulder CO 80301, USA
[16] Instituto de Física, Universidade Federal do Rio Grande do Sul, Caixa Postal 15051, Porto Alegre, RS - 91501-970, Brazil
[17] Max-Planck-Institut für Astronomie, Königstuhl 17, D-69117 Heidelberg, Germany
[18] Observatório Nacional, Rua Gal. José Cristino 77, Rio de Janeiro, RJ - 20921-400, Brazil
[19] Instituto de Astrofisica de Canarias, C/ Vía Láctea, s/n, 38205, La Laguna, Tenerife, Spain
[20] Departamento de Astrofísica, Universidad de La Laguna (ULL), E-38206 La Laguna, Tenerife, Spain
[21] Dept. of Physics and JINA-CEE: Joint Institute for Nuclear Astrophysics – Center for the Evolution of the Elements, Univ. of Notre Dame, Notre Dame, IN 46530 USA
[22] Department of Astronomy, Case Western Reserve University, Cleveland, OH 44106, USA
[23] New Mexico State University, Las Cruces, NM 88003, USA
[24] Department of Astronomy, University of Virginia, PO Box 400325, Charlottesville VA 22904-4325, USA
[25] ELTE Gothard Astrophysical Observatory, H-9704 Szombathely, Szent Imre herceg st. 112, Hungary
[26] Department of Astronomy, Indiana University, Bloomington, IN 47405, USA
[27] Dept. of Astronomy, University of Michigan, Ann Arbor, MI, 48104, USA
[28] Apache Point Observatory, PO Box 59, Sunspot, NM 88349, USA
[29] Astrophysics Research Institute, Liverpool John Moores University, IC2, Liverpool Science Park 146 Brownlow Hill Liverpool L3 5RF, UK
[30] Department of Astronomy and Astrophysics, The Pennsylvania State University, University Park, PA 16802
[31] Institute for Gravitation and the Cosmos, The Pennsylvania State University, University Park, PA 16802
[32] Mcdonald Observatory, University of Texas at Austin, HC75 Box 1337-MCD, Fort Davis, TX 79734, USA
[33] Vanderbilt University, Dept. of Physics & Astronomy, VU Station B 1807, Nashville, TN 37235, USA
[34] Johns Hopkins University, Dept. of Physics and Astronomy, 3701 San Martin Drive, Baltimore, MD 21210, USA

Acknowledgements. FA would like to dedicate this work to the memory of Prof. Angelo Cassatella†. He also thanks E. C. Herenz for stimulating discussions and critical thoughts that accompanied him during the past months. TSR acknowledges support from CNPq-Brazil. BM, FB, RP and RAG acknowledge financial support from the ANR program IDEE Interaction Des Étoiles et des Exoplanètes. JM acknowledges support from the ERC Consolidator Grant funding scheme (project STARKEY, G.A. No. 615604). LG and TSR acknowledge partial support from PRIN INAF 2014 - CRA 1.05.01.94.05. TM acknowledges financial support from Belspo for contract PRODEX GAIA-DPAC. AEGP, CAP, DAGH, and OZ acknowledge support provided by the Spanish Ministry of Economy and Competitiveness (MINECO) under grants AYA2014-56359-P, RYC-2013-14182, and AYA-2014-58082-P. TCB acknowledges partial support from grant PHY 14-30152 (Physics Frontier Center / JINA-CEE) awarded from the U.S. National Science Foundation. SaM acknowledges support from the NASA grant NNX12AE17G. SzM has been supported by the János Bolyai Research Scholarship of the Hungarian Academy of Sciences. The research leading to the presented results has received funding from the European Research Council under the European Community's Seventh Framework Programme (FP7/2007-2013)/ERC grant agreement No. 338251 (StellarAges).

The CoRoT space mission, launched on December 27 2006, was developed and operated by CNES, with the contribution of Austria, Belgium, Brazil, ESA (RSSD and Science Program), Germany and Spain. This research has made use of the ExoDat Database, operated at LAM-OAMP, Marseille, France, on behalf of the CoRoT/Exoplanet program.

Funding for the SDSS-III Brazilian Participation Group has been provided by the Ministério de Ciência e Tecnologia (MCT), Fundação Carlos Chagas Filho de Amparo à Pesquisa do Estado do Rio de Janeiro (FAPERJ), Conselho Nacional de Desenvolvimento Científico e Tecnológico (CNPq), and Financiadora de Estudos e Projetos (FINEP). Funding for SDSS-III has been provided by the Alfred P. Sloan Foundation, the Participating Institutions, the National Science Foundation, and the U.S. Department of Energy Office of Science. The SDSS-III web site is `http://www.sdss3.org/`. SDSS-III is managed by the Astrophysical Research Consortium for the Participating Institutions of the SDSS-III Collaboration including the University of Arizona, the Brazilian Participation Group, Brookhaven National Laboratory, Carnegie Mellon University, University of Florida, the French Participation Group, the German Participation Group, Harvard University, the Instituto de Astrofisica de Canarias, the Michigan State/Notre Dame/JINA Participation Group, Johns Hopkins University, Lawrence Berkeley National Laboratory, Max Planck Institute for Astrophysics, Max Planck Institute for Extraterrestrial Physics, New Mexico State University, New York University, Ohio State University, Pennsylvania State University, University of Portsmouth, Princeton University, the Spanish Participation Group, University of Tokyo, University of Utah, Vanderbilt University, University of Virginia, University of Washington, and Yale University.

3.A. PARAM sanity checks

3.A.1. Seismic vs. spectroscopic gravities

Figure 3.4 shows a comparison between seismic and (calibrated) ASPCAP $\log g$ as a function of effective temperature. An immediate result is that while asteroseismology provides an accurate benchmark for spectroscopic gravities, spectroscopy may serve as an important cross-check for the determined asteroseismic parameters, especially for fainter stars. By requiring that the difference in $\log g$ not be too large, we are able to sort out potentially flawed seismic (or spectroscopic) parameters. For DR12, the ASPCAP gravities were calibrated using seismic gravities from *Kepler* (Holtzman et al. 2015). An analysis of APOKASC stars with known evolutionary status demonstrated that for RGB stars that have not yet entered the helium-burning phase, the offset between seismic and spectroscopic gravity is larger than for red-clump (RC) stars. Hence, one would ideally use two different calibration relations for the RC and RGB stars. In the meantime, ASPCAP provides a $\log g$ calibration only for RGB stars, while a calibration for RC stars is reported in a separate catalogue (Bovy et al. 2014). The temperature dependence of the gravity offset also reflects the bias imposed by the adopted calibration relation: at lower temperatures (on the upper RGB), the systematic discrepancy vanishes.

3.A.2. Scaling relations vs. grid-based results

The concordance between the results obtained with PARAM and from the direct method has already been mentioned in Rodrigues et al. (2014), who used PARAM to estimate masses, radii, and gravities for the APOKASC sample. In the direct method, the quantities mass, radius, and gravity are calculated through seismic scaling relations (which involve seismic global parameters, and $T_{\rm eff}$, but no information on metallicity or stellar models).

Figure 3.18 presents the comparison of the two methods for our sample. The resulting mean differences and rms scatter are $(5.3 \pm 13.7)\%$ in mass, $(1.3 \pm 5.1)\%$ in radius, and 0.005 ± 0.012 dex $[0.2 \pm 0.5)\%]$ in $\log g$, comparable to what was reported by Rodrigues et al. (2014) for APOKASC.

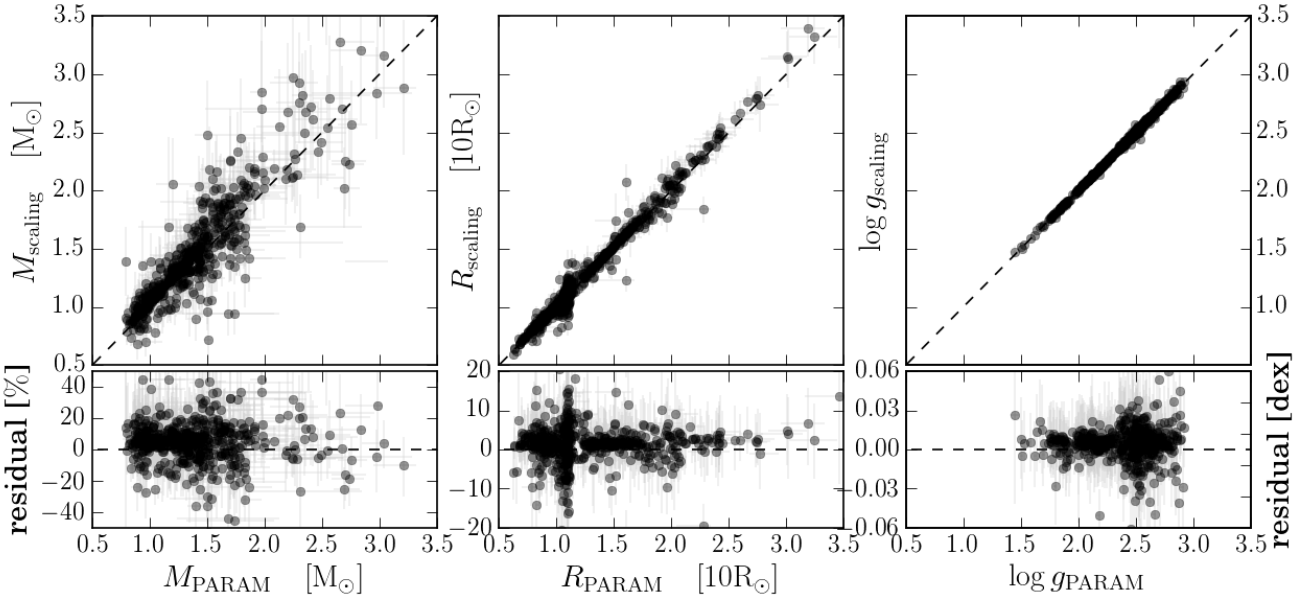

Figure 3.18. Comparison of our PARAM results for mass (left panel), radius (middle), and surface gravity (right) with the results obtained using seismic scaling relations. Compare also Fig. 4 of Rodrigues et al. (2014).

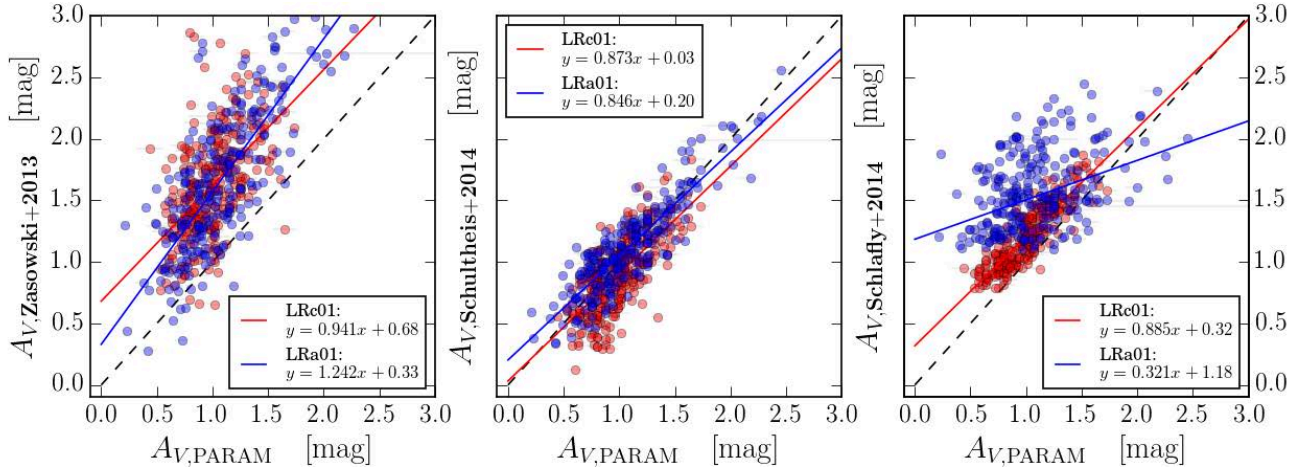

Figure 3.21. Comparison of our PARAM extinctions with the results obtained by the RJCE method (Zasowski et al. 2013; left panel), isochrone matching (Schultheis et al. 2014; middle panel), and the Pan-STARRS1 dust maps of Schlafly et al. (2014). As before, stars in LRa01 are plotted in blue, while LRc01 stars are plotted in red. The corresponding robust linear fits (using a Huber loss function; see e.g. Ivezić et al. 2013) are shown as solid lines, with the fit coefficients indicated in each panel.

3.A.3. Comparison with extinction maps

Another check is provided by Figs. 3.19 and 3.20 which show A_V extinction maps for the sample stars in the two CoRoT fields, and compare these results to the maps obtained using other methods: The Rayleigh-Jeans colour excess (RJCE) method (Majewski et al. 2011; Zasowski et al. 2013), the isochrone-matching method presented in Schultheis et al. (2014), and the 2D dust extinction maps derived from Pan-STARRS1 photometry (Schlafly et al. 2014). A quantitative comparison between our results and these literature methods, together with empirical fitting formulae for each extinction scale, is presented in Fig. 3.21. In summary, we can say the following:

- The RJCE method (Majewski et al. 2011) relies on the fact that the intrinsic NIR – mid-IR colours (e.g. $H_{\rm 2MASS} - W2_{\rm WISE}$) of a star depend very little on the spectral type, and therefore the observed minus intrinsic colour provides a measurement of the amount of dust in the sightline of an observer. The comparison with the extinction values calculated using this recipe (which was used for APOGEE targeting; Zasowski et al. 2013) shows that – assuming a particular extinction law (Nishiyama et al. 2009) – RJCE overpredicts the amount of V-band extinction in both LRa01 and LRc01 by about 0.5 mag. Of course, as APOGEE operates in the H band ($A_H/A_V \approx 1/6$), this systematic difference is of minor importance for APOGEE targeting purposes. However, our comparison shows that, when computing distances to APOGEE field stars (e.g. Anders et al. 2014; Santiago et al. 2016), we should be cautious in using the targeting extinction values; in particular, distant low-latitude stars will be assigned systematically greater distances.
- The isochrone-based method of Schultheis et al. (2014), tailored to quantifying 3D extinction towards the Galactic bulge, yields slightly lower extinction values than our method; there is only a minor zero-point offset of about 0.05 mag in the extinction scale with respect to PARAM (middle

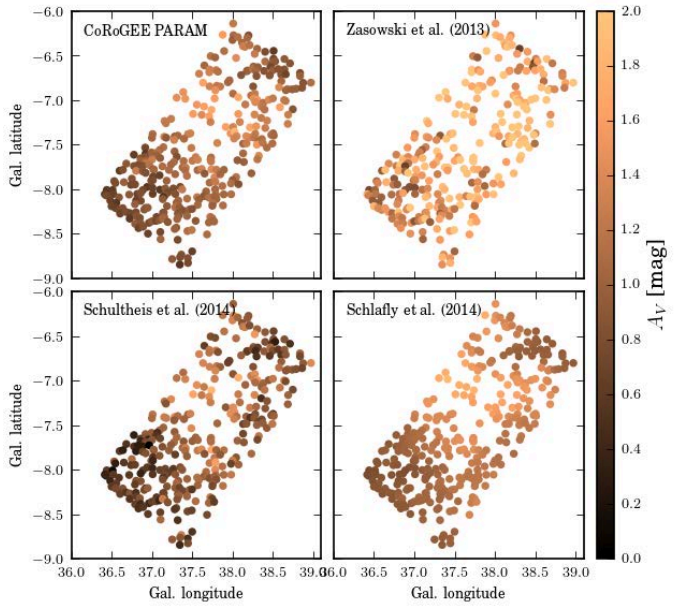

Figure 3.19. Comparison of our derived individual A_V extinction values for stars in the LRc01 field with extinction estimates derived by other (mostly independent) methods.

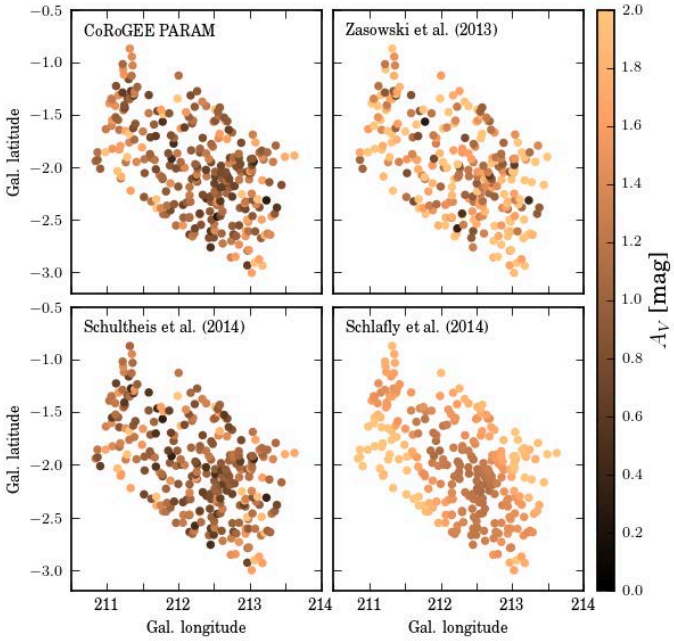

Figure 3.20. Same as Fig. 3.19, now for the LRa01 field.

panel of Fig. 3.21). When this effect is calibrated out, the rms scatter around the mean relation is about 0.2 mag in both fields.

– Schlafly et al. (2014) used multi-band photometry star-counts from Pan-STARRS1 (Kaiser et al. 2010) to create a 2D $E(B-V)$ reddening map, quantifying integrated interstellar extinction at heliocentric distances of 4.5 kpc. The resolution at low Galactic latitudes is typically 7′ and the systematic uncertainty in $E(B-V)$ around 0.03 mag. Our results show that while the overall amount of extinction for the bulk of the CoRoGEE sample is reproduced by the Pan-STARRS maps, the relation between our extinction estimates and those derived from Pan-STARRS is dominated by considerable scatter, especially in the LRc01 field. This result is expected, as most of our stars lie within the 4.5 kpc boundary, some even closer than 1 kpc from the Sun.

– Not shown in Fig. 3.21 is the comparison of our results with the classical 2D extinction SFD maps of Schlegel, Finkbeiner, & Davis (1998), as for Galactic astronomy purposes, they are surpassed in accuracy by the maps of Schlafly et al. (2014). It is worth mentioning, however, that in the LRc01 field (only 7° off the Galactic plane) our method agrees well with the SFD maps, also on a star-by-star level; we find a very tight relation between $A_{V,\mathrm{SFD}}$ and $A_{V,\mathrm{PARAM}}$ in this field, with an rms scatter of ~ 0.15 mag. This suggests that the extinction in this field is likely to be dominated by a nearby foreground cloud (as also visible in the WISE image of Fig. 3.1).
In the LRa01 field, however, the situation is not as favourable: The SFD maps overpredict the extinction in LRa01 by more than one magnitude on average, and the correlation with the PARAM results is marginal. This finding agrees with previous studies close to Galactic plane (e.g. Peek & Graves 2010; Schlafly & Finkbeiner 2011), and might be explained by significant additional amounts of dust beyond the bulk of the CoRoGEE stars (e.g. the Galactic warp).

3.B. Released data

In Table B.1, we shortly summarise the contents of this first set of CoRoGEE data that is released through the CDS Vizier Catalogue Service[19].

The present CoRoT-APOGEE dataset contains a large amount of information (206 columns) on the 606 successfully observed stars. In addition to the measurements derived directly from APOGEE and CoRoT observations, we include photometry from OBSCAT, APASS, SDSS, 2MASS, and WISE, information from the EXODAT archive, stellar parameters, distances and extinctions from PARAM and/or seismic scaling relations, cross-matches to the APOGEE DR12 RC catalogue (Bovy et al. 2014), the UCAC-4 catalogue (Zacharias et al. 2013), and additional information on the kinematics of the stars.

[19] `vizier.u-strasbg.fr/viz-bin/VizieR`

Table 3.0. Description and explanation of the contents of the CoRoT-APOGEE catalogue.

No.	Column	Data type	Shape	Unit	Description
\$1	CoRoT_ID	Integer			CoRoT Star Identifier - 10 digits number
\$2	APOGEE_ID	String			APOGEE Identifier
\$3	RA	Double		deg	Right Ascension (J2000.0, from 2MASS)
\$4	DEC	Double		deg	Declination (J2000.0, from 2MASS)
\$5	GLON	Double		deg	Galactic Longitude
\$6	GLAT	Double		deg	Galactic Latitude
\$7	FIELD	String			APOGEE Field
\$8	run_id	String			Identifier of the CoRoT mission run - format AAIIA
\$9	Seismic_results	String			Fitting method used to fit the frequency power spectrum (automatic or supervised)
\$10	numax	Float		muHz	Frequency of maximum oscillation power
\$11	e_numax	Float		muHz	Uncertainty of the frequency of maximum oscillation power
\$12	Dnu	Float		muHz	Large frequency separation
\$13	e_Dnu	Float		muHz	Uncertainty of the large frequency separation
\$14	evstat	String			Evolutionary stage (RGB: red-giant branch, or RC: red clump)
\$15	ASPCAP_ID	String			Unique ASPCAP identifier
\$16	FILE	String			File name of visit-combined APOGEE spectrum
\$17	TELESCOPE	String			String representation of of telescope used for observation (currently APO 1m or 2.5m)
\$18	LOCATION_ID	Short			APOGEE Field Location ID
\$19	TARGFLAGS	String			APOGEE Target flags[20]
\$20	NVISITS	Integer			Number of visits into combined spectrum
\$21	SNR	Float			median S/N per pixel in combined spectrum
\$22	STARFLAGS	String			APOGEE Star flags[21]
\$23	VHELIO_AVG	Float			APOGEE average radial velocity, weighted by S/N, using RVs determined from cross-correlation of ind. spectra with template spectrum
\$24	VSCATTER	Float			Scatter of individual visit RVs around average
\$25	VERR_MED	Float			Median of individual visit RV errors
\$26	PARAM	float[]	7		Empirically calibrated parameter array, using ASPCAP stellar parameters fit + calibrations, in the order: $T_{\rm eff}$, $\log g$, $v_{\rm micro}$, [M/H], [C/M], [N/M], [α/M]
\$27	FPARAM	float[]	7		Uncalibrated output parameter array from ASPCAP stellar parameters fit
\$28	PARAM_COV	float[]	49		Covariance of calibrated parameters, but with only diagonal elements from external uncertainty estimation
\$29	FPARAM_COV	float[]	49		Covariance of fitted parameters from ASPCAP
\$30	TEFF	Double		K	APOGEE $T_{\rm eff}$ from ASPCAP analysis of combined spectrum
\$31	TEFF_ERR	Double		K	APOGEE $T_{\rm eff}$ uncertainty
\$32	LOGG	Float		[dex]	APOGEE $\log g$ from ASPCAP analysis of combined spectrum
\$33	LOGG_ERR	Float		dex	APOGEE $\log g$ uncertainty
\$34	PARAM_M_H	Float		[dex]	APOGEE [M/H] from ASPCAP analysis of combined spectrum
\$35	MH_Anders	Float		[dex]	APOGEE [M/H] calibrated as in this paper and Santiago et al. (2016)
\$36	PARAM_M_H_ERR	Float		dex	APOGEE [M/H] uncertainty
\$37	PARAM_ALPHA_M	Float		[dex]	APOGEE [α/M] from ASPCAP analysis of combined spectrum
\$38	PARAM_ALPHA_M_ERR	Float		dex	APOGEE [α/M] uncertainty
\$39	ASPCAP_CHI2	Float			Reduced χ^2 of ASPCAP Fit
\$40	ASPCAPFLAGS	String			Flags for ASPCAP analysis
\$41	AL_H	Float		dex	[Al/H] from ASPCAP analysis of combined spectrum
\$42	CA_H	Float		dex	[Ca/H] from ASPCAP analysis of combined spectrum
\$43	C_H	Float		dex	[C/H] from ASPCAP analysis of combined spectrum
\$44	FE_H	Float		dex	[Fe/H] from ASPCAP analysis of combined spectrum
\$45	K_H	Float		dex	[K/H] from ASPCAP analysis of combined spectrum
\$46	MG_H	Float		dex	[Mg/H] from ASPCAP analysis of combined spectrum
\$47	MN_H	Float		dex	[Mn/H] from ASPCAP analysis of combined spectrum
\$48	NA_H	Float		dex	[Na/H] from ASPCAP analysis of combined spectrum
\$49	NI_H	Float		dex	[Ni/H] from ASPCAP analysis of combined spectrum
\$50	N_H	Float		dex	[N/H] from ASPCAP analysis of combined spectrum
\$51	O_H	Float		dex	[O/H] from ASPCAP analysis of combined spectrum
\$52	SI_H	Float		dex	[Si/H] from ASPCAP analysis of combined spectrum
\$53	S_H	Float		dex	[S/H] from ASPCAP analysis of combined spectrum
\$54	TI_H	Float		dex	[Ti/H] from ASPCAP analysis of combined spectrum
\$55	V_H	Float		dex	[V/H] from ASPCAP analysis of combined spectrum
\$56	AL_H_ERR	Float		dex	[Al/H] uncertainty from ASPCAP analysis of combined spectrum
\$57	CA_H_ERR	Float		dex	[Ca/H] uncertainty from ASPCAP analysis of combined spectrum
\$58	C_H_ERR	Float		dex	[C/H] uncertainty from ASPCAP analysis of combined spectrum
\$59	FE_H_ERR	Float		dex	[Fe/H] uncertainty from ASPCAP analysis of combined spectrum

[20] https://www.sdss.org/dr12/algorithms/bitmasks/#APOGEE_TARGET2
[21] https://www.sdss.org/dr12/algorithms/bitmasks/#APOGEE_STARFLAG

Table 3.0. Description and explanation of the contents of the CoRoT-APOGEE catalogue.

No.	Column	Data type	Shape	Unit	Description
\$60	K_H_ERR	Float		dex	[K/H] uncertainty from ASPCAP analysis of combined spectrum
\$61	MG_H_ERR	Float		dex	[Mg/H] uncertainty from ASPCAP analysis of combined spectrum
\$62	MN_H_ERR	Float		dex	[Mn/H] uncertainty from ASPCAP analysis of combined spectrum
\$63	NA_H_ERR	Float		dex	[Na/H] uncertainty from ASPCAP analysis of combined spectrum
\$64	NI_H_ERR	Float		dex	[Ni/H] uncertainty from ASPCAP analysis of combined spectrum
\$65	N_H_ERR	Float		dex	[N/H] uncertainty from ASPCAP analysis of combined spectrum
\$66	O_H_ERR	Float		dex	[O/H] uncertainty from ASPCAP analysis of combined spectrum
\$67	SI_H_ERR	Float		dex	[Si/H] uncertainty from ASPCAP analysis of combined spectrum
\$68	S_H_ERR	Float		dex	[S/H] uncertainty from ASPCAP analysis of combined spectrum
\$69	TI_H_ERR	Float		dex	[Ti/H] uncertainty from ASPCAP analysis of combined spectrum
\$70	V_H_ERR	Float		dex	[V/H] uncertainty from ASPCAP analysis of combined spectrum
\$71	AL_H_FLAG	Integer			[Al/H] Flag
\$72	CA_H_FLAG	Integer			[Ca/H] Flag
\$73	C_H_FLAG	Integer			[C/H] Flag
\$74	FE_H_FLAG	Integer			[Fe/H] Flag
\$75	K_H_FLAG	Integer			[K/H] Flag
\$76	MG_H_FLAG	Integer			[Mg/H] Flag
\$77	MN_H_FLAG	Integer			[Mn/H] Flag
\$78	NA_H_FLAG	Integer			[Na/H] Flag
\$79	NI_H_FLAG	Integer			[Ni/H] Flag
\$80	N_H_FLAG	Integer			[N/H] Flag
\$81	O_H_FLAG	Integer			[O/H] Flag
\$82	SI_H_FLAG	Integer			[Si/H] Flag
\$83	S_H_FLAG	Integer			[S/H] Flag
\$84	TI_H_FLAG	Integer			[Ti/H] Flag
\$85	V_H_FLAG	Integer			[V/H] Flag
\$86	AK_TARG	Float		mag	K_s-band extinction from APOGEE Targeting (Zasowski et al. 2013)
\$87	AK_TARG_METHOD	String			Extinction method used for APOGEE Targeting (Zasowski et al. 2013)
\$88	SFD_EBV	Float		mag	SFD $E(B-V)$ extinction (Schlegel et al. 1998)
\$89	RC_dist_kpc	Double		kpc	APOGEE Red Clump distance (Bovy et al. 2014)
\$90	VISITS	String			List of APOGEE visits going into combined spectrum
\$91	VISIT_PK	int[]	50		Index of MJDs of APOGEE visits used in combined spectrum
\$92	mag_b	Float		mag	OBSCAT Filter *B* magnitude
\$93	mag_b_err	Float		mag	OBSCAT Filter *B* magnitude error
\$94	mag_v	Float		mag	OBSCAT Filter *V* magnitude
\$95	mag_v_err	Float		mag	OBSCAT Filter *V* magnitude error
\$96	mag_r	Float		mag	OBSCAT Filter *R* magnitude
\$97	mag_r_err	Float		mag	OBSCAT Filter *R* magnitude error
\$98	mag_i	Float		mag	OBSCAT Filter *I* magnitude
\$99	mag_i_err	Float		mag	OBSCAT Filter *I* magnitude error
\$100	AllWISE	String			AllWISE ID
\$101	Jmag	Float		mag	2MASS *J* magnitude
\$102	e_Jmag	Float		mag	Mean error on *J* magnitude
\$103	Hmag	Float		mag	2MASS *H* magnitude
\$104	e_Hmag	Float		mag	Mean error on *H* magnitude
\$105	Kmag	Float		mag	2MASS K_s magnitude
\$106	e_Kmag	Float		mag	Mean error on K_s magnitude
\$107	W1mag	Float		mag	WISE *W*1 magnitude
\$108	e_W1mag	Float		mag	Mean error on *W*1 magnitude
\$109	W2mag	Float		mag	WISE *W*2 magnitude
\$110	e_W2mag	Float		mag	Mean error on *W*2 magnitude
\$111	W3mag	Float		mag	WISE *W*3 magnitude
\$112	e_W3mag	Float		mag	Mean error on *W*3 magnitude
\$113	W4mag	Float		mag	WISE *W*4 magnitude
\$114	e_W4mag	Float		mag	Mean error on *W*4 magnitude
\$115	magB	Float		mag	*B* magnitude from APASS
\$116	sigmagB	Float		mag	Error in *B* magnitude from APASS
\$117	magV	Float		mag	*V* magnitude from APASS
\$118	sigmagV	Float		mag	Error in *V* magnitude from APASS
\$119	magg	Float		mag	*g* magnitude from APASS
\$120	sigmagg	Float		mag	Error in *g* magnitude from APASS
\$121	magr	Float		mag	*r* magnitude from APASS
\$122	sigmagr	Float		mag	Error in *r* magnitude from APASS
\$123	magi	Float		mag	*i* magnitude from APASS
\$124	sigmagi	Float		mag	Error in *i* magnitude from APASS
\$125	RA_EXODAT	Double		deg	Rigth Ascension - J2000 decimal degrees
\$126	DEC_EXODAT	Double		deg	Declination - J2000 decimal degrees

Table 3.0. Description and explanation of the contents of the CoRoT-APOGEE catalogue.

No.	Column	Data type	Shape	Unit	Description
\$127	ccd_id	String			CoRoT CCD Id. either E1 or E2
\$128	win_id	Integer			CoRoT Window Identifier on the CCD
\$129	x	Double			X Target coordinate on the CoRoT CCD
\$130	y	Double			Y Target coordinate on the CoRoT CCD
\$131	spectral_type	String			EXODAT Spectral type of the star (from SED)
\$132	luminosity_class	String			EXODAT Luminosity class - (I II III IV V) (from SED)
\$133	color_temperature	Integer		K	EXODAT Color temperature estimation
\$134	ppmxl_id	String			Record identifier in the catalog PPMXL
\$135	usnob1_id	String			Record identifier in the catalog USNO-B1
\$136	twomass_id	String			Record identifier in the catalog TWOMASS
\$137	usnoa2_id	String			Record identifier in the catalog USNO-A2
\$138	cmc14_id	String			Record identifier in the catalog CMC-14
\$139	tycho2_id	Integer			Record identifier in the catalog TYCHO-2
\$140	ucac2_id	Integer			Record identifier in the catalog UCAC-2
\$141	UCAC4	String			UCAC4 recommended identifier (ZZZ-NNNNNN)
\$142	pmRA	Double		mas/yr	UCAC4 Proper motion in RA $\cdot$ cos(Dec)
\$143	e_pmRA	Float		mas/yr	Mean error on pmRA
\$144	pmDE	Double		mas/yr	UCAC4 Proper motion in Dec
\$145	e_pmDE	Float		mas/yr	Mean error on pmDE
\$146	UCAC4_combinedflag	Boolean			UCAC4 combined flag (as in Anders et al. 2014)
\$147	mass_scale	Float		$M_\odot$	Stellar mass from seismic scaling relations
\$148	logg_scale	Float		[dex]	log g from seismic scaling relations
\$149	radius_scale	Float		$R_\odot$	Stellar radius from seismic scaling relations
\$150	age_mode	Float		Gyr	PARAM Age (mode of the posterior PDF; Rodrigues et al. 2014)
\$151	age_mode_68L	Float		Gyr	PARAM Age Lower 68% Confidence Limit
\$152	age_mode_68U	Float		Gyr	PARAM Age Upper 68% Confidence Limit
\$153	age_mode_95L	Float		Gyr	PARAM Age Lower 95% Confidence Limit
\$154	age_mode_95U	Float		Gyr	PARAM Age Upper 95% Confidence Limit
\$155	sigage_isochrones	Double		Gyr	Systematic age uncertainty estimated from different isochrones
\$156	sigage_eta	Double		Gyr	Systematic age uncertainty related to mass loss
\$157	sigage_tot	Double		Gyr	Total age uncertainty (quadratic sum of statistical and systematic age uncertainties)
\$158	mass_mode	Float		$M_\odot$	PARAM Mass (mode of the posterior PDF; Rodrigues et al. 2014)
\$159	mass_mode_68L	Float		$M_\odot$	PARAM Mass Lower 68% Confidence Limit
\$160	mass_mode_68U	Float		$M_\odot$	PARAM Mass Upper 68% Confidence Limit
\$161	mass_mode_95L	Float		$M_\odot$	PARAM Mass Lower 95% Confidence Limit
\$162	mass_mode_95U	Float		$M_\odot$	PARAM Mass Upper 95% Confidence Limit
\$163	radius_mode	Float		$R_\odot$	PARAM Radius (mode of the posterior PDF; Rodrigues et al. 2014)
\$164	radius_mode_68L	Float		$R_\odot$	PARAM Radius Lower 68% Confidence Limit
\$165	radius_mode_68U	Float		$R_\odot$	PARAM Radius Upper 68% Confidence Limit
\$166	radius_mode_95L	Float		$R_\odot$	PARAM Radius Lower 95% Confidence Limit
\$167	radius_mode_95U	Float		$R_\odot$	PARAM Radius Upper 95% Confidence Limit
\$168	logg_mode	Float		[dex]	PARAM log g (mode of the posterior PDF; Rodrigues et al. 2014)
\$169	logg_mode_68L	Float		[dex]	PARAM log g Lower 68% Confidence Limit
\$170	logg_mode_68U	Float		[dex]	PARAM log g Upper 68% Confidence Limit
\$171	logg_mode_95L	Float		[dex]	PARAM log g Lower 95% Confidence Limit
\$172	logg_mode_95U	Float		[dex]	PARAM log g Upper 95% Confidence Limit
\$173	dist_mode	Float		pc	PARAM Distance (mode of the posterior PDF; Rodrigues et al. 2014)
\$174	dist_mode_68L	Float		pc	PARAM Distance Lower 68% Confidence Limit
\$175	dist_mode_68U	Float		pc	PARAM Distance Upper 68% Confidence Limit
\$176	dist_mode_95L	Float		pc	PARAM Distance Lower 95% Confidence Limit
\$177	dist_mode_95U	Float		pc	PARAM Distance Upper 95% Confidence Limit
\$178	Av_mode	Float		mag	PARAM V-band extinction (mode of the posterior PDF; Rodrigues et al. 2014
\$179	Av_mode_68L	Float		mag	PARAM V-band extinction Lower 68% Confidence Limit
\$180	Av_mode_68U	Float		mag	PARAM V-band extinction Upper 68% Confidence Limit
\$181	Av_mode_95L	Float		mag	PARAM V-band extinction Lower 95% Confidence Limit
\$182	Av_mode_95U	Float		mag	PARAM V-band extinction Upper 95% Confidence Limit
\$183	nfil	Short			Number of photometric filters used by PARAM
\$184	fils	String			Which photometric filters have been used by PARAM
\$185	Xg	Float		kpc	X coordinate in Galactocentric Cartesian coordinates
\$186	Xg_sig	Float		kpc	X coordinate uncertainty
\$187	Yg	Float		kpc	Y coordinate in Galactocentric Cartesian coordinates
\$188	Yg_sig	Float		kpc	Y coordinate uncertainty
\$189	Zg	Float		kpc	Z coordinate in Galactocentric Cartesian coordinates
\$190	Zg_sig	Float		kpc	Z coordinate uncertainty
\$191	Rg	Float		kpc	R coordinate in Galactocentric Cylindrical coordinates
\$192	Rg_sig	Float		kpc	R coordinate uncertainty

Table 3.0. Description and explanation of the contents of the CoRoT-APOGEE catalogue.

No.	Column	Data type	Shape	Unit	Description
$193	vT	Float		km/s	Transverse velocity
$194	vT_sig	Float		km/s	Transverse velocity uncertainty
$195	vXg	Float		km/s	*X*-axis space velocity
$196	vXg_sig	Float		km/s	*X*-axis space velocity uncertainty
$197	vYg	Float		km/s	*Y*-axis space velocity
$198	vYg_sig	Float		km/s	*Y*-axis space velocity uncertainty
$199	vZg	Float		km/s	*Z*-axis space velocity
$200	vZg_sig	Float		km/s	*Z*-axis space velocity uncertainty
$201	vRg	Float		km/s	Galactocentric radial velocity
$202	vRg_sig	Float		km/s	Galactocentric radial velocity uncertainty
$203	vPhig	Float		km/s	Azimuthal velocity
$204	vPhig_sig	Float		km/s	Azimuthal velocity uncertainty
$205	Rguide	Float		kpc	Guiding-centre radius
$206	Rguide_sig	Float		kpc	Uncertainty on guiding-centre radius

Chapter 4

Galactic Archaeology with CoRoT and APOGEE: Creating mock observations from a chemodynamical model

F. Anders[1,2], C. Chiappini[1,2], T. S. Rodrigues[2,3,4], T. Piffl[1], B. Mosser[5], A. Miglio[6], J. Montalbán[4], L. Girardi[3], I. Minchev[1], M. Valentini[1], and M. Steinmetz[1]

(Affiliations can be found after the references)

Abstract

In a companion paper, we have presented the combined asteroseismic-spectroscopic dataset obtained from CoRoT lightcurves and APOGEE infra-red spectra for 606 solar-like oscillating red giants in two fields of the Galactic disc (CoRoGEE). We have measured chemical abundance patterns, distances, and ages of these field stars which are spread over a large radial range of the Milky Way's disc. Here we show how to simulate this dataset using a chemodynamical Galaxy model. We also demonstrate how the observation procedure influences the accuracy of our estimated ages.

4.1. Introduction

Galactic models make predictions for the distribution of stars and gas in the multi-dimensional space consisting of time, kinematics and chemical composition. Therefore, one of the basic problems of Galactic Archaeology – the science of inferring the current state and the history of the Milky Way from present-day observations (e.g., Pagel 1997; Freeman & Bland-Hawthorn 2002) – is dimensionality reduction. For a given dataset, we are looking for the most robust and telling statistical relations to constrain these models.

Asteroseismology of red giants delivers new promising constraints to Milky Way models since it provides masses and ages of distant field stars with unprecedented precision (e.g., Miglio et al. 2013). The present work and an accompanying series of papers (Chiappini 2015; Anders et al. 2016) explore the power of asteroseismic constraints in Galactic Archaeology: we present one of the first attempts to combine stellar physics, asteroseismology, statistics, and spectroscopy – to learn about the chemo-dynamical history of our Galaxy. Specifically, we combine data from the infrared spectroscopic stellar survey APOGEE (Majewski et al. 2015) with asteroseismic data from the CoRoT mission (Baglin et al. 2006). In this paper, we describe how we simulated mock CoRoT-APOGEE (CoRoGEE) observations of the chemodynamical N-body Galaxy model of Minchev, Chiappini, & Martig (2013, 2014, MCM).

4.2. The dataset

We have assembled a comprehensive dataset (stellar parameters, elemental abundances, kinematics) of more than 600 solar-like oscillating red giant stars which have been observed by both CoRoT and APOGEE (CoRoGEE). Table 1 gives an overview of the dataset; Fig. 4.1 shows the distribution of our stars in Galactocentric cylindrical coordinates. The details of our analysis are provided in Anders et al. (2016).

Table 4.1. Summary of the available CoRoGEE data.

CoRoT-APOGEE stars	690
with "good" spectroscopic parameters	678
& "good" asteroseismic parameters	664
& $\lvert \log g_{\rm ASPCAP} - \log g_{\rm seismo} \rvert < 0.5$	617
Converged stellar parameters & distances	606
Field LRa01 (outer disc)	282
Field LRc01 (inner disc)	326

Using an updated version of the Bayesian stellar parameter estimation code PARAM (da Silva et al. 2006), we have determined the radii, masses, ages, and distances of the CoRoGEE stars by comparing the measured spectroscopic effective temperatures, metallicities, and asteroseismically determined $\Delta\nu$ and $\nu_{\rm max}$ with stellar evolutionary models. We achieve typical precicions of $\sim$ 3% in radius, $\sim$ 9% in mass, and $\sim$ 25% in age. By combining our stellar radii measurements with multi-wavelength photometry, we also derive very precise distances (precise to $\sim$ 2%) and extinctions. The details are described in Rodrigues et al. (2014).

The first result obtained with the CoRoT-APOGEE dataset was the discovery of a population of disc stars which do not follow the relation between the [α/Fe] abundance ratio and age predicted by canonical chemical evolution models of the Galactic disc. In Chiappini (2015), we discuss several scenarios that can be invoked to explain the existence of these objects, and the fact that these stars are much more prevalent in the inner CoRoT field. No conclusive explanation has been presented so far, but possible solutions involve stellar mimicry (old stars disguised as younger ones because of close-binary evolution (Yong et al. 2016) or stellar mergers), abundance anomalies in star-forming bubbles, and a peculiar chemical evolution near the corotation radius of the Galactic bar.

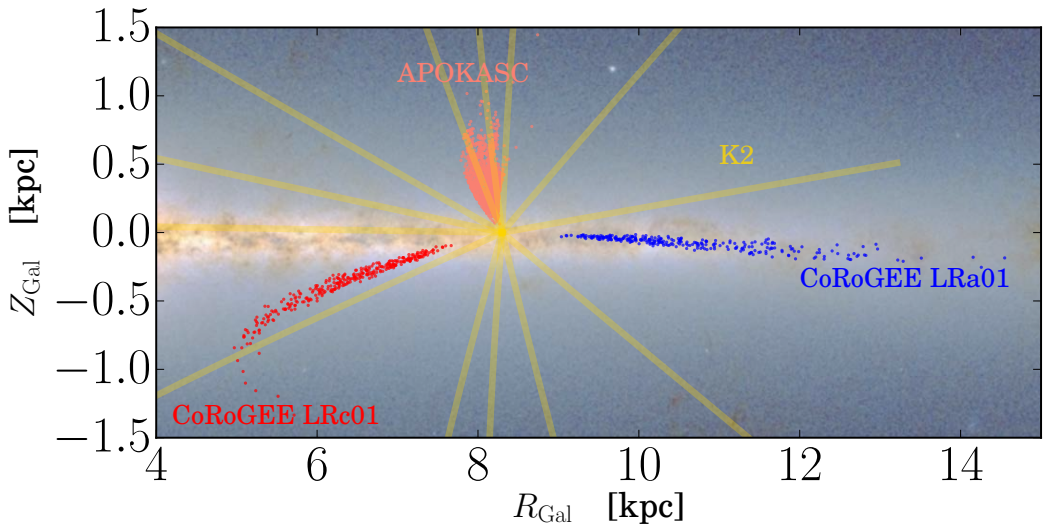

Figure 4.1. Location of the APOGEE samples with seismic and spectroscopic observations in Galactocentric cylindrical coordinates. The K2 mission and its spectroscopic follow-up campaigns are presently adding several new sightlines to this picture (*yellow rays*).

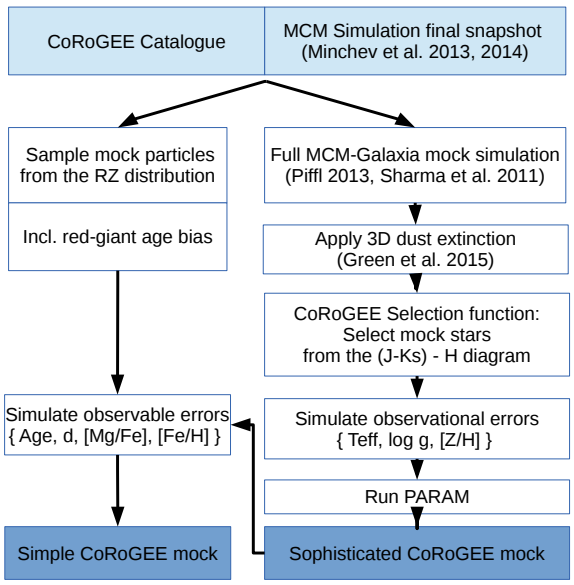

Figure 4.2. Scheme illustrating how our two versions of the CoRoGEE mock observations were obtained from the MCM model.

4.3. CoRoGEE mock samples from a chemo-dynamical model

The direct interpretation of astronomical survey data is often hampered by non-trivial selection effects. As pointed out in, e.g., Binney & Sanders (2015), the comparison of survey catalogues with a Galactic model is much easier when a mock observation of the model is created.

In this Section we describe how to select a CoRoGEE-like sample from an N-body simulation, using the example of the MCM model (Minchev et al. 2013, 2014). We have chosen two different paths to simulating the observations: a straightforward "simple" mock, and a more sophisticated one which uses a mock observation tool (Piffl 2013) based on the Galaxia stellar population synthesis code (Sharma et al. 2011). The procedures leading to the two versions of mock observations are sketched in Fig. 4.2.

4.3.1. Sophisticated mock

The original Galaxia population synthesis code (Sharma et al. 2011) uses the analytic Besançon Milky Way model (Robin et al. 2003) and creates synthetic Galactic stellar populations in a given part of the sky. Additionally, it allows the user to include a stellar halo from an N-body simulation, i.e. a model in which the kinematic distribution functions are not analytic any more, but are taken from the mass particle distributions of the input simulation. Piffl (2013)[1] generalised this idea and first used the MCM model as an input for the Galaxia code in the context of a simulated RAVE survey. By spawning mock stars from the MCM mass particles (each star inherits its age and chemical properties from the parent particle) he showed that the model could recover realistic correlations between the kinematics and the chemical abundances of the stars, while it was not possible to obtain an absolute match with star counts and global kinematic parameters of the Milky Way. Here, we use the same code to simulate a CoRoGEE-like sample from the MCM galaxy.

We first simulated a complete synthetic photometric all-sky survey from the solar position[2] up to a limiting magnitude of $H_0 = 13$ from the MCM galaxy using the modified Galaxia code (Piffl 2013). This translates the $9.5 \cdot 10^5$ input N-body particles into $7.8 \cdot 10^7$ mock stars (see density maps in Fig. 4.3). We then calculated observed magnitudes for the mock stars in the CoRoT fields using the new PanSTARRS-1 3D extinction map of Green et al. (2015)[3]. The resulting colour and magnitude distributions up to the magnitude limit of CoRoGEE ($H = 12.2$) are also shown in Fig. 4.3. As expected, the absolute star counts are not well matched by the MCM-Galaxia model, but the relative distributions in the colour-magnitude diagram (CMD) are reproduced (see Piffl 2013 for a discussion). In the next step, we applied the effective CoRoGEE selection function (assuming that it only

[1] `https://publishup.uni-potsdam.de/files/6790/piffl_diss.pdf`

[2] We assume $R_{\rm Gal,\odot} = 8.3$ kpc, in line with recent estimates (see e.g., Bland-Hawthorn & Gerhard 2016)

[3] `http://argonaut.skymaps.info/`

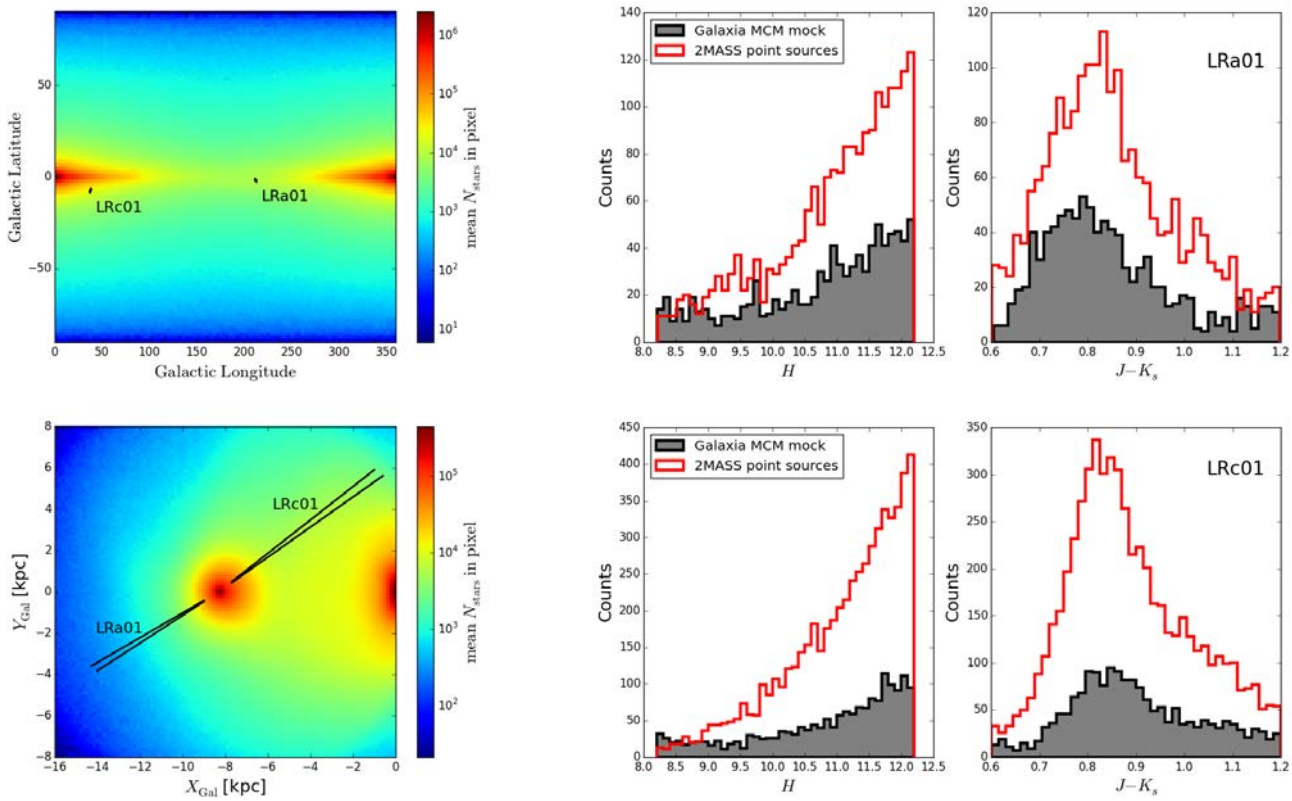

Figure 4.3. Star counts in the MCM Galaxy mock. *Left:* Density distribution of all simulated MCM stars (magnitude limit $H_0 = 13.0$) in $(l, b$; top left) and $(X_{\rm Gal}, Y_{\rm Gal}$; bottom left). *Middle and right: H* magnitude and $(J - K_s)$ star counts in the two CoRoT fields, comparing 2MASS (red histograms; Cutri et al. 2003) and the MCM mock Galaxy (grey histograms).

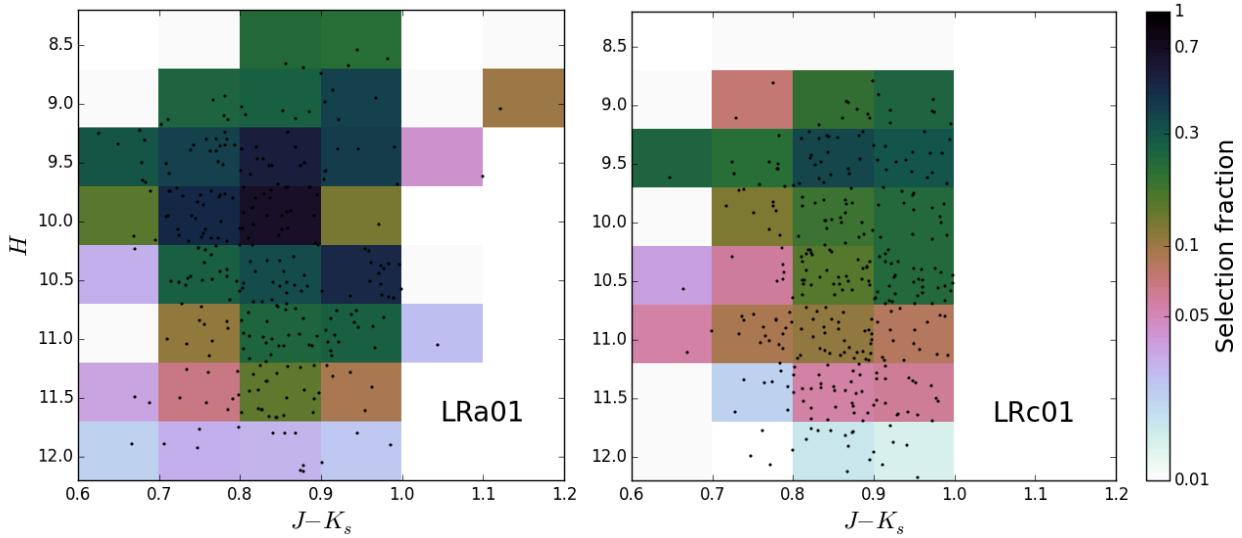

Figure 4.4. H vs. $J-K_s$ colour-magnitude diagram (CMD) for the two CoRoGEE fields. The colour in each CMD box shows the selection fraction ($N_{\rm CoRoGEE}/N_{\rm 2MASS}$) in this box. We used the same boxes to simulate the CoRoGEE selection function for the "sophisticated MCM mock".

depends on H and $J - K_s$) by randomly selecting the observed number of stars from small boxes in the CMD (see Fig. 4.4).[4] We further simulated Gaussian observational errors in the spectroscopic stellar parameters $T_{\rm eff}, \log g$, [Z/H] and magnitudes, and then ran the Bayesian parameter estimation code PARAM (Rodrigues et al. 2014) to recover measured masses, radii, and ages.

[4] The justification for this approximation of the CoRoGEE selection is given in Anders et al. (2016).

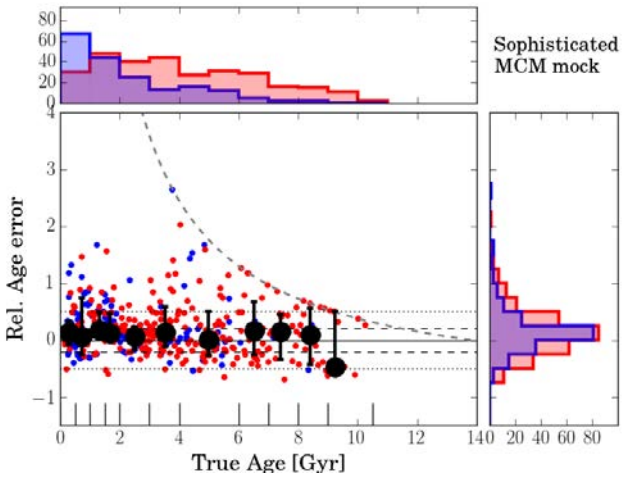

Figure 4.5. Relative PARAM age errors $\frac{\tau_{\rm PARAM}-\tau_{\rm true}}{\tau_{\rm true}}$ for the sophisticated version of the MCM-CoRoGEE mock as a function of the true age of the parent N-body particle. The simulated stars in LRa01 and LRc01 are shown in blue and red, respectively. The black symbols correspond to the median age error in each age bin indicated on the x-axis. The various lines correspond to a one-to-one relation, 20% and 50% deviation, and the age boundary at 13.7 Gyr.

4.3.2. Simple mock

A simpler way to simulate a CoRoGEE sample from the MCM simulation is to randomly select the most representative MCM particles from their distribution in configuration space. However, when we put the Sun at the correct distance to the Galactic center, the number of available particles is too small to yield enough mock stars in the two CoRoT fields. Therefore, we smoothed over the azimuthal angle in the Galactocentric cylindrical frame, and drew the mock stars directly from the observed distribution in the $R_{\rm Gal} - Z_{\rm Gal}$ plane. Because red giant stars do not sample all ages evenly, we simulated this red-giant age bias by assuming that a red giant of age τ is picked with a probability $\propto (\tau + 1\,{\rm Gyr})^{-0.7}$.[5]

Finally, we added typical observational errors in age, distance, and metallicity. While the distance and metallicity uncertainties could be assumed to be small and Gaussian ($\sim$ 2% and 0.04 dex, respectively), the statistical age errors are not straightforward to simulate. We therefore opted for the following data-driven approach: we use the sophisticated mock to estimate the age errors. For each star, a random age error was added according to the relative error distribution shown in Fig. 4.5.

4.3.3. Simulated age distributions

Fig. 4.5 shows how well our method is able to recover stellar ages, using the sophisticated MCM mock described above. It is evident that our individual age estimates should be used with caution, in particular for measured ages > 4 Gyr. However, we confirm that a small measured age does correspond to a true small age in almost all cases, thus strengthening the conclusions of Chiappini (2015). More details about statistical and systematic uncertainties involved in our age determinations are presented in Anders et al. (2016).

[5] From population synthesis modelling with TRILEGAL, we find that this bias depends very weakly on the position in the Galaxy. It is also consistent with the age bias that Casagrande et al. (2016) determined for the *Kepler* field with different methods (their Fig. 12d).

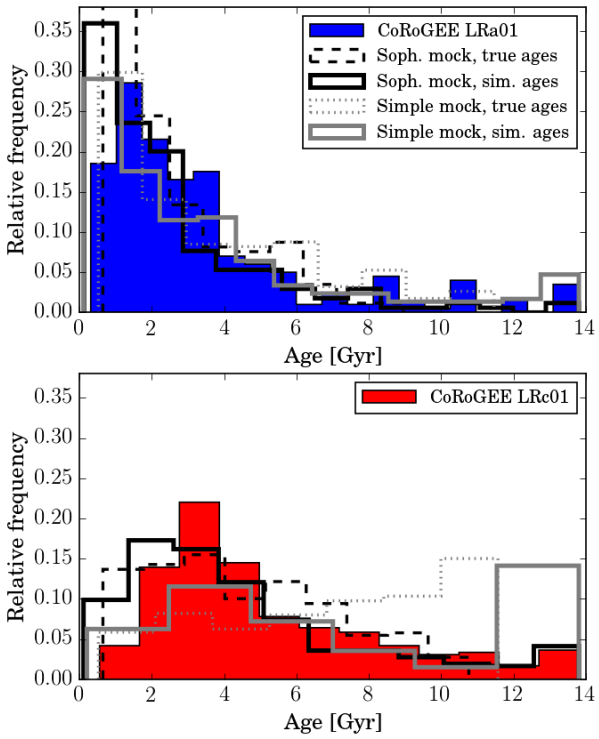

Figure 4.6. Simulated and recovered age distributions for the two CoRoGEE fields LRa01 (top) and LRc01 (bottom).

In Fig. 4.6, we take a first look at the simulated "true" age distributions in the two CoRoT fields (grey histograms), the effect of adding age errors on this distribution (black histograms), and compare these with the measured age distributions of the real data (filled histograms).

While the simulated age distributions of the sophisticated mock match the data surprisingly well in LRc01, we see striking differences in the relative number of old stars in LRa01. Conversely, the simple mock performs better for LRa01, while it overpredicts the number of old stars in LRc01. We suggest that this may be related to a) a more complex selection function, or b) a stronger age bias towards the inner Milky Way.

4.4. Summary

In our companion paper (Anders et al. 2016), we demonstrate, in line with previous works, that combining seismology and spectroscopy brings us one step further in obtaining meaningful ages of field stars. We also show that our sample can be used to formulate new chemodynamical constraints on the evolution of the Milky Way disc over a large range in Galactocentric distance and ages.

The simulations presented in this paper have shown that some notes of caution are due: we demonstrated that the absolute age scale of our isochrone ages is prone to systematic shifts. We also remind the data user to be very careful when interpreting small subsets of the data, and to refrain from interpreting single data points.

In follow-up works we will explore the individual-element abundance space opened by APOGEE and provide a detailed comparison with a (semi-)cosmological chemodynamical N-body simulation, using mock observation tools. One of the key questions of Galactic Archaeology which our sample should

help to answer is constraining the migration efficiency in the Galactic disc as a function of time and position.

Acknowledgements. We thank M. Schultheis for useful comments. TSR acknowledges support from CNPq-Brazil. BM acknowledges financial support from the ANR program IDEE Interaction Des Étoiles et des Exoplanètes. The CoRoT space mission, launched on December 27 2006, was developed and operated by CNES, with the contribution of Austria, Belgium, Brazil, ESA (RSSD and Science Program), Germany and Spain. This research has made use of the ExoDat Database, operated at LAM-OAMP, Marseille, France, on behalf of the CoRoT/Exoplanet program.

Funding for the SDSS-III Brazilian Participation Group was provided by the Ministério de Ciência e Tecnologia (MCT), Fundação Carlos Chagas Filho de Amparo à Pesquisa do Estado do Rio de Janeiro (FAPERJ), Conselho Nacional de Desenvolvimento Científico e Tecnológico (CNPq), and Financiadora de Estudos e Projetos (FINEP).
Funding for SDSS-III was provided by the Alfred P. Sloan Foundation, the Participating Institutions, the National Science Foundation, and the U.S. Department of Energy Office of Science. The SDSS-III web site is `http://www.sdss3.org/`.
SDSS-III was managed by the Astrophysical Research Consortium for the Participating Institutions of the SDSS-III Collaboration including the University of Arizona, the Brazilian Participation Group, Brookhaven National Laboratory, Carnegie Mellon University, University of Florida, the French Participation Group, the German Participation Group, Harvard University, the Instituto de Astrofisica de Canarias, the Michigan State/Notre Dame/JINA Participation Group, Johns Hopkins University, Lawrence Berkeley National Laboratory, Max Planck Institute for Astrophysics, Max Planck Institute for Extraterrestrial Physics, New Mexico State University, New York University, Ohio State University, Pennsylvania State University, University of Portsmouth, Princeton University, the Spanish Participation Group, University of Tokyo, University of Utah, Vanderbilt University, University of Virginia, University of Washington, and Yale University.

Bibliography

Anders, F., Chiappini, C., Rodrigues, T. S., et al. 2016, ArXiv e-prints
Baglin, A., Auvergne, M., Barge, P., et al. 2006, in ESA Special Publication, ed. M. Fridlund, A. Baglin, J. Lochard, & L. Conroy, Vol. 1306, 33
Binney, J. & Sanders, J. L. 2015, ArXiv e-prints
Bland-Hawthorn, J. & Gerhard, O. 2016, ArXiv e-prints
Casagrande, L., Silva Aguirre, V., Schlesinger, K. J., et al. 2016, MNRAS, 455, 987
Chiappini, C. 2015, in EAS Publications Series, Vol. 73, EAS Publications Series, 309–341
Cutri, R. M., Skrutskie, M. F., van Dyk, S., et al. 2003, 2MASS All Sky Catalog of point sources.
da Silva, L., Girardi, L., Pasquini, L., et al. 2006, A&A, 458, 609
Freeman, K. & Bland-Hawthorn, J. 2002, ARA&A, 40, 487
Green, G. M., Schlafly, E. F., Finkbeiner, D. P., et al. 2015, ApJ, 810, 25
Majewski, S. R., Schiavon, R. P., Frinchaboy, P. M., et al. 2015, ArXiv e-prints
Miglio, A., Chiappini, C., Morel, T., et al. 2013, MNRAS, 429, 423
Minchev, I., Chiappini, C., & Martig, M. 2013, A&A, 558, A9
Minchev, I., Chiappini, C., & Martig, M. 2014, A&A, 572, A92
Pagel, B. E. J. 1997, Nucleosynthesis and Chemical Evolution of Galaxies
Piffl, T. 2013, PhD thesis, Universität Potsdam
Robin, A. C., Reylé, C., Derrière, S., & Picaud, S. 2003, A&A, 409, 523
Rodrigues, T. S., Girardi, L., Miglio, A., et al. 2014, MNRAS, 445, 2758
Sharma, S., Bland-Hawthorn, J., Johnston, K. V., & Binney, J. 2011, ApJ, 730, 3
Yong, D., Casagrande, L., Venn, K. A., et al. 2016, MNRAS

[1] Leibniz-Institut für Astrophysik Potsdam (AIP), An der Sternwarte 16, 14482 Potsdam, Germany
[2] Laboratório Interinstitucional de e-Astronomia, - LIneA, Rua Gal. José Cristino 77, Rio de Janeiro, RJ - 20921-400, Brazil
[3] Osservatorio Astronomico di Padova – INAF, Vicolo dell'Osservatorio 5, I-35122 Padova, Italy
[4] Dipartimento di Fisica e Astronomia, Università di Padova, Vicolo dell'Osservatorio 2, I-35122 Padova, Italy
[5] LESIA, Observatoire de Paris, PSL Research University, CNRS, Université Pierre et Marie Curie, Université Denis Diderot, 92195 Meudon, France
[6] School of Physics and Astronomy, University of Birmingham, Edgbaston, Birmingham, B15 2TT, United Kingdom

Chapter 5

Young [α/Fe]-enhanced stars discovered by CoRoT and APOGEE: What is their origin?

C. Chiappini[1,2], F. Anders[1,2], T. S. Rodrigues[2,3,4], A. Miglio[5], J. Montalbán[4], B. Mosser[6], L. Girardi[2,3], M. Valentini[1], A. Noels[7], T. Morel[7], I. Minchev[1], M. Steinmetz[1], B. X. Santiago[2,8], M. Schultheis[9], M. Martig[10], L. N. da Costa[2,11], M. A. G. Maia[2,11], C. Allende Prieto[12,13], R. de Assis Peralta[6], S. Hekker[14,15], N. Themeßl[14,15], T. Kallinger[16], R. A. García[17], S. Mathur[18], F. Baudin[19], T. C. Beers[20], K. Cunha[11], P. Harding[21], J. Holtzman[22], S. Majewski[23], Sz. Mészáros[24,25], D. Nidever[26], K. Pan[22,27], R. P. Schiavon[28], M. D. Shetrone[29], D. P. Schneider[30,31], K. Stassun[32]

(Affiliations can be found after the references)

Abstract

We report the discovery of a group of apparently young CoRoT red-giant stars exhibiting enhanced [α/Fe] abundance ratios (as determined from APOGEE spectra) with respect to solar values. Their existence is not explained by standard chemical evolution models of the Milky Way, and shows that the chemical-enrichment history of the Galactic disc is more complex. We find similar stars in previously published samples for which isochrone-ages could be reliably obtained, although in smaller relative numbers. This might explain why these stars have not previously received attention. The young [α/Fe]-rich stars are much more numerous in the CoRoT-APOGEE (CoRoGEE) inner-field sample than in any other high-resolution sample available at present because only CoRoGEE can explore the inner-disc regions and provide ages for its field stars. The kinematic properties of the young [α/Fe]-rich stars are not clearly thick-disc like, despite their rather large distances from the Galactic mid-plane. Our tentative interpretation of these and previous intriguing observations in the Milky Way is that these stars were formed close to the end of the Galactic bar, near corotation – a region where gas can be kept inert for longer times than in other regions that are more frequently shocked by the passage of spiral arms. Moreover, this is where the mass return from older inner-disc stellar generations is expected to be highest (according to an inside-out disc-formation scenario), which additionally dilutes the in-situ gas. Other possibilities to explain these observations (e.g., a recent gas-accretion event) are also discussed.

5.1. Introduction

One of the pillars of Galactic Archaeology is the use of stellar [α/Fe] abundance ratios as an indirect age estimator: [α/Fe]-enhancement is an indication that a star has formed from gas enriched by core-collapse supernovae; longer-timescale polluters, such as supernovae of type Ia or asymptotic giant-branch stars, did not have sufficient time to enrich the interstellar medium (Pagel 2009; Matteucci 2001). High-resolution spectroscopy of the solar neighbourhood stars, for which Hipparcos parallaxes are available (e.g. Haywood et al. 2013), have indeed shown this paradigm to work well. One of the best examples is the very local ($d < 25$ pc) volume-complete sample of solar-like stars by Fuhrmann (2011, and references therein), for which it was possible to obtain robust isochrone ages for a small number of subgiants, which confirmed that stars exhibiting [α/Fe]-enhancements were all older than ~10 Gyr and identified them as thick-disc stars. Fuhrmann's data also show a clear chemical discontinuity in the [α/Fe] vs. [Fe/H] plane, which can be interpreted as the result of a star-formation gap between the thick and thin discs (Chiappini, Matteucci, & Gratton 1997; Fuhrmann 2011).

However, as we demonstrate in this Letter, α-enhancement is no guarantee that a star is actually old. Only recently has it become possible to obtain more precise ages for field stars far beyond the solar circle, thanks to asteroseismology, with CoRoT (Baglin et al. 2006) and *Kepler* (Gilliland et al. 2010). Even more important, the CoRoT mission allows for age and distance determination of stars spanning a wide range of Galactocentric distances, as shown by Miglio et al. (2013a,b). The latter authors have shown that when asteroseismic scaling relations are combined with photometric information, mass and age can be obtained to a precision of about 10% and 30%, respectively, even for distant objects[1]. High-resolution spectroscopy of the seismic targets plays a key role, not only allowing for more precise ages and distances, but also providing full chemical and kinematical information.

We have initiated a collaboration between CoRoT and APOGEE (the Apache Point Observatory Galactic Evolution Experiment; Majewski et al., in prep.). APOGEE is a high-resolution (R ~22,000) infrared survey ($\lambda = 1.51 - 1.69\,\mu$m) and part of the Sloan Digital Sky Survey III (Eisenstein et al. 2011, SDSS-III), which uses the Sloan 2.5 m telescope (Gunn et al. 2006). Here, we analyse data from the SDSS-III Data Release 12 (DR12; Alam et al. 2015), which contains 690 red-giant stars in the CoRoT fields LRa01 and LRc01 from an ancillary APOGEE campaign.

[1] The quoted uncertainties in Miglio et al. (2013a) were computed assuming global seismic parameter uncertainties from Mosser et al. (2010). Similar age uncertainties are found here, despite using spectroscopic information – as we have now adopted not only individual uncertainties but also a more conservative uncertainty estimate for the seismic parameters (details can be found in Anders et al. 2015, in prep.).

The CoRoT-APOGEE sample (CoRoGEE) studied here is briefly described in Sect. 6.2, while a more detailed description can be found in Anders et al. (2016, A&A; hereafter A16). The latter paper describes the analysis performed to extract the main stellar properties for this sample, such as masses, radii, ages, distances, extinctions, and kinematic parameters. The authors also present some immediate results that can be obtained with the CoRoGEE sample, such as the variation of the disc metallicity gradient with time or age-chemistry relations outside the solar vicinity. In the present Letter, we focus on a group of stars which, despite being enhanced in [α/Fe], appear to be relatively young. Because these stars, at first sight, challenge the currently accepted paradigm, we carry out several tests to consolidate our assigned ages and abundances in our companion paper. In Sect. 5.3 we identify the young high-[α/Fe] stars and describe their main properties, and in Sect. 5.4 we discuss possible interpretations for their origin. Our main conclusions are summarised in Sect. 5.5.

5.2. Observations

The CoRoT data we employed are a subset of the larger sample analysed by Miglio et al. (2013a). Red-giant oscillation spectra have been analysed as in Mosser et al. (2010). The global seismic parameters $\Delta\nu$ and $\nu_{\rm max}$ were measured following the method described in Mosser & Appourchaux (2009). When possible, a more precise determination of the large spacing was derived from the correlation of the power spectrum with the universal red-giant oscillation pattern (Mosser et al. 2011). Outliers to the $\Delta\nu$-$\nu_{\rm max}$ relation, which would correspond to unrealistic stellar masses, were excluded.

These targets were observed by APOGEE, and the high-resolution infrared spectra were analysed with the APOGEE Stellar Parameter and Chemical Abundances Pipeline (ASPCAP; Mészáros et al. 2013, García Pérez, al., in prep.). Here, we adopted internally calibrated DR12 abundances (Holtzman et al. 2015; see more details in A16.).

We used the Bayesian code PARAM (da Silva et al. 2006) to estimate stellar parameters. Masses, ages, distances, and extinctions were obtained with an updated version of the code (Rodrigues et al. 2014), which uses the combined photometric, seismic, and spectroscopic information to compute the probability density functions of these stellar properties. The final sample adopted here contains 622 red giant stars from the CoRoT LRa01 ($(l, b) = (212, -2)$) and LRc01 ($(l, b) = (37, -7)$) fields, for which a) high-quality spectroscopic criteria are fulfilled (APOGEE spectra with SNR > 90, 4000 K < $T_{\rm eff}$ <5300 K, 1 < $\log g$ <3.5), b) the PARAM code converged, and c) the seismic and calibrated spectroscopic $\log g$ are consistent within 0.5 dex. For this sample, statistical uncertainties of about 0.02 dex in $\log g$, 3% in radius, 8% in mass, 25% in age, and 2.5% in distance were obtained (more details can be found in A16.). As a caveat, stellar ages might still be affected by systematic uncertainties related to different stellar models and helium content, among other sources of errors (Lebreton et al. 2014; Lebreton & Goupil 2014; Martig et al. 2015; Miglio et al., in prep.).

Our dataset is complemented with similar information coming from two other high-resolution samples for which isochrone ages were available, the F & G solar-vicinity stars of Bensby, Feltzing, & Oey (2014), and the Gaia-ESO first internal data release of UVES spectra analysed in Bergemann et al. (2014). The total number of stars in each each sample is reported in Table A.2.

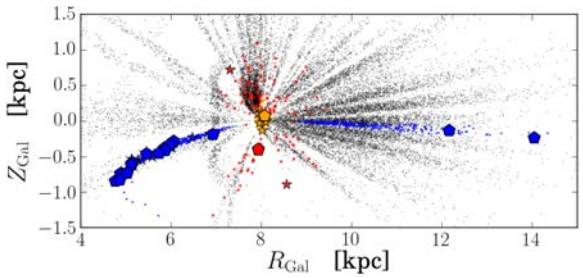

Figure 5.2. Location of the APOGEE high-quality sample of Anders et al. (2014) in a $Z_{\rm Gal}$ vs. $R_{\rm Gal}$ plane (grey points). Also shown are the locations of the CoRoGEE stars (*blue*), the subgiant stars from Bergemann et al. (2014, *red)*, and the Bensby et al. (2014) solar-vicinity dwarf stars (*orange*). As in Fig. 5.1, the discovered young [α/Fe]-rich stars are represented by the pentagons and stars.

5.3. Discovery of young [α/Fe]-rich stars in the Galactic disc

Figure 5.1 presents the age-[α/Fe] abundance relation for two local high-resolution spectroscopy samples: GES-UVES (Bergemann et al. 2014) and Bensby, Feltzing, & Oey (2014). The lower row shows the same relation for our CoRoGEE sample split into *1)* outer-field (LRa01) stars, *2)* inner-field (LRc01) stars with $Z_{\rm Gal}$ < 0.3 kpc, and *3)* inner-field stars with $Z_{\rm Gal}$ > 0.3 kpc. The latter is necessary because for the inner field, stars of different heights below the mid-plane span different Galactocentric distance ranges. This behaviour is a consequence of the way the LRc01 CoRoT field was positioned (see Fig 5.2; for more information on the population content of the LRc01 and LRa01 fields, see Miglio et al. 2013a).

We also show in Fig. 5.1 (upper-left panel) the predictions for the [Mg/Fe] vs. age chemical evolution of Chiappini (2009) for different Galactocentric annuli of the thick and thin discs. These models assume that the thick disc was formed on much shorter timescales and with a higher star formation efficiency than the thin disc. The shaded area corresponds to a parameter space not covered by a standard chemical evolution model of the thick and thin discs. Figure 5.1 demonstrates that while most of the data can be explained by standard chemical evolution models plus observational uncertainties (most probably accompanied by significant radial mixing, as discussed in Chiappini 2009 and Minchev, Chiappini, & Martig 2013, 2014), several stars are found to possess rather high [α/Fe] ratios, despite their young ages, and hence cannot be accounted for by the models. These stars are depicted as stars (1σ-outliers) and pentagons (2σ-outliers) in all figures. The young [α/Fe]-rich stars are more numerous in the inner field (see Fig. 5.2 and Table A.2).

Table A.2 shows the occurrance rates of young [α/Fe]-rich stars in the different analysed samples. Interestingly, there is a sudden rise in the fraction of young [α/Fe]-rich stars when smaller Galactocentric distances are sampled (which is the case of the CoRoT LRc01 field for $Z_{\rm Gal}$ > 0.3 kpc), and the absence of these stars in the Fuhrmann (2011) sample, as well as other less volumed-confined samples such as Ramírez et al. (2007) – which might be due to a statistical effect.

The young [α/Fe]-rich stars cover a wide range of stellar parameters ($4200\,{\rm K} < T_{\rm eff} < 5100\,{\rm K}, 1.7 < \log g < 2.7$; see also Fig. 10 of Martig et al. 2015). The abundance pattern of these stars compared to the entire CoRoGEE sample is displayed in Fig. 5.3. These stars are compatible with being formed from a gas that has not been processed by many stellar generations, as indicated by the systematically lower abundance of

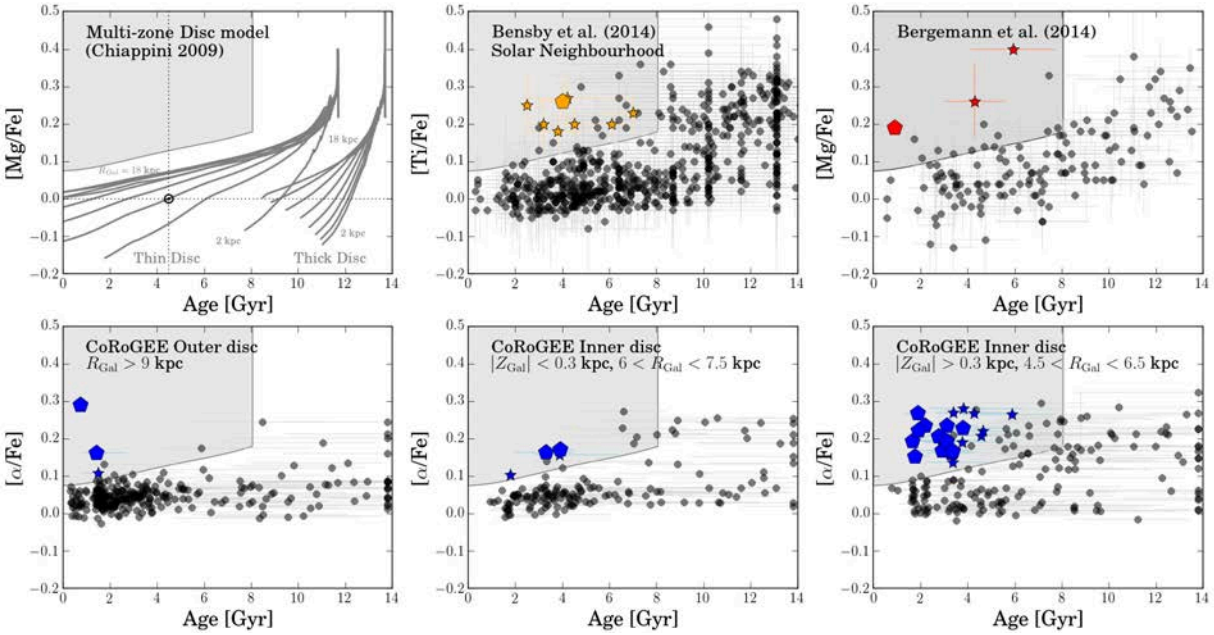

Figure 5.1. Age-[α/Fe] relation in different regions of the Galactic disc. *Upper left panel*: The grey curves indicate the predictions of the multi-zone Galactic chemical-evolution model of Chiappini (2009) for the thin and thick discs, where different tracks were calculated for different Galactocentric annuli situated between 2 and 18 kpc from the Galactic Centre. The solar position is indicated in the diagram for the 6 kpc curve, the distance of the most probable birth position of the Sun (Minchev, Chiappini, & Martig 2013). Within these models, it is not possible to explain stars that fall into the grey-shaded region of the diagram: young, [α/Fe]-enhanced stars. The grey shadings provide a heuristic estimate of the typical $N\sigma$ ($N = 1, 2, 3$) uncertainties in [Mg/Fe] and age. *Upper middle and right panels*: The solar cylinder data from Bensby et al. (2014, middle panel,) and the Gaia-ESO survey (Bergemann et al. 2014; right panel) show a clear correlation between isochrone-derived age estimates and relative [α/Fe] abundances. Stars whose age and abundance estimates are 1σ-incompatible with any of the chemical evolution curves are represented by stars; 2σ-outliers are represented by pentagons. *Lower panels*: The same diagram for the CoRoT-APOGEE sample. *Left*: the LRa01 outer-disc field. *Middle*: the LRc01 inner-disc field, close to the Galactic plane ($|Z_{\rm Gal}| < 0.3$ kpc, $R_{\rm Gal} > 6.0$ kpc). *Right*: the LRc01 field, below the Galactic plane ($Z_{\rm Gal} < -0.3$ kpc, $R_{\rm Gal} < 6.5$ kpc). In this region, the fraction of young α-enhanced stars is much larger than in all other regions. Considering *normal stars* alone, the age-[α/Fe] relation is much flatter than locally because the CoRoT stars span a wide range in Galactocentric distances.

Table 5.1. Abundance of young α-enhanced stars (yαr) in recent high-resolution spectroscopic surveys.

Sample	$R_{\rm Gal}{}^a$ [kpc]	N^b	1-σ / 2-σ yαr
Fuhrmann^c, $d < 25$ pc	8	424	0 / 0
Bensby et al.^{d}	8	714	8 (1.1%) / 1 (0.1%)
GES^e, $\lvert Z_{\rm Gal}\rvert < 0.3$ kpc	6 – 9	55	0 / 0
GES^e, $\lvert Z_{\rm Gal}\rvert > 0.3$ kpc	6 – 9	91	3 (3.3%) / 1 (1.1%)
LRa01^f	9 – 14	288	3 (1.0%) / 2 (0.7%)
LRc01^f, $\lvert Z_{\rm Gal}\rvert < 0.3$ kpc	6 – 7.5	151	4 (2.6%) / 2 (1.3%)
LRc01^f, $\lvert Z_{\rm Gal}\rvert > 0.3$ kpc	4 – 6.5	183	21 (11.5%) / 13 (7.1%)
APOKASC^g	7 – 8	1639	14 (0.8%)

Notes. (a) Galactocentric range covered by different samples (b) N = total number of stars in the sample, (c) The volume-complete sample of Fuhrmann (2011), (d) Hipparcos volume (Bensby, Feltzing, & Oey 2014), (e) *i*DR1 (Bergemann et al. 2014), (f) CoRoGEE, this work – see Appendix for detailed information on each star, (g) Martig et al. (2015). Outliers were defined in a different manner than in the present work.

iron-peak elements (lower contribution of type Ia supernovae to the chemical enrichment), as well as by the lower [N/O] and [C/O] abundance ratios (further indicating a mild contribution from intermediate-mass stars) with respect to the bulk of the CoRoGEE sample. However, when we restrict the comparison to stars with [O/H] < -0.2, no significant differences are detected any more.

We also investigated the kinematic properties of the young [α/Fe]-rich stars. Despite their [α/Fe] enhancements, many of them exhibit thin-disc like kinematics (although biased to hotter orbits because the inner CoRoT field samples Galactocentric distances below ~5 kpc only at larger distances from the mid-plane, $Z_{\rm Gal} > 0.3$ kpc). As a result of sample selection effects, stars with small Galactocentric distances are only reachable at large distances from the mid-plane and should not be mistaken for genuine thick-disc stars.

Focusing on the youngest stars (ages younger than 4 Gyr), where most of the $2-\sigma$ outliers are found (see Fig. 5.1), we checked the locus of the young [α/Fe]-rich stars in the [Fe/H] vs. Galactocentric distance diagram (Fig. 5.4, left panel) and in the [Fe/H] vs. guiding radius diagram (Fig. 5.4, right panel). Similar to Minchev, Chiappini, & Martig (2014), we estimated the guiding-centre radius of a stellar orbit using the approximation $R_g = \frac{L_z}{v_c} = \frac{v_\phi \cdot R_{\rm Gal}}{v_c}$, with L_z being the angular momentum, v_ϕ the ϕ-component of the space velocity in a Galactocentric cylindrical coordinate frame, and v_c the circular velocity at the star position – which for simplicity we assumed to be constant and equal to 220 km s^{-1} (see A16 for more details).

It is clear that most of the anomalous stars tend to be metal poor and to have small guiding radii ($R_g \lesssim 6$ kpc - dashed line in Fig. 5.4). This is also the case of the young [α/Fe]-rich stars in the other two more local samples. In particular, a large number of these anomalous objects appear near the corotation region (with the caveat that there are large uncertainties in the estimate of the guiding radii). It is expected that as the age increases, more of

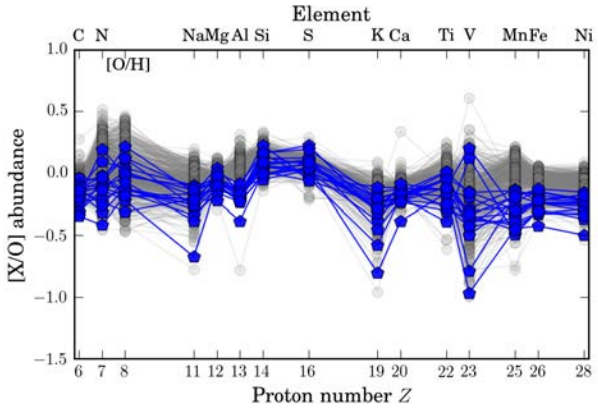

Figure 5.3. Chemical-abundance patterns relative to oxygen for the CoRoGEE stars marked as chemically peculiar in Fig. 5.1 (blue hexagons, 2σ-outliers in the age-[α/Fe] diagram). The chemical abundance pattern of the rest of the CoRoGEE sample is presented in grey for comparison.

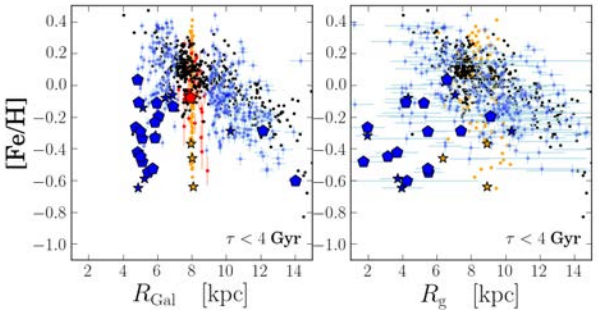

Figure 5.4. Radial [Fe/H] distribution (*left*: as a function of Galactocentric distance $R_{\rm Gal}$, *right*: w.r.t. the guiding radius R_g) over the extent of the Galactic disc (4-14 kpc range). As in Fig. 5.2, the CoRoGEE sample is shown in blue, the Bergemann et al. (2014) stars in red, and the Bensby et al. (2014) sample in orange. Again, hexagons and stars represent the young [α/Fe]-enhanced stars defined in Fig. 5.1. The locations of Galactic cepheids (*black*; data from Genovali et al. 2014) are also indicated.

these stars can also be found farther away from the corotation radius because radial migration would have had enough time to displace them from their birth position (Minchev, Chiappini, & Martig 2014). A larger age-baseline is discussed in A16, where we focus on the time evolution of abundance gradients.

5.4. What is their origin?

One possible interpretation is that the young [α/Fe]-rich stars might be evolved blue stragglers, that is, binary mergers. These have a higher mass and thus look like a young population. However, these stars should be present in all directions, at all metallicities, but in smaller numbers (see discussion in Martig et al. 2015).

The young α-rich stars appear to have been born from a relatively pristine gas, with metallicities above [Fe/H] ~ -0.7 (see Fig. 5.4, and Table 5.2). One possibility is that these are objects formed from a recent gas accretion event. One caveat here is that outliers are also present in older age bins, suggesting that the processes responsible for creating these stars have been continuously working during the Milky Way evolution. A more plausible interpretation is to assume that the region near the bar corotation is the site for the formation of the young [α/Fe]-rich stars. In this region, gas can be kept inert for longer times than in other regions that are more often shocked by the passage of the spiral arms (Bissantz et al. 2003; Combes 2014). Additional dilution is expected from gas restored from the death of old low-mass stars in this inner-disc region (Minchev, Chiappini, & Martig 2013).

If this interpretation holds and the process is still taking place in a region near the end of the Galactic bar, we also expect to find young metal-poor, [α/Fe]-enhanced stars in that same region of the Galactic plane. Interestingly, there are some intriguing young objects in the MW that might be related to the same phenomenon: *a)* the puzzling low-metallicity supergiants located near the end of the Galactic bar (Davies et al. 2009a,b, see discussion in Genovali et al. 2014 and Origlia et al. 2013), *b)* the young [α/Fe]-enchanced stars reported by Cunha et al. (2007) near the Galactic Centre, and, *c)* the unusual Cepheid BC Aql which, despite being young (Whitelock, priv. comm.) and located at $R_{\rm Gal}$ ~5 kpc, is also [α/Fe]-enhanced and metal-poor (Luck & Lambert 2011). Other Cepheids, recently discovered far from the Galactic plane on the opposite side of the Galaxy (Feast et al. 2014), also appear to be young (i.e., their period-age relations are compatible with ages $\lesssim$ 130 Myr).

Within our framework, we expect similar stars to have been forming in that same region (i.e., near the bar corotation) for the past 4-5 Gyr. As extensively discussed by Minchev, Chiappini, & Martig (2013, 2014), stars born at the corotation radius have a high probability of being expelled to an outer region via radial migration. This result suggests that the mechanism proposed here could have a strong effect on the thin disc by contaminating the entire disc with this metal-poor and [α/Fe]-rich population and that it might be related to the observed [Fe/H]~ -0.7 *floor* in the abundance gradients. One possible observable signature of this process might be the intermediate-age α-enhanced open clusters found by Yong, Carney, & Friel (2012, and references therein).

5.5. Conclusions

In this Letter we reported the discovery of young [α/Fe]-enhanced stars in a sample of CoRoT stars observed by APOGEE (CoRoGEE). These stars have a lower iron-peak element content than the rest of the CoRoGEE sample and are more abundant towards the inner Galactic disc regions. Almost all of the young [α/Fe]-rich stars we discovered have guiding radii $R_g \leq 6$ kpc. Therefore, we tentatively suggest that the origin of these stars is related to the complex chemical evolution that takes place near the corotation region of the Galactic bar.

Unfortunately, some ambiguity remains because the inner Galactic regions accessible to CoRoT are above $|Z_{\rm Gal}| = 0.3$ kpc. This situation is expected to improve by combining future APOGEE-2 data with *Kepler* seismology from the K2 Campaign (Howell et al. 2014), a goal for SDSS-IV. Further into the future, more information will be obtained from Gaia and the PLATO-2 mission (Rauer et al. 2014), both complemented by spectroscopy for example with the 4MOST facility (de Jong et al. 2014).

In a companion paper (Martig et al. 2015), we report the discovery of young-[α/Fe]-rich stars in the *Kepler* field (although in smaller numbers). Finally, in an ongoing Gaia-ESO follow-up of the CoRoT inner-field stars, more of these stars are found (Valentini et al., in prep.), providing better statistics and complementing the results shown in this Letter.

Acknowledgements. The CoRoT space mission, launched on December 27 2006, was developed and operated by CNES, with the contribution of Austria, Belgium, Brazil, ESA (RSSD and Science Program), Germany and

Spain. CC thanks A. Baglin, J. Storm and G. Cescutti for helpful discussions. T.S.R. acknowledges support from CNPq-Brazil. LG acknowledges support from PRIN INAF 2014. TM acknowledges financial support from Belspo for contract PRODEX GAIA-DPAC. SM acknowledges the support of the NASA grant NNX12AE17G. TCB acknowledges partial support from grants PHY 08-22648; Physics Frontier Center/JINA, and PHY 14-30152; Physics Frontier Center/JINA Center for the Evolution of the Elements (JINA-CEE), awarded by the US National Science Foundation. The research leading to the presented results has received funding from the European Research Council under the European Community's Seventh Framework Programme (FP7/2007-2013) / ERC grant agreement no 338251 (StellarAges). Funding for the SDSS-III Brazilian Participation Group has been provided by the Ministério de Ciência e Tecnologia (MCT), Fundação Carlos Chagas Filho de Amparo à Pesquisa do Estado do Rio de Janeiro (FAPERJ), Conselho Nacional de Desenvolvimento Científico e Tecnológico (CNPq), and Financiadora de Estudos e Projetos (FINEP). Funding for SDSS-III has been provided by the Alfred P. Sloan Foundation, the Participating Institutions, the National Science Foundation, and the U.S. Department of Energy Office of Science. The SDSS-III web site is http://www.sdss3.org/. SDSS-III is managed by the Astrophysical Research Consortium for the Participating Institutions of the SDSS-III Collaboration including the University of Arizona, the Brazilian Participation Group, Brookhaven National Laboratory, Carnegie Mellon University, University of Florida, the French Participation Group, the German Participation Group, Harvard University, the Instituto de Astrofisica de Canarias, the Michigan State/Notre Dame/JINA Participation Group, Johns Hopkins University, Lawrence Berkeley National Laboratory, Max Planck Institute for Astrophysics, Max Planck Institute for Extraterrestrial Physics, New Mexico State University, New York University, Ohio State University, Pennsylvania State University, University of Portsmouth, Princeton University, the Spanish Participation Group, University of Tokyo, University of Utah, Vanderbilt University, University of Virginia, University of Washington, and Yale University.

Bibliography

Alam, S., Albareti, F. D., Allende Prieto, C., et al. 2015, ArXiv e-prints:1501.00963
Anders, F., Chiappini, C., Santiago, B. X., et al. 2014, A&A, 564, A115
Baglin, A., Auvergne, M., Barge, P., et al. 2006, in ESA Special Publication, ed. M. Fridlund, A. Baglin, J. Lochard, & L. Conroy, Vol. 1306, 33
Bensby, T., Feltzing, S., & Oey, M. S. 2014, A&A, 562, A71
Bergemann, M., Ruchti, G. R., Serenelli, A., et al. 2014, A&A, 565, A89
Bissantz, N., Englmaier, P., & Gerhard, O. 2003, MNRAS, 340, 949
Chiappini, C. 2009, in IAU Symposium, Vol. 254, IAU Symposium, ed. J. Andersen, B. Nordström, & J. Bland-Hawthorn, 191–196
Chiappini, C., Matteucci, F., & Gratton, R. 1997, ApJ, 477, 765
Combes, F. 2014, in ASP Conference Series, Vol. 480, Structure and Dynamics of Disk Galaxies, ed. M. S. Seigar & P. Treuthardt, 211
Cunha, K., Sellgren, K., Smith, V. V., et al. 2007, ApJ, 669, 1011
da Silva, L., Girardi, L., Pasquini, L., et al. 2006, A&A, 458, 609
Davies, B., Origlia, L., Kudritzki, R.-P., et al. 2009a, ApJ, 694, 46
Davies, B., Origlia, L., Kudritzki, R.-P., et al. 2009b, ApJ, 696, 2014
de Jong, R. S., Barden, S., Bellido-Tirado, O., et al. 2014, in SPIE Conference Series, Vol. 9147, SPIE Conference Series
Eisenstein, D. J., Weinberg, D. H., Agol, E., et al. 2011, AJ, 142, 72
Feast, M. W., Menzies, J. W., Matsunaga, N., & Whitelock, P. A. 2014, Nature, 509, 342
Fuhrmann, K. 2011, MNRAS, 414, 2893
Genovali, K., Lemasle, B., Bono, G., et al. 2014, A&A, 566, A37
Gilliland, R. L., Brown, T. M., Christensen-Dalsgaard, J., et al. 2010, PASP, 122, 131
Gunn, J. E., Siegmund, W. A., Mannery, E. J., et al. 2006, AJ, 131, 2332
Haywood, M., Di Matteo, P., Lehnert, M. D., Katz, D., & Gómez, A. 2013, A&A, 560, A109
Holtzman, J. A., Shetrone, M., Johnson, J. A., et al. 2015, ArXiv e-prints:1501.04110
Howell, S. B., Sobeck, C., Haas, M., et al. 2014, PASP, 126, 398
Lebreton, Y. & Goupil, M.-J. 2014, ArXiv e-prints:1406.0652
Lebreton, Y., Goupil, M. J., & Montalbán, J. 2014, in EAS Publications Series, Vol. 65, EAS Publications Series, 99–176
Luck, R. E. & Lambert, D. L. 2011, AJ, 142, 136
Martig, M., Rix, H.-W., Silva Aguirre, V., et al. 2015, ArXiv e-prints:1412.3453
Matteucci, F., ed. 2001, Astrophysics and Space Science Library, Vol. 253, The chemical evolution of the Galaxy
Mészáros, S., Holtzman, J., García Pérez, A. E., et al. 2013, AJ, 146, 133
Miglio, A., Chiappini, C., Morel, T., et al. 2013b, in European Physical Journal Web of Conferences, Vol. 43, 3004
Miglio, A., Chiappini, C., Morel, T., et al. 2013a, MNRAS, 429, 423
Minchev, I., Chiappini, C., & Martig, M. 2013, A&A, 558, A9
Minchev, I., Chiappini, C., & Martig, M. 2014, A&A, 572, A92
Mosser, B. & Appourchaux, T. 2009, A&A, 508, 877
Mosser, B., Barban, C., Montalbán, J., et al. 2011, A&A, 532, A86
Mosser, B., Belkacem, K., Goupil, M.-J., et al. 2010, A&A, 517, A22
Origlia, L., Oliva, E., Maiolino, R., et al. 2013, A&A, 560, A46
Pagel, B. E. J. 2009, Nucleosynthesis and Chemical Evolution of Galaxies
Ramírez, I., Allende Prieto, C., & Lambert, D. L. 2007, A&A, 465, 271
Rauer, H., Catala, C., Aerts, C., et al. 2014, Experimental Astronomy, 38, 249
Rodrigues, T. S., Girardi, L., Miglio, A., et al. 2014, MNRAS, 445, 2758
Yong, D., Carney, B. W., & Friel, E. D. 2012, AJ, 144, 95

[1] Leibniz-Institut für Astrophysik Potsdam (AIP), An der Sternwarte 16, 14482 Potsdam, Germany
[2] Laboratório Interinstitucional de e-Astronomia, - LIneA, Rua Gal. José Cristino 77, Rio de Janeiro, RJ - 20921-400, Brazil
[3] Osservatorio Astronomico di Padova – INAF, Vicolo dell'Osservatorio 5, I-35122 Padova, Italy
[4] Dipartimento di Fisica e Astronomia, Università di Padova, Vicolo dell'Osservatorio 3, I-35122 Padova, Italy
[5] School of Physics and Astronomy, University of Birmingham, Edgbaston, Birmingham, B15 2TT, United Kingdom
[6] LESIA, Université Pierre et Marie Curie, Université Denis Diderot, Obs. de Paris, 92195 Meudon Cedex, France
[7] Institut d'Astrophysique et de Geophysique, Allée du 6 août, 17 - Bât. B5c, B-4000 Liège 1 (Sart-Tilman), Belgium
[8] Instituto de Física, Universidade Federal do Rio Grande do Sul, Caixa Postal 15051, Porto Alegre, RS - 91501-970, Brazil
[9] Observatoire de la Cote d'Azur, Laboratoire Lagrange, CNRS UMR 7923, B.P. 4229, 06304 Nice Cedex, France
[10] Max-Planck-Institut für Astronomie, Königstuhl 17, D-69117 Heidelberg, Germany
[11] Observatório Nacional, Rua Gal. José Cristino 77, Rio de Janeiro, RJ - 20921-400, Brazil
[12] Instituto de Astrofísica de Canarias, 38205 La Laguna, Tenerife, Spain
[13] Universidad de La Laguna, Departamento de Astrofísica, 38206 La Laguna, Tenerife, Spain
[14] Max-Planck-Institut für Sonnensystemforschung, Justus-von-Liebig-Weg 3, 37077 Göttingen, Germany
[15] Stellar Astrophysics Centre, Department of Physics and Astronomy, Aarhus University, Ny Munkegade 120, DK-8000 Aarhus C, Denmark
[16] Institut für Astronomie, Universität Wien, Türkenschanzstr. 17, Wien, Austria
[17] Laboratoire AIM, CEA/DSM – CNRS - Univ. Paris Diderot – IRFU/SAp, Centre de Saclay, 91191 Gif-sur-Yvette Cedex, France
[18] Space Science Institute, 4750 Walnut Street Suite 205, Boulder CO 80301, USA
[19] Institut d´Astrophysique Spatiale, UMR8617, CNRS, Université Paris XI, Bâtiment 121, 91405 Orsay Cedex, France
[20] Dept. of Physics and JINA-CEE: Joint Institute for Nuclear Astrophysics – Center for the Evolution of the Elements, Univ. of Notre Dame, Notre Dame, IN 46530 USA
[21] 57 Department of Astronomy, Case Western Reserve University, Cleveland, OH 44106, USA
[22] New Mexico State University, Las Cruces, NM 88003, USA
[23] Department of Astronomy, University of Virginia, PO Box 400325, Charlottesville VA 22904-4325, USA
[24] ELTE Gothard Astrophysical Observatory, H-9704 Szombathely, Szent Imre herceg st. 112, Hungary
[25] Department of Astronomy, Indiana University, Bloomington, IN 47405, USA
[26] Dept. of Astronomy, University of Michigan, Ann Arbor, MI, 48104, USA
[27] Apache Point Observatory PO Box 59, Sunspot, NM 88349, USA
[28] Astrophysics Research Institute, Liverpool John Moores University, IC2, Liverpool Science Park 146 Brownlow Hill Liverpool L3 5RF, UK

[29] Mcdonald Observatory, University of Texas at Austin, HC75 Box 1337-MCD, Fort Davis, TX 79734, USA
[30] Department of Astronomy and Astrophysics, The Pennsylvania State University, University Park, PA 16802
[31] Institute for Gravitation and the Cosmos, The Pennsylvania State University, University Park, PA 16802
[32] Vanderbilt University, Dept. of Physics & Astronomy, VU Station B 1807, Nashville, TN 37235, USA

5.A. Best-candidate young α-enhanced stars

Table 5.2 summarises our measured quantities for the best-candidate young α-enhanced stars (17 2σ-outliers; large pentagons in Fig. 5.1, and 11 1σ-outliers; stars in Fig. 5.1). We first report our input values: the adopted seismic parameters $\Delta\nu$ and $\nu_{\rm max}$ (as computed by automatic as well as supervised analyses of the CoRoT light curves), ASPCAP spectroscopic parameters $T_{\rm eff}$, [Fe/H], [α/Fe], and the number of APOGEE observations, $\rm N_{APO}$. We note that all stars in question have been observed at very high signal-to-noise ratios ($S/N > 140$ per resolution element). The radial-velocity scatter between subsequent observations is always smaller than 0.6 km/s; meaning that their values are consistent with all stars being single stars or widely separated binaries.

We also present the estimated stellar masses $\rm M_{scale}$, as determined from seismic scaling relations and the 1σ upper-limits for the ages (as determined by PARAM). A comparison of the masses estimated by PARAM and those inferred directly from the scaling relations is reported in A16 for the full CoRoGEE sample. Also listed are the current Galactocentric positions $R_{\rm Gal}$ and $Z_{\rm Gal}$ and the guiding radius R_g of each star.

We also show a note on the quality of the light curves (Q) and a flag based on the supervised analysis. Because the automated and supervised analyses sometimes yield different results, we recomputed masses and ages using the individually obtained $\Delta\nu$ and $\nu_{\rm max}$ values and updated uncertainties where necessary. As expected, the numbers of the young α-enhanced stars are slightly different. In Table 5.2, we only report the robust $2\sigma-$ and $1\sigma-$outliers.

However, these uncertainties have a small impact on our main result, as after the individual analysis, still 17 stars out of 20 seem to be younger than 4 Gyr. Individual supervised analysis shows that:

1. One star (CoRoT 101071033) had to be excluded from the parent sample due to the very poor quality of its light curve;
2. Four stars that seemed to be 2σ-outliers were shifted to older ages: CoRoT 101093867, 101071033, 102645343, and 10264381. Similarly, seven candidate 1σ-outliers fall out of the sample: CoRoT 101057962, 101041814, 102626343, 100886873, 101208801, 101212022, and 101227666.
3. CoRoT 101093867 is a complex case, where both $\Delta\nu$ values appear as possible solutions; for six other stars, another solution is possible, because the lightcurve SNR is not high enough to undoubtedly resolve the radial/dipole mode possible mismatch (such cases cannot be seen in the general blind automated analysis);
4. For CoRoT 100958571, the solution obtained through supervised fitting, close to the one found by the automated pipeline, should be preferred. Also, for most of the remaining stars, slight improvements in the determination of the seismic parameters are possible.

Table 5.2. Best-candidate young α-enhanced stars: seismic and spectroscopic adopted parameters and uncertainties, stellar masses and ages, current Galactocentric positions $R_{\rm Gal}$ and $Z_{\rm Gal}$, and guiding-centre radii $R_{\rm g}$.

CoRoT ID	APOGEE ID	$\Delta\nu$ [μHz]	$\nu_{\rm max}$ [μHz]	Q^a	$\Delta\nu_i{}^b$ [μHz]	$\nu_{{\rm max}_i}{}^b$ [μHz]	Flag^c	$N_{\rm APO}$	$T_{\rm eff}{}^d$ [K]	[Fe/H]	[α/Fe]	$M_{\rm scale}$ [$M_\odot$]	$\tau_{68U}{}^e$ [Gyr]	$\tau^{\rm i}_{68U}{}^f$ [Gyr]	$R_{\rm Gal}{}^g$ [kpc]	$Z_{\rm Gal}{}^h$ [kpc]	$R_{\rm g}$ [kpc]
2σ-outliers																	
100580176	2M19232036+0116385	1.2 ± 0.01	8.11 ± 0.22	OK	1.27	8.0	1	1	4200	−0.2 ± 0.03	0.16 ± 0.01	1.49 ± 0.22	2.5	4.5	6.06	−0.29	9.1 ± 0.5
100692726	2M19240121+0115468	2.71 ± 0.03	22.41 ± 0.58	OK	2.7	22.3	0	7	4390	−0.11 ± 0.03	0.16 ± 0.01	1.48 ± 0.14	4.3	4.3	4.91	−0.75	4.2 ± 1.2
100958571	2M19253009+0100237	1.94 ± 0.04	14.72 ± 0.65	OK	1.97	14.7	2	3	4410	−0.55 ± 0.04	0.20 ± 0.02	1.51 ± 0.24	3.4	4.7	5.46	−0.46	5.5 ± 0.9
101045095	2M19260245+0003446	2.78 ± 0.04	22.17 ± 0.64	poor	2.8	22.6	0	3	4400	−0.23 ± 0.03	0.23 ± 0.01	1.34 ± 0.14	6.0	5.7	5.87	−0.38	
101072104	2M19261545+0011507	3.01 ± 0.04	23.90 ± 0.71	OK	3.01	24.8	0	7	4580	−0.42 ± 0.04	0.24 ± 0.02	1.41 ± 0.14	5.8	3.6	4.87	−0.74	3.7 ± 1.2
101100354	2M19262657+0144163	4.56 ± 0.04	41.60 ± 0.93	poor	4.34	43.6	2	7	4520	−0.12 ± 0.03	0.21 ± 0.01	1.74 ± 0.14	7.6	3.0	5.97	−0.34	5.3 ± 0.7
101113416	2M19263149+0159448	1.11 ± 0.01	6.79 ± 0.20	OK	1.14	6.74	1	3	4360	−0.48 ± 0.04	0.24 ± 0.02	1.36 ± 0.15	3.6	4.5	5.14	−0.58	1.7 ± 1.2
101114706	2M19263197-0035004	0.97 ± 0.02	6.14 ± 0.31	OK	0.98	6.14	0	3	4170	−0.27 ± 0.03	0.19 ± 0.01	1.65 ± 0.29	3.5	3.8	4.76	−0.84	2.0 ± 1.0
101121769	2M19263465+0004069	1.34 ± 0.03	8.88 ± 0.35	OK	1.34	8.88	0	3	4340	−0.34 ± 0.03	0.17 ± 0.02	1.52 ± 0.23	4.0	4.0	5.12	−0.61	
101138968	2M19264111+0214048	2.46 ± 0.04	20.74 ± 0.73	OK	2.46	20.7	0	7	4500	−0.45 ± 0.04	0.27 ± 0.02	1.79 ± 0.22	2.1	2.3	5.03	−0.72	3.2 ± 1.1
101342375	2M19280053+0016331	2.06 ± 0.04	16.69 ± 0.74	OK	2.00	16.7	0	7	4340	0.03 ± 0.03	0.15 ± 0.01	2.03 ± 0.32	2.6	2.4	4.86	−0.83	6.6 ± 1.2
101386073	2M19282189+0010322	5.21 ± 0.07	48.40 ± 1.41	OK	5.23	51.2	0	7	4610	−0.33 ± 0.04	0.19 ± 0.02	1.37 ± 0.14	6.9	3.9	5.87	−0.41	
101415638	2M19283410+0006205	5.21 ± 0.11	47.68 ± 2.28	poor	4.80	47.7	1	7	4960	−0.53 ± 0.04	0.22 ± 0.02	1.48 ± 0.32	2.7	2.1	5.74	−0.45	5.5 ± 0.7
101594554	2M19294723+0007020	2.70 ± 0.03	21.52 ± 0.51	OK	2.72	21.73	0	7	4430	−0.29 ± 0.04	0.17 ± 0.01	1.35 ± 0.11	4.4	4.3	5.03	−0.73	5.5 ± 1.1
101748322	2M19305707-0008228	5.55 ± 0.03	53.17 ± 0.84	OK	5.40	52.4	2	3	4710	−0.14 ± 0.03	0.17 ± 0.01	1.34 ± 0.08	5.5	4.5	6.93	−0.19	
102673776	2M06430619-0103534	2.23 ± 0.05	16.83 ± 0.77	OK	2.23	16.8	0	4	5070	−0.61 ± 0.04	0.29 ± 0.02	1.69 ± 0.28	0.8	0.8	14.05	−0.25	4.3 ± 4.2
102733615	2M06442450-0100460	3.33 ± 0.09	30.93 ± 1.85	poor	3.06	30.9	1	4	4760	−0.29 ± 0.04	0.16 ± 0.02	2.28 ± 0.56	3.2	2.7	12.16	−0.14	7.4 ± 2.5
1σ-outliers																	
100667041	2M19235081+0111425	2.5 ± 0.03	19.85 ± 0.46	OK	2.59	19.8	2	7	4400	−0.34 ± 0.04	0.22 ± 0.02	1.23 ± 0.11	4.1	6.3	5.13	−0.53	
100889852	2M19250803+0152285	5.47 ± 0.1	53.41 ± 2.25	poor	5.62	56.1	2	7	4620	−0.32 ± 0.04	0.27 ± 0.02	1.36 ± 0.19	6.0	5.4	5.92	−0.33	2.0 ± 0.7
101029567	2M19255543+0014035	2.33 ± 0.04	17.76 ± 0.81	OK	2.35	17.7	0	7	4490	−0.65 ± 0.04	0.28 ± 0.02	1.34 ± 0.21	5.8	6.4	4.9	−0.71	4.0 ± 1.2
101073282	2M19261630+0116446	5.63 ± 0.09	56.33 ± 2.01	OK	5.53	56.9	0	3	4900	−0.08 ± 0.03	0.10 ± 0.01	1.65 ± 0.21	1.8	1.9	6.48	−0.24	4.3 ± 0.5
101200652	2M19270430+0120124	2.23 ± 0.04	17.11 ± 0.70	poor	2.36	17.5	1	7	4500	−0.59 ± 0.04	0.19 ± 0.02	1.38 ± 0.23	3.8	6.2	5.27	−0.55	3.7 ± 1.0
101364068	2M19281113-0020004	2.83 ± 0.04	21.34 ± 0.68	OK	2.84	22.2	0	3	4650	−0.21 ± 0.04	0.21 ± 0.01	1.30 ± 0.15	8.0	5.9	6.03	−0.38	2.8 ± 0.5
101392012	2M19282435+0117076	1.47 ± 0.02	9.12 ± 0.25	OK	1.50	9.06	1	3	4390	−0.65 ± 0.04	0.26 ± 0.02	1.10 ± 0.10	6.2	7.6	5.35	−0.55	4.5 ± 1.0
101419125	2M19283555-0013131	6.40 ± 0.09	63.78 ± 2.14	poor	6.57	65.8	1	7	4810	−0.49 ± 0.04	0.27 ± 0.02	1.25 ± 0.15	5.9	5.8	5.58	−0.50	4.9 ± 0.8
101476920	2M19285918+0036543	2.20 ± 0.03	16.63 ± 0.54	OK	2.25	17.3	0	7	4410	−0.14 ± 0.03	0.14 ± 0.01	1.45 ± 0.16	5.1	4.8	5.17	−0.64	
101665008	2M19302198+0018463	6.02 ± 0.05	61.93 ± 1.35	OK	6.30	62.6	1	3	4600	−0.06 ± 0.03	0.16 ± 0.01	1.28 ± 0.15	4.3	6.4	6.88	−0.20	7.1 ± 0.3
102768182	2M06451106-0032468	2.94 ± 0.06	27.18 ± 1.29	poor	2.94	27.0	0	3	4840	−0.29 ± 0.04	0.11 ± 0.02	2.17 ± 0.37	1.7	1.7	10.25	−0.05	10.3 ± 0.5

Notes. [a] Quality of CoRoT lightcurve and the automated global fits; [b] Results of individual supervised fit to the lightcurves; [c] Flag on supervised fits (0 = automated and supervised fit are consistent within 1σ. 1 = there are two possible solutions for $\Delta\nu$ or $\nu_{\rm max}$, due to the ambiguity of radial and dipole oscillation modes. 2 = supervised fit yields improved results); [d] Overall uncertainties: $\sigma T_{\rm eff}$ = 91 K (Holtzman et al. 2015); [e] 1σ age upper limit, using the seismic results from the automatic pipeline; [f] 1σ age upper limit, using the seismic results from the supervised seismic analysis; [g] Typical uncertainties: ∼ 0.1 kpc, for the most distant stars in LRa01 ∼ 0.5 kpc; [h] Typical uncertainties: < 0.1 kpc, for the most distant stars in LRc01 ∼ 0.4 kpc;

Chapter 6

Red giants observed by CoRoT and APOGEE: The evolution of the Milky Way's radial metallicity gradient

F. Anders[1,2], C. Chiappini[1,2], I. Minchev[1], A. Miglio[3], J. Montalbán[4], B. Mosser[5], T. S. Rodrigues[2,4,6], B. X. Santiago[2,7], F. Baudin[8], T. C. Beers[9], L. N. da Costa[2,10], R. A. García[11], D. A. García-Hernández[12,13], J. Holtzman[14], M. A. G. Maia[2,10], S. Majewski[15], S. Mathur[16], A. Noels-Grotsch[17], K. Pan[18,15], D. P. Schneider[19,20], M. Schultheis[21], M. Steinmetz[1], M. Valentini[1], O. Zamora[12,13]

(Affiliations can be found after the references)

Abstract

Using combined asteroseismic and spectroscopic observations of 418 red-giant stars close to the Galactic disc plane (6 kpc $< R_{\rm Gal} \lesssim$ 13 kpc, $|Z_{\rm Gal}| < 0.3$ kpc), we measure the age dependence of the radial metallicity distribution in the Milky Way's thin disc over cosmic time. The slope of the radial iron gradient of the young red-giant population (-0.058 ± 0.008 [stat.] ± 0.003 [syst.] dex/kpc) is consistent with recent Cepheid measurements. For stellar populations with ages of $1-4$ Gyr the gradient is slightly steeper, at a value of $-0.066 \pm 0.007 \pm 0.002$ dex/kpc, and then flattens again to reach a value of ~ -0.03 dex/kpc for stars with ages between 6 and 10 Gyr. Our results are in good agreement with a state-of-the-art chemo-dynamical Milky-Way model in which the evolution of the abundance gradient and its scatter can be entirely explained by a non-varying negative metallicity gradient in the interstellar medium, together with stellar radial heating and migration. We also offer an explanation for why intermediate-age open clusters in the solar neighbourhood can be more metal-rich, and why their radial metallicity gradient seems to be much steeper than that of the youngest clusters. Already within 2 Gyr, radial mixing can bring metal-rich clusters from the innermost regions of the disc to Galactocentric radii of 5 to 8 kpc. We suggest that these outward-migrating clusters may be less prone to tidal disruption and therefore steepen the local intermediate-age cluster metallicity gradient. Our scenario also explains why the strong steepening of the local iron gradient with age is not seen in field stars. In the near future, asteroseismic data from the K2 mission will allow for improved statistics and a better coverage of the inner-disc regions, thereby providing tighter constraints on the evolution of the central parts of the Milky Way.

6.1. Introduction

The time evolution of Galactic chemical-abundance distributions is *the* missing key constraint to the chemical evolution of our Milky Way (MW; e.g. Matteucci 2003). Several observational questions related to the shape of the present-day abundance distributions as functions of Galactocentric radius, azimuth, height above the disc mid-plane, and age, have been tackled in the past (e.g. Grenon 1972; Luck et al. 2003; Davies et al. 2009; Luck et al. 2011; Boeche et al. 2013; Genovali et al. 2013, 2014; Anders et al. 2014; Hayden et al. 2015; Huang et al. 2015). Especially the radial metallicity gradient, ∂[Fe/H]$/\partial R_{\rm Gal}$ – the dependence of the mean metallicity [Fe/H] of a tracer population on Galactocentric distance $R_{\rm Gal}$ – has been the subject of debate for a long time.

Apart from the mathematical representation of the radial metallicity distribution and its dependence on age, the *interpretation* of gradient data also remains partly unsettled. Galactic chemical-evolution (GCE) models that reproduce abundance patterns in the solar neighbourhood and the present-day abundance gradient can be degenerate in their evolutionary histories (e.g. Mollá et al. 1997; Maciel & Quireza 1999; Portinari & Chiosi 2000; Tosi 2000). One possibility is to start from a pre-enriched gas disc (with a metallicity floor; Chiappini et al. 1997, 2001), which then evolves faster in the central parts, thus steepening the gradient with time. The other possibility is to start with a primordial-composition disc with some metallicity in the central parts (i.e. a steep gradient in the beginning), which then gradually forms stars also in the outer parts, thus flattening the gradient with time (Ferrini et al. 1994; Allen et al. 1998; Hou et al. 2000; Portinari & Chiosi 2000). Additionally, radial mixing (through heating or migration, or, most likely, both) flattens the observed abundance gradients of older stars (e.g. Schönrich & Binney 2009; Minchev et al. 2013, 2014a; Grand et al. 2015; Kubryk et al. 2015a,b). Therefore, the gradient of an old population can be flat either because it was already flat when the stars were formed, or because it began steep and was flattened by dynamical processes.

The answer to the fundamental question of how the MW's abundance distribution evolved with cosmic time is encoded in the kinematics and chemical composition of long-lived stars and can be disentangled most efficiently if high-precision age information is available. To date, the only results that claim to trace the evolution of abundance gradients are based on planetary nebulae (PNe; e.g. Maciel & Chiappini 1994; Maciel & Quireza 1999; Stanghellini et al. 2006; Maciel & Costa 2009; Stanghellini & Haywood 2010) and star clusters (e.g. Janes 1979; Twarog et al. 1997; Carraro et al. 1998; Friel et al. 2002; Chen et al. 2003; Magrini et al. 2009; Yong et al. 2012; Frinchaboy et al. 2013; Cunha et al. 2016), but the former are based on uncertain age and distance estimates and remain inconclusive, while the latter essentially allow for only two wide age

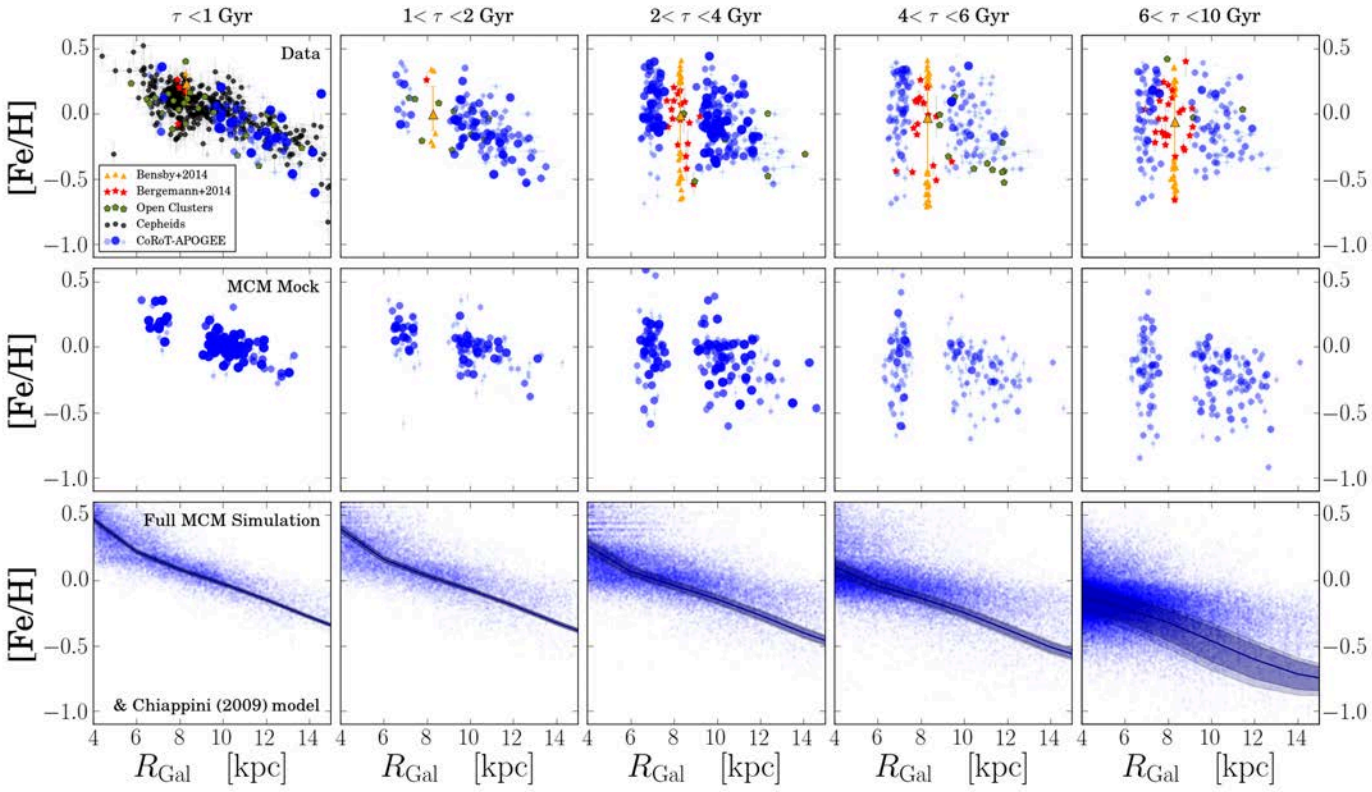

Figure 6.1. The [Fe/H] vs. $R_{\rm Gal}$ distribution close to the Galactic plane ($|Z_{\rm Gal}| < 0.3$ kpc) for five bins in age (from left to right, as indicated in each panel). *Top row:* data compilation. The CoRoGEE sample is shown in *blue*: For each star, we have calculated the fraction of the age PDF enclosed in each age bin – this fraction corresponds to the size of each dot and its transparency value. For comparison, we also show the open cluster compilations of Genovali et al. (2014) and Magrini & Randich (2015) as *green pentagons*, the subgiant sample from Bergemann et al. (2014, *red symbols)*, and Galactic Cepheids (Genovali et al. 2014; *black symbols*). The solar-neighbourhood FGK dwarf sample of Bensby et al. (2014) is plotted as *orange symbols*: The large orange triangles and their error bars denote the median metallicities and the 68% quantiles, while small triangles represent stars that fall outside this range. *Second row:* mock CoRoGEE sample from the chemodynamical simulation of Minchev, Chiappini, & Martig (2013, 2014a, MCM), including typical observational errors in age, distance, and metallicity (Anders et al. 2017, 2016). *Third row:* full MCM simulation without errors, and the underlying chemical-evolution model of Chiappini (2009).

bins, and are affected by low-number statistics and non-trivial biases due to the rapid disruption of disc clusters.

In addition to the value of the abundance gradient itself, the scatter of the $R_{\rm Gal}$−[Fe/H] relation can in principle be used to quantify the strength of radial heating and migration over cosmic time. In this paper, we use combined asteroseismic and spectroscopic observations of field red-giant stars to examine the evolution of the MW's radial abundance gradient in a homogeneous analysis. solar-like oscillating red giants are new valuable tracers of GCE, because they are numerous, bright, and cover a larger age range than classical tracers such as open clusters (OCs) or Cepheids. The combination of asteroseismology and spectroscopy further allows us to determine ages for these stars with unprecedented precision.

This paper is structured as follows: In Sec. 6.2 we present the data used in this study, and in Sec. 6.3 we derive our main result: we present and model the observed [Fe/H] vs. $R_{\rm Gal}$ distributions in six age bins, and discuss these results in detail in Secs. 6.4 and 6.5 (the latter focussing on a comparison with the literature). In Sec. 6.6, we revisit the peculiar finding that old open clusters in the solar neighbourhood tend to have higher metallicities than their younger counterparts. In Sec. 6.7, we analyse the [Mg/Fe] vs. $R_{\rm Gal}$ distributions, also as a function of age. Our conclusions are summarised in Sec. 6.8.

6.2. Observations

The CoRoT-APOGEE (CoRoGEE) sample (Anders et al. 2017) comprises 606 solar-like oscillating red-giant stars in two fields of the Galactic disc covering a wide range of Galactocentric distance (4.5 kpc < $R_{\rm Gal}$ < 15 kpc). For these stars, the CoRoT satellite obtained asteroseismic observations, while the Apache Point Observatory Galactic Evolution Experiment (SDSS-III/APOGEE; Eisenstein et al. 2011; Majewski et al. 2015) delivered high-resolution ($R \sim 22,500$), high signal-to-noise ($S/N > 90$, median $S/N = 240$) H-band spectra using the SDSS Telescope at APO (Gunn et al. 2006). The APOGEE Stellar Parameter and Chemical Abundances Pipeline (ASPCAP; Holtzman et al. 2015; García Pérez et al. 2016) was used to derive stellar effective temperatures, metallicities, and chemical abundances; the results are taken from the Sloan Digital Sky Survey's Twelfth data release (DR12; Alam et al. 2015). In Anders et al. (2017), we computed precise masses (∼ 9%), radii (∼ 4%), ages (∼ 25%), distances (∼ 2%), and extinctions (∼ 0.08 mag) for these stars using the Bayesian stellar parameter code PARAM (da Silva et al. 2006; Rodrigues et al. 2014), and studied the [α/Fe]-[Fe/H] relation as a function of Galactocentric distance, in three wide age bins. Here we slice the data into age bins again, this time examining the dependence of the thin-disc [Fe/H]-$R_{\rm Gal}$ relation on stellar age.

Our final sample comprises 418 stars with $|Z_{\rm Gal}| < 0.3$ kpc: 281 are located in the outer-disc field LRa01 ($l, b = 212, -2$), and 137 in the inner-disc field LRc01 ($l, b = 37, -7$). Because of the location of the CoRoT field LRc01, the cut in $Z_{\rm Gal}$ unfortunately reduces our radial coverage of the inner thin disc, so that we effectively sample Galactocentric distances between 6 and 13 kpc.[1] Our adopted definition of thin disc here is purely geometric (stars close to the disc mid-plane), as opposed to a definition as the low-[α/Fe] sequence in the [Fe/H]-[α/Fe] plane (e.g. Fuhrmann 1998; Lee et al. 2011; Anders et al. 2014). While these two definitions agree well at the solar radius, they do differ in the outer disc (see Minchev et al. 2015 for a discussion on this).

As our data exclude the direct solar neighbourhood, we complement our analysis by comparing our findings to other recent high-resolution studies focussing on the local Galactic environment: For example, Bensby et al. (2014) conducted a spectroscopic solar neighbourhood survey of 714 F & G dwarfs in the Hipparcos volume ($d \lesssim 100$ pc), and derived chemical abundances for 14 chemical elements, as well as stellar ages and orbital parameters. We use the 431 stars for which Bensby et al. (2014), using a kinematical criterion, quote a thin-to-thick-disc probability ratio greater than 1. Bergemann et al. (2014) analysed 144 subgiant stars in an extended solar neighbourhood volume (6.8 kpc $< R_{\rm Gal} <$ 9.5 kpc, -1.5 kpc $< Z_{\rm Gal} <$ 1.5 kpc) from the Gaia-ESO survey's first internal data release (*i*DR1) to derive accurate ages, Fe, and Mg abundances, and study age-chemistry relations in the MW disc. For this study we select the 51 stars with $|Z_{\rm Gal}| < 0.3$ kpc.

In order to compare our data to the young-population abundance distributions measured with Galactic Cepheid variables, we use the compilation of Genovali et al. (2014), which comprises spectroscopic iron abundances for several hundred classical Cepheids close to the Galactic mid-plane.

6.3. The variation of radial [Fe/H] distributions with age

Figure 6.1 shows the age variation of the radial metallicity distribution for stars close to the Galactic plane ($|Z_{\rm Gal}| < 0.3$ kpc), splitting the CoRoGEE stars into five bins in age (0 – 1 Gyr, 1 – 2 Gyr, 2 – 4 Gyr, 4 – 6 Gyr, 6 – 10 Gyr). The CoRoGEE sample is plotted as blue circles, where the size and transparency encode the weight, w_i, of a star in the age bin considered. For example, a star whose age PDF is fully contained in one age bin appears only one time in the diagram, as a large dark blue circle. A star with a broader age PDF will appear in multiple panels of the figure, with the symbol size and hue in each panel indicating the posterior probability for the star to lie in this age bin. For comparison, we also plot the radial abundance distribution as measured from Galactic Cepheids (black dots; compilation of Genovali et al. 2014), OCs (green dots; *ibid.*) and the GES *i*DR1 subgiant sample (red dots; Bergemann et al. 2014). In order to have a better comparison to the solar neighbourhood, we further show how the FGK dwarf sample of Bensby et al. (2014) is distributed in this diagram.

The second row of Fig. 6.1 shows the result of selecting a CoRoGEE-like sample from the N-body chemo-dynamical model of Minchev, Chiappini, & Martig (2013, 2014a, MCM). A detailed description of the MCM-CoRoGEE mock sample

[1] Throughout this paper, we assume $(R_{\rm Gal}, Z_{\rm Gal})_\odot$ = (8.30 kpc, 0.011 kpc), in line with recent estimates (see, e.g. Bland-Hawthorn & Gerhard 2016). All literature data are rescaled to these values.

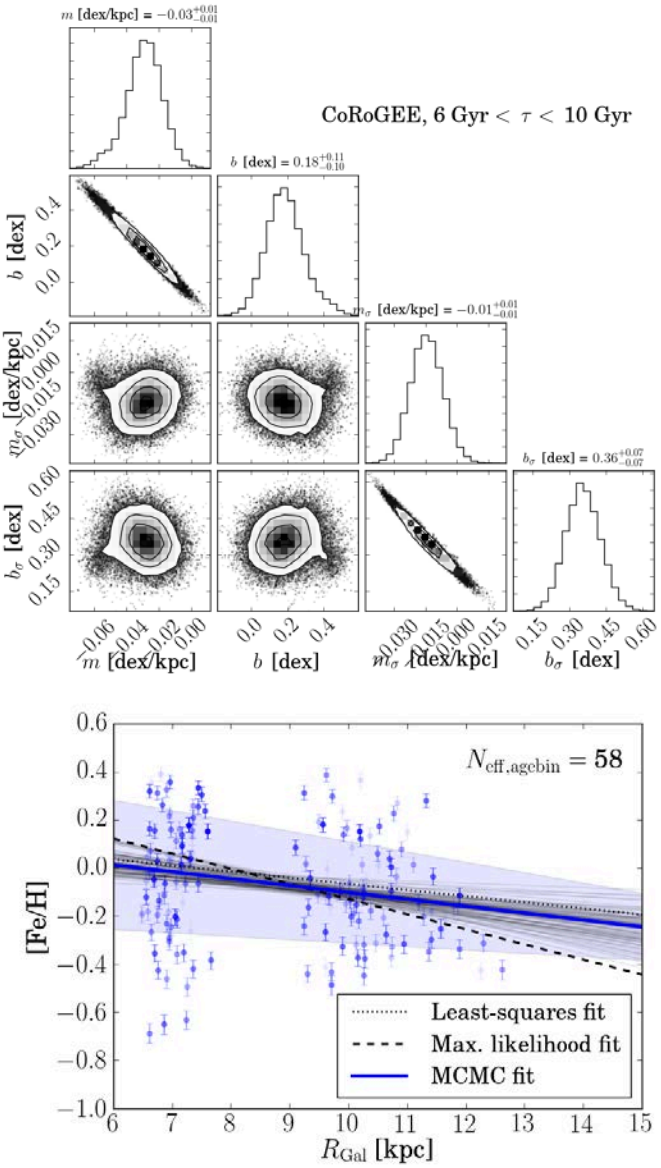

Figure 6.2. *Top panel:* "Corner plot" (Foreman-Mackey et al. 2016) showing an example of an MCMC fit result for the linear gradient + variable scatter model to CoRoGEE data, in the age bin 6 Gyr $< \tau <$ 10 Gyr. Histograms show the marginal posterior PDFs for the fit parameters $(m, b, m_\sigma, b_\sigma)$; the density-scatter plots show the joint marginal posteriors. *Bottom panel:* The resulting fit to the data in the $R_{\rm Gal}$ vs. [Fe/H] diagram. Faint grey lines show 50 MCMC samples; the thick blue line and the shaded band correspond to our best parameter estimates. For comparison, we also show the results of a least-squares linear fit (dotted line) and a maximum-likelihood fit (dashed line).

can be found in Anders et al. (2016, Sec. 3.2). In short, we select particles from the MCM model that follow the observed $R_{\rm Gal}-Z_{\rm Gal}$ distribution and a red giant-population age bias expected from stellar population-synthesis modelling. We also model the age errors introduced by our observations and statistical inference.

The third row shows how all the particles from the MCM simulation are distributed in the $R_{\rm Gal}$ vs. [Fe/H] plane, together with the predictions of the pure chemical-evolution thin-disc model of Chiappini (2009), which was used as an input for the MCM model. The chemical-evolution model was computed in

Galactocentric annuli of 2 kpc width, under the assumption of instantaneous mixing within each ring. The bands shown in Fig. 6.1 reflect the median and the 68% and 95% abundance spread within the particular age bin; for this paper we interpolate the model between the $R_{\rm Gal}$ bins. As in Chiappini et al. (2015), we scale the abundances of the chemical-evolution model such that the solar abundances are compatible with the model at the age of the Sun (4.5 Gyr) at the most probable birth position of the Sun (2 kpc closer to the Galactic Centre than today; Minchev et al. 2013). This calibration also agrees very well with the abundance scale defined by Galactic Cepheids along the Galactic disc (Genovali et al. 2014).

Fitting the [Fe/H] vs. $R_{\rm Gal}$ distributions

From Fig. 6.1 it is evident that the observed [Fe/H] vs. $R_{\rm Gal}$ distributions should not be fitted with a simple linear model, because the observed scatter is generally larger than the formal uncertainties associated with the measurements. We therefore opt to model the [Fe/H] vs. $R_{\rm Gal}$ distributions for each age bin with a Bayesian "linear gradient + variable scatter" model, as follows. Any measured metallicity value, $[{\rm Fe/H}]_i$, is assumed to depend linearly on the Galactocentric radius, $R_{\rm Gal,i}$, convolved with a Gaussian distribution that includes the individual Gaussian measurement uncertainty, $e_{\rm [Fe/H],i}$, and an intrinsic [Fe/H] abundance spread that is allowed to depend linearly on $R_{\rm Gal}$. If we neglect the small uncertainties in $R_{\rm Gal}$ ($\lesssim 2\%$), then the likelihood can be written as:

$$p(\{[{\rm Fe/H}], e_{\rm [Fe/H]}, R_{\rm Gal}, w\}_i | m, b, m_\sigma, b_\sigma) = \prod_{i=1}^{N} w_i \frac{\exp(-\frac{([{\rm Fe/H}]_i - [{\rm Fe/H}]_{R,i})^2}{2\sigma_{R,i}})}{\sqrt{2\pi}\sigma_{R,i}^2},$$

where

$$[{\rm Fe/H}]_{R,i} := m \cdot R_{\rm Gal,i} + b,$$
$$\sigma_{R,i} := \sqrt{e^2_{\rm [Fe/H],i} + (m_\sigma \cdot R_{\rm Gal,i} + b_\sigma)^2},$$

and the weight w_i of each star in a particular age bin is proportional to the integral of its age PDF in this bin:

$$w_i = \int_{\tau_{\rm min}}^{\tau_{\rm max}} d\tau p(\tau).$$

In each age bin, we therefore use an effective number of $N_{\rm eff,agebin} = \sum_i w_i$ stars for the fit.

We further assume flat priors for each of the fit parameters m (the slope of the radial [Fe/H] gradient), b (its intercept), m_σ (the slope of the [Fe/H] scatter as a function of radius), and b_σ (its intercept). The logarithm of the posterior PDF can then be written as:

$$L_p = -\frac{1}{2}\sum_{i=1}^{N}\left\{\ln\sigma^2_{R,i} + \frac{([{\rm Fe/H}]_i - [{\rm Fe/H}]_{R,i})^2}{2\sigma^2_{R,i}} - 2\ln w_i\right\},$$

modulo some arbitrary constant. We examine two possibilities: one where all four parameters $(m, b, m_\sigma, b_\sigma)$ are allowed to vary, and one where we fix $m_\sigma = 0$, that is, an intrinsic [Fe/H] scatter that does not vary with $R_{\rm Gal}$. In the majority of cases the four-parameter model provides a better fit to the data.

To explore the four-dimensional parameter space and estimate the best-fit parameters and their respective uncertainties, we use the Markov-chain Monte-Carlo (MCMC) code *emcee* (Foreman-Mackey et al. 2013). Fig. 6.2 shows an example outcome of our fitting algorithm. The grey lines in this figure indicate individual MCMC sample fits, and the blue line and shaded area represent our best-fit (median) results. For comparison, we also show the least-squares and maximum-likelihood results. As in the example case of Fig. 6.2, the three methods generally do not agree within $1\sigma-$uncertainties (especially for the older age bins), which is why we chose the robust Bayesian method (see, e.g. Hogg et al. 2010; Ivezić et al. 2013).

The results of our attempt to quantify the evolution of the radial [Fe/H] distribution (i.e., fitting for the gradient + scatter) are given in Appendix 6.A, where we provide the tabulated results of our four-parameter fits to the data gathered in Fig. 6.1.

Fig. 6.3 shows the main result of our paper, corresponding to the data compiled in Table 6.1: the five panels show the evolution of the [Fe/H] vs. $R_{\rm Gal}$ relation fit parameters with stellar age for the data and the models used in Fig. 6.1. The first and the third panel directly display the age-dependence of the fit parameters m and m_σ, respectively, while in the other three panels we show the mean [Fe/H] value at $R_{\rm Gal} = 6$ kpc and $R_{\rm Gal} = 12$ kpc, respectively, and the [Fe/H] abundance spread in the solar neighbourhood – these latter are linear combinations of the m, b, m_σ and b_σ. We discuss the implications of this plot in the following section.

6.4. Discussion

The CoRoGEE red-giant sample provides an unprecedented coverage of a large range of the Galactic thin disc ($6 < R_{\rm Gal} \lesssim 13$ kpc, $|Z_{\rm Gal} < 0.3$ kpc, 0.5 Gyr $\lesssim \tau \lesssim 13$ Gyr) with very precise measurements of [Fe/H], $R_{\rm Gal}$, and ages. Although our dataset is not free from biases and selection effects, we can quantify their impact on the derived structural parameters of the MW using mock observations of a chemo-dynamical model that we treat in exactly the same way as the data (Sec. 6.4.2; see also Cheng et al. 2012). In Sec. 6.5 we interpret the results of our analysis presented in Sec. 6.3 in the context of past observational literature. We pay special attention to the intriguing old high-metallicity open clusters in the solar neighbourhood in Sec. 6.6. First, however, we remind the reader of the several difficulties that arise when interpreting similar datasets.

6.4.1. The importance of fitting earnest(ly)

A fit to data can only be as good as the model assumed. The literature (more recently also the astronomical literature) provides good examples of how to find an appropriate model for the dataset considered (e.g. Press et al. 1992; Feigelson & Jogesh Babu 2012; Ivezić et al. 2013). However, in the case of the chemical-abundance gradients, the literature is full of overly simplistic approaches. Especially in the case of OCs and PNe, where data are traditionally sparse, biased, and often decomposed further into age bins (e.g. Janes 1979; Twarog et al. 1997; Friel et al. 2002; Frinchaboy et al. 2013; Magrini & Randich 2015; Jacobson et al. 2016), utmost care must be taken when fitting a straight line through very few datapoints and drawing conclusions about the evolution of the abundance gradient (see, e.g. Carraro et al. 1998; Daflon & Cunha 2004; Salaris et al. 2004; Stanghellini & Haywood 2010). Also, the least-squares method tends to considerably underestimate the uncertainties of the fit parameters when the linear model is inappropriate.

This problem could be mitigated if the number of data points were high enough. Fortunately, this is generally the case for our CoRoGEE sample. In all age bins, the agreement between a least-squares fit and our Bayesian fit for the parameters m and b is at the $1\sigma-$level. Similarly, the effect of including the recent

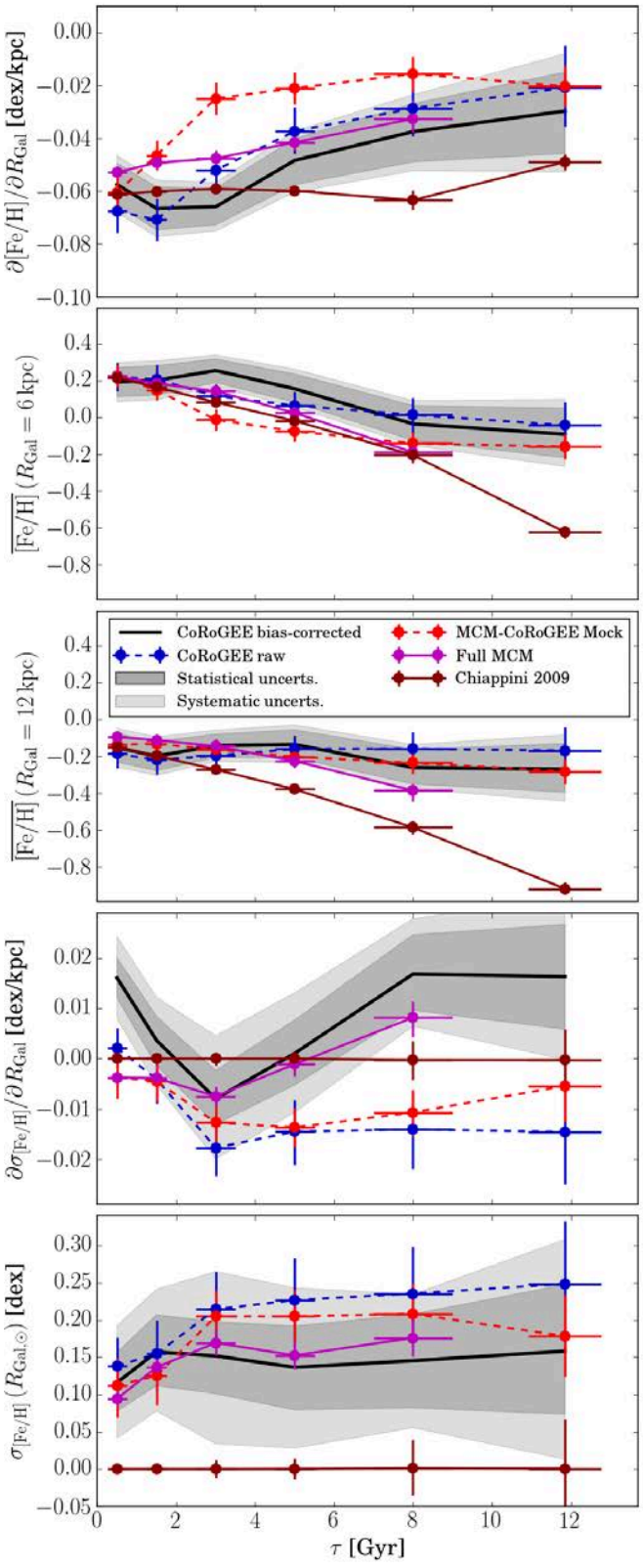

Figure 6.3. Results of our four-parameter fits: The evolution of the slope of the radial metallicity gradient between 6 and 13 kpc (*top panel*), the mean metallicity at $R_{\rm Gal}$ = 6 kpc (*second panel*), the mean metallicity at $R_{\rm Gal}$ = 12 kpc (*third panel*), the slope of the [Fe/H] scatter with Galactocentric radius (*fourth panel*), and the [Fe/H] scatter in the solar annulus (*bottom panel*), for the datasets considered here (error bars). The black line and the shaded bands around it correspond to the bias-corrected CoRoGEE measurements, their statistical uncertainties, and the systematic uncertainties stemming from the bias correction. The fit for the full MCM model did not converge in the last age bin.

literature data (see Sec. 2) in the fit (i.e. increasing the sample size) is minor ($\lesssim$ 0.005 dex/kpc for the gradient), except for the oldest age bin (τ > 10 Gyr, $N_{\rm eff}$ = 27) where the inclusion of literature data increases the sample by a factor of five, and yields a gradient value close to zero (corresponding to a +0.02 dex/kpc with respect to the pure CoRoGEE fit). The fits in this last age bin should therefore be used with caution.

Although our attempt to fit the radial abundance distribution is more elaborate than most methods found in the literature, future data will certainly show if the linear gradient + variable scatter model is sufficient for the part of the Galactic disc considered here. Although there are various indications in the literature (e.g. Vilchez & Esteban 1996; Afflerbach et al. 1997; Twarog et al. 1997; Yong et al. 2005; Lépine et al. 2011; Yong et al. 2012) that the radial abundance gradient flattens beyond a break radius $R_{\rm Gal} \sim 10-15$ kpc, our combined dataset can be well-fit without a two-fold slope or metallicity step. Another important simplification of our model lies in the assumption of Gaussian metallicity distributions at any given Galactocentric distance, which has been shown to be slightly violated in the inner as well as the outer parts of the Galactic disc (Hayden et al. 2015).

6.4.2. Comparison with mock observations of a chemo-dynamical model

As in Anders et al. (2017), we opt for the direct approach to compare our observations to CoRoGEE mock observations of a simulated MW-like galaxy that includes all important features of galaxy evolution (merging satellites, disc heating, radial migration, etc.) from high redshift to date. However, since we want to compare our findings to literature data and other models, in Sec. 6.4.2 we also provide a bias-corrected version of all the parameters that we measure. The bias corrections were obtained by comparing the fits to our mock observations with those to the full MCM model.

From the chemical-evolution model to the MCM model

As explained above, the MCM chemo-dynamical model used the pure chemical-evolution thin-disc model of Chiappini (2009) as an input. The Chiappini (2009) GCE model provided the chemistry for each MCM N-body particle of the cosmological MW-like disc simulation taken from Martig et al. (2012). The GCE model can thus be seen as the initial Galactic chemistry of the MCM model, which is then mixed by dynamical processes. In Figs. 6.1 and 6.3, we directly compare our data with these two models. But first, let us recall how the two models compare among themselves in those plots.

The four panels of Fig. 6.3 show the evolution of the main structural parameters of the [Fe/H] vs. $R_{\rm Gal}$ distribution returned by our MCMC fits. Looking at the Galactic models (see also the bottom panels of Fig. 6.1), the figure highlights the effects of the realistic Galaxy kinematics included in the MCM model on the [Fe/H] vs. $R_{\rm Gal}$ distributions. With look-back time, radial heating and migration gradually blur out the narrow distributions defined by the thin-disc model, and not only increase the amount of [Fe/H] scatter seen in the solar neighbourhood (Fig. 6.3, bottom panel), but also wash out the overall gradient (top panel; see also Minchev et al. 2013, Fig. 5), and increase the mean metallicity at fixed Galactocentric distance, especially in the outer disc (Fig. 6.3, third panel).

In the semi-analytic GCE model, the width of the [Fe/H] distribution at any fixed radius is entirely due to the finite width of

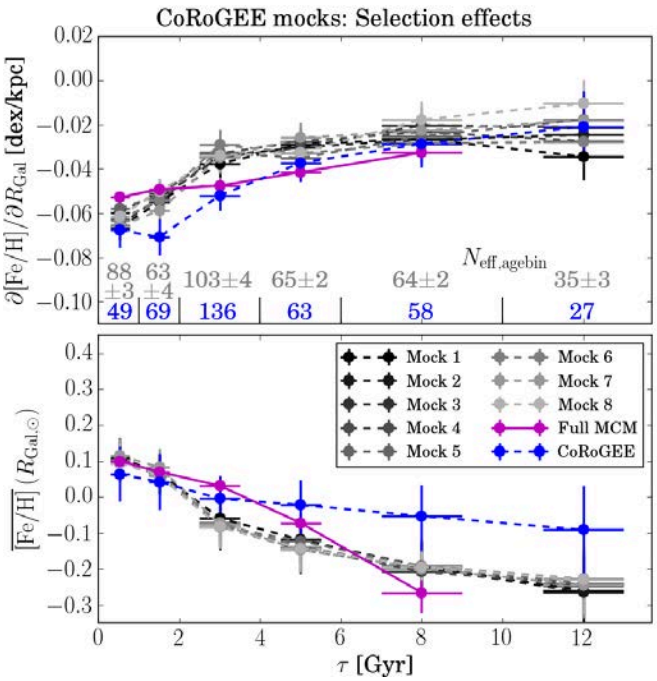

Figure 6.4. Combined effect of mock selection, age errors, and finite sample size on the measurement of the radial [Fe/H] gradients (top panel) and the mean metallicity in the solar neighbourhood (bottom), using eight realisations of the MCM-CoRoGEE mock (grey error bars). Also shown are the fit results of the CoRoGEE dataset (blue) and the full MCM model (magenta). The numbers in the top panel indicate the number of stars in each age bin.

the considered age bin, that is, the intrinsic metallicity spread of the model is negligible. In the MCM model, on the other hand, this abundance spread is caused by radial mixing, which already in the 0 – 1 Gyr bin widens the [Fe/H] distribution by 0.09 dex in the solar neighbourhood (Fig. 6.4). Already after 2 – 4 Gyr, a plateau of $\sigma_{[Fe/H],R_{Gal,\odot}} \simeq 0.15$ dex is reached.

Radial mixing also flattens the chemical gradients predicted by GCE models. In the MCM model, this effect starts to appear for ages $\gtrsim$ 1 Gyr: The Chiappini (2009) model predicts a negative radial [Fe/H] gradient of $\frac{\partial[Fe/H]}{\partial R_{Gal}} \approx -0.06$ dex/kpc that remains largely constant during the evolution of the MW. While the MCM model predicts an almost unchanged gradient for the very young population ($\tau < 1$ Gyr), the gradients of the older thin-disc populations have flattened to ~ -0.05 dex/kpc for 1 – 4 Gyr, and to ~ -0.02 dex/kpc for 6 – 10 Gyr. In the last age bin ($\tau > 10$ Gyr), the abundance distribution is so dominated by scatter that it is not well-fit by the linear gradient model any more; the MCMC chains did not converge.

Radial mixing also affects the mean metallicity in the solar neighbourhood and the outer disc, in the sense that it tends to bring more metal-rich stars from the inner disc into the solar neighbourhood than low-metallicity outer-disc stars, because of asymmetric drift and radial migration. This effect starts for ages $\gtrsim$ 2 Gyr, and produces an approximately constant mean-metallicity shift of $\sim +0.1$ dex in the solar neighbourhood, and $\sim +0.2$ dex at $R_{Gal} = 12$ kpc.

One effect that is evident from Fig. 6.1, but not entirely captured by our linear fitting model, is the emergence of extreme migrators from the inner disc with super-solar metallicities in the region 5 kpc $< R_{Gal} <$ 8 kpc. We discuss this result in the context of open-cluster observations in Sec. 6.6.

From the MCM model to the CoRoGEE mock: the impact of selection effects

In Fig. 6.4, we assess the impact of selection effects and stochasticity on the measured [Fe/H] gradient: We ran the CoRoGEE mock-selection algorithm (Anders et al. 2016) eight times and fit the linear gradient + variable scatter model to all resulting [Fe/H] vs. R_{Gal} distributions, as before. As can be clearly seen in the top panel of Fig. 6.4, the measured gradient in the CoRoGEE-like MCM mock varies by ±0.01 dex/kpc, depending on the realisation of the mock algorithm. The magnitude of these variations is comparable with the uncertainties derived with the MCMC fitting, which means that our quoted uncertainties are reliable. Since the fit parameters m and b are correlated, the stochasticity effect on the measured mean metallicity is minor.

However, there are also systematic differences between the fit results for the mock realisations and those for the full MCM model, most evidently in the age bins older than 2 Gyr. This is the regime where the combined effects of the red-giant selection bias and systematic age errors begin to matter. Specifically, the systematic biases introduced by the selection let the [Fe/H] gradient appear even flatter than in the model, most notably in the age bin 2–4 Gyr, where the effect has an average magnitude of +0.02 dex/kpc. A systematic selection effect on the measurement of the mean [Fe/H] near the Sun is also notable in the same age bins: the mock procedure leads to an underestimation of the "true" [Fe/H] of the MCM model for the intermediate age bins, and to a slight overestimation in the range 6–10 Gyr. In Sec. 6.4.2, we use these results to correct our CoRoGEE measurements for selection biases, to be able to compare to literature data and other Galactic models.

Comparing the mock results to the CoRoGEE observations

The second row of Fig. 6.1 shows one realisation of the MCM CoRoGEE mock. At first sight, the [Fe/H] vs. R_{Gal} distributions of data and model look remarkably similar, indicating a good overall performance of both the MCM model and the mock algorithm. However, the differences between the relative number of stars in each age bin and field are not within the expected stochastic fluctuations (see numbers in Fig. 6.4). This mismatch of the age distributions in the mock and the data was already shown in Anders et al. (2016, Fig. 6). We tentatively attribute it to an imperfect modelling of the age bias of the CoRoGEE sample.

Quantitative differences become apparent when looking at the fit results: Fig. 6.4 demonstrates that for $\tau < 4$ Gyr, the radial [Fe/H] gradients of all mock realisations are flatter than the observed, and that for ages larger than 2 Gyr the mean [Fe/H] in the solar neighbourhood is underestimated by the MCM mocks.

For both model and data, the negative radial metallicity gradient persists in the intermediate-age and old populations, although it gradually becomes shallower and the abundance scatter increases. The increase of this scatter with look-back time is due to a superposition of: a) growing age uncertainties towards intermediate ages (see Anders et al. 2017); b) dynamical processes of radial heating and migration (e.g. Sellwood & Binney 2002; Schönrich & Binney 2009; Minchev et al. 2010; Brunetti et al. 2011); and c) intrinsic time variations of the metallicity distribution (which in the MCM model are negligible; see Sec. 6.4.2). In Fig. 6.3 we show that the abundance scatter in the MCM model already saturates in the 2–4 Gyr bin, and that almost half of the abundance scatter measured in the subsequent age bins

for CoRoGEE may be explained by a combination of abundance and age errors (compare the magenta and red lines).

In the $\tau < 1$ Gyr panel of Fig. 6.1, the [Fe/H] abundance spread appears to increase somewhat towards very large Galactocentric distances – an effect that is not seen in the MCM model. The (fewer) data beyond $R_{\rm Gal} \sim 12$ kpc also seem compatible with a flat abundance distribution, as previously argued for in the OC literature (e.g. Twarog et al. 1997; Lépine et al. 2011; Yong et al. 2012). Part of the discrepancies between the data and the MCM model, such as the flattening of the [Fe/H] gradient in the local outer-disc quadrant, may be due to our averaging over the azimuthal angle in Galactocentric cylindrical coordinates (Minchev et al., in prep.).

Using the mock sample to correct for selection effects

Under the assumptions that the MCM model is an appropriate model of our Galaxy, and that our mock selection is a good approximation of the true selection function, we can use the differences found between the fits to the MCM mock and the full model (Sec. 6.4.2) to correct for the selection biases of the CoRoGEE sample. The first assumption has been extensively tested on a variety of datasets in Minchev et al. (2013, 2014a,b), and Piffl (2013). The second assumption was sufficiently validated recently in Anders et al. (2017, 2016). Of course, the bias correction comes at the price of an additional systematic uncertainty that is driven by the relatively small size of our sample.

In Figs. 6.3 and 6.5, we also plot the bias-corrected results for the fit parameters measured with CoRoGEE. In each panel the dark-grey bands correspond to the statistical uncertainties of the fit, while the light-grey bands correspond to the systematic uncertainty associated with the bias correction (which we conservatively estimate as the standard deviation of the mock results among different realisations). The additional uncertainty associated with this correction is most important for the fit parameters m and m_σ. For the oldest age bin, the corrections from the age bin 6 – 10 Gyr were used, since we could not perform a reliable fit for the full MCM model in this bin. The corrections for the oldest bin should therefore be used with caution.

We can now also compare the bias-corrected CoRoGEE results directly to the results obtained from the MCM model. Qualitatively, we reach the same conclusions as before: overall, the MCM model provides a very good model for our data, and in most of the age bins the fit parameters for data and model are 1σ-compatible (at most 2σ) with each other. As already shown by Minchev et al. (2013, 2014a), the dynamics of the model give a very good quantitative prescription of the secular processes taking place in the MW. The most important differences can probably be fine-tuned in the underlying chemical-evolution model: The observed radial [Fe/H] gradient appears to be slightly steeper than predicted by the model, and the evolution of the mean [Fe/H] from the solar neighbourhood inwards is slightly flatter than in the model. Also, at odds with the GCE model, the gradient of the youngest population (in concordance with Cepheid measurements) seems to be slightly shallower than the gradient of the 1–4 Gyr population. However, these discrepancies are marginal compared to other shortcomings of the model, such as the missing bimodality in the [α/Fe] diagram, and the systematic uncertainties still involved in stellar age, distance, and abundance estimates.

6.4.3. The impact of potential systematic age errors

Recently, observational as well as theoretical work has raised doubts about the zero-points of the asteroseismic scaling relations that lead to the precise mass and radius measurements for solar-like oscillating red-giant stars. The absolute scale of seismic masses can only be tested using star clusters and double-lined eclipsing binaries. Recent advances using these techniques for several small datasets (Brogaard et al. 2015, 2016; Miglio et al. 2016; Gaulme et al. 2016) indicate that asteroseismic scalings tend to overestimate red-giant masses and radii by approximately +10-15% and −5%, respectively. A +10% shift in the seismic masses would result in a $\sim$ +30% shift of our absolute age scale, and consequently our measurements of the evolution of Galactic structural parameters with stellar age would be affected at this level. However, another potentially important effect that has not previously been taken into account is a metallicity-dependent temperature offset between spectroscopic red-giant observations and stellar models (Tayar et al., in prep.). For PARSEC models, this effect likely decreases the absolute ages of sub-solar metallicity CoRoGEE stars by a small amount. Because a systematic analysis of the above effects is still premature, we here restrict ourselves to caution the reader about these caveats to our absolute age scale. For further discussion of systematic age uncertainties, see also Sec. 3 of Anders et al. (2017).

6.5. A comparison with the literature

As reviewed in the Introduction, the chemical-evolution literature of the past $\gtrsim$ 20 years has been accompanied by a controversy about both measurement and interpretation of the evolution of the Milky Way's radial abundance gradient. Fig. 6.5 illustrates the recent history of this controversy: it shows the radial [X/H] gradient as a function of tracer age, as reported by various groups in the literature (compare, e.g. Daflon & Cunha 2004; Chiappini 2006).

The datasets as well as the methods used to derive the results included in Fig. 6.5 are of course very diverse, and deserve a closer look, but the overall situation is clear: There is no consensus about the evolution of the Galactic radial metallicity gradient over cosmic time, not among groups using the same tracers, and sometimes not even among the same groups, or the same datasets. This is essentially due to five reasons:

1. Different radial and vertical ranges of the disc considered;
2. Different age, distance, and abundance scales among different groups, and between different tracer populations, especially in the case of PNe;
3. Different selection biases for the various tracers;
4. Insufficient statistics;
5. Different fitting methods, handling of outliers, etc. (Sec. 6.4.1).

The literature results included in Fig. 6.5 were derived using four different tracers (PNe, OCs, Cepheids, and low-mass field stars) that are discussed separately below. For the radial [Fe/H] gradient traced by the very young population (white star in Fig. 6.5) we use the recent result of Genovali et al. (2014), which is based on a sample of 450 Galactic Cepheids located at Galactocentric distances between 5 and 12 kpc, using data from Lemasle et al. (2007, 2008); Romaniello et al. (2008); Luck et al. (2011); Luck & Lambert (2011); Genovali et al. (2013). The authors find a gradient slope of −0.05 to −0.06 dex/kpc, slightly depending on the adopted cuts in $R_{\rm Gal}, |Z_{\rm Gal}|$. We therefore adopt a value -0.055 ± 0.05 dex/kpc, which coincides with

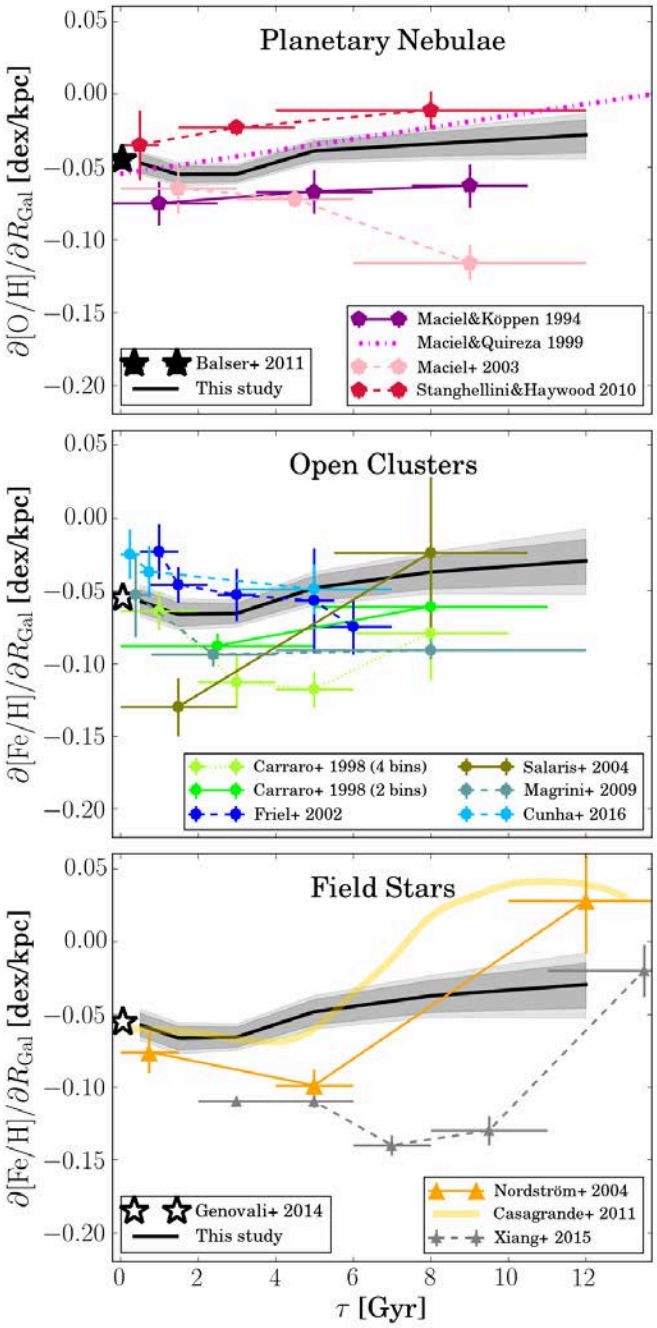

Figure 6.5. An incomplete but representative look into the literature: the dependence of the radial [X/H] gradient slope near the Sun on tracer age τ, as measured by different groups. For the open-cluster (*middle panel*) and field-star (*bottom*) studies, we plot the results for [Fe/H], for planetary-nebula studies (*top*) [O/H]. In all panels, the CoRoGEE results are overplotted as a black line and two grey-shaded bands that correspond to the statistical and systematic uncertainties.

their value for $|Z_{\rm Gal}| < 0.3$ kpc. For the [O/H] gradient, other young tracers such as OB stars or HII regions have to be used (Deharveng et al. 2000; Daflon & Cunha 2004; Rood et al. 2007; Balser et al. 2011); those studies report slightly flatter slopes ($\sim -0.04 \pm 0.01$ dex/kpc). In Fig. 6.5, we include the value -0.045 ± 0.005 dex/kpc as a representative datum, obtained by Balser et al. (2011) from high-quality radio observations of 133 HII regions covering a large azimuthal range of the Galactic disc.

The PNe-based results for the evolution of the radial [O/H] gradient are shown in the top panel of Fig. 6.5. We have used the same technique as before to also fit the radial [O/H] distribution (results can be found in table 6.2), and compare the resulting gradient slope to three representative values from the literature. The studies by Maciel & Köppen (1994) and Stanghellini & Haywood (2010) divided their objects into the three classical categories of disc PNe: type I, II, and III (Peimbert 1978; Faundez-Abans & Maciel 1987), corresponding to different masses and hence ages of the PNe's central stars. In their paper, Maciel & Köppen (1994) find hints that the radial [O/H] gradient flattens slightly with look-back time, starting from a steep value of -0.075 ± 0.015 dex/kpc for massive type-I PNe to -0.063 ± 0.015 for the low-mass type-III objects. Maciel & Quireza (1999) reach a similar conclusion and, extrapolating the trend to the early phases of the Galactic disc, calculate a first estimate of the temporal flattening of the [O/H] gradient with age: $\frac{\partial}{\partial\tau}\frac{\partial[\rm O/H]}{\partial R_{\rm Gal}} \sim -0.004\,\rm dex\,kpc^{-1}\,Gyr^{-1}$. This estimate is in overall agreement with the trend we derive from the CoRoT-APOGEE data. Stanghellini & Haywood (2010) also find that the radial [O/H] gradient flattens with look-back time, although their derived slopes are generally flatter.

However, the early findings of Maciel and collaborators are at odds with their later results (e.g. Maciel et al. 2003; Maciel & Costa 2009; Maciel et al. 2012) that report an opposite trend for the evolution of the radial [O/H] gradient. These later studies preferred different methods to assign PN ages over the traditional Peimbert classification scheme. For example, Maciel et al. (2003) derived ages using statistical relationships between [O/H] and [Fe/H], as well as an age-metallicity-$R_{\rm Gal}$ relationship, which makes their subsequent measurement of the radial metallicity gradient using these ages a rather circular exercise.

Because the PN studies still yield inconclusive results, we caution against arbitrary use of PN-derived abundance gradients (see also Stasińska 2004; Stanghellini et al. 2006; Stanghellini & Haywood 2010; García-Hernández et al. 2016 for additional remarks regarding the derivation of PN abundances and distances).

In Fig. 6.5, we also show several results derived from spectroscopic OC observations (Carraro et al. 1998; Friel et al. 2002; Salaris et al. 2004; Magrini et al. 2009; Cunha et al. 2016). This is by no means an exhaustive compilation, but the diversity of the conclusions reached is representative. As pointed out in Sec. 6.4.1, many of these results rely on very few datapoints, so that their linear fits are subject to significant influence by single outliers (e.g. Berkeley 29 and NGC 6791; see also Sec. 6.6), and sometimes the OC samples are dominated by outer-disc objects.

The 37 clusters studied by Carraro et al. (1998) span a wide range of Galactocentric distances (7 – 16 kpc), but also a considerable range of heights above the Galactic-disc plane (0 – 2.1 kpc). This makes their results difficult to compare, as the clusters located at high $|Z_{\rm Gal}|$ also tend to be at larger $R_{\rm Gal}$, that is, it is almost impossible to disentangle radial and vertical trends, and their quoted radial [Fe/H] gradients are therefore very likely to be significantly overestimated for the older age bins. Also, the authors demonstrate that the age binning impacts their conclusion about the evolution of the abundance gradient along the disc (compare dotted and solid lime-green curves: 4 bins vs. 2 bins), because of the lack of OCs older than > 2 Gyr.

This situation has improved slightly in the past few years; for example, in the works of Friel et al. (2002) and Chen et al. (2003) the number of chemically-studied OCs increased to over 100, and Friel et al. (2002) specifically focussed on old OCs to trace the evolution of the Galactic radial metallicity gradient.

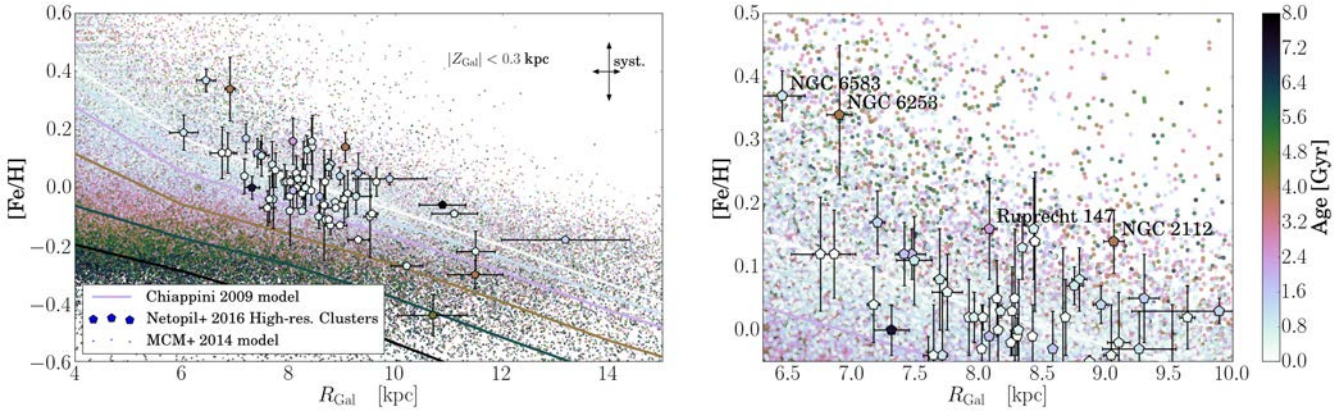

Figure 6.6. The [Fe/H] vs. $R_{\rm Gal}$ distribution, colour-coded by age, for the high-resolution OC compilation of Netopil et al. (2016, *pentagons)*, the MCM model close to the Galactic plane ($|Z_{\rm Gal}| < 0.3$ kpc; *small dots*), and the Chiappini (2009) thin disc model at six time snapshots (*thick lines*). The models have now been scaled to the abundance scale of young OCs in the Netopil et al. sample, which is $\lesssim 0.1$ dex lower than the Cepheid abundance scale of Genovali et al. (2014) used before. The arrows in the left panel symbolise the approximate uncertainties in the absolute metallicity scale and the distance to the Galactic centre. The *right panel* magnifies the interesting part of the left panel, such that it is clear that some older OCs have higher metallicities than both the younger ones and the local ISM. With the MCM model, these can be explained as surviving migrators from the inner disc.

Overall, the OC works of Friel et al. (2002); Chen et al. (2003); Magrini et al. (2009), and also the later studies of Frinchaboy et al. (2013) and Cunha et al. (2016), using APOGEE data, all reach the same conclusions: that the radial metallicity gradient has been steeper in the past. However, this paradigm has been challenged by Salaris et al. (2004) who, using the old OC sample of Friel (1995), reach the opposite conclusion, namely that the radial [Fe/H] gradient of the old OC population is shallower than the gradient of the young population. In summary, and similar to the case of the PN studies (but due to different reasons), OC studies still fail to conclusively answer the question of the evolution of the abundance gradient along the MW disc.

Some works based on field stars attempted to measure the age-dependence of the Galactic radial metallicity gradient, all of them derived from low-resolution spectroscopic stellar surveys. The Geneva-Copenhagen survey of the solar neighbourhood (GCS; Nordström et al. 2004, orange triangles in Fig. 6.5) derived kinematics, metallicities, and ages for 14,000 FGK dwarfs for which precise astrometric distances were delivered by the *Hipparcos* satellite (Perryman et al. 1997; van Leeuwen 2007). Because their sample does not extend beyond the immediate solar neighbourhood, the authors used the precise kinematic information to correct for the eccentricity of stellar orbits, and report metallicity distributions as a function of orbital guiding radii R_g (instead of $R_{\rm Gal}$), in three bins of age. While their result for the young population ($\tau < 2$ Gyr) is consistent with our findings, their intermediate-age population (4 Gyr $< \tau <$ 6 Gyr) exhibits a steeper negative gradient of ~ -0.1 dex/kpc (possibly related to the fact that they use R_g as a baseline), and the old population is consistent with no radial gradient.

The age estimates derived in Nordström et al. (2004) were later improved (Holmberg et al. 2007, 2009; Casagrande et al. 2011), and their results for the age dependence of the metallicity gradient were also revised by Casagrande et al. (2011). In the last panel of Fig. 6.5, we plot the smooth result that these authors obtain for the evolution of the radial metallicity gradient with respect to the mean orbital radius, computing the gradient in a Gaussian age window of 1.5 Gyr width, and using a kinematic cut to sort out halo stars. Because their sample (even in a given age window) is very large, the formal uncertainties on the gradient measurement are almost negligible. Again, the GCS data seem to indicate an initial steepening, then a rapid flattening with increasing age, although Casagrande et al. (2011) caution that this picture depends severely on selection effects. They invoke radial migration to explain the observed softening of the gradient at intermediate ages.

The main advantage of the solar-Neighbourhood studies of Nordström et al. (2004) and Casagrande et al. (2011) lies in their use of very precise kinematic parameters in combination with unprecedented statistics, an asset that will soon be provided for a much larger volume by the *Gaia* mission (Perryman et al. 2001). On the other hand, the GCS metallicities and – above all – ages are likely to be affected by significant systematic shifts, and contamination by thick-disc stars.

The other stellar survey that recently led to an estimation of the age-dependence of the radial metallicity gradient is the LAMOST Spectroscopic Survey of the Galactic Anti-Center (LSS-GAC; Liu et al. 2014). Xiang et al. (2015) have used 300,000 main-sequence turn-off stars selected from that survey to measure the radial and vertical stellar metallicity gradients as a function of stellar age, which they determine via isochrone fitting. With their impressive statistics, these authors can measure very precise relative stellar-population trends. After correcting for selection effects, they find that the radial [Fe/H] gradient close to the Galactic plane steepens with age until $\tau \sim 7-8$ Gyr before flattening again, and interpret these time spans as corresponding to two distinct phases of the assembly of the MW disc.

However, the analysis of Xiang et al. (2015) is based on low-resolution, low-signal-to-noise data, leading to much larger individual uncertainties in their ages, distances, and metallicities compared to our data. Although this is partly mitigated by the large number of stars, considerable systematic uncertainties and poor absolute calibrations are expected for their age and distance estimates, therefore we do not expect the absolute values of their reported gradients to perfectly match ours, nor other literature values.

Recently, several authors (Anders et al. 2014; Hayden et al. 2014; Bovy et al. 2014) have used data from the APOGEE survey to measure the radial disc metallicity gradient. Our bias-corrected values for the gradient slope are slightly shallower than theirs, but compatible with them within our quoted uncertainties. The differences in the absolute values of the metallicity gradient

are most probably due to different selection biases in previous works. For example, Bovy et al. (2014) measured a slope of −0.09 dex/kpc based on 971 RC stars very close to the plane ($Z_{\rm Gal} < 50$ pc), while our sample extends up to distances of 300 pc from the Galactic mid-plane. The APOGEE RC sample is also much more limited in age coverage ($\sim 0.8 - 4$ Gyr with a peak close to 1 Gyr, see e.g. Girardi 2016) than our sample. In contrast to the results of the above authors, and because our sample is considerably smaller, we have corrected our results for selection biases and included a corresponding systematic uncertainty.

6.6. Intermediate-age high-metallicity open clusters in the solar neighbourhood

Radial mixing (by migration and heating) can explain the presence of super-metal-rich stars in the solar neighbourhood (e.g. Grenon 1972, 1999; Chiappini 2009; Minchev et al. 2013; Kordopatis et al. 2015; Anders et al. 2017). Here we show that radial migration can also explain the existence of intermediate-age super-solar metallicity objects in the solar-vicinity thin disc ($R_{\rm Gal} = 7 - 9$ kpc). In the MCM model, those objects originate from the inner disc ($R_{\rm Gal} = 4 - 6$ kpc) and already start to appear in the solar vicinity after 2–4 Gyr after their birth (see Fig. 6.1, bottom row). In this Section we demonstrate this for the case of intermediate-age open clusters in the solar vicinity.

The left panel of Fig. 6.6 shows the [Fe/H] vs. $R_{\rm Gal}$ distribution of the homogenised OC compilation recently published by Netopil et al. (2016), colour-coded by cluster age. The right panel zooms closer in on the solar neighbourhood. For all of the clusters included in the plot, [Fe/H] was derived from high-resolution spectroscopy, in most cases by different groups (see Netopil et al. 2016 and references therein for details). In Fig. 6.6 we also show the MCM model for $|Z_{\rm Gal}| < 0.3$ kpc and the thin-disc model of Chiappini (2009), for snapshots at $\tau = 0, 1, 2, 4, 6,$ and 8 Gyr. Because we found the Fe abundance scales of OCs and Cepheids to be slightly offset with respect to each other ($\lesssim 0.1$ dex), for this plot the models' [Fe/H] values were rescaled to match the abundance scale defined by the youngest OCs of Netopil et al. (2016) in the solar neighbourhood.

It can be clearly seen from Fig. 6.6 that, while the chemical-evolution model alone cannot explain the location of all of the clusters in the [Fe/H] vs. $R_{\rm Gal}$ plane, the MCM model can: for each cluster there is an N-body particle in the model with very similar properties $\{R_{\rm Gal}, [{\rm Fe/H}], \tau\}$. In particular, the MCM model predicts that slightly older clusters can be found at larger metallicities than the youngest ones, in the $5 - 8$ kpc region of the disc (see also Netopil et al. 2016). Contrary to the interpretation of Jacobson et al. (2016), this effect is entirely due to radial mixing, and does not mean that the local ISM had a higher metallicity in the past, nor that the radial [Fe/H] gradient was significantly steeper in the past.

We remind the reader that the fact that for each OC we find a model particle with similar properties does not mean that the model fits perfectly: the selection function (as a function of age and position) of any OC catalogue would be required for any meaningful comparison of the *distributions* of model and data points in Fig. 6.6. This, in turn, requires knowledge about the disruption timescales of clusters as a function of their masses and kinematics, survival rates, initial mass functions, and so on that still remain uncertain. The absence of lower-metallicity intermediate-age OCs in the inner disc (Fig. 6.6, left panel) especially suggests that non- or inward-migrating OCs may be more prone to disruption. This would lead to a higher rate of high-metallicity OCs in the $R_{\rm Gal} = 6-8$ kpc regime, and consequently a significantly steeper (up to a factor of 2) local gradient of the intermediate-age OC population, as measured in the OC literature (e.g. Carraro et al. 1998; Friel et al. 2002; Jacobson et al. 2016). The prediction of the MCM model is that this does not happen for the general field-star population of the same age, which is confirmed by the CoRoGEE data.

6.7. The variation of radial [Mg/Fe] distributions with age

Among many other elements, the APOGEE/ASPCAP pipeline also delivers Mg abundances for our red-giant sample. These can be compared to the predictions of chemical-evolution and chemo-dynamical models. In Fig. 6.7, we show the [Mg/Fe] vs. $R_{\rm Gal}$ distributions for the same data and in the same age bins as in Fig. 6.1.

The behaviour of [Mg/Fe] with time and Galactocentric radius reflects the star-formation history of the Galactic disc. In an inside-out forming disc (such as the MCM model and its underlying GCE model; bottom row of Fig. 6.7), the inner parts of the disc form more stars per unit of time than the outer parts, which results in a positive radial [Mg/Fe] gradient that slowly evolves with look-back time. Although the observational effects affecting our CoRoGEE sample smear out this clear signature in the [Mg/Fe]−$R_{\rm Gal}$ diagram (middle row of Fig. 6.7), the data clearly confirm the inside-out formation of the thin disc.

While the [Mg/Fe] vs. $R_{\rm Gal}$ distributions from the pure chemical-evolution model seem to follow a quadratic rather than linear trend, the data in the range 6 kpc $< R_{\rm Gal} \lesssim 13$ kpc can be well-fit with the same linear gradient + variable scatter model presented in Sec. 6.3. We therefore also provide fits to this model in Appendix 6.A, Table 6.3, and show the evolution of the fit parameters as a function of stellar age in Fig. 6.8.

As for the case of the radial [Fe/H] gradients, the MCM model matches the qualitative trends in the data extremely well, and also agrees with the data in an absolute sense in all age bins at a 2σ level. This is not a completely natural outcome, since the main observational constraints used to construct the GCE model were the present-day star-formation rate and [Fe/H] gradient, and the metallicity distribution in the solar neighbourhood. The comparison between the GCE and the MCM model (bottom panels of Fig. 6.7) shows that the radial [Mg/Fe] distributions are not affected as severely by radial migration as the [Fe/H] gradients shown in Fig. 6.1 (see also Minchev et al. 2014a). This is likely to be due to the shallow slope of the radial [Mg/Fe] gradient, and its slow evolution (flattening at greater ages). The [Mg/Fe] scatter in the MCM models decreases slightly with Galactocentric distance, an effect that is also seen in the data. The [Mg/Fe] scatter at the solar radius in both model and (bias-corrected) data saturates already for ages $\gtrsim 2$ Gyr at a level of $\simeq 0.05$ dex.

An obvious drawback of our approach is that we do not explicitly fit the observationally-confirmed high-[α/Fe] sequence (Fuhrmann 2011; Anders et al. 2014; Nidever et al. 2014) separately, and therefore our thin-disc [Mg/Fe]-gradient measurement is slightly biased: high-[α/Fe] stars with $|Z_{\rm Gal}| < 0.3$ kpc, old or young, contribute to the scatter seen in the first row of Fig. 6.7. While their number clearly increases with age, a small number of them is seen in the younger panels. As discussed in Chiappini et al. (2015), this is in disagreement with GCE predictions. It is still under debate whether these stars are truly young or either the product of close-binary evolution, or inaccurate mass measurements (Martig et al. 2015; Brogaard et al. 2016; Jofré et al. 2016;

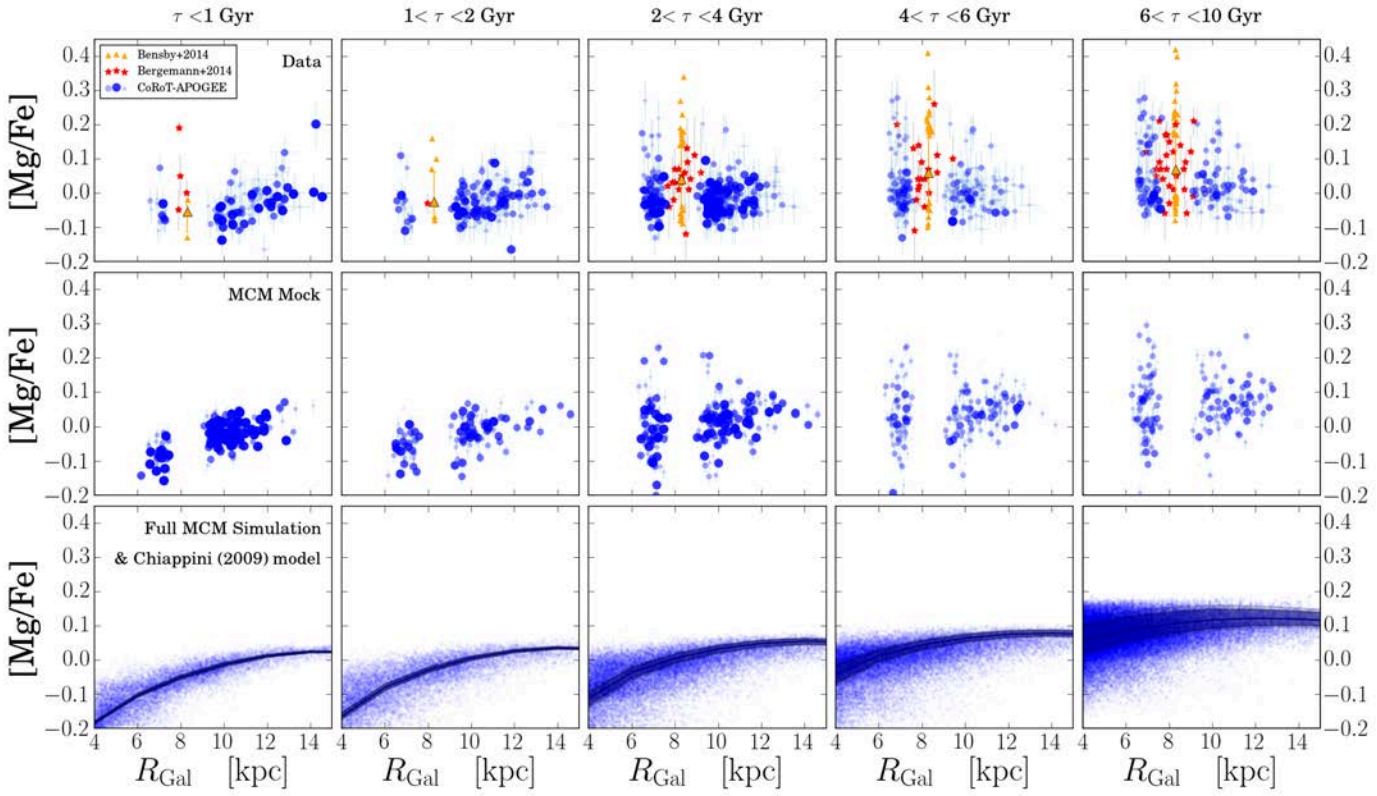

Figure 6.7. The [Mg/Fe] vs. $R_{\rm Gal}$ distributions close to the Galactic plane ($|Z_{\rm Gal}| < 0.3$ kpc), in the same style as Fig. 6.1.

Yong et al. 2016). Our CoRoGEE results (Chiappini et al. 2015) appear to favour a physical origin, since the observed number of these peculiar objects is much higher in the inner-disc field LRc01 (at $R_{\rm Gal} < 6$ kpc, for which $|Z_{\rm Gal}| > 0.3$ kpc).

6.8. Conclusions

We have used the wide coverage of the CoRoT-APOGEE sample in age and Galactocentric distance to study the age dependence of the Galactic radial [Fe/H] and [Mg/Fe] gradients in the range $\{6 < R_{\rm Gal} \lesssim 13$ kpc, $|Z_{\rm Gal}| < 0.3$ kpc, 0.5 Gyr $\lesssim \tau \lesssim 13$ Gyr$\}$. When corrected for selection biases, we find that the slope of the [Fe/H] gradient is constant at a value of $\simeq -0.07$ dex/kpc in the age range $1 < \tau < 4$ Gyr, and slightly flatter for the youngest age bin, in agreement with Cepheid results. For older ages (where our age measurements are more uncertain), the slope flattens to reach values compatible with a flat distribution. We further confirm that the mean metallicity in the solar neighbourhood has remained approximately constant at solar values during the last ~ 5 Gyr. At the same time, the [Fe/H] abundance spread in the solar neighbourhood does not increase significantly with age, within our uncertainties, and remains around 0.15 dex for $\tau \gtrsim 1$ Gyr.

We have compared our results with mock observations of the chemo-dynamical Milky-Way model by Minchev et al. (2013, 2014a), and find a surprisingly good quantitative agreement for the [Fe/H]-$R_{\rm Gal}$, as well as for the [Mg/Fe]-$R_{\rm Gal}$ distributions. This enabled us to use the mock results to correct our measurements for selection biases; the bias-corrected results can be directly compared to other models as well as results from the literature. They agree well with previous estimates of the evolution of the radial metallicity gradient from the Geneva-Copenhagen survey (Nordström et al. 2004; Casagrande et al. 2011), while they disagree with the recent LAMOST study of Xiang et al. (2015) as well as most PN and OC results. These differences can be explained by systematic shifts in the distance and/or age scales for the case of the PNe and LAMOST turn-off stars, and by strong non-trivial selection biases and small-number statistics in the case of the OCs.

We also investigate in more detail why, in the 5−8 kpc region of the disc, intermediate-age OCs are found at larger metallicities than the youngest ones. Within the MCM model, we can explain this effect by strong radial mixing (due to both heating and migration) from the inner disc. Together with our proposition that non- and inward-migrating clusters are disrupted faster, the model can also explain the puzzling observation that the radial [Fe/H] gradient of the intermediate-age cluster population seems to be much steeper than both the young-population gradient and the gradient traced by intermediate-age field stars.

Due to the high accuracy and precision of our distances and [Fe/H] estimates, in combination with sufficient statistics and easily-accountable selection biases, field-star studies like ours are likely to supersede gradient studies using open clusters or planetary nebulae as abundance tracers. Even though the absolute age scale of red-giant asteroseismology is not settled yet (e.g. Brogaard et al. 2015, 2016; Miglio et al. 2016), relative ages seem to be robustly determined for the vast majority of stars. In the near future, many more fields in the K2 asteroseismic ecliptic-plane survey (Howell et al. 2014) will be co-observed by the major spectroscopic stellar surveys (e.g. Stello et al. 2015; Valentini et al. 2016). A joint spectroscopic and asteroseismic analysis of these fields will allow for a much larger sample, and consequently a more precise measurement of the Milky Way's chemo-dynamical history.

Acknowledgements. The authors thank the anonymous referee for her/his suggestions that helped improve the quality of the paper. FA thanks Omar

Choudhury for the right tip at the right moment, and Martin Netopil for providing his open cluster data. TSR acknowledges support from CNPq-Brazil. BM acknowledges financial support from the ANR program IDEE Interaction Des Étoiles et des Exoplanètes. JM acknowledges support from the ERC Consolidator Grant funding scheme (project STARKEY, G.A. No. 615604). LG and TSR acknowledge partial support from PRIN INAF 2014 - CRA 1.05.01.94.05. TCB acknowledges partial support for this work from grant PHY 14-30152; Physics Frontier Center/JINA Center for the Evolution of the Elements (JINA-CEE), awarded by the US National Science Foundation. RAG received funding from the CNES PLATO grant at CEA. SM acknowledges support from the NASA grant NNX12AE17G. DAGH was funded by the Ramón y Cajal fellowship number RYC-2013-14182. DAGH and OZ acknowledge support provided by the Spanish Ministry of Economy and Competitiveness (MINECO) under grant AYA-2014-58082-P.

The CoRoT space mission, launched on December 27 2006, was developed and operated by CNES, with the contribution of Austria, Belgium, Brazil, ESA (RSSD and Science Program), Germany and Spain.

Funding for the SDSS-III Brazilian Participation Group has been provided by the Ministério de Ciência e Tecnologia (MCT), Fundação Carlos Chagas Filho de Amparo à Pesquisa do Estado do Rio de Janeiro (FAPERJ), Conselho Nacional de Desenvolvimento Científico e Tecnológico (CNPq), and Financiadora de Estudos e Projetos (FINEP). Funding for SDSS-III has been provided by the Alfred P. Sloan Foundation, the Participating Institutions, the National Science Foundation, and the U.S. Department of Energy Office of Science. The SDSS-III web site is `http://www.sdss3.org/`.
SDSS-III was managed by the Astrophysical Research Consortium for the Participating Institutions of the SDSS-III Collaboration including the University of Arizona, the Brazilian Participation Group, Brookhaven National Laboratory, Carnegie Mellon University, University of Florida, the French Participation Group, the German Participation Group, Harvard University, the Instituto de Astrofisica de Canarias, the Michigan State/Notre Dame/JINA Participation Group, Johns Hopkins University, Lawrence Berkeley National Laboratory, Max Planck Institute for Astrophysics, Max Planck Institute for Extraterrestrial Physics, New Mexico State University, New York University, Ohio State University, Pennsylvania State University, University of Portsmouth, Princeton University, the Spanish Participation Group, University of Tokyo, University of Utah, Vanderbilt University, University of Virginia, University of Washington, and Yale University.

Bibliography

Afflerbach, A., Churchwell, E., & Werner, M. W. 1997, ApJ, 478, 190
Alam, S., Albareti, F. D., Allende Prieto, C., Anders, F., & Anderson, S. F., e. 2015, ApJS, 219, 12
Allen, C., Carigi, L., & Peimbert, M. 1998, ApJ, 494, 247
Anders, F., Chiappini, C., Rodrigues, T. S., et al. 2017, A&A, 597, A30
Anders, F., Chiappini, C., Rodrigues, T. S., et al. 2016, Astronomische Nachrichten, 337, 926
Anders, F., Chiappini, C., Santiago, B. X., et al. 2014, A&A, 564, A115
Balser, D. S., Rood, R. T., Bania, T. M., & Anderson, L. D. 2011, ApJ, 738, 27
Bensby, T., Feltzing, S., & Oey, M. S. 2014, A&A, 562, A71
Bergemann, M., Ruchti, G. R., Serenelli, A., et al. 2014, A&A, 565, A89
Bland-Hawthorn, J. & Gerhard, O. 2016, ARA&A, 54, 529
Boeche, C., Chiappini, C., Minchev, I., et al. 2013, A&A, 553, A19
Bovy, J., Nidever, D. L., Rix, H.-W., et al. 2014, ApJ, 790, 127
Brogaard, K., Jessen-Hansen, J., Handberg, R., et al. 2016, Astronomische Nachrichten, 337, 793
Brogaard, K., Sandquist, E., Jessen-Hansen, J., Grundahl, F., & Frandsen, S. 2015, Astrophysics and Space Science Proceedings, 39, 51
Brunetti, M., Chiappini, C., & Pfenniger, D. 2011, A&A, 534, A75
Carraro, G., Ng, Y. K., & Portinari, L. 1998, MNRAS, 296, 1045
Casagrande, L., Schönrich, R., Asplund, M., et al. 2011, A&A, 530, A138
Chen, L., Hou, J. L., & Wang, J. J. 2003, AJ, 125, 1397
Cheng, J. Y., Rockosi, C. M., Morrison, H. L., et al. 2012, ApJ, 746, 149
Chiappini, C. 2006, Abundance Ratios and the Formation of the Milky Way, ed. S. Randich & L. Pasquini, 358
Chiappini, C. 2009, in IAU Symposium, Vol. 254, IAU Symposium, ed. J. Andersen, B. Nordström, & J. Bland-Hawthorn, 191–196
Chiappini, C., Anders, F., Rodrigues, T. S., et al. 2015, A&A, 576, L12
Chiappini, C., Matteucci, F., & Gratton, R. 1997, ApJ, 477, 765
Chiappini, C., Matteucci, F., & Romano, D. 2001, ApJ, 554, 1044
Cunha, K., Frinchaboy, P. M., Souto, D., et al. 2016, Astronomische Nachrichten, 337, 922
da Silva, L., Girardi, L., Pasquini, L., et al. 2006, A&A, 458, 609
Daflon, S. & Cunha, K. 2004, ApJ, 617, 1115
Davies, B., Origlia, L., Kudritzki, R.-P., et al. 2009, ApJ, 696, 2014
Deharveng, L., Peña, M., Caplan, J., & Costero, R. 2000, MNRAS, 311, 329
Eisenstein, D. J., Weinberg, D. H., Agol, E., et al. 2011, AJ, 142, 72
Faundez-Abans, M. & Maciel, W. J. 1987, A&A, 183, 324
Feigelson, E. D. & Jogesh Babu, G. 2012, Modern Statistical Methods for Astronomy
Ferrini, F., Molla, M., Pardi, M. C., & Diaz, A. I. 1994, ApJ, 427, 745
Foreman-Mackey, D., Conley, A., Meierjurgen Farr, W., et al. 2013, emcee: The MCMC Hammer, Astrophysics Source Code Library
Foreman-Mackey, D., Vousden, W., Price-Whelan, A., et al. 2016, corner.py: corner.py v1.0.2
Friel, E. D. 1995, ARA&A, 33, 381
Friel, E. D., Janes, K. A., Tavarez, M., et al. 2002, AJ, 124, 2693
Frinchaboy, P. M., Thompson, B., Jackson, K. M., et al. 2013, ApJ, 777, L1
Fuhrmann, K. 1998, A&A, 338, 161
Fuhrmann, K. 2011, MNRAS, 414, 2893
García-Hernández, D. A., Ventura, P., Delgado-Inglada, G., et al. 2016, MNRAS, 458, 118
García Pérez, A. E., Allende Prieto, C., Holtzman, J. A., et al. 2016, AJ, 151, 144
Gaulme, P., McKeever, J., Jackiewicz, J., et al. 2016, ApJ, 832, 121
Genovali, K., Lemasle, B., Bono, G., et al. 2014, A&A, 566, A37
Genovali, K., Lemasle, B., Bono, G., et al. 2013, A&A, 554, A132
Girardi, L. 2016, ARA&A, 54, 95
Grand, R. J. J., Kawata, D., & Cropper, M. 2015, MNRAS, 447, 4018
Grenon, M. 1972, in IAU Colloq. 17: Age des Etoiles, ed. G. Cayrel de Strobel & A. M. Delplace, 55
Grenon, M. 1999, Ap&SS, 265, 331
Gunn, J. E., Siegmund, W. A., Mannery, E. J., et al. 2006, AJ, 131, 2332
Hayden, M. R., Bovy, J., Holtzman, J. A., et al. 2015, ApJ, 808, 132
Hayden, M. R., Holtzman, J. A., Bovy, J., et al. 2014, AJ, 147, 116
Hogg, D. W., Bovy, J., & Lang, D. 2010, ArXiv e-prints, arxiv:1008.4686
Holmberg, J., Nordström, B., & Andersen, J. 2007, A&A, 475, 519
Holmberg, J., Nordström, B., & Andersen, J. 2009, A&A, 501, 941
Holtzman, J. A., Shetrone, M., Johnson, J. A., et al. 2015, AJ, 150, 148
Hou, J. L., Prantzos, N., & Boissier, S. 2000, A&A, 362, 921
Howell, S. B., Sobeck, C., Haas, M., et al. 2014, PASP, 126, 398
Huang, Y., Liu, X.-W., Zhang, H.-W., et al. 2015, Research in Astronomy and Astrophysics, 15, 1240
Ivezić, Ž., Connolly, A., VanderPlas, J., & Gray, A. 2013, Statistics, Data Mining, and Machine Learning in Astronomy
Jacobson, H. R., Friel, E. D., Jílková, L., et al. 2016, A&A, 591, A37
Janes, K. A. 1979, ApJS, 39, 135
Jofré, P., Jorissen, A., Van Eck, S., et al. 2016, A&A, 595, A60
Kordopatis, G., Binney, J., Gilmore, G., et al. 2015, MNRAS, 447, 3526
Kubryk, M., Prantzos, N., & Athanassoula, E. 2015a, A&A, 580, A126
Kubryk, M., Prantzos, N., & Athanassoula, E. 2015b, A&A, 580, A127
Lee, Y. S., Beers, T. C., Allende Prieto, C., et al. 2011, AJ, 141, 90
Lemasle, B., François, P., Bono, G., et al. 2007, A&A, 467, 283
Lemasle, B., François, P., Piersimoni, A., et al. 2008, A&A, 490, 613
Lépine, J. R. D., Cruz, P., Scarano, Jr., S., et al. 2011, MNRAS, 417, 698
Liu, X.-W., Yuan, H.-B., Huo, Z.-Y., et al. 2014, in IAU Symposium, Vol. 298, Setting the scene for Gaia and LAMOST, ed. S. Feltzing, G. Zhao, N. A. Walton, & P. Whitelock, 310–321
Luck, R. E., Andrievsky, S. M., Kovtyukh, V. V., Gieren, W., & Graczyk, D. 2011, AJ, 142, 51
Luck, R. E., Gieren, W. P., Andrievsky, S. M., et al. 2003, A&A, 401, 939
Luck, R. E. & Lambert, D. L. 2011, AJ, 142, 136
Maciel, W. J. & Chiappini, C. 1994, Ap&SS, 219, 231
Maciel, W. J. & Costa, R. D. D. 2009, in IAU Symposium, Vol. 254, The Galaxy Disk in Cosmological Context, ed. J. Andersen, B. Nordström, & J. Bland-Hawthorn, 38
Maciel, W. J., Costa, R. D. D., & Uchida, M. M. M. 2003, A&A, 397, 667
Maciel, W. J. & Köppen, J. 1994, A&A, 282, 436
Maciel, W. J. & Quireza, C. 1999, A&A, 345, 629
Maciel, W. J., Rodrigues, T., & Costa, R. 2012, in IAU Symposium, Vol. 283, IAU Symposium, 424–425
Magrini, L. & Randich, S. 2015, ArXiv e-prints, arXiv:1505.08027
Magrini, L., Sestito, P., Randich, S., & Galli, D. 2009, A&A, 494, 95
Majewski, S. R., Schiavon, R. P., Frinchaboy, P. M., et al. 2015, ApJS, submitted, arXiv:1509.05420
Martig, M., Bournaud, F., Croton, D. J., Dekel, A., & Teyssier, R. 2012, ApJ, 756, 26
Martig, M., Rix, H.-W., Aguirre, V. S., et al. 2015, MNRAS, 451, 2230
Matteucci, F. 2003, The Chemical Evolution of the Galaxy
Miglio, A., Chaplin, W. J., Brogaard, K., et al. 2016, MNRAS, 461, 760
Minchev, I., Boily, C., Siebert, A., & Bienayme, O. 2010, MNRAS, 407, 2122
Minchev, I., Chiappini, C., & Martig, M. 2013, A&A, 558, A9
Minchev, I., Chiappini, C., & Martig, M. 2014a, A&A, 572, A92

Minchev, I., Chiappini, C., Martig, M., et al. 2014b, ApJ, 781, L20
Minchev, I., Martig, M., Streich, D., et al. 2015, ApJ, 804, L9
Mollá, M., Ferrini, F., & Díaz, A. I. 1997, ApJ, 475, 519
Netopil, M., Paunzen, E., Heiter, U., & Soubiran, C. 2016, A&A, 585, A150
Nidever, D. L., Bovy, J., Bird, J. C., et al. 2014, ApJ, 796, 38
Nordström, B., Mayor, M., Andersen, J., et al. 2004, A&A, 418, 989
Peimbert, M. 1978, in IAU Symposium, Vol. 76, Planetary Nebulae, ed. Y. Terzian, 215–223
Perryman, M. A. C., de Boer, K. S., Gilmore, G., et al. 2001, A&A, 369, 339
Perryman, M. A. C., Lindegren, L., Kovalevsky, J., et al. 1997, A&A, 323, L49
Piffl, T. 2013, PhD thesis, Universität Potsdam
Portinari, L. & Chiosi, C. 2000, A&A, 355, 929
Press, W. H., Teukolsky, S. A., Vetterling, W. T., & Flannery, B. P. 1992, Numerical recipes in FORTRAN. The art of scientific computing
Rodrigues, T. S., Girardi, L., Miglio, A., et al. 2014, MNRAS, 445, 2758
Romaniello, M., Primas, F., Mottini, M., et al. 2008, A&A, 488, 731
Rood, R. T., Quireza, C., Bania, T. M., Balser, D. S., & Maciel, W. J. 2007, in Astronomical Society of the Pacific Conference Series, Vol. 374, From Stars to Galaxies: Building the Pieces to Build Up the Universe, ed. A. Vallenari, R. Tantalo, L. Portinari, & A. Moretti, 169
Salaris, M., Weiss, A., & Percival, S. M. 2004, A&A, 414, 163
Schönrich, R. & Binney, J. 2009, MNRAS, 396, 203
Sellwood, J. A. & Binney, J. J. 2002, MNRAS, 336, 785
Stanghellini, L., Guerrero, M. A., Cunha, K., Manchado, A., & Villaver, E. 2006, ApJ, 651, 898
Stanghellini, L. & Haywood, M. 2010, ApJ, 714, 1096
Stasińska, G. 2004, in Cosmochemistry. The melting pot of the elements, ed. C. Esteban, R. García López, A. Herrero, & F. Sánchez, 115–170
Stello, D., Huber, D., Sharma, S., et al. 2015, ApJ, 809, L3
Tosi, M. 2000, in Astrophysics and Space Science Library, Vol. 255, Astrophysics and Space Science Library, ed. F. Matteucci & F. Giovannelli, 505
Twarog, B. A., Ashman, K. M., & Anthony-Twarog, B. J. 1997, AJ, 114, 2556
Valentini, M., Chiappini, C., Davies, G. R., et al. 2016, A&A, accepted, arXiv:1609.03826
van Leeuwen, F., ed. 2007, Astrophysics and Space Science Library, Vol. 350, Hipparcos, the New Reduction of the Raw Data
Vilchez, J. M. & Esteban, C. 1996, MNRAS, 280, 720
Xiang, M.-S., Liu, X.-W., Yuan, H.-B., et al. 2015, Research in Astronomy and Astrophysics, 15, 1209
Yong, D., Carney, B. W., & Friel, E. D. 2012, AJ, 144, 95
Yong, D., Carney, B. W., & Teixera de Almeida, M. L. 2005, AJ, 130, 597
Yong, D., Casagrande, L., Venn, K. A., et al. 2016, MNRAS

[1] Leibniz-Institut für Astrophysik Potsdam (AIP), An der Sternwarte 16, 14482 Potsdam, Germany
[2] Laboratório Interinstitucional de e-Astronomia, - LIneA, Rua Gal. José Cristino 77, Rio de Janeiro, RJ - 20921-400, Brazil
[3] School of Physics and Astronomy, University of Birmingham, Edgbaston, Birmingham, B15 2TT, United Kingdom
[4] Dipartimento di Fisica e Astronomia, Università di Padova, Vicolo dell'Osservatorio 3, I-35122 Padova, Italy
[5] LESIA, Université Pierre et Marie Curie, Université Denis Diderot, Obs. de Paris, 92195 Meudon Cedex, France
[6] Osservatorio Astronomico di Padova – INAF, Vicolo dell'Osservatorio 5, I-35122 Padova, Italy
[7] Instituto de Física, Universidade Federal do Rio Grande do Sul, Caixa Postal 15051, Porto Alegre, RS - 91501-970, Brazil
[8] Institut d´Astrophysique Spatiale, UMR8617, CNRS, Université Paris XI, Bâtiment 121, 91405 Orsay Cedex, France
[9] Dept. of Physics and JINA-CEE: Joint Institute for Nuclear Astrophysics – Center for the Evolution of the Elements, Univ. of Notre Dame, Notre Dame, IN 46530 USA
[10] Observatório Nacional, Rua Gal. José Cristino 77, Rio de Janeiro, RJ - 20921-400, Brazil
[11] Laboratoire AIM, CEA/DSM – CNRS - Univ. Paris Diderot – IRFU/SAp, Centre de Saclay, 91191 Gif-sur-Yvette Cedex, France
[12] Instituto de Astrofísica de Canarias, 38205 La Laguna, Tenerife, Spain
[13] Universidad de La Laguna, Departamento de Astrofísica, 38206 La Laguna, Tenerife, Spain
[14] New Mexico State University, Las Cruces, NM 88003, USA
[15] Department of Astronomy, University of Virginia, PO Box 400325, Charlottesville VA 22904-4325, USA
[16] Space Science Institute, 4750 Walnut Street Suite 205, Boulder CO 80301, USA
[17] Institut d'Astrophysique et de Geophysique, Allée du 6 août, 17 - Bât. B5c, B-4000 Liège 1 (Sart-Tilman), Belgium
[18] Apache Point Observatory PO Box 59, Sunspot, NM 88349, USA
[19] Department of Astronomy and Astrophysics, The Pennsylvania State University, University Park, PA 16802
[20] Institute for Gravitation and the Cosmos, The Pennsylvania State University, University Park, PA 16802
[21] Observatoire de la Cote d'Azur, Laboratoire Lagrange, CNRS UMR 7923, B.P. 4229, 06304 Nice Cedex, France

6.A. Tabulated fit results

Table 6.1. Results of our four-parameter fits (linear slope + variable scatter) to the [Fe/H] vs. $R_{\rm Gal}$ distributions of the various samples for 6 kpc < $R_{\rm Gal}$ < 15 kpc, in six age bins.

Sample	τ < 1 Gyr	1 < τ < 2 Gyr	2 < τ < 4 Gyr	4 < τ < 6 Gyr	6 < τ < 10 Gyr	τ > 10 Gyr
			m [dex/kpc]			
CoRoGEE raw fit	$-0.068^{+0.008}_{-0.008}$	$-0.071^{+0.008}_{-0.008}$	$-0.052^{+0.007}_{-0.007}$	$-0.037^{+0.008}_{-0.009}$	$-0.029^{+0.011}_{-0.011}$	$-0.021^{+0.015}_{-0.016}$
CoRoGEE bias-corrected	$-0.057^{+0.008}_{-0.008} \pm 0.003$	$-0.066^{+0.008}_{-0.008} \pm 0.003$	$-0.066^{+0.007}_{-0.007} \pm 0.002$	$-0.048^{+0.008}_{-0.009} \pm 0.003$	$-0.037^{+0.011}_{-0.011} \pm 0.003$	$-0.03^{+0.015}_{-0.016} \pm 0.007$
MCM-CoRoGEE mock	$-0.061^{+0.006}_{-0.006}$	$-0.046^{+0.006}_{-0.006}$	$-0.025^{+0.006}_{-0.006}$	$-0.021^{+0.006}_{-0.006}$	$-0.016^{+0.007}_{-0.007}$	$-0.02^{+0.008}_{-0.008}$
Full MCM model	$-0.053^{+0.002}_{-0.002}$	$-0.049^{+0.003}_{-0.003}$	$-0.048^{+0.003}_{-0.003}$	$-0.041^{+0.003}_{-0.004}$	$-0.033^{+0.005}_{-0.007}$	Not converged
Chiappini 2009 model	$-0.061^{+0.0}_{-0.0}$	$-0.06^{+0.001}_{-0.001}$	$-0.059^{+0.001}_{-0.001}$	$-0.06^{+0.001}_{-0.001}$	$-0.063^{+0.004}_{-0.004}$	$-0.049^{+0.003}_{-0.003}$
			b [dex]			
CoRoGEE raw fit	$0.62^{+0.08}_{-0.08}$	$0.63^{+0.09}_{-0.09}$	$0.43^{+0.07}_{-0.07}$	$0.29^{+0.09}_{-0.08}$	$0.18^{+0.11}_{-0.1}$	$0.08^{+0.15}_{-0.14}$
CoRoGEE bias-corrected	$0.54^{+0.08}_{-0.08} \pm 0.03$	$0.6^{+0.09}_{-0.09} \pm 0.03$	$0.65^{+0.07}_{-0.07} \pm 0.02$	$0.44^{+0.09}_{-0.08} \pm 0.03$	$0.19^{+0.11}_{-0.1} \pm 0.03$	$0.08^{+0.15}_{-0.14} \pm 0.05$
MCM-CoRoGEE mock	$0.59^{+0.06}_{-0.06}$	$0.43^{+0.06}_{-0.06}$	$0.14^{+0.06}_{-0.06}$	$0.05^{+0.06}_{-0.06}$	$-0.05^{+0.06}_{-0.07}$	$-0.04^{+0.07}_{-0.07}$
Full MCM model	$0.54^{+0.02}_{-0.02}$	$0.48^{+0.02}_{-0.02}$	$0.43^{+0.03}_{-0.03}$	$0.27^{+0.04}_{-0.03}$	$0.0^{+0.06}_{-0.04}$	Not converged
Chiappini 2009 model	$0.58^{+0.01}_{-0.01}$	$0.52^{+0.01}_{-0.01}$	$0.44^{+0.01}_{-0.01}$	$0.34^{+0.01}_{-0.01}$	$0.17^{+0.04}_{-0.04}$	$-0.33^{+0.04}_{-0.04}$
			m_σ [dex/kpc]			
CoRoGEE raw fit	$0.002^{+0.004}_{-0.004}$	$-0.004^{+0.005}_{-0.005}$	$-0.018^{+0.006}_{-0.005}$	$-0.015^{+0.007}_{-0.006}$	$-0.014^{+0.008}_{-0.007}$	$-0.015^{+0.01}_{-0.01}$
CoRoGEE bias-corrected	$0.016^{+0.004}_{-0.004} \pm 0.004$	$0.004^{+0.005}_{-0.005} \pm 0.004$	$-0.008^{+0.006}_{-0.005} \pm 0.007$	$0.001^{+0.007}_{-0.006} \pm 0.005$	$0.017^{+0.008}_{-0.007} \pm 0.003$	$0.016^{+0.01}_{-0.01} \pm 0.006$
MCM-CoRoGEE mock	$-0.004^{+0.004}_{-0.005}$	$-0.005^{+0.004}_{-0.004}$	$-0.013^{+0.004}_{-0.004}$	$-0.014^{+0.004}_{-0.004}$	$-0.011^{+0.005}_{-0.005}$	$-0.005^{+0.007}_{-0.006}$
Full MCM model	$-0.004^{+0.001}_{-0.001}$	$-0.004^{+0.002}_{-0.002}$	$-0.008^{+0.002}_{-0.002}$	$-0.001^{+0.002}_{-0.002}$	$0.008^{+0.004}_{-0.003}$	Not converged
Chiappini 2009 model	$0.0^{+0.001}_{-0.001}$	$-0.0^{+0.001}_{-0.001}$	$-0.0^{+0.001}_{-0.001}$	$-0.0^{+0.001}_{-0.001}$	$-0.0^{+0.004}_{-0.004}$	$-0.0^{+0.006}_{-0.006}$
			b_σ [dex]			
CoRoGEE raw fit	$0.12^{+0.04}_{-0.04}$	$0.19^{+0.05}_{-0.05}$	$0.36^{+0.05}_{-0.06}$	$0.35^{+0.06}_{-0.06}$	$0.35^{+0.07}_{-0.07}$	$0.37^{+0.1}_{-0.09}$
CoRoGEE bias-corrected	$-0.02^{+0.04}_{-0.04} \pm 0.04$	$0.13^{+0.05}_{-0.05} \pm 0.04$	$0.22^{+0.05}_{-0.06} \pm 0.07$	$0.13^{+0.06}_{-0.06} \pm 0.06$	$0.01^{+0.07}_{-0.07} \pm 0.03$	$0.02^{+0.1}_{-0.09} \pm 0.07$
MCM-CoRoGEE mock	$0.14^{+0.05}_{-0.04}$	$0.16^{+0.04}_{-0.04}$	$0.31^{+0.04}_{-0.04}$	$0.32^{+0.04}_{-0.04}$	$0.3^{+0.05}_{-0.05}$	$0.22^{+0.06}_{-0.06}$
Full MCM model	$0.13^{+0.01}_{-0.01}$	$0.17^{+0.02}_{-0.02}$	$0.23^{+0.02}_{-0.02}$	$0.16^{+0.02}_{-0.02}$	$0.11^{+0.03}_{-0.03}$	Not converged
Chiappini 2009 model	$0.0^{+0.01}_{-0.01}$	$0.0^{+0.01}_{-0.01}$	$0.0^{+0.01}_{-0.01}$	$0.0^{+0.01}_{-0.02}$	$0.0^{+0.04}_{-0.04}$	$0.0^{+0.07}_{-0.07}$

Table 6.2. Results of our four-parameter fits (linear slope + variable scatter) to the [O/H] vs. $R_{\rm Gal}$ distributions of the various samples for 6 kpc < $R_{\rm Gal}$ < 15 kpc, in six age bins.

Sample	$\tau < 1$ Gyr	$1 < \tau < 2$ Gyr	$2 < \tau < 4$ Gyr	$4 < \tau < 6$ Gyr	$6 < \tau < 10$ Gyr	$\tau > 10$ Gyr
			m [dex/kpc]			
CoRoGEE raw fit	$-0.051^{+0.006}_{-0.006}$	$-0.055^{+0.006}_{-0.006}$	$-0.045^{+0.005}_{-0.005}$	$-0.035^{+0.006}_{-0.007}$	$-0.03^{+0.008}_{-0.008}$	$-0.024^{+0.01}_{-0.012}$
CoRoGEE bias-corrected	$-0.047^{+0.006}_{-0.006} \pm 0.001$	$-0.055^{+0.006}_{-0.006} \pm 0.002$	$-0.055^{+0.005}_{-0.005} \pm 0.002$	$-0.039^{+0.006}_{-0.007} \pm 0.002$	$-0.034^{+0.008}_{-0.008} \pm 0.003$	$-0.028^{+0.01}_{-0.012} \pm 0.004$
MCM-CoRoGEE mock	$-0.039^{+0.004}_{-0.004}$	$-0.035^{+0.003}_{-0.004}$	$-0.023^{+0.005}_{-0.005}$	$-0.017^{+0.005}_{-0.005}$	$-0.017^{+0.005}_{-0.005}$	$-0.022^{+0.006}_{-0.006}$
Full MCM model	$-0.033^{+0.002}_{-0.002}$	$-0.03^{+0.003}_{-0.003}$	$-0.029^{+0.003}_{-0.004}$	$-0.025^{+0.004}_{-0.005}$	$-0.023^{+0.005}_{-0.006}$	Not converged
Chiappini 2009 model	$-0.033^{+0.001}_{-0.001}$	$-0.034^{+0.001}_{-0.001}$	$-0.041^{+0.002}_{-0.002}$	$-0.047^{+0.001}_{-0.001}$	$-0.056^{+0.002}_{-0.002}$	$-0.052^{+0.003}_{-0.003}$
			b [dex]			
CoRoGEE raw fit	$0.5^{+0.07}_{-0.07}$	$0.52^{+0.06}_{-0.06}$	$0.42^{+0.05}_{-0.05}$	$0.35^{+0.06}_{-0.06}$	$0.29^{+0.08}_{-0.07}$	$0.22^{+0.12}_{-0.1}$
CoRoGEE bias-corrected	$0.46^{+0.07}_{-0.07} \pm 0.01$	$0.52^{+0.06}_{-0.06} \pm 0.02$	$0.55^{+0.05}_{-0.05} \pm 0.02$	$0.42^{+0.06}_{-0.06} \pm 0.01$	$0.31^{+0.08}_{-0.07} \pm 0.02$	$0.24^{+0.12}_{-0.1} \pm 0.04$
MCM-CoRoGEE mock	$0.39^{+0.04}_{-0.04}$	$0.33^{+0.04}_{-0.03}$	$0.16^{+0.05}_{-0.04}$	$0.08^{+0.05}_{-0.05}$	$0.05^{+0.05}_{-0.05}$	$0.07^{+0.06}_{-0.06}$
Full MCM model	$0.31^{+0.02}_{-0.02}$	$0.27^{+0.03}_{-0.02}$	$0.25^{+0.04}_{-0.03}$	$0.18^{+0.04}_{-0.03}$	$0.08^{+0.05}_{-0.04}$	Not converged
Chiappini 2009 model	$0.32^{+0.01}_{-0.01}$	$0.32^{+0.01}_{-0.01}$	$0.35^{+0.02}_{-0.02}$	$0.35^{+0.01}_{-0.01}$	$0.31^{+0.02}_{-0.02}$	$0.01^{+0.03}_{-0.03}$
			m_σ [dex/kpc]			
CoRoGEE raw fit	$-0.002^{+0.003}_{-0.003}$	$-0.006^{+0.004}_{-0.004}$	$-0.013^{+0.004}_{-0.004}$	$-0.009^{+0.005}_{-0.005}$	$-0.01^{+0.005}_{-0.006}$	$-0.011^{+0.008}_{-0.008}$
CoRoGEE bias-corrected	$0.007^{+0.003}_{-0.003} \pm 0.002$	$-0.001^{+0.004}_{-0.004} \pm 0.003$	$-0.005^{+0.004}_{-0.004} \pm 0.002$	$0.003^{+0.005}_{-0.005} \pm 0.002$	$0.009^{+0.005}_{-0.006} \pm 0.001$	$0.008^{+0.008}_{-0.008} \pm 0.006$
MCM-CoRoGEE mock	$-0.011^{+0.004}_{-0.005}$	$0.0^{+0.002}_{-0.002}$	$-0.007^{+0.003}_{-0.003}$	$-0.009^{+0.003}_{-0.003}$	$-0.01^{+0.004}_{-0.004}$	$-0.005^{+0.004}_{-0.005}$
Full MCM model	$0.001^{+0.001}_{-0.001}$	$0.005^{+0.001}_{-0.001}$	$0.001^{+0.002}_{-0.002}$	$0.006^{+0.003}_{-0.002}$	$0.009^{+0.004}_{-0.003}$	Not converged
Chiappini 2009 model	$0.006^{+0.001}_{-0.001}$	$-0.007^{+0.001}_{-0.001}$	$-0.006^{+0.001}_{-0.001}$	$0.004^{+0.001}_{-0.001}$	$0.0^{+0.002}_{-0.003}$	$0.0^{+0.007}_{-0.007}$
			b_σ [dex]			
CoRoGEE raw fit	$0.14^{+0.04}_{-0.03}$	$0.18^{+0.04}_{-0.04}$	$0.27^{+0.04}_{-0.04}$	$0.25^{+0.04}_{-0.04}$	$0.27^{+0.05}_{-0.05}$	$0.28^{+0.07}_{-0.07}$
CoRoGEE bias-corrected	$0.05^{+0.04}_{-0.03} \pm 0.02$	$0.14^{+0.04}_{-0.04} \pm 0.02$	$0.16^{+0.04}_{-0.04} \pm 0.03$	$0.11^{+0.04}_{-0.04} \pm 0.02$	$0.06^{+0.05}_{-0.05} \pm 0.01$	$0.07^{+0.07}_{-0.07} \pm 0.07$
MCM-CoRoGEE mock	$0.15^{+0.05}_{-0.04}$	$0.07^{+0.02}_{-0.02}$	$0.2^{+0.03}_{-0.03}$	$0.23^{+0.03}_{-0.03}$	$0.24^{+0.04}_{-0.03}$	$0.18^{+0.04}_{-0.04}$
Full MCM model	$0.03^{+0.01}_{-0.01}$	$0.02^{+0.01}_{-0.01}$	$0.07^{+0.02}_{-0.02}$	$0.04^{+0.02}_{-0.02}$	$0.03^{+0.03}_{-0.03}$	Not converged
Chiappini 2009 model	$-0.05^{+0.01}_{-0.01}$	$0.06^{+0.01}_{-0.01}$	$0.06^{+0.01}_{-0.01}$	$-0.04^{+0.01}_{-0.01}$	$-0.0^{+0.03}_{-0.03}$	$-0.0^{+0.08}_{-0.08}$

Table 6.3. Results of our four-parameter fits (linear slope + variable scatter) to the [Mg/Fe] vs. $R_{\rm Gal}$ distributions of the various samples for 6 kpc < $R_{\rm Gal}$ < 15 kpc, in six age bins.

Sample	τ < 1 Gyr	1 < τ < 2 Gyr	2 < τ < 4 Gyr	4 < τ < 6 Gyr	6 < τ < 10 Gyr	τ > 10 Gyr
			m [dex/kpc]			
CoRoGEE raw fit	$0.009^{+0.004}_{-0.004}$	$0.006^{+0.003}_{-0.005}$	$-0.003^{+0.002}_{-0.003}$	$-0.005^{+0.003}_{-0.004}$	$-0.008^{+0.003}_{-0.004}$	$-0.011^{+0.005}_{-0.005}$
CoRoGEE bias-corrected	$0.007^{+0.004}_{-0.004} \pm 0.002$	$0.004^{+0.003}_{-0.005} \pm 0.002$	$0.004^{+0.002}_{-0.003} \pm 0.003$	$-0.003^{+0.003}_{-0.004} \pm 0.001$	$-0.008^{+0.003}_{-0.004} \pm 0.002$	$-0.014^{+0.005}_{-0.005} \pm 0.002$
MCM-CoRoGEE mock	$0.012^{+0.002}_{-0.002}$	$0.011^{+0.002}_{-0.002}$	$0.004^{+0.002}_{-0.002}$	$0.003^{+0.002}_{-0.002}$	$0.001^{+0.003}_{-0.003}$	$-0.002^{+0.003}_{-0.003}$
Full MCM model	$0.015^{+0.001}_{-0.008}$	$0.011^{+0.001}_{-0.002}$	$0.013^{+0.001}_{-0.004}$	$0.008^{+0.001}_{-0.005}$	$0.004^{+0.001}_{-0.002}$	$0.001^{+0.002}_{-0.003}$
Chiappini 2009 model	$0.014^{+0.001}_{-0.001}$	$0.012^{+0.001}_{-0.001}$	$0.009^{+0.0}_{-0.0}$	$0.006^{+0.0}_{-0.0}$	$0.003^{+0.001}_{-0.001}$	$-0.002^{+0.001}_{-0.001}$
			b [dex]			
CoRoGEE raw fit	$-0.13^{+0.04}_{-0.04}$	$-0.09^{+0.05}_{-0.03}$	$0.02^{+0.03}_{-0.02}$	$0.06^{+0.04}_{-0.03}$	$0.1^{+0.04}_{-0.03}$	$0.15^{+0.05}_{-0.04}$
CoRoGEE bias-corrected	$-0.12^{+0.04}_{-0.04} \pm 0.02$	$-0.08^{+0.05}_{-0.03} \pm 0.02$	$-0.08^{+0.03}_{-0.02} \pm 0.03$	$0.02^{+0.04}_{-0.03} \pm 0.02$	$0.13^{+0.04}_{-0.03} \pm 0.02$	$0.31^{+0.05}_{-0.04} \pm 0.02$
MCM-CoRoGEE mock	$-0.15^{+0.02}_{-0.02}$	$-0.13^{+0.02}_{-0.02}$	$-0.01^{+0.02}_{-0.02}$	$0.01^{+0.02}_{-0.02}$	$0.05^{+0.03}_{-0.03}$	$0.1^{+0.03}_{-0.03}$
Full MCM model	$-0.18^{+0.07}_{-0.01}$	$-0.13^{+0.02}_{-0.01}$	$-0.13^{+0.04}_{-0.01}$	$-0.06^{+0.05}_{-0.01}$	$0.05^{+0.02}_{-0.01}$	$0.2^{+0.03}_{-0.02}$
Chiappini 2009 model	$-0.16^{+0.01}_{-0.01}$	$-0.12^{+0.01}_{-0.01}$	$-0.06^{+0.0}_{-0.01}$	$-0.0^{+0.0}_{-0.0}$	$0.08^{+0.01}_{-0.01}$	$0.2^{+0.01}_{-0.01}$
			m_σ [dex/kpc]			
CoRoGEE raw fit	$0.002^{+0.011}_{-0.015}$	$-0.014^{+0.006}_{-0.004}$	$-0.01^{+0.003}_{-0.004}$	$-0.011^{+0.003}_{-0.004}$	$-0.01^{+0.003}_{-0.004}$	$-0.012^{+0.004}_{-0.005}$
CoRoGEE bias-corrected	$0.008^{+0.011}_{-0.015} \pm 0.009$	$-0.016^{+0.006}_{-0.004} \pm 0.006$	$-0.019^{+0.003}_{-0.004} \pm 0.023$	$-0.014^{+0.003}_{-0.004} \pm 0.017$	$-0.005^{+0.003}_{-0.004} \pm 0.002$	$-0.005^{+0.004}_{-0.005} \pm 0.003$
MCM-CoRoGEE mock	$0.004^{+0.002}_{-0.002}$	$-0.005^{+0.002}_{-0.002}$	$-0.009^{+0.002}_{-0.002}$	$-0.007^{+0.002}_{-0.002}$	$-0.005^{+0.002}_{-0.002}$	$-0.004^{+0.002}_{-0.002}$
Full MCM model	$-0.002^{+0.003}_{-0.001}$	$-0.005^{+0.003}_{-0.001}$	$-0.004^{+0.002}_{-0.001}$	$-0.004^{+0.005}_{-0.001}$	$-0.003^{+0.001}_{-0.001}$	$-0.001^{+0.003}_{-0.001}$
Chiappini 2009 model	$0.004^{+0.0}_{-0.0}$	$-0.004^{+0.0}_{-0.0}$	$0.0^{+0.001}_{-0.001}$	$-0.0^{+0.001}_{-0.001}$	$-0.0^{+0.001}_{-0.001}$	$-0.0^{+0.001}_{-0.001}$
			b_σ [dex]			
CoRoGEE raw fit	$-0.01^{+0.14}_{-0.12}$	$0.14^{+0.05}_{-0.05}$	$0.14^{+0.05}_{-0.03}$	$0.15^{+0.04}_{-0.03}$	$0.15^{+0.04}_{-0.03}$	$0.17^{+0.05}_{-0.04}$
CoRoGEE bias-corrected	$-0.04^{+0.14}_{-0.12} \pm 0.1$	$0.18^{+0.05}_{-0.05} \pm 0.09$	$0.21^{+0.05}_{-0.03} \pm 0.23$	$0.16^{+0.04}_{-0.03} \pm 0.17$	$0.07^{+0.04}_{-0.03} \pm 0.02$	$0.08^{+0.05}_{-0.04} \pm 0.03$
MCM-CoRoGEE mock	$-0.06^{+0.02}_{-0.02}$	$0.08^{+0.02}_{-0.02}$	$0.15^{+0.02}_{-0.02}$	$0.13^{+0.02}_{-0.02}$	$0.12^{+0.02}_{-0.02}$	$0.1^{+0.02}_{-0.02}$
Full MCM model	$0.05^{+0.01}_{-0.01}$	$0.08^{+0.01}_{-0.01}$	$0.08^{+0.01}_{-0.01}$	$0.08^{+0.01}_{-0.02}$	$0.07^{+0.01}_{-0.01}$	$0.05^{+0.01}_{-0.02}$
Chiappini 2009 model	$-0.04^{+0.0}_{-0.0}$	$0.04^{+0.0}_{-0.0}$	$-0.0^{+0.01}_{-0.01}$	$0.0^{+0.01}_{-0.01}$	$0.0^{+0.01}_{-0.01}$	$0.0^{+0.01}_{-0.01}$

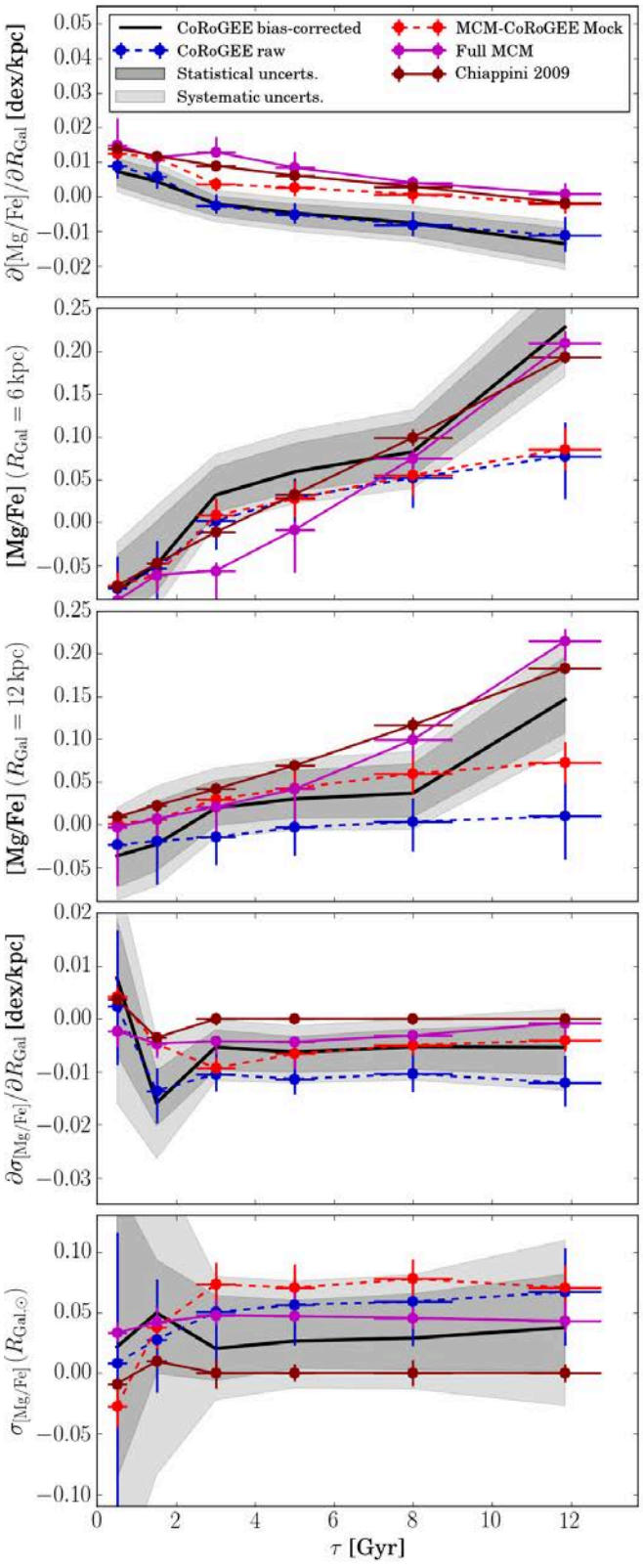

Figure 6.8. Results of our four-parameter fits for the [Mg/Fe] vs. $R_{\rm Gal}$ distributions, in the same style as Fig. 6.3.

Chapter 7

Summary & Outlook

7.1. Results of this work

This thesis comprises a number of chemodynamical analyses using observations of the SDSS-III/APOGEE survey and the CoRoT asteroseismic program. It relies on complex datasets provided by large research collaborations, as well as no-less-complex state-of-the-art chemodynamical MW models provided by other researchers, and is therefore primarily a work of statistical data analysis and astrophysical interpretation. Additional photometric, astrometric, asteroseismic, and spectroscopic data had to be assembled for comparison, calibration and complementation purposes, and new data pipelines had to be written, tested, and run. The work presented here primarily aims at finding new constraints for chemodynamical MW simulations, at revealing problems of currently available models, and at exploring the new parameter space opened up by spectroscopic stellar surveys. In this chapter I will shortly summarise the results of the previous chapters, highlight some remaining difficulties, and venture an outlook on near-term future work.

7.1.1. Early chemodynamics results from APOGEE

Chapter 2 (Anders et al. 2014) was partly developed during my diploma thesis (Anders 2013) within a larger project of the SDSS-III/APOGEE collaboration (Eisenstein et al. 2011; Majewski et al. 2015). The project maturated in parallel to the first APOGEE data release (Ahn et al. 2014), which was on the one hand a guarantee for the novelty of our findings; on the other hand, the data required more careful quality checks than subsequent works. The analysis took advantage of several ingredients: on the data side, we relied on the good performance of the APOGEE Stellar Parameters and Chemical Abundances Pipeline (ASPCAP; Mészáros et al. 2013; García Pérez et al. 2016), preliminary seismic data from CoRoT and *Kepler* (courtesy of the CoRoT Red-Giant Working Group and the APOKASC Collaboration, respectively) to calibrate spectroscopic surface gravities, and the new proper motions from UCAC-4 (Zacharias et al. 2013). On the computational side, our group (the Brazilian Participation Group within SDSS-III) was the first to determine Bayesian spectrophotometric distances for APOGEE (Appendix A; Santiago et al. 2016), which was a very important asset. We also profited highly from the availability of an early version of the open-source orbit integration package *galpy* (Bovy 2015).

The main results of that work can be summarised as follows. First, we demonstrated the reliability of APOGEE data products, in particular the chemical abundances for [M/H] and [α/M], by comparing with high-resolution optical surveys. The high quality of the APOGEE abundance determinations in our unambiguous detection of a gap/dip in the [α/Fe] vs. [Fe/H] diagram reported in previous high-resolution optical studies (Fuhrmann 1998, 2011; Adibekyan et al. 2011). We argue that, similar to the volume-complete sample of Fuhrmann (2011), this is unlikely to be caused by selection effects. We further corroborate, with unprecendented statistics at high resolution, the result of Bensby et al. (2011) and Cheng et al. (2012) who found evidence for a shorter scale-length of the high-[α/Fe] population. When cleaning the extended solar-vicinity sample from stars passing by on eccentric orbits, we also found that the metallicity distribution of the local thin disc extends to below -0.5, making a strong case for efficient radial migration. Motivated by from RAVE and GCS (Boeche et al. 2013a,b), we also measured the dependence of the radial [M/H] gradient on their distance from the Galactic plane. For stars in the geometric thick disc ($|Z_{\rm Gal}| > 1$ kpc), we found the surprising result that the gradient becomes positive, which we interpreted as a signature of flaring of younger star populations in the outer disc (Minchev et al. 2012, 2014b, see also Minchev et al. 2017). Finally, the first-year APOGEE data hinted slightly different chemical signatures for the bulge and the thick disc, which would suggest different star-formation histories for the two components. However, more inner-Galaxy data are needed to support this finding.

In the course of this project, I contributed to the SDSS DR10 paper (Ahn et al. 2014) and several other SDSS papers (see Appendix B).

7.1.2. Galactic archaeology with asteroseismology and spectroscopy: the CoRoT-APOGEE dataset

In Chapters 3-6, we introduced the CoRoT-APOGEE (CoRoGEE) dataset and used it to demonstrate the usefulness of a combined analysis of asteroseismic and spectroscopic data for Galactic archaeology. In Chapter 3 (Anders et al. 2017b), we described the data analysis that permitted us to calculate masses, radii, ages, distances and extinctions for more than 600 red giants observed in the two CoRoT exoplanet fields LRa01 and LRc01. Our Bayesian stellar-model fitting with the PARAM code resulted in statistical uncertainties of $\lesssim 2\%$ in distance, 0.08 mag in A_V, $\sim 4\%$ in radius, $\sim 9\%$ in mass and $\sim 25\%$ in age, where the individual age probability distributions can be very complex in shape, favouring the use of wide age bins in subsequent analyses. We also evaluated systematic uncertainties that may affect the absolute scale of our derived ages. A number of checks (surface gravity comparison, grid-based vs. scaling relation results, extinction maps) demonstrate the overall reliability of our work.

In Chapter 3, we also studied, for the first time, the [α/Fe]-[Fe/H] relation of the disc as a function of age and Galactocentric distance. Considering the small sample size and the uncertainties still involved in our age estimates, we could place surprisingly strong constraints on the chemical evolution of the Milky Way stellar disc: When we compared our results to the multi-zone chemical-evolution model of Chiappini (2009) that treats the thin and thick disc separately, we found that the thin-disc models generally provide a good description of the main abundance-age trends, with the exception of the flat [α/Fe] trend at high metallicity. The results improved when the stellar guiding-centre radius was used instead of the current Galactocentric distance. When we compared our results with the predictions of the chemo-dynamical model of Minchev, Chiappini, & Martig (2013, 2014b), we further discovered that the model, while matching many solar-vicinity constraints, cannot reproduce the number of super-metal-rich stars we found in the outer disc. This could be resolved by either a stronger radial mixing or the inclusion of a chemical thick-disc/bulge component that formed stars for more than 3 Gyr and thus produced super-metal-rich stars. In addition, the age distribution of the [α/Fe]-enhanced sequence in the CoRoGEE inner-disc field was much broader than expected from a combination of radial mixing and observational errors. This result was discussed in more detail in a separate Letter (Chapter 5; Chiappini et al. 2015).

Chapter 4 (Anders et al. 2016) is a short companion paper to Chapter 3, focussing (also for the first time in a published paper) on how to simulate the CoRoGEE dataset using a chemodynamical MW model, using the example of the MCM model (Minchev et al. 2013, 2014a). We compared two different ways of simulating the observations: a "simple" mock drawn from the observed spatial distribution of the stellar sample, and sophisticated mock that that used a modified version of the Galaxia population-synthesis code (Piffl 2013; Sharma et al. 2011). Neither of the two mock versions could reproduce all projections of the data simulateously: while the sophisticated mock matched the observed age distributions in the two CoRoT fields better, the simple mock performed much better in reproducing the chemo-kinematic-age relations studied in Anders et al. (2017b,a).

In Chapter 5 (Chiappini et al. 2015) we reported the discovery of a population of apparently young [α/Fe]-enhanced CoRoGEE stars that is difficult to explain within standard disc chemical-evolution models. These stars were found to have a lower iron-peak element content than the rest of the CoRoGEE sample and were primarily found in the inner-disc field LRc01, with guiding radii $R_g \leq 6$ kpc. We therefore suggested that their origin might be related to the complex chemical evolution (e.g. star-formation pockets) that has been suggested to occur near the corotation region of the Galactic bar. Our results provoked a considerable repercussion in the literature, including the finding of young [α/Fe]-enhanced stars in the *Kepler* field (Martig et al. 2015) and searches for companion stars that could explain the apparent youth of those stars by past mass transfer (evolved blue-straggler scenario; Brogaard et al. 2016; Yong et al. 2016; Jofré et al. 2016; Fuhrmann & Chini 2017).

Finally, in Chapter 6 (Anders et al. 2017a) we used the 418 CoRoGEE stars closest to the Galactic disc plane (6 kpc $< R_{\rm Gal} \lesssim$ 13 kpc, $|Z_{\rm Gal}| < 0.3$ kpc) to measure the age dependence of the thin disc's radial abundance profile for [Fe/H], [O/H], and [Mg/Fe]. The slope of the radial iron gradient of the young red-giant population (-0.058 ± 0.008 [stat.] ± 0.003 [syst.] dex/kpc) was found to be consistent with the most recent Cepheid measurements. For the age range of $1-4$ Gyr, the gradient steepened slightly ($-0.066 \pm 0.007 \pm 0.002$ dex/kpc), before flattening again to reach a value of ~ -0.03 dex/kpc for stars with ages between 6 and 10 Gyr. Again we compared our results to mock observations of the MCM model (Minchev et al. 2013, 2014a), concluding that the evolution of the abundance gradient and its scatter could be explained by a nearly-constant negative metallicity gradient in the interstellar medium over the last $\sim$ 10 Gyr, together with stellar radial heating and migration. Other scenarios remain possible, however. Since the question whether the radial metallicity gradient flattened or steepened with time had not been conclusively answered despite various observational efforts, we thoroughly discussed our results in the planetary-nebula, open-cluster, and field-star literature on that matter. We thereby found an explanation for the puzzling observation that the radial metallicity gradient of intermediate-age open clusters seems to be much steeper than that of the youngest clusters. If radial mixing is as efficient as in the MCM model, it can bring metal-rich clusters from the innermost regions of the disc to Galactocentric radii of 5 to 8 kpc within 2 Gyr. And if these outward-migrating clusters were less affected by tidal disruption, they would then steepen the local intermediate-age cluster metallicity gradient, because the non-migrating clusters rapidly dissolve. Our scenario also explains naturally why this strong steepening of the local iron gradient with age is not seen in field stars.

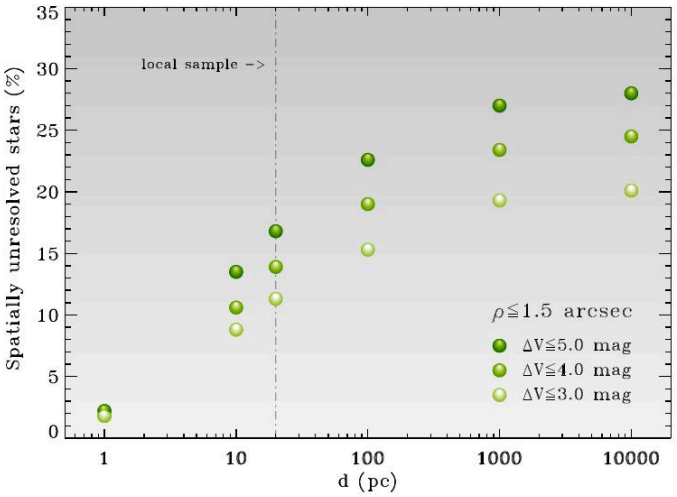

Figure 7.1. The fraction of spatially unresolved (angular separations 1.5") solar-type stars as a function of distance, extrapolating from a volume-complete $d < 25$ pc sample. Figure from Fuhrmann et al. (2017).

7.2. Remaining challenges

Despite the unprecedented quality of the presently available spectroscopic, asteroseismic, and astrometric data, their analysis remains affected by several systematic uncertainties related to stellar and Galactic evolution. First and foremost, stellar ages (or in general, the stellar parameters that one obtains by comparing observations to stellar models) can only be as accurate as the stellar models used. Unfortunately, the overall impact of a number of hydrodynamic processes (such as rotation, atomic diffusion, thermohaline mixing, mass-loss law) occuring inside stars, on the main sequence and during the giant phase, still remains subject of discussion (Noels et al. 2016 and references therein; see also Lagarde et al. 2016, 2017).

On top of the uncertainties of single-star models, samples of low-mass stars can be expected to be significantly contaminated

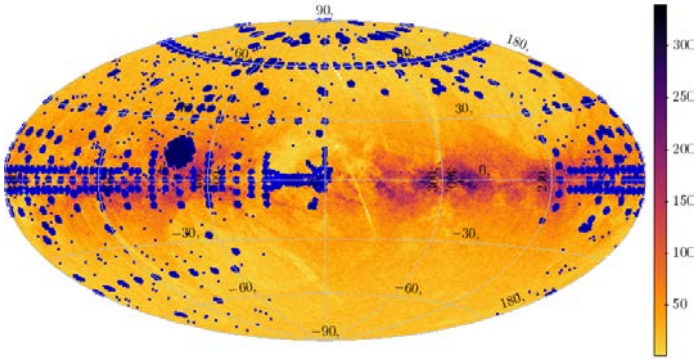

Figure 7.2. Footprint of the DR13 APOGEE-TGAS sample, superimposed on the TGAS source density sky map (Gaia Collaboration et al. 2016a).

by unresolved companion stars (Fig. 7.1) as well as past binary interaction (Roche-lobe overflow or stellar mergers). While the first case (non-interacting binary companions) can in principle be resolved by multiple spectroscopic observations, and may even be negligible for red-giant populations due to the generally low relative flux of the secondary, the second case (interacting or post-interacting binary) may lead to significant errors in the age determination of the target star (e.g. Fuhrmann & Chini 2017). While we can hope to uncover cases of stellar mimikry in the solar vicinity thanks to the high angular resolution of *Gaia*, this will be impossible for distant stellar samples. A careful modelling of binary populations is therefore required in the next generation of population-synthesis codes.

Another important limitation of our CoRoGEE work was the avaiability of only two lines of sight. An first, almost all-sky view of the ages of red-giants in the extended solar vicinity will be possible by joining APOGEE observations with *Gaia* data.

7.3. The future: *Gaia* and next-generation surveys

In this section, I briefly discuss near-term-future plans for projects related to the scope of this thesis, focussing on APOGEE synergies with the *Gaia* mission (Gaia Collaboration et al. 2016b) and the K2 asteroseismology program (Howell et al. 2014).

The first data release of the Gaia mission (Gaia Collaboration et al. 2016a) contains parallaxes and proper motions for more than 2 million stars contained in the Tycho-2 catalogue, among them $> 40,000$ stars contained in the upcoming APOGEE DR14 catalogue (Fig. 7.2). The combined dataset presents an ideal opportunity for chemo-dynamical tagging studies beyond the Hipparcos volume. In an upcoming publication (Anders et al. 2017, in prep.), we will provide precise astrophysical parameters, chemical abundances, astro-spectro-photometric ages, distances, and extinctions, as well as orbital parameters for $\gtrsim 4,000$ APOGEE-TGAS stars in a 1 kpc sphere, using an improved version of the `StarHorse` code (Queiroz et al. 2017, in prep.). By comparing the distribution of APOGEE-TGAS stars in the space {[Fe/H], [Mg/Fe], age} with the volume-complete high-resolution solar-vicinity survey ($d < 25$ pc) of Fuhrmann et al. (2017), we will revisit the chemo-dynamic correlations in the extended solar neighbourhood. The unprecedented precision of APOGEE-TGAS orbital parameters (see 7.3) enables us to remove stars passing on eccentric orbits with much higher fidelity than in Anders et al. (2014), and to effectively constrain the efficiency of radial migration.

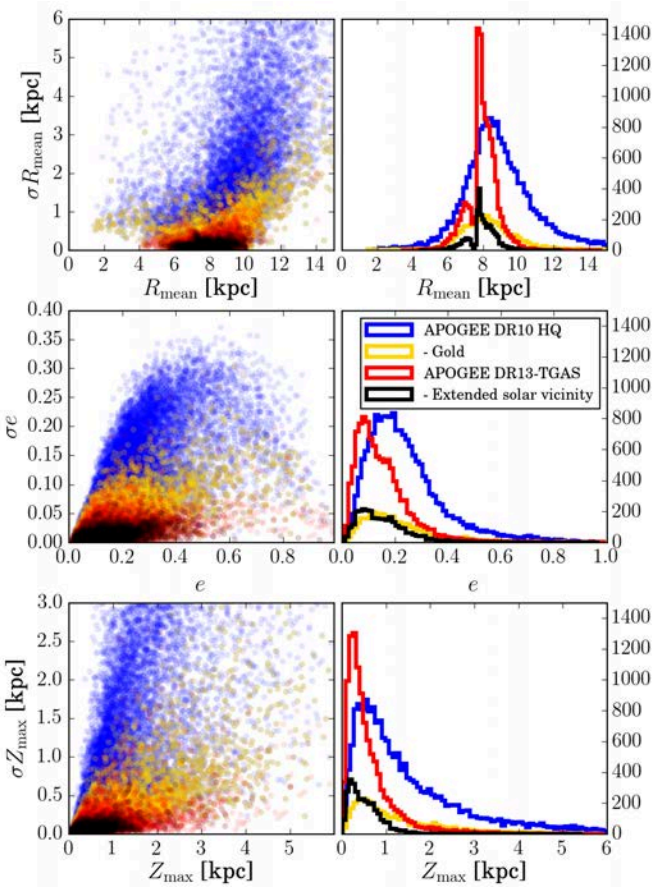

Figure 7.3. Illustration of the improvement of stellar orbital parameters with *Gaia* DR1. Left panels: Orbital-parameter uncertainty distributions of the APOGEE DR10 HQ sample (blue), the DR10 Gold sample (gold), the DR13 APOGEE-TGAS sample (red), and the APOGEE-TGAS extended solar-vicinity sample (black). Right panels: Corresponding orbital-parameter histograms.

From the perspective of joint spectroscopic-seismic surveys, the CoRoGEE project was certainly a scientific breakthrough, and an important pathfinder for the massive survey that the *Kepler*-2 mission (K2; Howell et al. 2014) is currently undertaking. The K2 Galactic Archaeology Program (Stello et al. 2015) will deliver seismic parameters for thousands of red giants in more than 17 fields distributed along the ecliptic plane, and most of the targets will be co-observed by spectroscopic surveys. Combined with the CoRoT fields and the original *Kepler* field, as well as *Gaia* data, the coverage of the Galactic disc with red giants with precise age, abundance, and kinematic information will increase by a factor of 10 at least, heralding the golden age of Galactic archaeology of the MW disc.

The next generation of multi-object spectrographs, such as WEAVE, 4MOST, and MOONS, will complement the atrometry and low/medium-resolution spectroscopy obtained by *Gaia*. On the asteroseismology side, the PLATO 2.0 mission (Rauer et al. 2014) with its huge field of view will enlarge the asteroseismic red-giant sample to $\sim 10^6$ stars, enabling more and more detailed tests of stellar and Galactic evolution.

Bibliography

Adibekyan, V. Z., Santos, N. C., Sousa, S. G., & Israelian, G. 2011, A&A, 535, L11
Ahn, C. P., Alexandroff, R., Allende Prieto, C., et al. 2014, ApJS, 211, 17

Anders, F. 2013, Diploma Thesis: *Chemodynamical constraints on Milky Way models from spectroscopic stellar surveys*, Technische Universität Dresden
Anders, F., Chiappini, C., Minchev, I., et al. 2017a, A&A, in press, http://dx.doi.org/10.1051/0004-6361/201629363
Anders, F., Chiappini, C., Rodrigues, T. S., et al. 2017b, A&A, 597, A30
Anders, F., Chiappini, C., Rodrigues, T. S., et al. 2016, Astronomische Nachrichten, 337, 926
Anders, F., Chiappini, C., Santiago, B. X., et al. 2014, A&A, 564, A115
Bensby, T., Alves-Brito, A., Oey, M. S., Yong, D., & Meléndez, J. 2011, ApJ, 735, L46
Boeche, C., Chiappini, C., Minchev, I., et al. 2013a, A&A, 553, A19
Boeche, C., Siebert, A., Piffl, T., et al. 2013b, A&A, 559, A59
Bovy, J. 2015, ApJS, 216, 29
Brogaard, K., Jessen-Hansen, J., Handberg, R., et al. 2016, Astronomische Nachrichten, 337, 793
Cheng, J. Y., Rockosi, C. M., Morrison, H. L., et al. 2012, ApJ, 752, 51
Chiappini, C. 2009, in IAU Symposium, Vol. 254, IAU Symposium, ed. J. Andersen, B. Nordström, & J. Bland-Hawthorn, 191–196
Chiappini, C., Anders, F., Rodrigues, T. S., et al. 2015, A&A, 576, L12
Eisenstein, D. J., Weinberg, D. H., Agol, E., et al. 2011, AJ, 142, 72
Fuhrmann, K. 1998, A&A, 338, 161
Fuhrmann, K. 2011, MNRAS, 414, 2893
Fuhrmann, K. & Chini, R. 2017, ApJ, 834, 114
Fuhrmann, K., Chini, R., Kaderhandt, L., & Chen, Z. 2017, MNRAS, 464, 2610
Gaia Collaboration, Brown, A. G. A., Vallenari, A., et al. 2016a, A&A, 595, A2
Gaia Collaboration, Prusti, T., de Bruijne, J. H. J., et al. 2016b, A&A, 595, A1
García Pérez, A. E., Allende Prieto, C., Holtzman, J. A., et al. 2016, AJ, 151, 144
Howell, S. B., Sobeck, C., Haas, M., et al. 2014, PASP, 126, 398
Jofré, P., Jorissen, A., Van Eck, S., et al. 2016, A&A, 595, A60
Lagarde, N., Bossini, D., Miglio, A., Vrard, M., & Mosser, B. 2016, MNRAS, 457, L59
Lagarde, N., Robin, A. C., Reylé, C., & Nasello, G. 2017, ArXiv e-prints
Majewski, S. R., Schiavon, R. P., Frinchaboy, P. M., et al. 2015, ApJS, submitted, arXiv:1509.05420
Martig, M., Rix, H.-W., Aguirre, V. S., et al. 2015, MNRAS, 451, 2230
Mészáros, S., Holtzman, J., García Pérez, A. E., et al. 2013, AJ, 146, 133
Minchev, I., Chiappini, C., & Martig, M. 2013, A&A, 558, A9
Minchev, I., Chiappini, C., & Martig, M. 2014a, A&A, 572, A92
Minchev, I., Chiappini, C., & Martig, M. 2014b, in IAU Symposium, Vol. 298, IAU Symposium, ed. S. Feltzing, G. Zhao, N. A. Walton, & P. Whitelock, 130–141
Minchev, I., Famaey, B., Quillen, A. C., et al. 2012, A&A, 548, A127
Minchev, I., Steinmetz, M., Chiappini, C., et al. 2017, ApJ, 834, 27
Noels, A., Montalbán, J., & Chiappini, C. 2016, Astronomische Nachrichten, 337, 982
Piffl, T. 2013, PhD thesis, Universität Potsdam
Rauer, H., Catala, C., Aerts, C., et al. 2014, Experimental Astronomy, 38, 249
Santiago, B. X., Brauer, D. E., Anders, F., et al. 2016, A&A, 585, A42
Sharma, S., Bland-Hawthorn, J., Johnston, K. V., & Binney, J. 2011, ApJ, 730, 3
Stello, D., Huber, D., Sharma, S., et al. 2015, ApJ, 809, L3
Yong, D., Casagrande, L., Venn, K. A., et al. 2016, MNRAS
Zacharias, N., Finch, C. T., Girard, T. M., et al. 2013, AJ, 145, 44

1

Chapter A

Spectro-photometric distances to stars: A general-purpose Bayesian approach

Basílio X. Santiago[1,2], Dorothée E. Brauer[3], Friedrich Anders[3,2], Cristina Chiappini[3,2], Anna B. Queiroz[1,2], Léo Girardi[4,2], Helio J. Rocha-Pinto[5,2], Eduardo Balbinot[1,2], Luiz N. da Costa[6,2], Marcio A.G. Maia[6,2], Mathias Schultheis[7], Matthias Steinmetz[3], Andrea Miglio[8], Josefina Montalbán[9], Donald P. Schneider[10,11], Timothy C. Beers[12], Peter M. Frinchaboy[13], Young Sun Lee[14], and Gail Zasowski[15]

(Affiliations can be found after the references)

Abstract

Determining distances to individual field stars is a necessary step towards mapping Galactic structure and determining spatial variations in the chemo-dynamical properties of stellar populations in the Milky Way. In order to provide stellar distance estimates for various spectroscopic surveys, we have developed a code that estimates distances to stars using measured spectroscopic and photometric quantities. We employ a Bayesian approach to build the probability distribution function over stellar evolutionary models given these data, delivering estimates of model parameters (including distances) for each star individually. Our method provides several alternative distance estimates for each star in the output, along with their associated uncertainties. This enables the use of our method even in the absence of some measurements. The code was first tested on simulations, successfully recovering input distances to mock stars with $\lesssim 1\%$ bias. We found the uncertainties scale with the uncertainties in the adopted spectro-photometric parameters. The method-intrinsic random distance uncertainties for typical spectroscopic survey measurements amount to around 10% for dwarf stars and 20% for giants, and are most sensitive to the quality of $\log g$ measurements. The code was then validated by comparing our distance estimates to parallax measurements from the *Hipparcos* mission for nearby stars (< 300 pc), to asteroseismic distances of CoRoT red giant stars, and to known distances of well-studied open and globular clusters. The photometric data of these reference samples cover both optical and infrared wavelengths. The spectroscopic parameters are also based on spectra taken at various wavelengths, with varying spectral coverage and resolution: the Sloan Digital Sky Survey programs SEGUE and APOGEE, as well as various ESO instruments. The external comparisons confirm that our distances are subject to very small systematic biases with respect to the fundamental *Hipparcos* scale (+0.4% for dwarfs, and +1.6% for giants). The typical random distance scatter is 18% for dwarfs, and 26% for giants. For the CoRoT-APOGEE sample, which spans Galactocentric distances of $4 - 14$ kpc, the typical random distance scatter is $\simeq 15\%$, both for the nearby and farther data. Our distances are systematically larger than the CoRoT ones by about +9%, which can mostly be attributed to the different choice of priors. The comparison to known distances of star clusters from SEGUE and APOGEE has led to significant systematic differences for many cluster stars, but with opposite signs, and with substantial scatter. Finally, we tested our distances against those previously determined for a high-quality sample of giant stars from the RAVE survey, again finding a small systematic trend of +5% and an rms scatter of 30%. Efforts are underway to provide our code to the community by running it on a public server.

A.1. Introduction

A crucial step towards studying stellar populations and their variation across the Galaxy is to measure reliable stellar distances. The parallax method is currently viable only for very local stars, although the recently launched Gaia satellite (Perryman et al. 2001) is expected to dramatically increase the number of parallax and proper motion measurements within a significant portion of the Milky Way. Precise distances may also be obtained from asteroseismology, but only for a fraction of stars subject to systematic variability studies (Miglio 2012; Rodrigues et al. 2014). Indirect methods of distance determination, based on photometric and spectroscopic quantities and their relation to stellar absolute magnitudes, can be used for much more distant stars. Photometric distances have been applied to multi-band optical and near infra-red data from different surveys to model the spatial distribution of Galactic stars and to study its substructures (e.g., Jurić et al. 2008; Correnti et al. 2010; Minniti et al. 2011). Recent Sloan Digital Sky Survey III (SDSS-III, Eisenstein et al. 2011) spectroscopic surveys, such as the Sloan Extension for Galactic Understanding and Exploration (SEGUE, Yanny et al. 2009) and the Apache Point Observatory Galactic Evolution Experiment (APOGEE, Allende Prieto et al. 2008a) have produced many more observational constraints, including stellar atmospheric parameters, kinematical and chemical data, that can be used to estimate reliable distances to tens of thousands of stars sampled from the SDSS and 2MASS (Skrutskie et al. 2006) photometric data. These surveys have already had a clear impact on our understanding of the Galaxy (Carollo et al. 2007, 2010; Lee et al. 2011a; Schlesinger et al. 2012; Carollo et al. 2012; Cheng et al. 2012; Bovy et al. 2012b,a; Anders et al. 2014; Hayden et al. 2015). The recently completed RAdial Velocity Experiment (RAVE) survey (Steinmetz et al. 2006) has also provided atmospheric parameters, radial velocities and chemical abundances for six individual elements for more than 400 000 stars (Kordopatis et al. 2013). Ongoing spectroscopic surveys, such as the Gaia-ESO Survey (GES; Gilmore 2012), the Galactic Archaeology with HERMES survey (GALAH; Zucker et al. 2012), or the LAMOST Experiment for

Galactic Understanding and Exploration (LEGUE; Deng et al. 2012), are continuously increasing the number of stars with available spectroscopic information. In fact, these large spectro-photometric data sets will, when analysed together, allow a description of the structure and substructures of the Galaxy with unprecedented detail, excellent statistics, and full use of the 6D phase-space information. Phase-space reconstruction of stellar distributions, coupled to spectroscopic abundances for large samples, will continue to provide challenging quantitative tests to models of Galaxy formation and evolution.

In order to take full advantage of the large set of available spectroscopic and photometric parameters from recent surveys, probabilistic inference has been used by several authors to infer ages, absolute magnitudes, extinction, distances, among other parameters (e.g., Pont & Eyer 2004; Jørgensen & Lindegren 2005; Bailer-Jones 2011; Serenelli et al. 2013; Schönrich & Bergemann 2014). In the context of stellar distances, a series of papers with increasing levels of sophistication has been presented by the RAVE collaboration (Breddels et al. 2010; Zwitter et al. 2010; Burnett & Binney 2010). Burnett & Binney (2010) make use of a comprehensive set of measured parameters and their estimated uncertainties to infer, for each star, the probability distribution that a set of chosen stellar models generate the data. The method was further refined by Burnett et al. (2011) and Binney et al. (2014), and later used to study Galactic chemo-dynamics in, e.g.,Boeche et al. (2013a,b); Binney (2014) or Kordopatis et al. (2015).

In this paper, we follow a similar theoretical background as those authors, and implement a code that computes spectro-photometric distances with the goal of mapping large stellar samples in three dimensions or in phase-space. We are motivated by the analyses of SDSS-III SEGUE and APOGEE data being led by the Brazilian Participation Group (BPG) and the Leibniz-Institut für Astrophysik Potsdam (AIP), which are presented in Anders et al. (2014) and Brauer (2015; PhD thesis, subm.). These papers use APOGEE giants and SEGUE G-dwarfs, respectively, to improve chemo-dynamical constraints to the Galactic components, especially the discs (see discussions in Minchev et al. 2014b; Chiappini et al. 2015). Since SEGUE and APOGEE targets were selected based on different photometric data and have different spectral coverage and resolution, our basic challenge is to ensure that accurate distances are computed for datasets of vastly different provenance, in a homogeneous way. Our emphasis is therefore on confronting our distance estimates with as many reference samples as possible. A direct comparison with the RAVE distances obtained by Binney et al. (2014) for the high-quality giant sample studied in Boeche et al. (2013a) is also provided. In Table A.1 we list the main characteristic of the surveys we have applied our method to.

The outline of the paper is as follows. In Sec. A.2. we review the method, introduce our notation, and show the results of initial validation tests. An analysis of the performance of our code in terms of internal accuracy and precision is provided. We further discuss how biased stellar parameters and prior assumptions influence the estimated distances. In Sec. A.3. we compare our distances to several previous distance determinations that can be used as a reference, given their higher precision and more controlled systematics. We also compare our results for a high-quality sample of RAVE giant stars to those obtained by the RAVE collaboration. Our summary, conclusions, and future plans are provided in Sec. A.4..

A.2. The Method

The general method adopted for this study uses a set of measured photometric and spectroscopic parameters, such as metallicity, [Fe/H], alpha element enhancement, [α/Fe], effective temperature, $T_{\rm eff}$, surface gravity, $\log g$, intrinsic apparent magnitude, m, and colors, to estimate the distance to individual stars. These quantities are compared to predictions from stellar evolutionary models. The comparison between model and measured parameters follows a statistical approach that is similar to previous works (Burnett & Binney 2010; Burnett et al. 2011; Binney et al. 2014).

In brief, assuming that the errors in the measured parameters follow a normal distribution, the probability that a measured value of some quantity, $x\pm\sigma_x$, is consistent with some theoretical value, x_0, is given by

$$P(x,\sigma_x|x_0) = \mathcal{N}_{x_0,\sigma}(x) = \frac{1}{\sqrt{2\pi}\,\sigma_x}\exp\left[-\frac{(x-x_0)^2}{2\sigma_x^2}\right]. \quad (1)$$

We can easily extend this reasoning to a set of (independent) measured parameters, $\boldsymbol{x} = \{x_1, ..., x_n\}$, with associated Gaussian uncertainties, $\boldsymbol{\sigma_x}$, whose theoretical values according to a given model are $\boldsymbol{x_0}$, by writing:

$$P(\boldsymbol{x},\boldsymbol{\sigma_x}|\boldsymbol{x_0}) = \prod_i \mathcal{N}_{x_{0,i},\sigma_i}(x_i) \quad (2)$$

where the product is taken over all the measured parameters of a single star being confronted to the model values. The expression above gives the likelihood of measuring the set $\{\boldsymbol{x},\boldsymbol{\sigma_x}\}$ given a model $\boldsymbol{x_0}$. According to Bayes's theorem, we may compute the posterior probability distribution (the probability of the model, given the data) as:

$$P(\boldsymbol{x_0}|\boldsymbol{x},\boldsymbol{\sigma_x}) = \frac{P(\boldsymbol{x},\boldsymbol{\sigma_x}|\boldsymbol{x_0})\;P(\boldsymbol{x_0})}{P(\boldsymbol{x},\boldsymbol{\sigma_x})}, \quad (3)$$

where the numerator contains the likelihood and the model prior probability, and the denominator depends only on the measured parameters and their uncertanties.[1]

In order to evaluate the probability of some specific model quantity, $\theta := x_{0,i}$, we consider the marginal posterior probability distribution for this quantity, which is obtained by integrating over all variables of Equation (3), except θ:

$$p(\theta) := P(\theta|\boldsymbol{x},\boldsymbol{\sigma_x}) = \int \mathrm{d}x_{0,0}...\mathrm{d}x_{0,i-1}\mathrm{d}_{0,i+1}...\mathrm{d}x_n P(\boldsymbol{x_0}|\boldsymbol{x},\boldsymbol{\sigma_x}) \quad (4)$$

As mentioned earlier, a typical set of measured parameters includes $\boldsymbol{x} = \{[\mathrm{M/H}], T_{\rm eff}, \log g, \mathrm{colors}, m\}$. As for the stellar models, besides the theoretical values of the same parameters, they also involve other quantities such as mass $m_\star$, age τ, and absolute magnitude $M_{\rm abs}$. And we take $\theta = d$, where d is the star's model distance computed as $d\,[\mathrm{pc}] = 10^{0.2(m-M_{\rm abs}+5)}$.

A.2.1. Distance Uncertainties

Our code can deliver various statistics for the desirable quantity. In this work, and following Rodrigues et al. (2014), we compute a star's distance d as the median of the marginalised posterior

[1] Because we are only interested in inferring the best model parameter (in our case the distance) for a specific set of models, this term is dropped in further computations, as it merely represents a constant which can be normalised out (e.g. Ivezić et al. 2013, Chap. 5).

Table A.1. Spectroscopic stellar surveys for which distances were computed using the method presented in this paper. For each case we provide basic information, such as duration, number of stars for different signal-to-noise ratios (SNR), spatial and spectral coverage, and spectral resolving power.

Survey	Year	$N_{\rm stars}$	Spatial coverage	Typical SNR	λ range	R
SEGUE (DR9 G dwarfs)	2004-2008	$\simeq$ 120,000 (35,000)	$\simeq$ 1,300 deg^2	25 (35)	0.38 – 0.92μm	2,000
APOGEE (DR10 HQ giants)	2011-2014	$\simeq$ 100,000 (22,000)	$\simeq$ 2,800 deg^2	100 (120)	1.5 – 1.7μm	22,500
RAVE (DR4 HQ giants)	2006-2013	$\simeq$ 500,000 (9,000)	$\simeq$ 20,000 deg^2	30 (70)	0.84 – 0.88μm	7,500

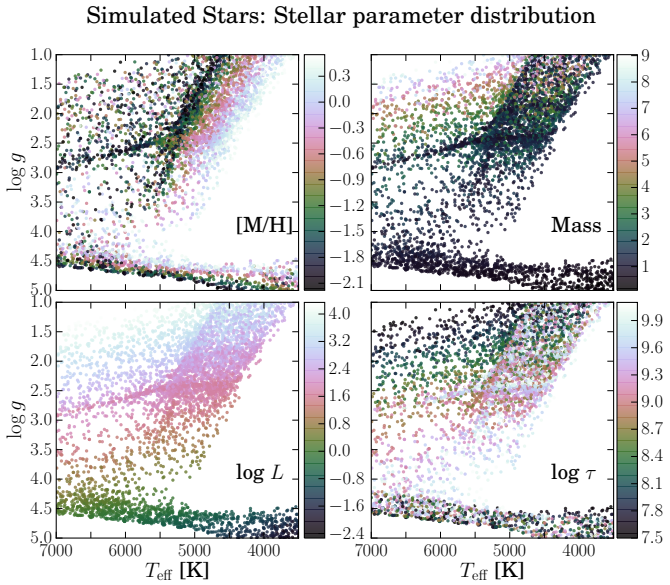

Figure A.1. Stellar parameter distributions of the simulated PARSEC sample in the $T_{\rm eff}$–log g diagram (without observational errors added). *Upper left:* solar-scaled metallicity, *upper right:* mass (in $M_\odot$), *lower left:* luminosity (in $L_\odot$), *lower right:* age (in years).

probability distribution, $p(d)$ (Eq. 4). To estimate the uncertainties, we report the 68% and 95% upper and lower credible intervals of the median, $d_{68L}, d_{68U}, d_{95L}$, and d_{95U}. When quoting a single uncertainty value, we use the definition

$$\sigma(d) := 0.5 \cdot (d_{68U} - d_{68L}).$$

Whenever there is some ambiguity, we use the subscript "BPG" to denote our Bayesian distance estimates[2].

A.2.2. A test suite of simulated stars

In order to verify the method and our implementation, we use a set of simulated stars drawn from a grid of PARSEC 1.2S stellar models (Bressan et al. 2012; Tang et al. 2014; Chen et al. 2015) with a narrow metallicity step of Δ[M/H] = 0.1 and spanning the range $-2.2 \leq$ [M/H] ≤ 0.6, and age steps of $\log \tau$ [yr] = 0.05 in the range $7.5 \leq \log \tau\,[\mathrm{yr}] \geq 10.15$. Specifically, we randomly select 5000 models which fall into the parameter regime targeted by large-scale spectroscopic surveys, by restricting model space to $3000 < T_{\rm eff} < 7000$ K and $1 < \log g < 5$ (see Fig. A.1). These simulated stars are assigned random distances between 0.1 and 6 kpc, drawn from a uniform distribution. The simulated photometry is in the 2MASS JHK_s system (Cutri et al. 2003), with no extinction applied.

[2] BPG is short for the SDSS-III Brazilian Participation Group

By adding typical (conservative) Gaussian random errors to the model observables, we then create two sets of spectrophotometric "observations" from this file: a "high-resolution-like" set of spectroscopically measured quantities ($e_{T_{\rm eff}} = 100$ K, $e_{\log g} = 0.1$ dex, $e_{\rm [Z/H]} = 0.1$ dex)[3], and a "low-resolution-like" set ($e_{T_{\rm eff}} = 200$ K, $e_{\log g} = 0.2$ dex, $e_{\rm [Z/H]} = 0.15$ dex). We assume that the errors are uncorrelated and the observational uncertainties are correctly estimated. Photometric errors are also assumed to be Gaussian and of the order of 0.01 mag.

Some of the effects of possible deviations from these assumptions are discussed in the next Sections (stellar parameter biases, incomplete parameter sets, extinction, Galactic density priors). Other effects (e.g., [α/Fe]-enhanced isochrones, correlated and non-Gaussian stellar parameter errors) are beyond the scope of this paper, and deferred to a future investigation.

A.2.3. Internal accuracy and precision

Fig. A.2 summarises our results from the test with the simulated PARSEC sample with "high-res.-like" observational errors, when using the following set of measured quantities as an input: $\boldsymbol{x} = \{[\mathrm{M/H}], T_{\rm eff}, \log g, m, \mathrm{colors}\}$. In each panel except for the last, we show the relative deviations of our estimated values from the true distances, $(d_{\rm BPG} - d_{\rm true})/d_{\rm true}$, as a function of the model parameters.

The first row of this Figure demonstrates that our distance errors are typically below 20% and do not show any strong systematics with the measured quantities $T_{\rm eff}$, [Z/H] and $\log g$ themselves. However, especially the upper right panel (distribution of distance errors in the $T_{\rm eff} - \log g$ diagram) reveals that our distances for main-sequence and subgiant stars are much better recovered than for giants (mean deviation −0.5%, root-mean-square scatter 10.6% vs. 1.8% and 23.3%, respectively). This is a known problem, because of the larger overlap of models with very different luminosities in the giant region of the Hertzsprung-Russell diagram (see Fig. A.1).

The second row of Fig. A.2 examines the dependency of our distance errors with the model parameters which are not directly measured through spectroscopic observations: mass, age and distance. While there is no correlation between the distance errors and the true distances themselves, we do see some systematic trends with mass and age. In particular, our code tends to slightly overpredict the distances to very old, very-low-mass giant stars, while it underpredicts the distances for very young ($\tau < 100$ Myr) giants with super-solar masses. However, when taking into account the Galactic star-formation history and initial mass function (IMF), these groups typically represent a negligible minority of the stars targeted by large spectroscopic stellar surveys; their fraction is clearly overrepresented in our test

[3] These values can be considered "typical" for stellar parameters obtained from high signal-to-noise-ratio (SNR) spectra from a multi-object high-resolution spectrograph like FLAMES/GIRAFFE or APOGEE. For very-high-resolution spectra from, e.g., HARPS or UVES, these values may even be lower by about a factor of 2.

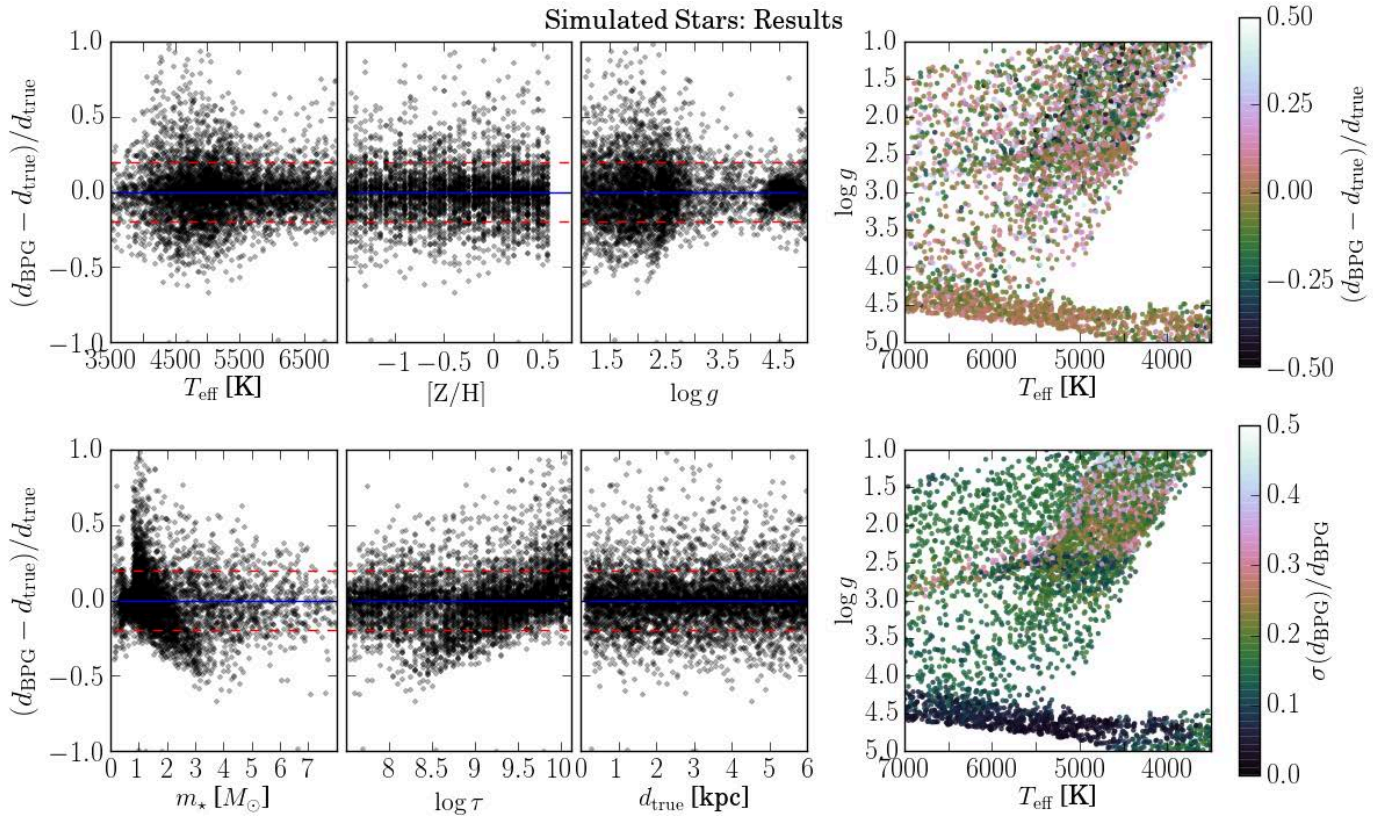

Figure A.2. Results from the test with the simulated PARSEC sample with "high-res.-like" observational errors ($e_{T_{\rm eff}}$ = 100K, $e_{\rm [Z/H]}$ = 0.1 dex, $e_{\log g}$ = 0.1 dex, and $e_{m_{\rm obs}}$ = 0.01 mag.), using the full input parameter set (Set 1: $\boldsymbol{x}$ = {[M/H], $T_{\rm eff}$, $\log g$, m, colors}). *Left six panels:* Relative distance errors (observed – true) of the simulated stars shown as a function of the (true) main stellar model parameters $T_{\rm eff}$, [M/H], $\log g$, mass $m_\star$, age τ, and distance $d_{\rm true}$. The solid line marks the identity line, the dashed lines indicate distance deviations of 20%. *Upper right panel:* Relative distance error distribution in the $T_{\rm eff} - \log g$ diagram. *Lower right panel:* Relative distance uncertainty distribution in the $T_{\rm eff} - \log g$ diagram. Clearly, distances to giant stars are much more prone to systematics and have larger uncertianties.

sample. We can therefore be confident that our code delivers unbiased distance estimates for the vast majority of stars.

Finally, in the lower right panel of Fig. A.2, we show the distance uncertainties for the simulated stars, again as a function of $T_{\rm eff}$ and $\log g$. Evidently, the internal precision of our method is much better for main-sequence stars than for giants (excluding the red-clump/horizontal-branch stars at $\log g \sim 2.5$, for which we also find accurate and precise distances). A comparison between the upper and lower right panels of this Figure also shows that our code determines reliable and unbiased statistical uncertainties.

A.2.4. Sensitivity to input observables

Initial tests showed that, among the input measured quantities, $\log g$ is most critical to estimate unbiased distances, since it is the quantity that best discriminates between low-luminosity dwarfs and more luminous giants, which otherwise share similar values of temperature, metallicities and colors. Dropping $\log g$ from the fitting procedure leads to overestimated distances for dwarf stars, and underestimated distances to giants, respectively. Similar tests also showed that cutting models with $|\boldsymbol{x_0} - \boldsymbol{x}| > 3\boldsymbol{\sigma_x}$ decreases the processing time without appreciably changing the final distance estimates.

Based on these initial assessments, we implemented a code that estimates distances using the method described above and based on four distinct sets $\boldsymbol{x}$:

1. $\boldsymbol{x}$ = {[M/H], $T_{\rm eff}$, $\log g$, m, colors}
2. $\boldsymbol{x}$ = {[M/H], $T_{\rm eff}$, $\log g$, m}
3. $\boldsymbol{x}$ = {[M/H], $\log g$, m, colors}
4. $\boldsymbol{x}$ = {[M/H], m, colors}, but with a cut in models whose $\log g$ differ by more than 0.5 dex from the measured value.

The code can accommodate other sets if so desired. The advantage of implementing different sets of parameters for distance determination is to provide flexibility: distances can be estimated even in the absence of one or two parameters from the set with the largest number of parameters (Set 1). Furthermore, the alternative distance estimates may be intercompared to provide a means to evaluate the sensitivity of the method to the particular combination of spectroscopic and photometric parameters adopted.

Often, the data set in a given sample includes only [Fe/H] values, which are used in place of [M/H]. When [α/Fe] values are available, we adopt the empirical relation [M/H] = [Fe/H]+[α/Fe] for the comparison to PARSEC isochrones (e.g., Anders et al. 2014). Another important issue is extinction: the photometric data, m and colors, must be corrected for extinction and redenning before comparing with the models. The exact procedure depends on the bandpasses used, on the available extinction estimates and on the assumed extinction coefficients.

The top panels of Fig. A.3 show the results of applying the method to our simulated observations (see Sec. A.2.2.). The distribution of the relative distance errors, $(d_{\rm BPG} - d_{\rm true})/d_{\rm true}$, are displayed for the four parameter sets listed above, for both the

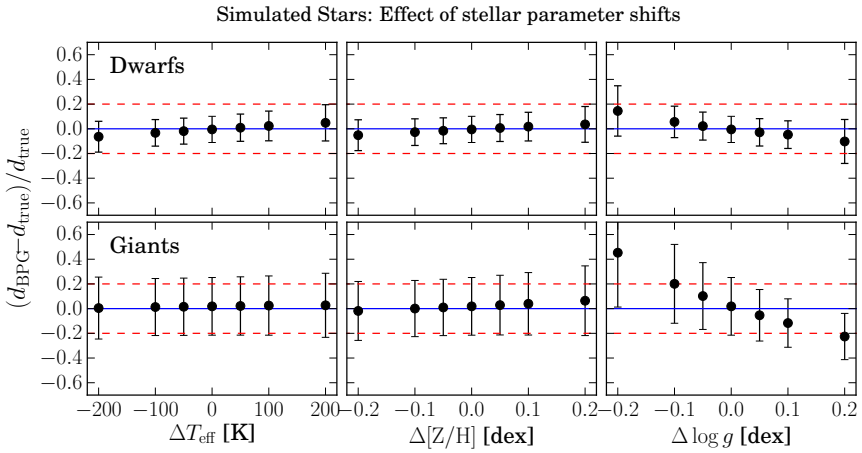

Figure A.4. Effects of systematic shifts in the spectroscopically observed stellar parameters $T_{\rm eff}$ (*left*), [Z/H] (*middle*) and $\log g$ (*right panels*) on our determined distances. For this exercise, we again use the simulated PARSEC sample with "high-res.-like" observational errors and the full input parameter set (Set 1: $\boldsymbol{x}$ = {[M/H], $T_{\rm eff}$, $\log g$, m, colors}). In each panel, the errorbars show the mean and standard deviation of the relative distance errors, as a function of the value of a fixed shift in the particular stellar parameter. Dwarfs ($\log g > 4$) and giants are displayed separately in the top and bottom rows, respectively.

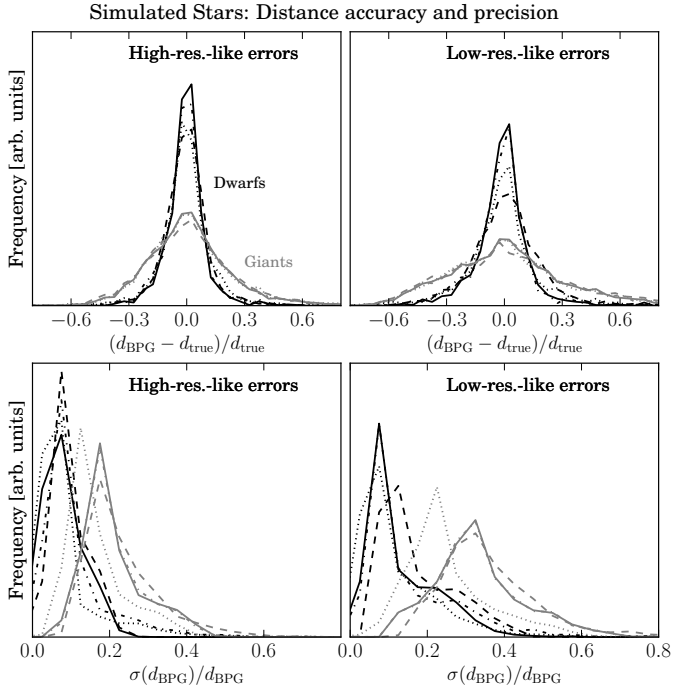

Figure A.3. Distance accuracy and precision for the four input observable sets introduced in Sec. A.2.4.. *Upper panels:* Distribution of relative distance errors, $(d_{\rm BPG} - d_{\rm true})/d_{\rm true}$, for the sample of simulated stars drawn from PARSEC models (see Fig. A.1) with "high-resolution-like" observational errors (*left*; see Sec. A.2.2.) and "low-resolution-like" errors (*right*). In each panel, we are using the distances based on the four sets of measured parameters listed in Sec. A.2.4.. The results for dwarfs are shown in *black*, the results for the giants in *grey*. *Solid lines*: Set 1 ($\boldsymbol{x}$ = {[M/H], $T_{\rm eff}$, $\log g$, m, colors}); *dashed lines*: Set 2 ($\boldsymbol{x}$ = {[M/H], $T_{\rm eff}$, $\log g$, m}); *dash-dotted lines*: Set 3 ($\boldsymbol{x}$ = {[M/H], $\log g$, m, colors}); *dotted lines*: Set 4 ($\boldsymbol{x}$ = {[M/H], m, colors}, with a cut at $|\Delta \log g| < 0.5$ dex). *Bottom panels:* Distributions of our relative (internal) distance uncertainties, $\sigma(d_{\rm BPG})/d_{\rm BPG}$.

"high-res.-like" (left panel) and the "low-res.-like" simulations, and for giants and dwarfs separately.

The four distance estimates proposed lead to reasonable results as attested by these error distributions. Surprisingly, there is only a very small systematic degradation in the precision of our distances as we move down from set 1 to 4. As noted above, set 1 in the "high-resolution" case yields mean distance errors of −0.5% with an rms scatter of 10.6% for main-sequence stars ($\log g > 4.0$), while for giants the numbers are expectedly a bit worse (+1.8% bias and 23.3% precision).

For the other three sets, these numbers are $-0.2\% \pm 11.3\%$, $-0.7\% \pm 13.1\%$, $-2.9\% \pm 21.5\%$ for dwarfs, and $+1.7\% \pm 24.3\%$, $+1.8 \pm 23.4\%$, $+2.8\% \pm 25.1\%$ for giants, respectively. This trend is expected, at least in the context of simulations, since usage of more measured parameters will tend to better constrain the stellar models that best describe each star.

As can be seen in Fig. A.3 (top right panel), these numbers are slightly worse for the "low-resolution" case. The relevant numbers for this and all other comparison samples are listed in Table A.3. In the following, we will use only the full input parameter set (Set 1: $\boldsymbol{x}$ = {[M/H], $T_{\rm eff}$, $\log g$, m, colors}).

The bottom panels of Fig. A.3 show the distributions of our distance uncertainties, $\sigma(d_{\rm BPG})/d_{\rm BPG}$, for each of the four input sets, and for dwarfs and giants separately. Again, we also show the numbers for the "low-resolution" case. As expected, the uncertainty distributions for dwarfs peak at < 10%, while the distributions for giants are broader and peak at larger values.

A.2.5. Effect of systematic stellar parameter errors

In order to gain some insight into the robustness of our method to systematics in the stellar parameters used, we have studied the effect of constant shifts in each of the spectroscopic input parameters on our distance estimates. Fig. A.4 shows the results of this experiment: in each panel, all except for one input parameter are kept constant for the whole simulated "high-res." sample, while the remaining parameter is shifted by a certain amount, and the effect on the relative distance error (observed – true) as a function of this shift. As before, we treat dwarfs and giants separately, because these two groups display distinct systematic trends.

The most striking observation from Fig. A.4 is that even a substantial systematic shift in the temperature ($|\Delta T_{\rm eff}| \lesssim 200$ K) or metallicity scale ($|\Delta$[Z/H]$| \lesssim 0.2$ dex) does not terribly affect neither accuracy nor precision of our distances. This is in stark contrast to systematic shifts in the surface gravity parameter (which are in fact quite commonly found even in high-resolution spectroscopic surveys – e.g., Holtzman et al. 2015).

A.2.6. The model priors

In order to determine distances to stars in the Milky Way, we use our current knowledge about the Galaxy and its components to build the model prior probability distribution, $P(\boldsymbol{x_0})$. This in-

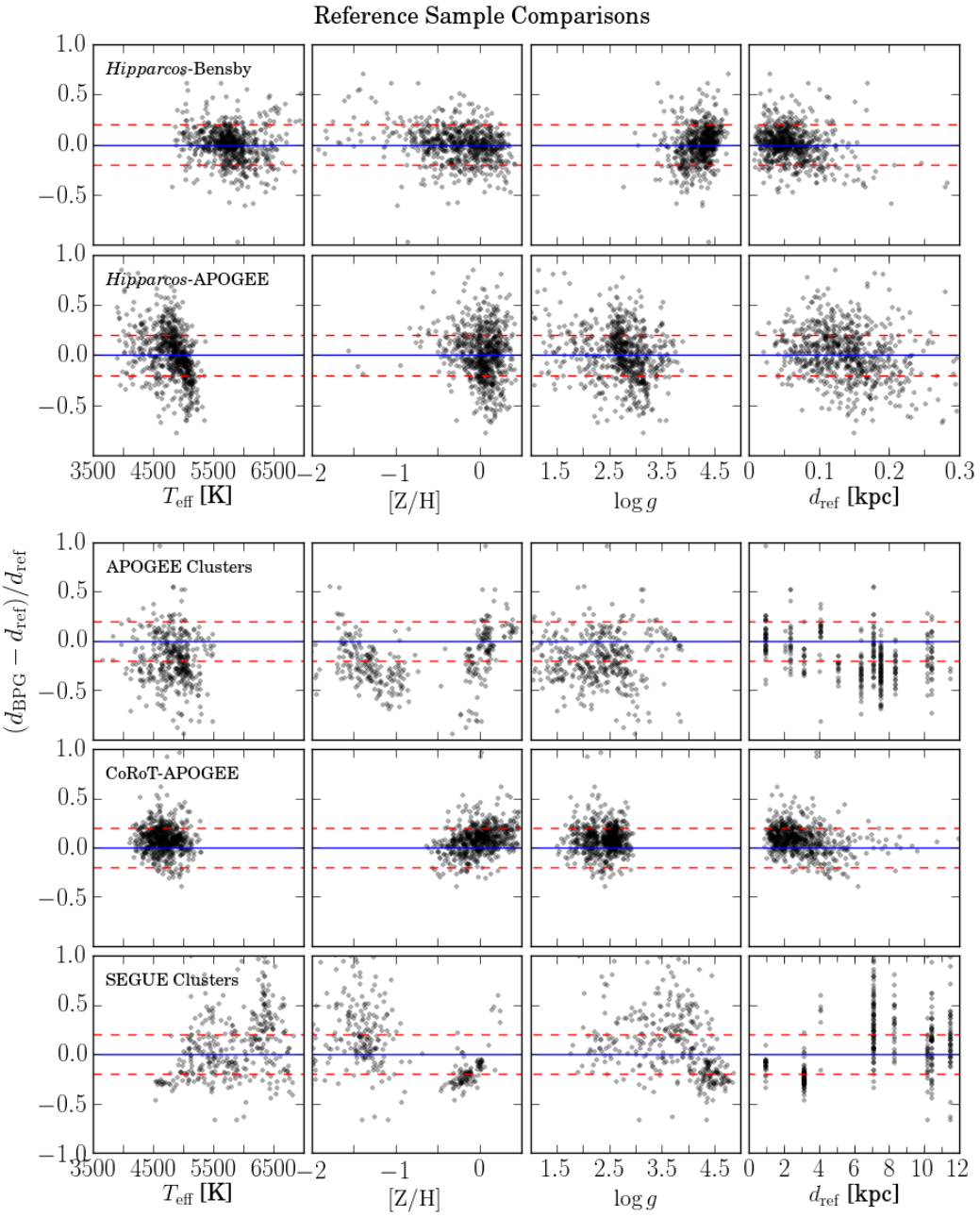

Figure A.5. Relative distance residuals (estimated – reference) as a function of the main spectroscopic parameters $T_{\rm eff}$, [Z/H] and $\log g$ as well as the reference distances $d_{\rm ref}$. *Top rows*: Comparison to the astrometric distance scale provided by the *Hipparcos* satellite, using the Bensby et al. (2014) FGK dwarf sample (1st row) and the APOGEE-*Hipparcos* giant sample (2nd row). *3rd row*: APOGEE clusters. *4th row*: CoRoT-APOGEE sample. *5th row*: SEGUE clusters. The central dashed line is the identity line, whereas the upper and lower ones indicate deviations at the 20% level.

cludes basic information concerning the distributions of stars as a function of position, mass, age, and metallicity.

In particular, we assume that all stars follow a Chabrier initial mass function (Chabrier 2003) and incorporate the probability that a randomly selected star falls within a given mass range, $p(m_\star)$. This involves an integral over the mass function which is provided by the model isochrones.

We take into account the effect of observing a given star in a small but finite solid angle, by applying a geometric prior $\propto s^2 {\rm d}s$ called the volume element, where s is the model distance. We further assume different age and spatial distributions for the basic Galactic components, namely the thin disc, the thick disc, and the spheroid. We here adopt the same Galactic structural parameters as Binney et al. (2014), and refer to this work for a detailed justification.

The age distributions, $p(\tau)$, are taken to be uniform with an upper limit of 10 Gyrs for the thin disc, and lower limits of 8 and 10 Gyrs for the thick disc and halo, respectively.

The spatial priors for the thin and thick discs are given, respectively, by

$$p_{\rm thin}(R,Z) \propto s^2 {\rm d}s \cdot \exp(-R/h_{R,{\rm thin}}) \cdot \exp(-|Z|/h_{Z,{\rm thin}}),$$

$$p_{\rm thick}(R,Z) \propto s^2 {\rm d}s \cdot \exp(-R/h_{R,{\rm thick}}) \cdot \exp(-|Z|/h_{Z,{\rm thick}}),$$

where (R, Z) are cylindrical coordinates with origin at the Galactic center, whose values are computed given the model distance s and a direction (l, b), and h_R and h_Z are the respective scale lenghts and heights. In computing the cylindrical coordinates, we use $R_0 = 8.33$ kpc as the distance from the Sun to the Galactic Centre.

For the halo, we assume a power-law density profile with spherical symmetry:

$$p_{\rm halo}(r, l, b) \propto s^2 {\rm d}s \cdot r^{-\gamma},$$

where $r(s, l, b)$ is a radial spherical coordinate. Again, as in Binney et al. (2014), we adopt $\gamma = 3.39$.

The three density profiles are normalised at the solar location, which, for simplicity, we take to be $(R, z) = (R_0, 0)$ and $r = R_0$, respectively, in cylindrical and spherical coordinates. The normalization values are again from Binney et al. (2014).

We assume that the three basic Galactic components follow Gaussian metallicity distribution functions (MDFs), $p_i([{\rm Z/H}])$, exactly as described by Binney (2014). Our final model prior is then given as

$$P(\boldsymbol{x_0}) = p(m_\star) \sum_i p_i(\tau)\ p_i(\boldsymbol{r})\ p_i([Z/H]).$$

A.3. External Validation

In this section, we present results of the application of our method described in the previous section to a number of reference samples for distance determination. These include distances computed from astrometric parallaxes obtained by ESA's *Hipparcos* mission (Perryman 1989; Perryman et al. 1997; van Leeuwen 2007), precise asteroseismic distances produced by the CoRoT-APOGEE collaboration for a set of solar-like oscillating red giant stars (Anders et al. 2015, subm.), and distances to well-studied open and globular clusters. As in the previous sections, we use $d_{\rm BPG}$ to refer to our distances in all figures. Those taken as reference are referred to as $d_{\rm ref}$. In Table A.2, we provide information about the sources, derivation methods and precision of the parameters in the reference samples. The results of the comparison with the reference samples are summarised in Fig. A.5 and Table A.3. We also compare our distance estimates with those obtained by Binney et al. (2014) for a sample of giant stars from the RAVE survey. This last comparison represents a cross-check of the implementation of the algorithm rather than a benchmark test, as the authors follow a similar theoretical background.

Fig. A.5 presents the comparison of our spectro-photometric distances (BPG) to those from the reference samples. The first three panels of each row show our relative distance residuals with respect to the reference set, as a function of the main spectroscopic parameters $T_{\rm eff}$, [Z/H] and $\log g$. The last panel of each shows the residuals as a function of the reference distance. Each row corresponds to a particular reference sample discussed in this Section.

A.3.1. Comparison with the Hipparcos scale - The FGK star sample of Bensby et al. (2014)

As a first validation test of our spectro-photometric distance algorithm, we use the high-resolution FGK dwarf sample of 714 solar-neighborhood stars with well-determined atmospheric parameters by Bensby et al. (2014). Hereafter, we will refer to this sample as the *Hipparcos*–Bensby sample, because for these stars precision parallaxes from *Hipparcos* (van Leeuwen 2007) are available. We use the optical photometry from the Tycho-2 catalogue (Høg et al. 2000), and set $mag = V_T$, $M_{\rm abs} = M_{V_T}$ and colors = $\{B_T - V_T\}$ in the set of parameters to be compared to the models. As throughout this paper, the models used for this comparison are from the PAdova TRieste Stellar Evolution Code (PARSEC 1.2S, Bressan et al. 2012; Tang et al. 2014; Chen et al. 2015), with a narrow metallicity step of [M/H] = 0.1 and age steps of $\log \tau(yrs) = 0.05$.

The top row of Fig. A.5 shows the results of our distance code for the *Hipparcos*–Bensby sample. There is little or no systematics in the residuals with the parameters themselves. The mean and rms residuals over all stars are 0.4% and 18.2%. In fact, the observed rms residual is comparable to the expected errors in the parallaxes and in our distances based on the "high-res." simulation (presented in Sec. A.2.2.) combined together. Because the *Hipparcos*–Bensby sample combines high-resolution spectroscopic data for nearby dwarf stars with accurate parallaxes, it is arguably the best reference sample to test our code against.

We have validated that, as in our simulation tests described in Sec. 2, the four sets of parameters yield acceptable distances. In the subsequent validation analyses in this paper, we will concentrate on the full parameter set $\{T_{\rm eff}$, [Z/H], $\log g$, colors$\}$, since it makes full use of the set of spectroscopic and photometric parameters which is common to the surveys to which we are applying our method.

A.3.2. APOGEE

The SDSS-III project APOGEE has acquired high-resolution near infra-red (NIR) spectra ($R \simeq 22,500$) of $> 100,000$ stars selected from the 2MASS Point Source Catalogue (Cutri et al. 2003), most of which are red giant stars located at low Galactic latitudes. APOGEE is providing a unique spectroscopic sample of disc-dominated stars with unprecedented volume coverage, for which precision kinematical and abundance measurements are available. For more details about APOGEE data, we refer to Ahn et al. (2014); Alam et al. (2015), and Holtzman et al. (2015). Validation of APOGEE stellar parameters partly relies on calibrating star clusters with many probable member stars with well-determined parameters (Mészáros et al. 2013; Holtzman et al. 2015). In this section we use two APOGEE subsamples to test our distances. In Sec. A.3.2., we use a set of 678 CoRoT stars in the exoplanet fields LRa01 and LRc01 (e.g., Miglio et al. 2013) which have been co-observed within an APOGEE ancillary campaign, and whose asteroseismic analysis has provided high-precision surface gravities (Anders et al. 2015, subm.). In Sec. A.3.2., we make use of the APOGEE calibration cluster dataset.

In the case of APOGEE, we set $m = K_s$, $M_{\rm abs} = M_{Ks}$, and colors = $\{(J - H), (H - K_s)\}$, all of which are corrected for extinction before computing the distances. For the cluster stars, extinction values are based on the Rayleigh-Jeans Color Excess method (RJCE, Majewski et al. 2011; Nidever et al. 2012; Zasowski et al. 2013). This method is based on stellar colour excesses measured using fluxes in near and mid infra-red bands, where almost all stellar spectra are in the Rayleigh-Jeans regime and therefore have very similar intrinsic colours. For the stars in common with CoRoT, we use the precise extinctions calculated by Anders et al. (2015), using the method described in Rodrigues et al. (2014).

We use the calibrated stellar parameters determined by the APOGEE Stellar Parameters and Chemical Abundances Pipeline (ASPCAP; Holtzman et al. 2015, García Pérez et al.

Table A.2. Summary of the reference data: parameter ranges, uncertainties, and provenance. $\log g$ values in the CoRoT-APOGEE sample are based on asteroseismic measurements. All other non-photometric parameters were derived spectroscopically; the relevant references are given in the footnotes indicated in the third column.

Sample	dist. range [kpc]	$\sigma(T_{\rm eff})$ [K]	$T_{\rm eff}$ range [K]	$\sigma \log g$	$\log g$ range	σ [Fe/H]	[Fe/H] range	photom.	magnitude range
Simulated sample	0.1 – 6	100	3000 – 7000	0.1	1.0 – 5.0	0.1	−2.2 – 0.5	JHK_s	distance-limited
Hipparcos-Bensby	< 0.3 [1]	30 – 100 [2]	4800 – 7000	0.1	3.0 – 4.8	0.1	−2.5 – 0.5	$B_T V_T$ [3]	$V < 9$ [2]
Hipparcos-APOGEE	< 0.3 [1]	90	3800 – 5500	0.2	1.0 – 4.0	0.1	∼ −1.0 – 0.5	JHK_s [5]	$(J-K)_0 > 0.5; H < 7$
CoRoT-APOGEE	1 – 6 [4]	100 [4]	4000 – 5300	0.05	1.6 – 3.0	0.1	−0.8 – 0.5	JHK_s [5]	$(J-K)_0 > 0.5; H < 13.8$ [4]
APOGEE Clusters	1 – 6 [6,7]	100 [8]	3700 – 5000	0.2	1.0 – 3.4	0.1	−1.0 – 0.5	JHK_s	$(J-K)_0 > 0.5; H < 13.8$ [9]
SEGUE Clusters	1 – 12 [6,7]	130 [10]	4700 – 7000	0.21	1.6 – 5.0	0.11	−3.0 – 0.0	$ugriz$ [11]	$0.48 < (g-r)_0 < 0.55; r_0 < 20.2$ [12]

References. (1) van Leeuwen (2007); (2) Bensby et al. (2014); (3) Høg et al. (2000); (4) Anders et al. (2015) and references therein; (5) Cutri et al. (2003); (6) WEBDA Database; (7) Harris (1996); (8) Ahn et al. (2014); (9) Zasowski et al. (2013); (10) Ahn et al. (2012); (11) Fukugita et al. (1996); (12) Lee et al. (2008a)

2015, subm.). Some minor improvements on the DR12 calibrations of metallicity and surface gravity have been applied; they are described in Appendix A.A. Since [α/Fe] is again available, we assume that [M/H] = [Fe/H] + [α/Fe] for APOGEE stars[4]

For the comparison with the CoRoT sample (Sec. A.3.2.), APOGEE surface gravities were replaced by those from asteroseismic scaling relations (e.g., Miglio et al. 2013). Table A.2 summarises the data provenance.

The Hipparcos–APOGEE sample

Through a fiber feed from the New Mexico State University 1m telescope at Apache Point Observatory to the APOGEE spectrograph, it is also possible to use APOGEE to observe smaller numbers of bright stars, one at a time (Holtzman et al. 2015, Sec. 2.3). Apart from calibration, this setup is also being used within an ancillary campaign to observe several hundred red giant stars with measured *Hipparcos* parallaxes (Feuillet et al, *in prep.*). The data processing and stellar parameter determination works in exactly the same way as for the data taken with the SDSS 2.5m telescope.

We have used the DR12 *Hipparcos*–APOGEE sample of 712 stars with precise parallaxes ($\sigma(\pi)/\pi < 10\%$) to fundamentally validate our stellar distance estimates also for giant stars. The second row of Fig. A.5 shows our results. The mean and rms residuals amount to +1.6% and 26.4%, respectively.

Recalling the tests performed in Sec. A.2., we find that these numbers are very much comparable with the trends found for the giant sample of simulated "high-resolution" stars (see Table A.3). Taking further into account that the *Hipparcos* parallaxes for these relatively distant objects are also affected by uncertainties of order 10%, the results indeed supersede expectations. Furthermore, we find no systematic trends with either of the stellar parameters.

APOGEE - comparison with asteroseismology: the CoRoT-APOGEE sample

Another important test for our distance method is the comparison with asteroseismically derived distances. It has been shown by recent studies (e.g., Miglio 2012; Silva Aguirre et al. 2012, 2013) that stellar distances (or equivalently, radii) determined from CoRoT and Kepler lightcurves, either via asteroseismic scaling relations or by comparing asteroseismic parameters to predicted values from a grid of models, agree within a few percent with Hipparcos parallaxes and eclipsing binary data. For example, Silva Aguirre et al. (2012) show that distances can be derived with 5% precision for solar-like stars by coupling the infra-red flux method to determine $T_{\rm eff}$ and bolometric fluxes to the grid-modelling of the measured values of the frequency of maximum oscillation power, $\nu_{\rm max}$, and of the frequency difference between dominant oscillation modes, $\Delta\nu$. We therefore compared our spectro-photometric distances based on APOGEE stellar parameters with the distances obtained from CoRoT data for 678 stars in the fields LRa01 and LRc01, which have been successfully observed by both instruments. The reference distance scale is that of Anders et al. (2015) who used the well-tested stellar parameter estimation code PARAM (da Silva et al. 2006; Rodrigues et al. 2014), which is based on a similar theoretical background as this paper, but differs in a number of details. PARAM utilises the parameter set $\{T_{\rm eff}, [{\rm Z/H}], \Delta\nu, \nu_{\rm max}\}$ to first estimate the posterior probability over the stellar models (i.e., it delivers mass, radius, age and absolute magnitude pdfs). In a second separate step, it compares the derived absolute magnitude pdfs with a number of broad-band photometric measurements to derive individual stellar distances and extinctions. The code has been extensively tested in Rodrigues et al. (2014) and Anders et al. (2015); it delivers very precise distances for asteroseismic targets ($\sigma(d) \lesssim 2\%$). Because we use the same data and similar methods to derive stellar distances, the distance scale of Anders et al. (2015) does not provide a completely independent benchmark. However, it serves as an important cross-check for the implementation of our code.

The comparison is shown in the 4th row of Fig. A.5. We again show the relative distances residuals between our distances (BPG) and those from CoRoT-APOGEE. The general picture is reassuring, despite the limited number statistics. Our code converged for 644 stars, the mean and rms relative distance residuals are +8.7% and 14.9%, respectively. No strong trends are seen with metallicity, effective temperature or surface gravity.

The systematic differences between the two methods may arise from the different handling of priors, while the rms scatter is more likely to be attributed to our use of only three photometric passbands instead of the multi-wavelength photometry used by PARAM, and to minor differences in building the distance pdf. For simplicity, and because of the high quality of acquired data, Anders et al. (2015) opted to use an IMF prior plus flat priors on Galactic structure, to derive distances. However, their sample extends over a large range of Galactocentric distances, so that small systematic shifts like the one measured here are not excluded.

In summary, we find a very good agreement between the two methods, modulo a small systematic trend which we attribute to our choice of more comprehensive priors, and a scatter of ∼ 15%

[4] We here refer to ASPCAP's cluster-calibrated [M/H] values (Alam et al. 2015; Holtzman et al. 2015) as [Fe/H], as ASPCAP metallicities were calibrated on literature [Fe/H]values.

Table A.3. Summary of the results for the reference distance samples used in this work.

Sample	$N_{\rm stars}$	Dist. Range [kpc]	Mean rel. residuals [%]	RMS rel. residuals [%]
Simulated "high-res." stars	5000	0.1 – 6	+1.2	20.9
Dwarfs ($\log g > 4$)	1248	0.1 – 6	−0.5	10.6
Giants ($\log g < 4$)	3752	0.1 – 6	+1.8	23.3
Simulated "low-res." stars	5000	0.1 – 6	+3.3	33.4
Dwarfs ($\log g > 4$)	1248	0.1 – 6	−0.6	15.5
Giants ($\log g < 4$)	3752	0.1 – 6	+4.6	37.4
Hipparcos-Bensby dwarfs	714	$\lesssim 0.2$	+0.4	18.2
Hipparcos-APOGEE giants	712	< 0.3	+1.6	26.4
CoRoT-APOGEE giants	644	1 – 12	+8.7	14.9
APOGEE clusters – cluster age prior	392	1 – 15	−16.5	29.9
SEGUE clusters – field priors	419	1 – 12	+14	43
Δ log g =+0.25 dex; field priors	425	1 – 12	−2	35
Δ log g =+0.25 dex; clus. age priors	385	1 – 12	+13	39

Table A.4. Summary of the properties of star clusters used as reference for APOGEE and SEGUE distance estimates: dereddened cluster distance moduli, ages, metallicities, reddenings, and numbers of stars observed by APOGEE and SEGUE. Almost all of the listed clusters were used for APOGEE calibration, while SEGUE targeted a larger number of cluster members in some selected calibration clusters.

Cluster	$(m-M)_0$	$\log(\tau)$	[Fe/H]	E(B-V)	$N_{\rm APO}$	$N_{\rm SEGUE}$
NGC 188	11.55	9.63	−0.02	0.082	5	
NGC 2158	13.52	9.02	−0.23	0.36	15	10
NGC 2420	12.45	9.05	−0.26	0.029	16	125
NGC 5466	16.02	10.13	−1.98	0.0	5	
NGC 6791	13.06	9.64	+0.15	0.117	22	37
NGC 6819	11.86	9.17	+0.07	0.238	23	
NGC 7789	11.84	9.23	−0.08	0.217	4	
M 2	15.50	10.11	−1.65	0.06	3	64
M 3	15.07	9.69	−1.5	0.12	18	35
M 5	14.46	10.02	−1.29	0.03	84	
M 13	14.33	10.06	−1.53	0.02	46	149
M 15	15.39	10.07	−2.37	0.10	31	78
M 35	10.37	7.97	−0.16	0.262		6
M 53	16.32	10.10	−2.1	0.02	13	
M 67	9.79	9.41	0.00	0.059	48	50
M 71	13.01	10.00	−0.78	0.25	2	
M 92	14.65	10.14	−2.31	0.02	34	39
M 107	15.05	10.14	−1.02	0.33	39	
Be 29	15.86	9.025	−0.44	0.157	9	

which could be reduced by the inclusion of more photometric observations in our dataset.

APOGEE - Cluster comparison

In the third row of Fig. A.5, we compare our spectro-photometric distances with those obtained from isochrone fitting of star cluster color-magnitude diagrams (CMDs). We again restrict the comparison to the spectro-photometric distances based on the parameter set (1) in Sec. A.2.. We use a subsample of the ∼ 400 open and globular cluster stars that are used for calibration of ASPCAP, as described in Mészáros et al. (2013); Holtzman et al. (2015). We again refer to Table A.2 for a summary of the data used. Most of the stars with reliable parameters belong to the globular clusters M5, M13, M15, M92, M107, and to the open cluster M 67. The cluster distances and ages are adopted from the WEBDA cluster database in the case of open clusters and Harris (1996) for the globular clusters. Table A.4 summarises the cluster properties.

The right panel in this comparison shows a hint that our distances are being underestimated for more distant clusters. The global mean residual is −16.5%, with an rms scatter of 30%. All clusters, except for NGC 2420 ($d_{\rm ref} \simeq 3$ kpc), have most of their stars with residuals smaller than 30%. Instead of the field star priors discussed in Sec. A.2.6., we have used a simple age prior for each cluster. This adopted cluster prior simply assumes a lognormal distribution of cluster stellar ages, whose mean is the literature age estimate for the cluster and the dispersion is taken as $d\log\tau = 0.1$. We find that for most APOGEE clusters this prior is irrelevant, but the age prior improves the agreement with the reference distances for NGC 2420 and NGC 2158, while it negatively affects M71, which is the oldest and most metal poor cluster in the list.

The comparison suggests that our spectro-photometric method, despite the scatter, yields distances that are in general agreement with the cluster scale, but subject to significant systematics, especially as a function metallicity (see Fig. A.5, third row, second panel). The fact that we do not see these systematic trends in the comparisons with the *Hipparcos* scale suggests that the cluster distances might be subject to improvements in the underlying stellar physics (e.g., the inclusion of rotation; Brandt & Huang 2015b), and less of a gold standard than commonly assumed. Another important caveat is the possible contamination of the cluster sample with non-members.

Regarding the uncertainty of isochrone-based cluster distances, it has been shown by Pinsonneault et al. (2000) that open cluster distances (which are usually determined via measuring the main-sequence shift relative to the Hyades cluster) may be subject to zero-point shifts, based on changes in the adopted distance to the Hyades and interstellar reddening, as well as to the metal and helium abundance, and the age, of the Hyades (e.g. Brandt & Huang 2015a). However, assuming a conservative error of 0.1 mag for the cluster distance moduli, the uncertainties in the spectroscopic distances are still by far the most important.

A.3.3. SEGUE Clusters

The Sloan Extension for Galactic Understanding and Exploration (SEGUE) is a large optical spectroscopic survey at low resolution ($R \simeq 2,000$, Smee et al. 2013). Its goal is to deepen our knowledge about the Galactic structural components and their stellar content, sampling them mostly at high latitudes (Yanny et al. 2009; Eisenstein et al. 2011). In

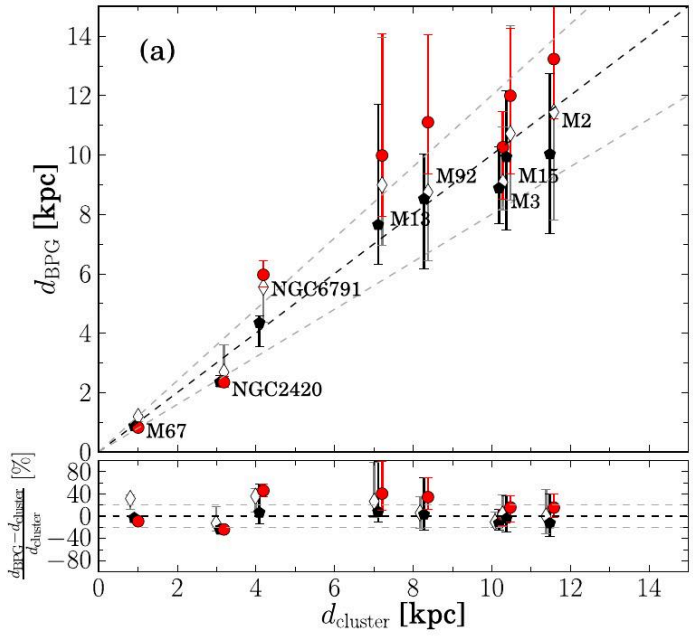

Figure A.6. Comparison of our distances and the host cluster distances $d_{\rm cluster}$ for a subsample of clusters with SEGUE observations. For each cluster the median distance and the 68% quantiles (as error bars) are shown assuming the following different scenarios: *open diamonds* - uncalibrated SSPP DR9 parameters with field priors, *black pentagons* - a $\log g$ shift of 0.25 dex and field priors, and *red circles* - a shifted $\log g$ and a simple cluster age prior. For visibility the different symbols are slightly offset with respect to $d_{\rm cluster}$. The lower panel shows the distance residuals, similarly to the right column of panels in Fig. A.5.

this sense, SEGUE is largely complementary to APOGEE in terms of coverage of the Galactic components. For more info on the spectra and instruments we refer to Gunn et al. (2006) and Smee et al. (2013). SEGUE data have been processed through the SEGUE Stellar Parameter Pipeline (SSPP), which is described, along with its improvements, in a series of papers (Lee et al. 2008a,b; Allende Prieto et al. 2008b; Smolinski et al. 2011; Lee et al. 2011b). Particularly important to the SSPP is the validation of the derived stellar parameters. Field stars with high-resolution spectra and known members of well studied star clusters have been used for that purpose (Allende Prieto et al. 2008b; Lee et al. 2008b; Smolinski et al. 2011).

As in the case of APOGEE (see Sec. A.3.2.), we here use the sample of cluster stars, whose distances are well-known from isochrone fitting, to further test our distance estimates. In the case of SEGUE data, we set mag = g, $M_{\rm abs} = M_g$, and colors = $\{(u-g),(g-r),(r-i),(i-z)\}$ (see Gunn et al. (1998) for a description of the SDSS camera and Fukugita et al. (1996) for information on the photometric system). The spectroscopic and photometric data are from the SDSS *Ninth Data Release* (DR9; Ahn et al. 2012) database. Since [α/Fe] is available for all SEGUE stars in our reference clusters, we assume that [M/H] = [Fe/H]+[α/Fe] in order to compare the data to the model [M/H] values. As previously mentioned, all measured quantities have associated uncertainties. The measured photometric quantities also must be corrected for extinction and reddening to allow a direct comparison to the models. Again, the data for the clusters used here are listed in Table A.4.

The original sample contained 11 clusters, among open and globular, totalling a bit over 1000 stars. For 593 stars, a complete set of spectroscopic and photometric parameters and associated uncertainties allowed us the use of parameter set (1) to estimate distances. As the sample is spectroscopic, in all other cases the missing parameter(s) was(were) photometric. Distances were successfully computed (i.e., at least one model was found within 3 σ of all the measured quantities) for 425 out of the 593 stars, pertaining to the eight clusters listed in the table. We include only those clusters with at least five confirmed members and successfully derived distances using our approach. Their distances, ages and metallicities were again taken from the WEBDA database in the case of open clusters, and from Harris (1996) in the case of the globular clusters.

In the last row of Fig. A.5, we show the distance residuals of individual stars against [Fe/H], $T_{\rm eff}$, $\log g$, and reference cluster difference, similarly to what we did with the other samples in this Section. The scatter is larger than in previous samples, attesting the lower resolution of the data. Still, most of the stars have residuals close to or within the 20% lines and do not exibit any strong systematics with the spectroscopic parameters. The more deviant points correspond to a fraction of the low metallicity ([Fe/H] < -1.0) giant and subgiant ($\log g \leq 4.0$) stars, located beyond $\simeq 6$ kpc. The mean and rms residuals over all stars are 0.14 ± 0.43 after applying a 3-σ clipping. Our individual distances are biased towards large values for a significant fraction of the stars in the more distant globular clusters. This trend is opposite to what was observed in the case of APOGEE clusters (see Sec. A.3.2.). If we consider only the 3 clusters with $d_{\rm ref} < 5$ kpc, the mean and rms scatter are reduced to 0.03 ± 0.27.

We investigated further the cause of this systematic overestimate of the distances to part of the SEGUE stars in the more distant clusters. In analyzing the distribution of different SEGUE spectroscopic parameters, it became clear that the $\log g$ parameter for our sample, as published in DR9, appears to be underestimated for most stars in those clusters. Recalling that $\log g$ is the most important quantity to efficiently separate dwarf and giant stellar models, we have decided to heuristically correct for this shift in this work.

The contours (black) in Fig. A.7 show the distribution of a large sample of SEGUE G-dwarf stars (sample compiled from DR9 and described and analysed in Brauer 2015 (PhD thesis, subm.)) in the $\log g$ *vs.* $T_{\rm eff}$ (left panel) and $\log g$ *vs.* [Fe/H] (right panel) plane. For comparison, we also present the density distributions for a mock sample of G-dwarf stars obtained from TRILEGAL simulations (Girardi et al. 2005, 2012) covering the same SEGUE plates as present in the SEGUE G-dwarf data sample. These simulations were carried out using ADDSTAR, a web based tool that uses parallel processing to efficiently run TRILEGAL in many independent pointings (Balbinot et al. 2012). The TRILEGAL G-dwarf mock sample shown here has been compiled by applying the same overall cuts to the simulation that were used for the SEGUE G-dwarf data sample including the colour-magnitude limits for SEGUE G-dwarfs. For a detailed description of the TRILEGAL mock sample see Brauer (2015).

A clear shift is seen in both panels, in the sense that the data have systematically lower values of $\log g$ for a fixed $T_{\rm eff}$ or metallicity by $\simeq 0.25$ dex. The comparion with the population synthesis model reveals that the SSPP $\log g$ values published in DR9 are underestimated, and that shifting the $\log g$ values for the SEGUE stars is clearly needed, at least for the purpose of deriving reliable distances. Further details about the TRILEGAL mock G-dwarf sample, the discrepancies seen in stellar parameters between data and simulation, and the underestimated surface gravity values published with DR9 are given in Brauer (2015).

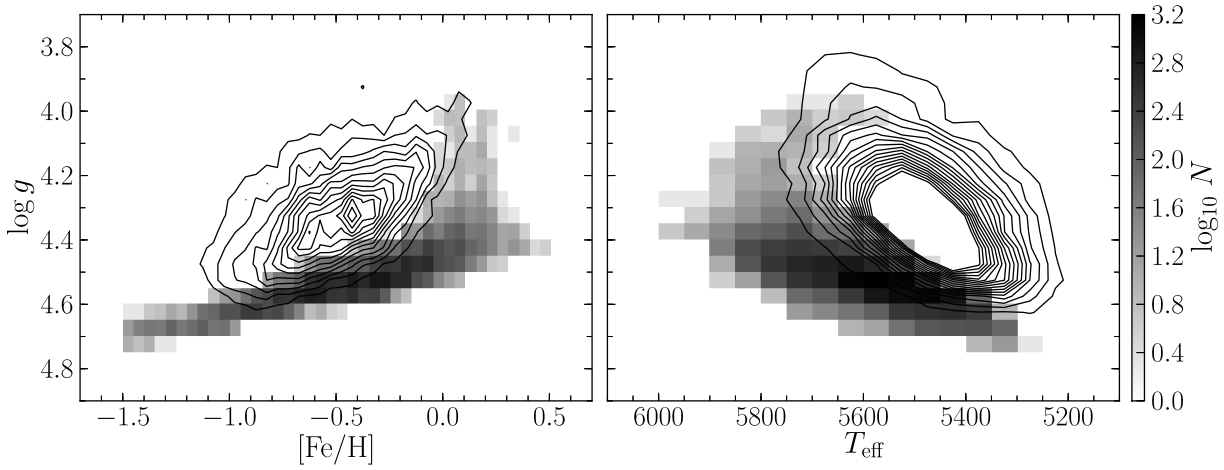

Figure A.7. Left panel: The contours show the density of SEGUE dwarfs in the $\log g$ *vs.* [Fe/H] plane. The colour density map corresponds to the same type of stars simulated by the TRILEGAL code. Right panel: same as in the previous panel, but stars are shown in the $\log g$ *vs.* $T_{\rm eff}$ plane.

We thus decided to test the effect of applying a shift of 0.25 dex to the $\log g$ values when computing the distances. The results are shown in Fig. A.6, where we compare the median spectro-photometric distances of each cluster with the reference cluster distances for different $\log g$ calibrations and/or priors used. The open diamonds correspond to median cluster distances using the SEGUE data as they come from DR9. The black pentagons show the effect of shifting $\log g$ as explained above. The global mean offset relative to the reference distances has been reduced to -2.4%, although the rms relative residual remains high (35%). For the three more nearby clusters, the distances become systematically underestimated by -18% although the scatter around the mean residual has decreased considerably to 12%. The result of adopting a simple age prior for the clusters, as done for APOGEE data, is shown as the red circles of Fig. A.6. This choice has a sizable effect on the distances in the sense of increasing them for the more distant clusters, yielding a mean and rms relative residual of $+0.13 \pm 0.39$.

We conclude that, despite the large scatter in distances of individual cluster stars, there is a general agreement between our median distances for SEGUE cluster stars and those from CMD fitting. A fraction of the stars at lower metallicities and $\log g$, and located in the more distant globular clusters, have their distances overestimated by our method. This seems to be because the SEGUE $\log g$ scale is systematically too low, as attested by simulated samples of SEGUE stars.

Finally, we emphasize that the SEGUE data is very distinct from APOGEE in terms of spectral range and resolution. These data also probes much larger distances than the *Hipparcos* based data used in Sec. A.3.1..

A.3.4. RAVE

RAVE collected medium-resolution ($R \sim 7,500$) CaII triplet spectra of $\gtrsim 400,000$ stars with $9 < I < 13$. For $> 200,000$ of these stars, Burnett et al. (2011) have been able to derive spectro-photometric distances using spectroscopic parameters from the RAVE pipeline (Kordopatis et al. 2011) as well as near infra-red photometry from 2MASS (Skrutskie et al. 2006; Cutri et al. 2003). Their method has provided the background for the work presented in this paper, which is largely based on the Bayesian approach proposed by Burnett et al. (2011). More recently, Binney et al. (2014) presented an improved version of the method. In this section, we use their distances for a high S/N sample containing $\gtrsim$ 9000 giant stars (Boeche et al. 2013a) to cross-check the implementation of our method (details in Appendix A.C). The spectroscopic parameters are taken from the RAVE Data Release 4 (DR4; Kordopatis et al. 2013), the photometry is from 2MASS.

In order to derive distances for RAVE stars, we set $m = K_s$, $M_{\rm abs} = M_{K_s}$, and colors $= \{(J-H),(H-K)\}$. We adopt the A_V extinction values that have been computed for individual RAVE objects by Binney et al. (2014) to deredden the NIR magnitudes of the stars. The conversion between the extinction in the optical and near-IR wavelength range is performed following Rieke & Lebofsky (1985). We adopted the [Fe/H] and [α/Fe] estimates from the chemical RAVE pipeline (Boeche et al. 2011; Kordopatis et al. 2013) to make our metallicity scale more compatible with the stellar models, as in the previous sections.

Despite the use of a very similar theoretical framework, we note that there are some differences between the way distances are estimated by Binney et al. (2014) and in this paper. The Padova isochrone grid these authors used (Bertelli et al. 2008) is not the same as the one used for this paper, and it was restricted to [Fe/H] ≥ -1. Also, they use a slightly different IMF (Aumer & Binney 2009), and apparently they did not use the volume element $s^2 ds$ in the density priors presented in Sec. A.2.6.. They also apply a kinematic correction for their distances (Schönrich et al. 2012). From the data side, we have used a slightly different metallicity scale, namely that of the RAVE chemical pipeline instead of the RAVE stellar parameter pipeline, together with a different handling of α-enhancement.

Fig. A.8 shows the comparison of our distance estimates with the distances from Binney et al. (2014) for the giant sample analysed in Boeche et al. (2013a). For compatibility with our approach described in Sec. A.2., we use the $\langle s \rangle$ distance estimate from the calibrated DR4 catalogue from Binney et al. (2014) in this comparison, which is the expectation value computed from their model pdf over distances instead of their corresponding parallaxes. Because neither of the distances being compared are supposed to be at the same level of precision as those in our reference samples, we change the way we compare them. Instead of computing the relative residual with respect to any one of the estimates, we normalise the residual by the combined uncer-

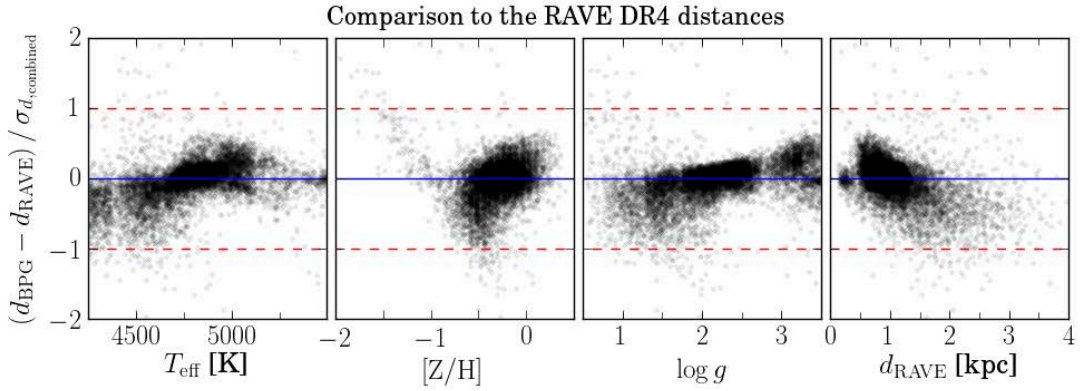

Figure A.8. Comparison of our distance estimates against the RAVE DR4 distances from Binney et al. (2014) for the high-SNR sample of Boeche et al. (2013a). In each panel the vertical axis shows the absolute distance residuals normalised to the combined uncertainty from both methods, $\sigma_{d_{\rm combined}} = \sqrt{\sigma(d_{\rm BPG})^2 + \sigma(d_{\rm RAVE})^2}$, as a function of the main spectroscopic parameters $T_{\rm eff}$, [Z/H] and $\log g$ as well as the RAVE distance, $d_{\rm RAVE}$.

tainty from both, which are added in quadrature. Our distance scale seems to be slightly compressed relative to RAVE DR4: we have systematically larger (smaller) distances than RAVE for stars with $d_{\rm RAVEDR4} < 1$ ($d_{\rm RAVEDR4} > 1$) kpc. The effect, however, is small. The vast majority of the stars have distance residuals well acommodated by the expected uncertainties in the two estimates being compared. The mean and rms normalised residuals are 0.00 ± 0.33, after a 3-σ clipping to eliminate the very few strongly deviant points between the two methods. Looking separately at the two distances regimes, we have mean relative residuals of 6% and -16%, respectively for $d_{\rm RAVEDR4} < 1$ and $d_{\rm RAVEDR4} > 1$ kpc.

A.3.5. Effect of different priors

In Fig. A.9, we assess the effect of the adopted model priors on our distance estimates. For this purpose, we use the high quality RAVE sample ($\simeq$ 9000 stars) presented in Sec. A.3.4..

The aim of this exercise is merely to be able to quantify the effect of the adopted priors on a particular stellar population, not the justification of these priors (which is discussed in Sec. A.2.6.). Note that for the internal consistency checks discussed in Secs. A.2.3., A.2.4. and A.2.5., we did not use any priors, which is the appropriate decision for our simulation, but not for real Milky Way stellar populations.

The top row panels in Fig. A.9 compare distances based on no assumed priors, as used in the simulations, to those using only the IMF prior, as presented in Sec. A.2.6., and a correction for a uniform age distribution. The distances in the middle panels include the spatial priors, but still exclude the specific age distributions and MDFs of individual Galactic components presented in Sec. A.2.6.. The comparison with the distances that also take these later into account is left to the bottom panels in the figure.

It is clear from the figure that inclusion of age and metallicity priors both tend to systematically reduce the distances of a significant fraction of the stars. Restricting the thick disc and halo samples to old ages, in particular, prevents models of young luminous stars to be included in their distance estimates. Similarly, associating disc stars to relatively metal-rich models also tends to reduce their distances. A large number of stars are unaffected by the specific choice of model priors. Using all stars with estimated distances $s < 6$ kpc (when all priors are included, comprising the vast majority of the RAVE high quality sample) we obtain a mean residual of 5% and a scatter of 6% between the *all priors* and *spatial priors only* distances. This is, in fact, smaller than the systematic residuals and scatter found with respect to more precisely determined distances, as discussed in Sec. A.3..

A.4. Summary and conclusions

We have implemented a code to estimate distances to field stars based on their measured spectroscopic and photometric parameters. The theoretical background is very similar to that of Burnett & Binney (2010) and subsequent papers from the same authors. Briefly, given a set of measured quantities, these are compared to model values and, using a Bayesian approach, the posterior probability distribution function is derived for each star. The distance is then determined as the median value of the posterior pdf marginalised over the other parameters.

We used simulated stars from PARSEC models as a first validation test of our distances. We showed that distances based on 4 different sets of parameters are well recovered, without significant systematic biases, and statistical uncertainties that scale with the uncertainties of the input parameters. Distances to dwarf stars are more accurately recovered, with < 1% mean residual and 10% rms errors for a "high-resolution" simulated sample; typical errors for giant stars are about twice those values. The method is most sensitive to $\log g$, and starts breaking down if this parameter is removed from the data set, also yielding strong systematic distance errors as a function of bias in this parameter.

Our simulations also show that the estimated distance uncertainties are in general agreement with the errors, with the uncertainty distribution peaking at $\simeq$ 10% ($\simeq$ 20%) for dwarf (giant) stars in a mock high-resolution sample, reaching significantly larger values when spectroscopic parameters are less precise.

We demonstrated that distances of nearby stars with parallaxes from Hipparcos and precise atmospheric parameters are successfully recovered, with only very small systematic trends, and random errors consistent with the expected combination of errors in the parallaxes and in our distances. The relative random errors are of the order of 20% or less, with < 1% systematic errors, for nearby FGK dwarf stars. For giants with *Hipparcos* parallaxes, the random and systematic residuals in our distance estimates are also as expected based on our mock samples.

For more distant stars, we have validated the code using giant stars with asterosismic obervations, as well as certain members of well-studied star clusters. In the later case, we compared our distances to the cluster distances taken from the literature.

Our distances for giant stars in common between APOGEE and CoRoT typically agree within 15% of each other. A system-

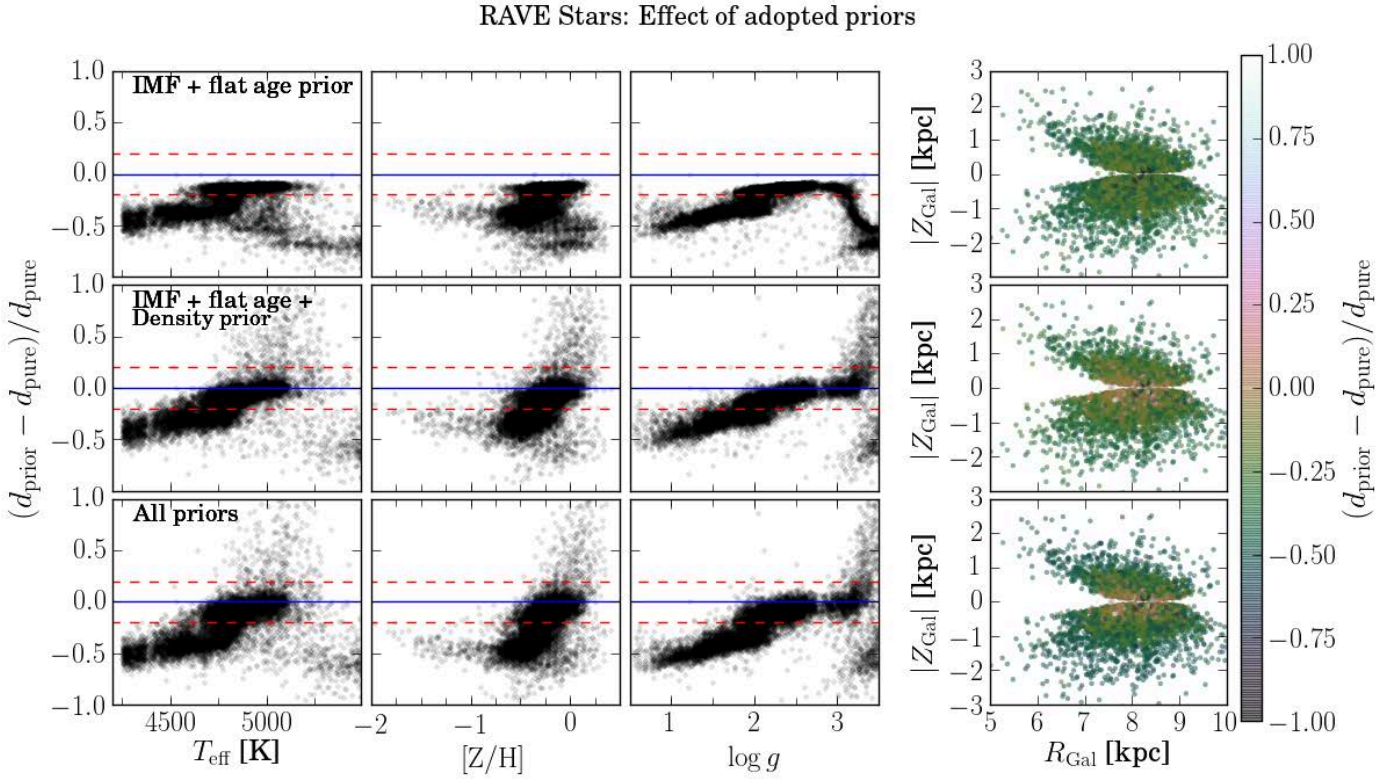

Figure A.9. The effect of the adopted priors (Sec. A.2.6.) on our spectro-photometric distances (BPG), illustrated for the case of the RAVE sample. In each panel, we show the relative distance residuals (priors – no priors) with respect to the case where no priors were used, as a function of the main stellar parameters $T_{\rm eff}$, [Z/H], $\log g$, and as a function of position in the Galaxy (right panels). The *top row* shows the results for distances computed using the IMF prior and a flat prior in age instead of the logarithmic one implicit in the spacing of isochrones in $\log \tau$. The *middle row* also includes the spatial density priors. Finally, the *bottom row* includes the MDF and age priors for the different Galactic components.

atic overestimate in our distances in comparison to those inferred from asteroseismology at the level of $\simeq 9\%$ may result from using a more set of comprehensive Galactic priors and a less comprehensive set of photometric measurements than our reference.

We used star clusters included in the SDSS-III SEGUE and APOGEE samples for a final set of validation tests, this time covering a larger range in distances, out to $\simeq$ 12 kpc. The distance scatter among individual cluster stars is larger than the distance residuals for the more nearby stars with parallax measurements. For APOGEE clusters, there is a small trend with distance itself, in the sense of underestimating the distances to the more distant cluster stars ($d \gtrsim 6$ kpc).

In the case of SEGUE, scatter tends to be higher than APOGEE, consistent with the lower resolution of the spectra. In particular, for a fraction of the low-metallicity giant and subgiant stars that predominate in the more distant globular clusters used, our distances tend to be overestimated, contrary to the trend seen in APOGEE. We have identified the probable origin for this discrepancy as a systematic bias in the SEGUE $\log g$ values. Applying a shift of 0.25 dex to the SEGUE $\log g$ reduces the mean distance residual over individual stars from 14% to -2% when all clusters are considered. The scatter is also significantly reduced for the more nearby cluster SEGUE stars. Despite the large scatter observed for a subset of the SEGUE stars, the inferred average distances to the SEGUE clusters are in good agreement with those quoted in the literature.

We have also compared our distances to those for a sample of high-quality RAVE stars, determined with similar approaches to the one presented here (Binney et al. 2014). Despite the large scatter and a slight systematic trend, our distances for the same sample of red giant stars studied in Boeche et al. (2013a) agree, within the expected uncertainties, with those derived by Binney et al. (2014).

The validation results are all summarised in Table A.3, where we show the dataset used, the number of stars and the range of reference distances in each, and the mean and rms relative residuals. The table allows a global evaluation of the distances, specially when confronted to those from astrometry, asteroseismology, and well calibrated star clusters. The systematic residuals are usually less than 9% while the scatter scales with the quality of the input spectro-photometric parameters, with the most distant SEGUE clusters being our worst case.

The code presented and validated in this paper is being used by the Brazilian Participation Group on SDSS-III to derive distances for tens of thousands of stars belonging to the SEGUE and APOGEE surveys. These surveys are complementary in many ways, including the directions and Galactic components they probe more efficiently. When analysed together, provided that reliable distances are available, they allow a 3D mapping of Galactic structure using different stellar tracers, determination of chemo-kinematic relations in the Galaxy, and ultimately, confrontation of these constraints with models of Galactic formation and evolution (Minchev et al. 2013, 2014a). Initial science analyses based on these distances are provided by Junqueira et al. (2015) and Anders et al. (2014).

Acknowledgements. The authors thank C. Boeche and G. Kordopatis for useful discussions about RAVE.

This research has made use of the WEBDA database, operated at the Institute for Astronomy of the University of Vienna.

Funding for SDSS-III has been provided by the Alfred P. Sloan Foundation, the Participating Institutions, the National Science Foundation, and the U.S. Department of Energy. The SDSS-III web site is http://www.sdss3.org/.

SDSS-III is managed by the Astrophysical Research Consortium for the Participating Institutions of the SDSS-III Collaboration including the University of Arizona, the Brazilian Participation Group, Brookhaven National Laboratory, University of Cambridge, University of Florida, the French Participation Group, the German Participation Group, the Instituto de Astrofisica de Canarias, the Michigan State/Notre Dame/JINA Participation Group, Johns Hopkins University, Lawrence Berkeley National Laboratory, Max Planck Institute for Astrophysics, New Mexico State University, New York University, the Ohio State University, University of Portsmouth, Princeton University, University of Tokyo, the University of Utah, Vanderbilt University, University of Virginia, University of Washington, and Yale University.

Funding for the Brazilian Participation Group has been provided by the Ministério de Ciência e Tecnologia (MCT), Fundação Carlos Chagas Filho de Amparo à Pesquisa do Estado do Rio de Janeiro (FAPERJ), Conselho Nacional de Desenvolvimento Científico e Tecnológico (CNPq), and Financiadora de Estudos e Projetos (FINEP).

Bibliography

Ahn, C. P., Alexandroff, R., Allende Prieto, C., et al. 2014, ApJS, 211, 17
Ahn, C. P., Alexandroff, R., Allende Prieto, C., et al. 2012, ApJS, 203, 21
Alam, S., Albareti, F. D., Allende Prieto, C., Anders, F., & Anderson, S. F., e. 2015, ApJS, 219, 12
Allende Prieto, C., Majewski, S. R., Schiavon, R., et al. 2008a, Astronomische Nachrichten, 329, 1018
Allende Prieto, C., Sivarani, T., Beers, T. C., et al. 2008b, AJ, 136, 2070
Anders, F., Chiappini, C., Santiago, B. X., et al. 2014, A&A, 564, A115
Aumer, M. & Binney, J. J. 2009, MNRAS, 397, 1286
Bailer-Jones, C. A. L. 2011, MNRAS, 411, 435
Balbinot, E., Santiago, B., Girardi, L., et al. 2012, in Astronomical Society of the Pacific Conference Series, Vol. 461, Astronomical Data Analysis Software and Systems XXI, ed. P. Ballester, D. Egret, & N. P. F. Lorente, 287
Bensby, T., Feltzing, S., & Oey, M. S. 2014, A&A, 562, A71
Bertelli, G., Girardi, L., Marigo, P., & Nasi, E. 2008, A&A, 484, 815
Binney, J. 2014, ArXiv e-prints
Binney, J., Burnett, B., Kordopatis, G., et al. 2014, MNRAS, 437, 351
Boeche, C., Chiappini, C., Minchev, I., et al. 2013a, A&A, 553, A19
Boeche, C., Siebert, A., Piffl, T., et al. 2013b, A&A, 559, A59
Boeche, C., Siebert, A., Williams, M., et al. 2011, AJ, 142, 193
Bovy, J., Allende Prieto, C., Beers, T. C., et al. 2012a, ApJ, 759, 131
Bovy, J., Nidever, D. L., Rix, H.-W., et al. 2014, ApJ, 790, 127
Bovy, J., Rix, H.-W., Hogg, D. W., et al. 2012b, ApJ, 755, 115
Brandt, T. D. & Huang, C. X. 2015a, ApJ, 807, 58
Brandt, T. D. & Huang, C. X. 2015b, ApJ, 807, 24
Breddels, M. A., Smith, M. C., Helmi, A., et al. 2010, A&A, 511, A90
Bressan, A., Marigo, P., Girardi, L., et al. 2012, MNRAS, 427, 127
Burnett, B. & Binney, J. 2010, MNRAS, 407, 339
Burnett, B., Binney, J., Sharma, S., et al. 2011, A&A, 532, A113
Carollo, D., Beers, T. C., Bovy, J., et al. 2012, ApJ, 744, 195
Carollo, D., Beers, T. C., Chiba, M., et al. 2010, ApJ, 712, 692
Carollo, D., Beers, T. C., Lee, Y. S., et al. 2007, Nature, 450, 1020
Chabrier, G. 2003, PASP, 115, 763
Chen, Y., Bressan, A., Girardi, L., et al. 2015, ArXiv e-prints
Cheng, J. Y., Rockosi, C. M., Morrison, H. L., et al. 2012, ApJ, 752, 51
Chiappini, C., Minchev, I., Anders, F., et al. 2015, Astrophysics and Space Science Proceedings, 39, 111
Correnti, M., Bellazzini, M., Ibata, R. A., Ferraro, F. R., & Varghese, A. 2010, ApJ, 721, 329
Cutri, R. M., Skrutskie, M. F., van Dyk, S., et al. 2003, 2MASS All Sky Catalog of point sources.
da Silva, L., Girardi, L., Pasquini, L., et al. 2006, A&A, 458, 609
Deng, L.-C., Newberg, H. J., Liu, C., et al. 2012, Research in Astronomy and Astrophysics, 12, 735
Eisenstein, D. J., Weinberg, D. H., Agol, E., et al. 2011, AJ, 142, 72
Fukugita, M., Ichikawa, T., Gunn, J. E., et al. 1996, AJ, 111, 1748
Gilmore, G. 2012, in Astronomical Society of the Pacific Conference Series, Vol. 458, Galactic Archaeology: Near-Field Cosmology and the Formation of the Milky Way, ed. W. Aoki, M. Ishigaki, T. Suda, T. Tsujimoto, & N. Arimoto, 147
Girardi, L., Barbieri, M., Groenewegen, M. A. T., et al. 2012, TRILEGAL, a TRIdimensional modeL of thE GALaxy: Status and Future, ed. A. Miglio, J. Montalbán, & A. Noels, 165
Girardi, L., Groenewegen, M. A. T., Hatziminaoglou, E., & da Costa, L. 2005, A&A, 436, 895
Gunn, J. E., Carr, M., Rockosi, C., et al. 1998, AJ, 116, 3040
Gunn, J. E., Siegmund, W. A., Mannery, E. J., et al. 2006, AJ, 131, 2332
Harris, W. E. 1996, AJ, 112, 1487
Hayden, M. R., Bovy, J., Holtzman, J. A., et al. 2015, ArXiv e-prints
Høg, E., Fabricius, C., Makarov, V. V., et al. 2000, A&A, 355, L27
Holtzman, J. A., Shetrone, M., Johnson, J. A., et al. 2015, ArXiv e-prints:1501.04110
Ivezić, Ż., Connolly, A., VanderPlas, J., & Gray, A. 2013, Statistics, Data Mining, and Machine Learning in Astronomy
Jørgensen, B. R. & Lindegren, L. 2005, A&A, 436, 127
Junqueira, T. C., Chiappini, C., Lépine, J. R. D., Minchev, I., & Santiago, B. X. 2015, MNRAS, 449, 2336
Jurić, M., Ivezić, Ž., Brooks, A., et al. 2008, ApJ, 673, 864
Kordopatis, G., Binney, J., Gilmore, G., et al. 2015, MNRAS, 447, 3526
Kordopatis, G., Gilmore, G., Steinmetz, M., et al. 2013, AJ, 146, 134
Kordopatis, G., Recio-Blanco, A., de Laverny, P., et al. 2011, A&A, 535, A106
Lee, Y. S., Beers, T. C., Allende Prieto, C., et al. 2011a, AJ, 141, 90
Lee, Y. S., Beers, T. C., An, D., et al. 2011b, ApJ, 738, 187
Lee, Y. S., Beers, T. C., Sivarani, T., et al. 2008a, AJ, 136, 2022
Lee, Y. S., Beers, T. C., Sivarani, T., et al. 2008b, AJ, 136, 2050
Majewski, S. R., Zasowski, G., & Nidever, D. L. 2011, ApJ, 739, 25
Matijevič, G., Zwitter, T., Bienaymé, O., et al. 2012, ApJS, 200, 14
Mészáros, S., Holtzman, J., García Pérez, A. E., et al. 2013, AJ, 146, 133
Miglio, A. 2012, Asteroseismology of Red Giants as a Tool for Studying Stellar Populations: First Steps, ed. A. Miglio, J. Montalbán, & A. Noels, 11
Miglio, A., Chiappini, C., Morel, T., et al. 2013, in European Physical Journal Web of Conferences, Vol. 43, 3004
Minchev, I., Chiappini, C., & Martig, M. 2013, A&A, 558, A9
Minchev, I., Chiappini, C., & Martig, M. 2014a, A&A, 572, A92
Minchev, I., Chiappini, C., & Martig, M. 2014b, in EAS Publications Series, Vol. 67, EAS Publications Series, 323–329
Minniti, D., Saito, R. K., Alonso-García, J., Lucas, P. W., & Hempel, M. 2011, ApJ, 733, L43
Nidever, D. L., Zasowski, G., Majewski, S. R., et al. 2012, ApJ, 755, L25
Perryman, M. A. C. 1989, Nature, 340, 111
Perryman, M. A. C., de Boer, K. S., Gilmore, G., et al. 2001, A&A, 369, 339
Perryman, M. A. C., Lindegren, L., Kovalevsky, J., et al. 1997, A&A, 323, L49
Pinsonneault, M. H., Elsworth, Y., Epstein, C., et al. 2014, ApJS, 215, 19
Pinsonneault, M. H., Terndrup, D. M., & Yuan, Y. 2000, in Astronomical Society of the Pacific Conference Series, Vol. 198, Stellar Clusters and Associations: Convection, Rotation, and Dynamos, ed. R. Pallavicini, G. Micela, & S. Sciortino, 95
Pont, F. & Eyer, L. 2004, MNRAS, 351, 487
Rieke, G. H. & Lebofsky, M. J. 1985, ApJ, 288, 618
Rodrigues, T. S., Girardi, L., Miglio, A., et al. 2014, MNRAS, 445, 2758
Schlesinger, K. J., Johnson, J. A., Rockosi, C. M., et al. 2012, ApJ, 761, 160
Schönrich, R. & Bergemann, M. 2014, MNRAS, 443, 698
Schönrich, R., Binney, J., & Asplund, M. 2012, MNRAS, 420, 1281
Serenelli, A. M., Bergemann, M., Ruchti, G., & Casagrande, L. 2013, MNRAS, 429, 3645
Silva Aguirre, V., Basu, S., Brandão, I. M., et al. 2013, ApJ, 769, 141
Silva Aguirre, V., Casagrande, L., Basu, S., et al. 2012, ApJ, 757, 99
Skrutskie, M. F., Cutri, R. M., Stiening, R., et al. 2006, AJ, 131, 1163
Smee, S. A., Gunn, J. E., Uomoto, A., et al. 2013, AJ, 146, 32
Smolinski, J. P., Lee, Y. S., Beers, T. C., et al. 2011, AJ, 141, 89
Steinmetz, M., Zwitter, T., Siebert, A., et al. 2006, AJ, 132, 1645
Tang, J., Bressan, A., Rosenfield, P., et al. 2014, MNRAS, 445, 4287
van Leeuwen, F., ed. 2007, Astrophysics and Space Science Library, Vol. 350, Hipparcos, the New Reduction of the Raw Data
Yanny, B., Rockosi, C., Newberg, H. J., et al. 2009, AJ, 137, 4377
Zasowski, G., Johnson, J. A., Frinchaboy, P. M., et al. 2013, AJ, 146, 81
Zucker, D. B., de Silva, G., Freeman, K., Bland-Hawthorn, J., & Hermes Team. 2012, in Astronomical Society of the Pacific Conference Series, Vol. 458, Galactic Archaeology: Near-Field Cosmology and the Formation of the Milky Way, ed. W. Aoki, M. Ishigaki, T. Suda, T. Tsujimoto, & N. Arimoto, 421
Zwitter, T., Matijevič, G., Breddels, M. A., et al. 2010, A&A, 522, A54

[1] Instituto de Física, Universidade Federal do Rio Grande do Sul, Caixa Postal 15051, Porto Alegre, RS - 91501-970, Brazil
[2] Laboratório Interinstitucional de e-Astronomia - LIneA, Rua Gal. José Cristino 77, Rio de Janeiro, RJ - 20921-400, Brazil

[3] Leibniz-Institut für Astrophysik Potsdam (AIP), An der Sternwarte 16, 14482, Potsdam, Germany
[4] Osservatorio Astronomico di Padova - INAF, Vicolo dell'Osservatorio 5, I - 35122 Padova, Italy
[5] Universidade Federal do Rio de Janeiro, Observatório do Valongo, Ladeira do Pedro Antônio 43, 20080-090 Rio de Janeiro, Brazil
[6] Observatório Nacional, Rua Gal. José Cristino 77, Rio de Janeiro, RJ - 20921-400, Brazil
[7] Observatoire de la Cote d'Azur, Laboratoire Lagrange, CNRS UMR 7923, B.P. 4229, 06304 Nice Cedex, France
[8] School of Physics and Astronomy, University of Birmingham, Edgbaston, Birmingham, B15 2TT, United Kingdom
[9] Institut d'Astrophysique et de Géophysique, Allée du 6 août, 17 - Bât. B5c, B-4000 Liège 1 (Sart-Tilman), Belgium
[10] Department of Astronomy and Astrophysics, The Pennsylvania State University, University Park, PA 16802
[11] Institute for Gravitation and the Cosmos, The Pennsylvania State University, University Park, PA 16802
[12] Department of Physics and JINA Center for the Evolution of the Elements, University of Notre Dame, Notre Dame, IN 46556, USA
[13] Department of Physics & Astronomy, Texas Christian University, TCU Box 298840, Fort Worth, TX 76129
[14] Department of Astronomy and Space Science, Chungnam National University, Daejeon 34134, Republic of Korea
[15] Dept of Physics and Astronomy, Johns Hopkins University, Baltimore, MD, 21210, USA

A.1. APOGEE distances and calibration of stellar parameters

For the computation of distances to APOGEE stars, we make use of the ASPCAP stellar parameters bundled in the twelth data release of the Sloan Digital Sky Survey (SDSS DR12; Alam et al. 2015). The APOGEE data products contained in this release are described in detail in Holtzman et al. (2015). While we generally use the stellar parameter calibrations provided by these authors, we have adopted slightly different calibrations for metallicity and surface gravity, which are explained below.

Our APOGEE distances will be released within an SDSS DR12 value-added APOGEE distance catalogue.

Surface gravity for red-clump stars: Holtzman et al. (2015) use the very accurate and precise surface gravities from the APOGEE-*Kepler* sample (Pinsonneault et al. 2014) to calibrate out systematic shifts in the surface gravities delivered by ASPCAP. They demonstrate (their Fig. 4) that these systematics are different for red-giant branch (RGB) and core-He burning red-clump stars (RC). The offset between both groups is about 0.2 dex. However, the authors only provide a surface gravity calibration for RGB (their formula 3), and for RC stars defer the reader to the APOGEE RC catalogue described by Bovy et al. (2014) who provide very precise distances to these stars. Because we wanted to test our distance code on *all* APOGEE giant stars, we have separately fit the calibration relation for the stars contained in the RC catalogue:

$$\log g_{\rm RC} = \log g_{\rm calib} - (7.21 \cdot 10^{-5} \cdot (T_{\rm eff}[{\rm K}] - 4400) + 0.129)$$

Metallicities in the super-solar regime: ASPCAP metallicities have been calibrated using open and globular cluster metallicities from the literature. Fig. 6 of Holtzman et al. (2015) shows the result of the "external" metallicity calibration: in the metal-poor regime, the raw ASPCAP metallicities are up to 0.3 dex too high compared to the literature, while the values are similar at solar metallicities. The authors have therefore opted to fit a second-order polynomial to the data (their formula 6). But because there are very few calibration clusters above solar metallicity, the quadratic calibration relation may be overfitting the data at the metal-rich end, and therefore overestimate metallicities in this regime. We have thus opted to use the calibrated values *only when* [Z/H]< 0.0, and to otherwise use the uncalibrated values.

A.2. SEGUE distances

For the computation of SEGUE distances, we use the results of the SEGUE Stellar Parameter Pipeline (SSPP; Lee et al. 2008a,b, 2011a; Smolinski et al. 2011) for a clean sample of G dwarfs (details will be provided in Brauer 2015). From SDSS DR8 to DR9, it underwent a couple of modifications providing improved stellar parameters for all SEGUE objects within the scope of DR9. In particular, there are some obvious systematic shifts in the individual parameters when comparing DR8 and DR9 SSPP values for the same objects.

The most significant deviation is observed for the surface gravity showing a clear overall decrease of the parameter by 0.2 dex to 0.3 dex to lower values. This finding is in agreement with the fact that the DR9 surface gravity is in general lower by about $\sim$ 0.2 dex (Rockosi et al. 2015, in prep.). Possible explanations for the decrease are the following: (1) the surface gravity estimates from the re-analysis of the high-resolution spectra that are used to calibrate the DR9 SSPP results are in general lower by 0.13 dex than those from the older high-resolution analysis, (2) for some of the $\log g$ estimation methods utilised by the SSPP, new synthetic spectral grids were used, and (3) the line index methods `MgH` and `CaI2` were not considered any longer – which may have had a substantial effect since those estimators produced higher $\log g$ values compared to others. The overall lower gravity is certainly caused by a combination of the above facts.

Besides the shift in surface gravity, the temperatures in DR9 tend to be systematically larger than in DR8 by $\sim$ 50 K. This temperature shift occurs due to the IRFM temperature scale being utilised to calibrate the SSPP DR9 temperature estimators.

While the metallicity scale did not change significantly, the [α/Fe] abundances shifted to higher values by about 0.1 dex.

$\log g$ *calibration:* As shown in Sec. A.4, accurate absolute surface gravity values are crucial for computing spectro-photometric distances. Any systematic under- or overestimation of the surface gravity will lead to significant under- or overestimation of our distances. Hence, as justified in Sec. A.3.3., we decided to calibrate the SEGUE DR9 surface gravity values by applying a shift of 0.25 dex and thus increasing the *logg* of each object in the G-dwarf sample by the same amount. Apart from this modification, we use the SEGUE DR9 values delivered by the SSPP.

A.3. RAVE distances

In this work, we have used the RAVE giant sample assembled by Boeche et al. (2013a). It comprises stars with the highest quality spectra and abundances. The following quality criteria have been applied: (1) only spectra with a signal-to-noise ratio of at least 60 were selected on which the RAVE pipeline converged to a single point of the parameter space (Flag `Algo_Conv = 0`), (2) the chemical pipeline converged ($\chi^2 < 1000$), (3) the number of defective pixels along the spectrum is small (`frac` > 0.99), and (4) every object that is not classified as a normal star according to the morphological classification described in Matijevič et al. (2012) was excluded. Like Binney et al. (2014), we use the stellar parameters from DR4 (Kordopatis et al. 2013). The applied

cuts to select RAVE giants are 0.5 dex $< \log g <$ 3.5 dex and 4000 K $< T_{\rm eff} <$ 5500 K. This ensures that only cool giants are selected and problems with the grid limits of the automated pipeline are avoided by setting the lower limit in $\log g$. The resulting RAVE giant sample comprises 9098 stars.

We will also provide distances for the full RAVE DR4 sample in the near future.

Chapter B

Publications

The author of this thesis contributed to the following publications during his PhD time. Versions of the first- and second-author publications are presented in chapters 2-6.

A.1. Refereed First-author publications

- F. Anders, C. Chiappini, B. X. Santiago, H. J. Rocha-Pinto, L. Girardi, L. N. da Costa, et al. (2014) *Chemodynamics of the Milky Way. I. The first year of APOGEE data*, A&A 564, A115, arXiv:1311.4549
- F. Anders, C. Chiappini, T. S. Rodrigues, A. Miglio, J. Montalbán, B. Mosser, L. Girardi, M. Valentini, A. Noels, et al. (2016) *Galactic Archaeology with asteroseismology and spectroscopy: Red giants observed by CoRoT and APOGEE*, A&A 597, A30, arXiv:1604.07763
- F. Anders, C. Chiappini, T. S. Rodrigues, T. Piffl, B. Mosser, A. Miglio, J. Montalbán, L. Girardi, I. Minchev, M. Valentini, M. Steinmetz (2016) *Galactic Archaeology with CoRoT and APOGEE: Creating mock observations from a chemodynamical model*, AN 337, 8-9, 926, arXiv:1604.07771
- F. Anders, C. Chiappini, I. Minchev, A. Miglio, J. Montalbán, , T. S. Rodrigues, B. X. Santiago, et al. (2017) *Red giants observed by CoRoT and APOGEE: The evolution of the Milky Way's radial metallicity gradient*, A&A, in press, arXiv:1608.04951

A.2. Refereed co-author publications

- E. Fernández-Alvar, L. Carigi, C. Allende Prieto, ..., F. Anders, et al. (2017): *Chemical trends in the Galactic halo from APOGEE data*, MNRAS 465, 2, 1586, arXiV:1611.01249
- R. Schiavon, O. Zamora, R. Carrera, ..., F. Anders, ... (2017): *Chemical tagging with APOGEE: discovery of a large population of N-rich stars in the inner Galaxy*, MNRAS 465, 1, 501, arXiV:1606.05651
- I. Minchev, M. Steinmetz, C. Chiappini, M. Martig, F. Anders, G. Matijevic, R. S. de Jong (2017): *The Relationship between Mono-abundance and Mono-age Stellar Populations in the Milky Way Disk*, ApJ 834, 1, 27, arXiV:1608.04737
- J. G. Fernández-Trincado, A. C. Robin, ..., F. Anders, et al. (2016): *Discovery of a Metal-poor Field Giant with a Globular Cluster Second-generation Abundance Pattern*, ApJ 833, 2, 132, arXiV:1604.01279
- D. Souto, K. Cunha, V. Smith, ..., F. Anders, et al. (2016): *Chemical Abundances in a Sample of Red Giants in the Open Cluster NGC 2420 from APOGEE*, ApJ 830, 1, 35, arXiV:1607.06102
- G. Kordopatis, R. F. G. Wyse, C. Chiappini, I. Minchev, F. Anders, B. Santiago (2016): *Cardinal kinematics: I. Rotation fields of the APOGEE Survey*, submitted to MNRAS, arXiV:1609.04394
- M. Valentini, C. Chiappini, A. Miglio, J. Montalbán, T. S. Rodrigues, B. Mosser, F. Anders, the CoRoT Red-Giant Working Group, the GES Consortium (2016): *The CoRoT-GES Collaboration: Improving red giants spectroscopic surface gravitity and abundances with asteroseismology*, AN 337, 8-9, 970, arXiV:1609.04280
- S. R. Majewski, APOGEE Team, APOGEE-2 Team (2016): *The Apache Point Observatory Galactic Evolution Experiment (APOGEE) and its successor, APOGEE-2*, AN 337, 8-9, 863
- The SDSS Collaboration: F. D. Albareti, C. Allende Prieto, A. Almeida, F. Anders, et al. (2016): *The Thirteenth Data Release of the Sloan Digital Sky Survey: First Spectroscopic Data from the SDSS-IV Survey MApping Nearby Galaxies at Apache Point Observatory*, submitted to ApJS, arXiV:1608.02013
- B. X. Santiago, D. E. Brauer, F. Anders, C. Chiappini, A. B. Queiroz, L. Girardi, et al. (2016): *Spectro-photometric distances to stars: A general purpose Bayesian approach*, A&A 585, A42, arXiV:1501.05500
- M. Schultheis, K. Cunha, G. Zasowski, ..., F. Anders, et al. (2016): *Evidence for a metal-poor population in the inner Galactic bulge*, A&A 584, A45, arXiV:1509.07104
- J. A. Holtzman, M. D. Shetrone, J. A. Johnson, C. Allende Prieto, F. Anders, et al. (2015): *Abundances, Stellar Parameters, and Spectra from the SDSS-III/APOGEE Survey*, AJ 150, 5, 148, arXiV:1501.04110
- M. Martig, H.-W. Rix, V. Silva Aguirre, ..., F. Anders, et al. (2015): *Young α-enriched giant stars in the solar neighbourhood*, MNRAS 451, 2, 2230, arXiV:1412.3453
- M. R. Hayden, J. Bovy, J. A. Holtzman, ..., F. Anders, et al. (2015): *Chemical Cartography with APOGEE: Metallicity Distribution Functions and the Chemical Structure of the Milky Way Disk*, ApJ 808, 2, 132, arXiV:1503.02110

- S. Alam, F. D. Albareti, C. Allende Prieto, F. Anders, et al. (2015): *The Eleventh and Twelfth Data Releases of the Sloan Digital Sky Survey: Final Data from SDSS-III*, ApJS 219, 1, 12, arXiV:1501.00963
- C. Chiappini, F. Anders, T. S. Rodrigues, A. Miglio, J. Montalbán, B. Mosser, et al. (2015): *Young [α/Fe]-enhanced stars discovered by CoRoT and APOGEE: What is their origin?*, A&A 576, L12, arXiV:1503.06990
- E. C. Herenz, L. Wisotzki, M. Roth & F. Anders (2015) - *Where is the Fuzz? Undetected Lyman α Nebulae around QSOs at z~2.3*, A&A 576, A115, arXiv:1502.05132
- T. S. Rodrigues, L. Girardi, A. Miglio, D. Bossini, . . . , F. Anders, et al. (2014) - *Bayesian distances and extinctions for giants observed by Kepler and APOGEE*, MNRAS 445, 3, 2758, arXiv:1410.1350
- D. L. Nidever, J. Bovy, J. Bird, B. H. Andrews, . . . , F. Anders, et al. (2014) - *Tracing Chemical Evolution over the Extent of the Milky Way's Disk with APOGEE Red Clump Stars*, MNRAS 445, 3, 2758, arXiv:1409.3566
- T. S. Rodrigues, L. Girardi, A. Miglio, D. Bossini, . . . , F. Anders, et al. (2014) - *Bayesian distances and extinctions for giants observed by Kepler and APOGEE*, ApJ 796, 1, 38, arXiv:1410.1350
- M. Schultheis, G. Zasowski, C. Allende Prieto, F. Anders, et al. (2014) - *Extinction Maps toward the Milky Way Bulge: Two-dimensional and Three-dimensional Tests with APOGEE*, AJ 148, 1, 24, arXiv:1405.2180
- C. P. Ahn, R. Alexandroff, C. Allende Prieto, F. Anders, et al. (2014) - *The Tenth Data Release of the Sloan Digital Sky Survey: First Spectroscopic Data from the SDSS-III Apache Point Observatory Galactic Evolution Experiment*, ApJS 211, 2, 17, arXiv:1307.7735

A.3. Unrefereed publications

- M. Kuehnel, P. Kretschmar, E. Nespoli, . . . , F. Anders, et al. (2015): *The Be X-ray Binary Outburst Zoo II*, Proceedings of "A Synergistic View of the High Energy Sky" - 10th INTEGRAL Workshop (INTEGRAL 2014). Published online at http://pos.sissa.it/cgi-bin/reader/conf.cgi?confid=228
- F. Anders, C. Chiappini, T. S. Rodrigues, A. Miglio, J. Montalbán, B. Mosser, L. Girardi, M. Valentini, M. Steinmetz (2015): *Synergies of CoRoT asteroseismology and APOGEE spectroscopy – Applications to Galactic Archaeology*, IAU General Assembly, Meeting 29, id.2256879
- M. Valentini, C. Chiappini, A. Miglio, J. Montalbán, B. Mosser, T. Morel, T. S. Rodrigues, F. Anders, M. Steinmetz, L. Girardi (2015): *The CoRoT-GES Collaboration: the joint-action of asteroseismology and spectroscopy in the field of Galactic Archaeology*, IAU General Assembly, Meeting 29, id.2257176
- C. Chiappini, I. Minchev, F. Anders, D. E. Brauer, C. Boeche, M. Martig (2015): *New Observational Constraints to Milky Way Chemodynamical Models*, Asteroseismology of Stellar Populations in the Milky Way, Astrophysics and Space Science Proceedings 39, 111, arXiv:1409.2275
- J. Sobeck, S. Majewski, F. Hearty, . . . , F. Anders, et al. (2014): *APOGEE-2: The Second Phase of the Apache Point Observatory Galactic Evolution Experiment in SDSS-IV*, American Astronomical Society, AAS Meeting #223, id.440.06

Chapter C

Acknowledgements

This work would not have been possible without the support and help of my family, my friends, and many of my colleagues. I am very grateful to all of them.

I want to thank first and foremost Cristina Chiappini without whom I would probably not have started a PhD position, and who supported me enormously during my AIP time. I realise that not all PhD candidates have the fortune to have such an emphatic, intelligent, experienced, sharing, and trusting supervisor...

I am also indebted to Matthias Steinmetz, Roelof de Jong and Matthias Steffen for their confidence in me and their help whenever it was needed. A big thanks also goes to Adriane Liermann, Lutz Wisotzki and Carsten Denker for organising the Leibniz Garduate School at AIP.

Furthermore, I would like to thank my Brazilian colleagues Basílio Santiago, Anna Queiroz, Thaíse Rodrigues, Beatriz Barbuy, Léo Girardi, Hélio Rocha-Pinto, Hélio Perottoni, Katia Cunha, Luiz Nicolaci and Marcio Maia, my AIP colleagues Karl-Heinz Böning, Marica Valentini, Christian Herenz and Kris Youakim, the valued Drs. Klaus Fuhrmann (ING La Palma) and Mathias Schultheis (OCA Nice), as well as my CoRoT collaborators Andrea Miglio, Benoît Mosser and Josefina Montalbán for their collaborative spirit that really made a difference...

Finally, I send my love to Franzi because she is the best. ;)